Modeling, control, and optimization of fuel/air mixing in a lean premixed swirl combustor using fuel staging to reduce pressure pulsations and NOx emissions

vorgelegt von
Diplom-Ingenieur
Arnaud Lacarelle

Von der Fakultät V – Verkehrs- und Maschinensysteme
der Technischen Universität Berlin
zur Erlangung des akademischen Grades

Doktor der Ingenieurwissenschaften
– Dr.-Ing. –

genehmigte Dissertation

Promotionsausschuss:

Vorsitzender:	Prof. Dr.-Ing. Jürgen Thorbeck
Gutachter:	Prof. Dr.-Ing. Christian Oliver Paschereit
Gutachter:	Prof. Dr. Laszlo Fuchs

Tag der wissenschaftlichen Aussprache: 20. Juli 2011

Berlin 2011
D 83

ISBN 978-3-7983-2381-0 (Print)
ISBN 978-3-7983-2382-7 (Online-Version)

Berlin 2011

∞ Gedruckt auf säurefreiem alterungsbeständigem Papier

Druck/ Printing:	docupoint GmbH Magdeburg Otto-von-Guericke-Allee 14, D-39179 Barleben
Vertrieb/ Publisher:	Universitätsverlag der TU Berlin Universitätsbibliothek Fasanenstr. 88 (im VOLKSWAGEN-Haus) D-10623 Berlin Tel.: +49(0)30 314-76131; Fax: +49(0)30 314-76133 E-Mail: publikationen@ub.tu-berlin.de http://www.univerlag.tu-berlin.de

À mes parents

Danksagung

Nach einem halben Jahrzehnt in einem Institut und nach etwas mehr als einem viertel Jahrhundert auf der Welt gibt es viele Personen, bei denen man sich bedanken kann. Diese Leute haben bewusst oder unbewusst dazu beigetragen, dass die vorliegende Arbeit und der Autor, der sie geschrieben hat, so geworden sind, wie sie heute sind. An dieser Stelle möchte ich mich zuerst und insbesondere bei meinem Doktorvater Prof. Dr.-Ing. C. O. Paschereit dafür bedanken, dass er mir die Möglichkeit gegeben hat, über die Thematik der Mischung in Gasbrennern zu forschen. Bei ihm habe ich gelernt, dass aus dem Nichts etwas entstehen kann. Er hat mir nicht nur ermöglicht, fachlich zu wachsen. Vielmehr habe ich durch seine sehr offene und persönliche, fordernde aber auch fördernde Art sehr viel von ihm gelernt. Ich möchte mich auch bei Prof. Dr. L. Fuchs für die Annahme des Beisitzes des Promotionsauschusses sowie bei Prof. Dr.-Ing J. Thorbek für die Übernahme der Leitung des Promotionsauschusses bedanken. Außerdem möchte ich mich bei Prof. Dr. B. R. Noack und Prof. Dr. D. Greenblatt für die fachlichen Diskussionen bedanken. Ein besonderer Dank gebührt auch Dr.-Ing. C. N. Nayeri für seine Offenheit, sein Verständnis und seine anhaltend positive Einstellung.

Den Kollegen des Hermann Föttinger Instituts ist natürlich ebenfalls für sehr viel (darunter Zeit, Kompetenz, Humor, Diskussionen,...) zu danken. Vor allem möchte ich mich bei der ersten Generation von Mitarbeitern bedanken: Daniel, Frank, Jonas, Mirko und Peter. Einen wichtigen Beitrag zu der Entstehung dieser Arbeit haben auch zahlreiche Studenten und Diplomanden geleistet. Hier zu erwähnen sind u.a. Mario, Lars, Andy, Nick, Daniel, Luna, Ashley, Alexander und Sabine. Hinzu kommen viele weitere Kollegen und andere Mitarbeiter des Instituts, u.a. die ganze Verbrennungstruppe (Ahmed, Sebastian S., Sebastian G., Katharina, Christina, Christian, Holger), die Kollegen der Aerodynamik (Stefan, Kilian, Yousef, Yogesh) und weitere wichtige Mitarbeiter (Lilli, Frau Pätzold, Heiko, T.

Dessin, Willy, Horst, Basti, Rainer). Bei den Kollegen vom SFB möchte ich mich auch herzlich bedanken: Gregor, Jens, Mark, Oliver, Tino.

Während der Erstellung der Dissertation gab es natürlich viele, für mich sehr wichtige Wegbegleiter und an dieser Stelle möchte ich mich bei Mirco, David, Antoine, Sebastien und Marie, die Leute von der Improtruppe Schnürsenkel und mal wieder bei Peter bedanken. Sie haben das Leben in Berlin viel schöner gemacht. Was das Leben außerhalb Deutschlands betrifft, bedanke ich mich bei Gregory, Benjamin und Joanny für ihre treue Freundschaft. Um diesen Absatz abzuschließen: Es wäre nicht viel entstanden ohne die Unterstützung von meinem Onkel Alain, meiner Tante Gilberte und meiner Schwester Blandine sowie seit ein paar Jahren von Judith.

Zusammenfassung

Diese Arbeit beschäftigt sich mit der Luft/Brennstoff Vermischung in einem vorgemischten drallinduzierten Brenner für Gasturbinen. Die Schwerpunkte liegen in der Modellierung, Kontrolle und Optimierung des Mischungsvorgangs, um Druckpulsationen (auch thermoakustische Schwingungen genannt) und NO_x-Emissionen zu kontrollieren. Das Modell stützt sich hauptsächlich auf Untersuchungen, die in einem Wasserkanal durchgeführt werden. Die Standard-Gaseindüsung des Brenners wird mit zwei weiteren Brennstoffeindüsungsstufen ergänzt. Durch Anpassung der Brennstoffverteilung können thermoakustische Oszillationen deutlich reduziert werden, ohne dass es zu höheren NO_x-Emissionen als bei der Standard-Eindüsung führt. Messungen der mittleren, turbulenten und kohärenten Strömungsfelder sowie des passiven skalaren Konzentrationsfeldes bestätigen die Ähnlichkeit zwischen Wasserkanal und Brennkammer. Desweiteren zeigen Messungen im reagierenden Fall, dass die Flamme einen geringen Einfluss auf das Strömungsfeld stromaufwärts der Verbrennungszone hat wenn diese nicht innerhalb des Brenners verankert ist. Somit ist die Modellierung aus Untersuchungen in nicht reagierenden Systemen gerechtfertigt.

Die Qualität der Mischung am Brenneraustritt wird für verschiedene Betriebsbedingungen und an verschiedenen Stellen modelliert. Um die Genauigkeit des Modells zu verbessern, wird die Position der Flamme aufgenommen, um die Mischungsqualitaet an der Flamme abzuschaetzen. Mithilfe einer empirischen Korrelation können dann die NO_x-Emissionen genauer vorhergesagt werden. Ein wichtiges Werkzeug zur Entwicklung von stabilen Brennern ist die Flammentransferfunktion. In nicht reagierender Strömung kann zuerst die sogenannte Mischungstransferfunktion gemessen werden. Diese wird aus der Sprungantwort der Mischung und mithilfe von Hochgeschwindigkeits-Konzentrationsmessungen im Wasserkanal gemessen. Die Mischungstransferfunktion wird dann mit der Flammenposition kombiniert, um eine Abschätzung der reagierenden Flammentransferfunktion

zu bekommen. Die Ergebnisse zeigen, dass sich die geschätzte Flammentransferfunktion der in der Brennkammer gemessenen gut annähert.

Um die Brennstoffverteilung am Brenner optimal einstellen zu können, wird ein sogenannter Extremwertregler implementiert. Der Regler stellt die Brennstoffverteilung so ein, dass Druckpulsationen und NO_x-Emissionen reduziert werden können. Die Fähigkeit des Reglers, lokale Minima zu umgehen, kann durch den Einbau der Stabilitäts- und Emissionsmodelle verbessert werden. Letztlich wurden sowohl aktive als auch passive Maßnahmen eingesetzt, um die Mischungsqualität am Brenneraustritt zu verbessern. In Wasser kann eine Verbesserung der Vermischung am Brenneraustritt mithilfe von rechteckigen Brennstoffpulsationen nachgewiesen werden. Des Weiteren können selbst-oszillierende (fluidische) Aktuatoren an einer generischen Konfiguration sehr gute Ergebnisse erzielen, bei der die Qualität der Mischung, gemessen mit dem Danckwerts "Unmixedness" Kriterium, um etwa 50% verbessert werden kann.

Abstract

This work deals with the fuel/air mixing process in a lean premixed gas turbine combustor and how it can be modeled, controlled and optimized to reduce pressure pulsations and NO_x emissions. The methodology used to derive models is primarily based on cold flow measurements conducted in a water test rig. The standard fuel injection of the swirl-inducing burner is completed with two additional fuel injection stages. Through adjustment of the fuel distribution, stabilization of the combustion chamber can be achieved, with NO_x emissions comparable to the ones produced by standard fuel injection. Measurements of the mean turbulent and coherent flow fields as well as passive scalar mixing properties confirm the similarity of water test rig and combustion chamber. Furthermore, velocity and chemiluminescence measurements with combustion show that the flame has a weak influence on the mean and coherent flow properties just upstream of its stabilization location when it is not anchored inside the burner, validating the cold flow modeling approach.

The fuel/air mixing quality at the burner outlet is measured in the water test rig for numerous operating conditions at different axial locations and the flame position recorded in the combustion chamber is used to predict the real mixing quality at the flame. The information gained is then implemented using an experimental fit to more accurately predict the NO_x emissions of the burner over a wide operating range. A method is then developed to record and model the temporal response of the burner to fuel/air fluctuations. The so-called measured mixing transfer function confirms that variation of the fuel distribution in the burner strongly influences the convective time delays and partly explains the stabilizing effect of switching the fuel distribution. Using the recorded flame shape recorded by a camera, an estimation of the response of the flame to fuel/air fluctuations is obtained. Comparison with the directly measured flame transfer function shows that a satisfying estimation of the response of the flame to fuel/air fluctuations can be obtained with the new method.

Abstract

An extremum seeking controller (ESC) is implemented on the fuel distribution for the purpose of reduced pressure pulsations and NO_x emissions. The chemiluminescence signal is used as a surrogate of the NO_x emissions to increase the controller speed. The ESC is then able to track the best injection configuration when the operating conditions are varied as well as avoid local minimum when the cold flow model is taken into account. Passive and active fuel injection methods are then tested to improve the mixing quality at the burner outlet. The investigations show that high frequency fuel injection pulsations can improve the mixing quality recorded at the burner outlet. A fluidic injector array is then developed and implemented at the inlet of the burner. For this configuration, the mixing quality is only weakly influenced by the fluidic injector. However, tested in a generic configuration, these fluidic actuators improved the mixing quality by up to 50% over a wide range of operating conditions, confirming thus the effectivity of such devices.

Résumé

Le présent travail a pour sujet l'étude du procédé de mélange air/méthane dans un brûleur prémélangé pour turbine à gaz. L'accent est mis sur la modélisation, le contrôle et l'opti-misation de ce procédé pour contrôler les instabilités des combustions, connues sous le nom d'instabilités thermoacoustiques, ainsi que les émissions d'oxydes d'azote NO_x. Le model développé s'appuie en particulier sur de nombreuses expériences en environnement non réactif (canal à eau). L'injec-tion standard du brûleur est complétée par deux étages d'injection de gaz. Les instabilités thermoacoustiques peuvent être fortement réduites lorsque la répartition de méthane entre les 3 injecteurs est modifiée. Dans le cas d'une chambre de combustion stable, les nouvelles injections entraînent des émissions de NO_x comparable à l'injection standard. Des mesures de champs de courants moyens, turbulents et cohérents ainsi que d'un traceur passif montrent que le canal à eau et la chambre de combustion sans flamme donnent des résultats similaires. De plus lorsque la flamme se stabilise en aval du brûleur, l'influence de cette dernière sur le champ de courant est marginale. Les mesures en environnement non réactif décrivent ainsi très bien le système réactif, validant la modélisation à partir d'investigations dans le canal à eau.

La qualité du mélange à la sortie du brûleur est modélisée à différentes positions en fonction de différents paramètres de combustion dont la distribution de carburant. Pour augmenter la qualité du modèle, l'information sur la position axiale de la flamme est prise en compte. Une régression faite à partir d'une expression empirique permet de prédire quantitativement les émissions de NO_x. Ensuite, la fonction de transfert de la flamme est estimée à partir de mesures de concentrations instationnaires dans le canal à eau. La fonction de transfert du mélange ainsi obtenue est combinée avec la forme et la position de la flamme pour obtenir une estimation de la fonction de transfert de la flamme. Les résultats obtenus pour différentes distributions de gaz montrent que cette dernière approche raisonnablement bien la

fonction de transfert de la flamme mesurée directement dans la chambre de combustion.

Afin d'optimiser la distribution de gaz dans le brûleur, un contrôleur chercheur de valeurs extrêmes est implémenté. Le contrôleur ajuste la distribution de gaz afin de minimiser l'amplitude des oscillations de pression ainsi que les émissions de NO_x. Les modèles décrivant la qualité du mélange ainsi que le domaine de stabilité peuvent être intégrés dans le contrôleur pour éviter par exemple des minimas locaux. Enfin, des mesures passives et actives sont testées pour améliorer la qualité du mélange. Des tests conduits dans le canal à eau, il en ressort qu'un forçage carré de l'injection de carburant permet d'obtenir une nette amélioration de la micro homogénéisation. Afin de s'affranchir de valves mécaniques, des injecteurs oscillant de manière propre (type fluidic) remplacent les trous d'injection standards de gaz. D'excellents résultats sont obtenus, ces injecteurs permettant, dans une configuration générique, d'améliorer le mélange d'environ 50% (critère de Danckwerts).

Contents

Danksagung iv

Zusammenfassung vii

Abstract ix

Résumé xi

Nomenclature xxi

1 Introduction and Motivations 1

1.1 Generalities on dry low NO_x combustors 1

1.2 Fuel/air mixing and its impact on thermoacoustic instabilities and NO_x emissions 3

1.2.1 Thermoacousitc instabilities 3

1.2.2 Thermoacoustic instabilities, NO_x emissions and fuel/air mixing 6

1.3 On the modeling of turbulent mixing 9

1.3.1 What is mixing? 9

1.3.2 Mixing modeling 10

1.3.3 Mixing in oscillating flows 11

1.4 State of the art of fuel injection designs 12

1.4.1 Experimental steps 12

1.4.2 Fuel injection in gas turbine burners 13

1.5 Optimization of crossflow fuel injections 16

1.5.1 Passive modifications 16

1.5.2 Active forcing of the fuel injection 16

1.6 Control of the fuel/air mixing 18

1.7 Objectives, methodology and outline of the thesis 20

2 Technical background **25**
2.1 Turbulent flows . . . 25
2.1.1 Phenomenologies . . . 25
2.1.2 Statistical description of turbulent flows . . . 26
2.1.3 Length scales and energy cascade . . . 28
2.1.3.1 Integral length scales . . . 28
2.1.3.2 Micro-length scales . . . 29
2.1.3.3 Dissipation length scales . . . 29
2.2 Swirling flows . . . 35
2.2.1 The burner and mean flow field . . . 35
2.2.2 Swirl number . . . 36
2.2.3 Coherent structures . . . 39
2.3 Equations of turbulent flows . . . 40
2.3.1 General equations . . . 40
2.3.2 Scalar transport . . . 42
2.3.3 Scalar variance evolution . . . 43
2.3.4 Response to temporal fluctuations (Mixing Transfer Function) . . . 45
2.4 Jet in crossflow mixing . . . 48
2.4.1 Jet mixing regions and structures . . . 49
2.4.2 Scaling laws . . . 51
2.4.3 Mixing optimization of array of jets in crossflow . . . 52
2.4.3.1 Jet shape . . . 53
2.4.3.2 Passive injector arrangement . . . 53
2.4.3.3 Pulsed jets . . . 55
2.5 Water/air scalar mixing similitude . . . 55
2.5.1 Key dimensionless numbers . . . 55
2.5.2 Conversion from water to air . . . 56
2.5.3 Mixing quality evaluation . . . 61
2.5.4 Discussion about the limitations of the water/air analogy . . . 62
2.6 Combustion . . . 64
2.6.1 Laminar premixed flames . . . 64
2.6.2 Turbulent flames . . . 65
2.6.3 Flame regimes . . . 66
2.6.4 NO_x formation mechanisms . . . 70
2.6.4.1 Classification of the formation mechanisms 70

2.6.4.2 NO_x models 73
2.7 Acoustics 75
2.7.1 Wave equation and solutions 75
2.7.2 Influence of heat release on the wave equation 77

3 Experimental setup, measurement techniques, and post-processing 79
3.1 Fluorescence and Chemiluminescence 79
3.1.1 Physical principle 79
3.1.2 Formation mechanisms of OH* and CH* 80
3.1.3 OH*, CH*, CO_2* chemiluminescence 82
3.1.3.1 Characterization of chemiluminescence response of a combustor flame 82
3.1.3.2 Chemiluminescence and NO_x emissions . . 83
3.2 Burner and secondary fuel injections 84
3.3 Cold flow investigations 86
3.3.1 The water test rig 86
3.3.2 Hydrophone measurement 88
3.3.3 Laser Induced Fluorescence (LIF) for quantitative concentration measurements 89
3.3.3.1 Setup for LIF in water 89
3.3.3.2 Quantitative measurement principle 91
3.3.3.3 Homogeneous concentration 93
3.3.3.4 Measurement accuracy 95
3.3.3.5 Influence of mean flow on fluorescence intensity 95
3.4 Reacting flow investigations 96
3.4.1 The combustion chamber 96
3.4.2 Measurement techniques 97
3.4.2.1 Exhaust gas analysis 97
3.4.2.2 OH*/CH* - Chemiluminescence and spectrometry 99
3.4.2.3 Microphones and flame transfer function measurements 101
3.4.3 Thermoacoustic network model 105
3.5 Velocity measurement techniques 108
3.5.1 Particle image velocimetry (PIV) 108
3.5.2 Laser Doppler anemometry (LDA) 109

3.6 PIV/LIF Measurement 112
3.7 Proper Orthogonal Decomposition (POD) 112

4 Combustion chamber and burner flow field characteristics 115
4.1 Thermoacoustic behavior 115
4.1.1 Acoustic measurements and model 115
4.1.2 Stability analysis 117
4.2 Combustion control using staged injection 120
4.2.1 Characterization of the standard burner 120
4.2.2 Staged injection : control of an unstable case 122
4.2.3 Performance of the staged injection with stable combustor 124
4.3 Flow and scalar fields 125
4.3.1 Characterization of the standard burner flow field . 125
4.3.1.1 Flame shape 125
4.3.1.2 Cold flow structure 125
4.3.2 Burner flow and scalar fields with staged injection . 129
4.3.2.1 Burner flow field with modified injections . 129
4.3.2.2 Scalar mixing at the burner outlet 131
4.3.2.3 Helical structure and scalar mixing 132

5 Flow similarity and scaling laws 135
5.1 Burner flow similarity in air and water 135
5.1.1 Mean and turbulent flow fields 135
5.1.2 Scalar mixing 136
5.1.3 Influence of combustion on the mean flow field . . . 139
5.1.4 Coherent structures and combustion 141
5.2 Toward the Borghi diagram 146
5.2.1 Temporal length scales from LDA 147
5.2.2 Spatial length scales from PIV 150
5.2.3 Characteristic scales in the combustion chamber . . 157
5.2.4 The Borghi diagram 157
5.3 Conclusion on the similitude air/water 158

6 A quantitative link between mixture PDF and NO_x emissions 163
6.1 Experimental scalar mixing model 163
6.1.1 Identification of the experimental mixing model . . . 163

6.1.2 Influence of the fuel distribution of the flame position 165
6.1.3 Flame / flow field interaction increasing the mixing quality . . . 169
6.1.4 Empirical correlation . . . 171
6.2 A quantitative link between the PDF of the mixture and NO_x emissions . . . 174
6.2.1 PDF of the mixture . . . 175
6.2.2 NOx prediction from reactor network model and empirical PDF of the mixture . . . 176
6.3 Evolution of the flame position and shape as a function of operating conditions . . . 179
6.4 PDF of the mixture, NO_x emissions and chemiluminescence 184
6.5 Summary . . . 189

7 Flame transfer function 191
7.1 Cold flow convective mixing model of the burner . . . 191
7.1.1 Methods . . . 191
7.1.2 Measurement of time delays with fuel splitting . . . 194
7.1.3 Mixing model with recirculation zone . . . 198
7.1.4 Variation of the parameters of the mixing model . . 203
7.1.4.1 Cold response . . . 203
7.1.4.2 Mixing transfer function without recirculation zones . . . 204
7.1.5 Model parameters and system identification . . . 206
7.1.5.1 Parameter identification from geometry and velocity measurements . . . 206
7.1.5.2 Response of the fuel injection . . . 208
7.1.5.3 Fitting procedure . . . 210
7.1.5.4 Model parameters identification . . . 212
7.1.6 Hot mixing transfer function . . . 215
7.1.7 Variation of the combustion chamber geometry . . . 216
7.2 Flame transfer function estimation . . . 218
7.2.1 Impact of the fuel injection on flame position and shape for OPA . . . 220
7.2.2 Impact of the fuel injection on the velocity field . . . 221
7.2.3 A statistical link between the Lagrangian cold RTD and the heat release location . . . 224

7.2.4 Heat release location and band-pass filtered OH* chemiluminescence . . . 226
7.2.5 Model for the optically-measured flame transfer function . . . 230
7.3 Summary . . . 236

8 Control of combustion instabilities and NO_x emissions 239
8.1 Control of emissions and pulsations with standard ESC . . 240
8.1.1 Extremum-seeking control, the principle . . . 240
8.1.2 Improvements to the ESC . . . 242
8.1.3 Control of NO_x emissions with an ESC controller (SISO control) . . . 242
8.2 Control of emissions and pulsations with extended ESC (SIDO control) . . . 245
8.3 Summary . . . 248

9 Scalar mixing quality enhancement 251
9.1 Motivation . . . 251
9.2 Passive control . . . 252
9.3 Active flow control . . . 254
9.3.1 Influence of forcing on the velocity field . . . 254
9.3.2 Impact of axisymmetric forcing on the passive scalar field . . . 256
9.3.3 Impact of fuel flow pulsation on the mixing quality . 259
9.4 Pulsations without moving parts: Fluidic injectors . . . 264
9.4.1 Mixing improvement with fluidic implemented in a generic configuration . . . 268
9.5 Summary . . . 271

A Compressible jet mass flow 281

B Forcing mechanism of the water test rig 283
B.1 Forcing mounted in the bypass of the pump . . . 283
B.2 Forcing mounted upstream of the test rig . . . 285

C Fluidic oscillator in a generic crossflow configuration 287
C.1 Oscillation frequency recorded at the fluidic outlet . . . 287

C.2 Mixing comparison at one axial location 289
C.2.1 Time-averaged concentration 289
C.2.2 Concentration fluctuations 290
C.3 Mixing quality improvement 291
C.3.1 Evolution of the unmixedness parameters at x/d_h=22 and x/d_h=112 291
C.3.2 Evolution of U_x and U_t for J=17.7 293

Bibliography **295**

Author's Publications **314**

Nomenclature

Latin characters

C	Concentration	mol/l
c	Sound velocity	m/s
C_0	Initial concentration of the jet	mol/l
C_K	Kolmogorov constant	-
C_m	Concentration of the jet centerline	mol/l
C_p	Specific heat capacity	J/kgK
D	Diameter	m
d	Diameter	m
D_s	Unmixedness decay coefficient	m^{-1}
E	Energy spectrum	m^2/s
f	Frequency	s^{-1}
f	Probability density function	-
$\boldsymbol{g}$	Gravity forces	m/s^2
H	Duct height	m
h	Hydrophone signal	V
J_{eq}	Equivalent jet-to-cross flow momentum (fuel distribution $(\alpha, \beta) = (0, 0.5)$)	-
$\dot{I}_\theta$	Azimuthal momentum	$kg.m^2/s$
$\dot{I}_x$	Axial momentum	kg.m/s
$i = \sqrt{-1}$	Complex number	-
k	Turbulent kinetic energy	m^2/s^2
l	Spatial wave length	m
l_b	Batchelor length scale	m
l_k	Kolmogorov length scale	m
$\dot{m}$	Mass flow	kg/s
m	Mass	kg
m	Mode number	-
p	Pressure	Pa
Q	Global heat release	J

Q	Volume flow	m^3/s
q	Volumetric heat release	J/m^3
$\boldsymbol{r}$	Spatial direction vector	m
$\boldsymbol{x} = (x, y, z)$	Position vector in Cartesian coordinate system	m
R	Radius	m
R	Specific gas constant	J/kgK
r	Radius	m
$r = \sqrt{J}$	Square root of jet-to-cross flow momentum	-
R^2	Coefficient of determination of regression	-
R_{ij}	Correlation coefficient	-
$\boldsymbol{S}$	Rate of strain tensor	s^{-1}
S	Fuel injection spacing	m
S	Swirl number	s^{-1}
$s = \sigma/C_\infty$	Coefficient of variation (unmixedness parameter)	-
S_L^0	Unperturbed laminar flame speed	m/s
S_T	Turbulent flame speed	m/s
A_0	Laminar flame area	m^2
A_T	Turbulent flame surface	m^2
T	Period or time interval	s
T	Temperature	K
t	Time	s
T_{fl}	Adiabatic flame temperature	K
$\boldsymbol{u} = (u, v, w)$	Velocity vector in Cartesian coordinate system	m/s
$\boldsymbol{u} = (u_x, u_r, u_t)$	Velocity vector in cylindrical coordinate system	m/s
U_0	Mean bulk velocity at the burner outlet (Area based on D)	m/s
u_k	Kolmogorov velocity scale	m/s
U_t	Temporal degree of segregation (unmixedness parameter)	-
U_x	Spatial degree of segregation (unmixedness parameter)	-
V	Volume	m^3
x_{fl}	Axial flame position	m
Y_f	Fuel mole fraction	mol/mol
$\mathcal{Z}$	Acoustic impedance	$kg.s.m^{-2}$
Z_f	Fuel mass fraction	kg/kg

Greek symbols

α	Fuel distribution parameter	-
β	Fuel distribution parameter	-

δ_L	Laminar flame thickness	m
ϵ	Dye extinction coefficient	$\mathrm{m}^{-1}.\mathrm{mol}^{-1}$
ϵ	Turbulent total dissipation	$\mathrm{m}^2/\mathrm{s}^{-3}$
ϕ	Equivalence ratio	-
ϕ	Passive scalar value	-
Γ	Diffusion coefficient	m^2/s
γ	Adiabatic index	-
κ	Thermal diffusion coefficient	m^2/s
κ	Wave number	m^{-1}
λ	Wave length	m
$\Lambda_{u_i,u_i}^{\boldsymbol{r},t}$	General integral length scale definition	m
λ_f	Taylor axial length scale	m
λ_g	Taylor transversal length scale	m
μ	Dynamic viscosity	$\mathrm{kg}.\mathrm{s}^{-1}.\mathrm{m}^{-1}$
ν	Kinematic viscosity	m^2/s
θ	Angle	-
ρ	Density	kg/m^3
σ	Standard deviation	-
τ	Time delay	s
τ_c	Chemical time scale	s
τ_k	Kolmogorov time scale	s
τ_t	Turbulent time scale	s
Ω	Azimuthal vorticity	s^{-1}
ω	Chemical source termy	$\mathrm{kg}.\mathrm{m}^{-3}.\mathrm{s}^{-1}$
ω	Frequency	s^{-1}

Dimensionless numbers

$Da = \frac{\tau_t}{\tau_{chem}}$	Turbulent Dahmköhler number	-
$Ka = \frac{\tau_c}{\tau_k}$	Karlowitz number	-
$J = \frac{\rho_j u_j^2}{\rho_a U_a^2}$	Jet-to-crossflow momentum	-
$Pe_t = \frac{U_0 L}{D_t}$	Turbulent Péclet Number	-
$Re = \frac{U_0 D}{\nu}$	Reynolds Number	-
$Re_t = \frac{\Lambda_x u'}{\nu}$	Turbulent Reynolds Number	-
$Sc = \frac{\nu}{D}$	Schmidt number	-
$St = \frac{fD}{U_0}$	Strouhal Number	-
$St = f\tau_{ref}$	Axial Strouhal Number	-

$Tu = \frac{u'_x}{U_0}$ Degree of turbulence 1d -

Subscripts

$(\cdot)_\infty$	Perfectly homogenized mixture
$(\cdot)_a$	Air
$(\cdot)_{fl}$	Flame
$(\cdot)_{dye}$	Fluorescent dye
$(\cdot)_f$	Fuel
$(\cdot)_w$	Water

Superscripts

$'$	Temporal fluctuation
$''$	Temporal random fluctuation
$(\cdot)^*$	Excited chemiluminescent state
$(\cdot)^*$	Normalized value
$\dot{(\cdot)}$	Flux
$\hat{(\cdot)}$	Fourier transformation
$\tilde{(\cdot)}$	Temporal coherent fluctuation

Functions and operators

$\mathcal{F}$	Fourier transformation
$\mathcal{H}$	Heaviside function
$\underline{\langle\cdot\rangle}$	Spatial averaging operator
$\overline{(\cdot)}$	Temporal averaging operator

Acronyms

dc	Duty cycle
EINOx	Emission index NOx
ERZ	External Recirculation Zone
HS-LIF	High Speed LIF
IRZ	Internal Recirculation Zone
LDA	Laser Doppler Anamometry
LIF	Laser Induced Fluorescence
MDFF	Momentum Dominated Far Field
MDNF	Momentum Dominated Near Field
OPA	Operating point A
MTF	Mixing Transfer Function
PDF	Probability density function

PIV	Particle Image Velocimetry
POD	Proper Orthogonal Decomposition
ppm	Particle per million
PVC	Precessing vortex core
RTD	Residence Time Distribution
WSR	Well Stirred Reactor

Chapter 1

Introduction and Motivations

1.1 Generalities on dry low NO_x combustors

In order to react to even more stringent emission limitations, lean combustion became the state of the art for modern gas turbines within the last few decades as it allows for flame temperature and hence pollutant emissions like nitrogen oxides (NO_x) to be reduced. This technology change, combined with other combustor modifications, has helped to achieve a continuous decreasing trend of emissions of this pollutant over the last 20 years. Regarding the situation in the United States, a recent report from the Environmental Protection Agency confirms that the NO_x emissions coming from fuel combustion sources decreased by 41% between 1990 and 2006 (Fig. 1.1). This change occurred mostly between 1998 and 2006. What is the main positive impact of these reductions? In the U.S., a reduction of smog and acid rain has been recorded as NO_x are, as is sulfur dioxide SO_2, causes of these environment damaging phenomena.

The biggest step in reducing the NO_x emissions has been achieved through a reduction of the combustion temperature and an improvement of the combustor/oxidizer mixing quality in gas turbines as well as furnaces and other industrial processes working with the combustion of fossil fuels. This decrease in combustion temperature is obtained when the ratio of fuel to air is decreased in the combustor, below the stoichiometric conditions. In contrast to a diffusion flame, the fuel and air are mixed well upstream of the reaction zone. For these reasons, this process is called lean premixed combustion, which is the combustion used in dry low emissions (DLE) combustors.

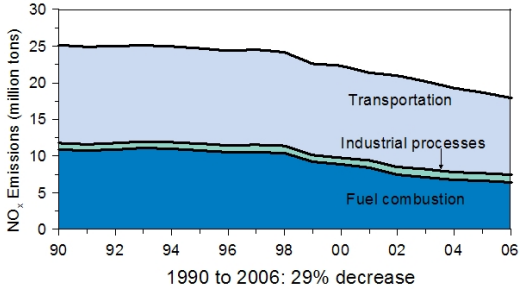

Figure 1.1: NO_x emission decrease over the last century in the United States [EPA08].

The main drawback of lean combustion technology is that it is much more prone to generating heat release fluctuations than when rich mixtures (equivalence ratio $\phi \approx 1$) are used (Lieuwen and Zinn[LZ98]). Coupled with the acoustic boundaries of the system, they can lead to strong combustion instabilities. These instabilities are also called thermoacoustic instabilities, as they can occur if the heat release fluctuations match the resonant acoustic modes of the combustion system. In the harmless case, they lead to an increase of the overall noise of the gas turbine; in case of high amplitudes, mechanical fatigue can lead to material failure and destruction of the combustor.

The influence of fuel/air equivalence ratio on the emissions of NO_x, unburned hydrocarbons UHC, and carbon monoxide CO is depicted schematically in Fig. 1.2. When going to lean conditions, CO and UHC increase as a consequence of the incomplete combustion, whereas higher equivalence ratios produce more NO_x and smoke. Hence, only a small operating window around $\phi \approx 0.6$ is available to ensure a good combustion efficiency (i.e. low UCH or CO) associated with low NO_x emissions.

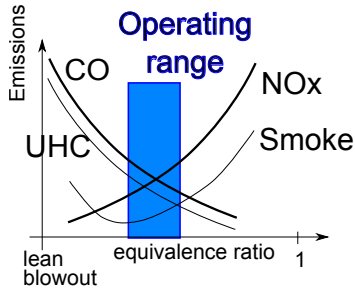

Figure 1.2: Combustion emissions depending on the fuel/air equivalence ratio illustrating the operating range of a lean premixed combustor.

1.2 Fuel/air mixing and its impact on thermoacoustic instabilities and NO_x emissions

1.2.1 Thermoacousitc instabilities

The first observation of the phenomenon, which was later to be called themoacoustic instability, was made by Higgins in 1777 who reported the existence of a "singing flame" when a hydrogen flame was enclosed within tubes of defined lengths [Bro11]. This phenomenon was reported in a few works on similar configurations over the following 100 years (including the work of Rijke in 1859 in the eponym tube who used a preheated gauze instead of a flame to generate heat) without satisfactory physical explanation until 1878, when Lord Rayleigh focused on the topic in a lecture at the Royal Institution of Great Britain [Ray78]. He observed that if pressure (or acoustic) fluctuations p' and the volumetric heat release rate fluctuations $\dot{q}'$ of an enclosed system are in phase over the time interval considered T, then acoustic energy will be added to the system. He then formulated the well-known Rayleigh criterion R

$$R = \frac{1}{T}\int_{t}^{t+T} \dot{q}'p'\,dt > 0\,. \tag{1.1}$$

This criterion is not a necessary criterion for instabilities. It is valid only if the acoustics losses of the system are zero, which is an assumption seldom valid in practical application. The generalized Rayleigh criterion derived from the acoustic energy balance reads [BMP09]

$$\frac{1}{T}\int_t^{t+T}\int_V \frac{(\gamma-1)\dot{q}'p'}{\bar{\rho}\bar{c}^2}\,dV\,dt > \frac{1}{T}\int_t^{t+T}\oint_S p'\boldsymbol{u}'\cdot d\boldsymbol{S}dV\,dt\,. \tag{1.2}$$

The left-hand side describes the acoustic energy gained from combustion and the right-hand side the acoustic losses across the boundaries. γ is the adiabatic index, $\boldsymbol{S}$ is the surface vector of the volume considered to be oriented outwards, and $\bar{\rho}$ and $\bar{c}$, the mean flow density and acoustic velocity respectively. Equation 1.2 is valid for systems without mean flow, which is an extremal case not completely invalid for practical gas turbines, due to the low Mach number M present in the burner and combustor. More exhaustive derivations, taking into account the effect of mean flow [Chu65] or viscous effects [NP05] can be found in literature. The expression of the acoustic energy balance (Eq. 1.2) shows that, in case of periodically oscillating systems, the phase between pressure and heat release rate oscillations is a key parameter which can stabilize or, on the contrary, destabilize an enclosed system where heat can be periodically released. If one wants to control such instabilities, this phase difference must be respectively adjusted, e.g., by setting pressure and heat oscillations out of phase. The modeling and controlling tasks thus consist of answering the following two questions:

1. What are the sources of the phase difference between pressure and heat release fluctuations in modern combustors?

2. Is it possible to control such phase differences and if yes, how?

The phase difference is a consequence of physical time lags inherent to the system such as, for example, the convective time needed by the fuel to travel down to the flame front. This time lag is present in every combustor, and can trigger or suppress thermoacoustic instabilities. For now more than 60 years, since the first combustion instabilities led to strong damages in industrial furnaces [Put71], ramjets or rocket engines, the identification of

the mechanisms leading to such time lags has been extensively performed. As summarized by Candel [Can02], these mechanisms involve, among others, acoustic boundary conditions, equivalence ratio fluctuations, flame area fluctuations, reaction kinetics, atomization process, entropy waves, etc. Independent from its physical origin, the transport of a physical fluctuation with a certain velocity toward the flame will create fluctuations in heat release at the flame location with a certain frequency and phase relative to another physical signal. If this heat release oscillation frequency matches the frequency of an acoustic mode of the system, then a combustion instability might occur. This mechanism is illustrated by the schematic propagation of an equivalence ratio fluctuation wave of a single fuel injector in Fig. 1.3.

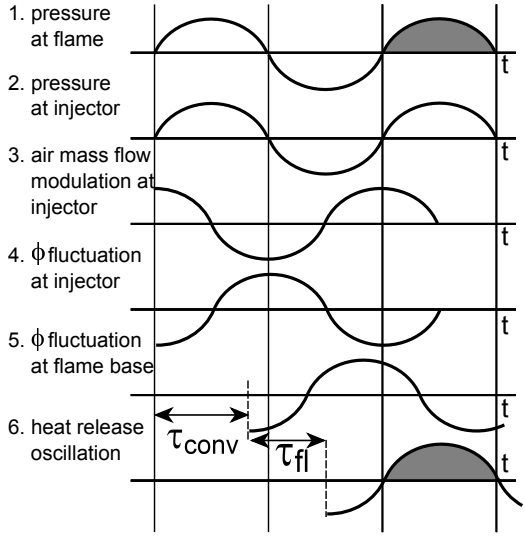

Figure 1.3: Propagation of oscillation in equivalence ratio leading to combustion instability (from [LTJZ01]).

The works of Putnam [Put71], Lieuwen [LTJZ01] or recently Richards [RR08] illustrated also the importance of acoustic impedance of the inflow and outflow boundaries (such as air inlet, fuel injection or combustor outlet) of the system in the generation of thermoacoustic instabilities. The choice of the geometry and boundary conditions is therefore critical for the combustor

stability. Changes in the geometry can be used to decouple the heat release oscillations from the acoustics of the system by either increasing the absorption of acoustic energy (Helmholtz dampers) or changing the phase of system impedances (by changing the fuel feed line length or, as shown recently by Bothien [BMP09], actively controlling the impedance of the outlet of the combustor).

1.2.2 Thermoacoustic instabilities, NO_x emissions and fuel/air mixing

Figure 1.4 summarizes how the fuel/air mixing process is involved in the control of the pressure pulsations and NO_x emissions of a DLE combustor.

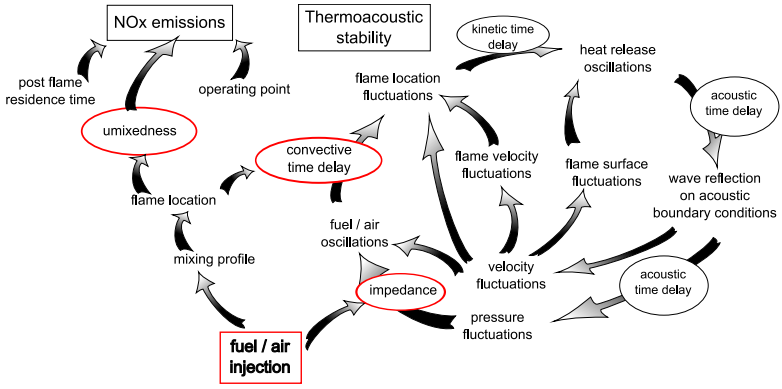

Figure 1.4: Controlling emissions and combustion instabilities in gas turbines

Even if it is not the only mechanism responsible for thermoacoustic instabilities, fuel/air convective time delay - i.e. the time which is needed for a fuel pocket to travel from the fuel injector to the flame front - appears to be one of the most critical mechanisms for the stability of a premixed combustor. Changing the values of those time delays as well as their temporal probability density functions (PDF), also called residence time distribution RTD, allows to control the system stability as shown by Sattelmayer [Sat03], Paschereit et al. [PFS01], Lieuwen [LTJZ01], McManus et

al. [MHD+04], or Bothien et al. [BMLP07]. In these works, simple time lag models, sometimes completed with a Gaussian PDF shape, are used. Good agreements are obtained for predicting the stable and unstable boundaries of the system with linear stability analysis tools. In particular, the works of Sattelmayer and Paschereit as well as one of Kato et al.[KFDK05] demonstrated the generally positive effect of temporal spreading (i.e. the variance) of the time delays on the combustor stability. Therefore, a proper adjustment of the RTD of the fuel from the fuel injection to the flame may be sufficient to control a combustor.

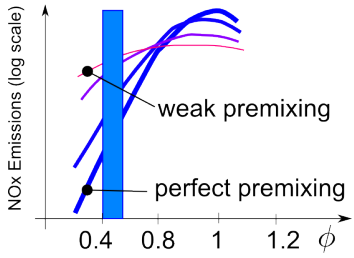

Figure 1.5: Impact of fuel/air mixing quality on the NO_x emissions for different fuel/air equivalence ratios ϕ, from Joos [Joo06]

By adjusting the residence time distribution of the fuel, good mixing quality must be ensured, as it remains a key parameter in the limitation of NO_x emissions. In all combustion systems, parameters like the residence time in the combustor, flame temperature, pressure and heat losses are relevant in the generation of NO_x. When these parameters are set (through the power output required and the geometry of the system) a minimization of these emissions in DLE combustors is achieved when the fuel/air mixing quality is optimized, i.e. when the mixture is as homogeneous as possible which means that the mixture unmixedness is minimized, as illustrated in Fig. 1.5. Such improvements have been reported first by Fric [Fri93] and in practical engines by Stufflebeam et al. [SKS99], Tanimura et al.[TNI+08], among others. However, this is not true for mixtures with equivalence ratio corresponding to stoichiometric conditions Fig. 1.5.

One can therefore summarize that coherent temporal fluctuations are responsible for thermoacoustic instabilities while spatial inhomogeneities,

combined also with temporal fluctuations, control the NO_x emissions. A perfect premixer, i.e. thermoacoustically stable and generating low NO_x emissions, should thus have the widest residence time distribution possible but the sharpest equivalence ratio probability density function, as illustrated in Fig. 1.6. The "worst case", illustrated on the right picture in Fig. 1.6, depends on the thermoacoustic modes of the combustion system involved. Critical times at risk of exciting one thermoacoustic mode are not only equal to the period of the dominant frequency of the mode involved but also to the period of mode's harmonics. Furthermore, acoustic modes with different critical times are susceptible to becoming unstable in complex geometries. Therefore, many critical times are generally involved, which also depend on the operating conditions.

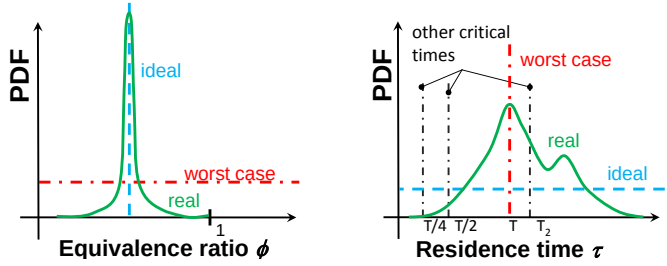

Figure 1.6: Typical mixture quality PDF (left) and residence time distribution (right) for the ideal real and worse mixer design

A trivial solution to achieve such perfect mixing is to give the fuel and air enough time to mix. Because of safety, costs, and weight considerations for an engine, the best mixing quality should technically be achieved within the shortest possible time or mixing length. The perfect premixing will thus seldomly occur and the designed mixing injection has to be optimized under the given size constraints. In particular, the mean convective time delay must be adjusted to ensure stable combustion. Therefore, regarding the numerous parameters involved, there is a need to characterize the mixing process and develop models able to predict the main features of the mixing and its coupling with the combustion system considered.

1.3 On the modeling of turbulent mixing

1.3.1 What is mixing?

Before discussing mixing modeling, it is useful to summarize briefly what is to be understood when dealing with mixing phenomena. As mentioned by Pratt [Pra75], the classical mechanistic in fluid mechanics has been mostly interested in modeling the turbulence itself, and little attention has been paid to the scalar mixing until recently. The first modeling attempts considered simply the scalar mixing as a diffusive process which could be obtained from the mean concentration profiles. From extensive study of so-called coherent structures between the 1970's and the 1990's in even very simple configurations at various Reynolds numbers (see shear layer of Konrad [Kon76], Dimotakis and Brown [DB76]) brought new insight into the mechanism of homogenization of two fluids. Most of these observations were summarized in the work of Broadwell and Breidenthal [BB82] as well as in the later work of Broadwell and Mungal [BM91]. They show that molecularly mixed fluids have to be distinguished from simply stirred fluids and that large-scale coherent structure play a key role in the homogenization of scalar flow properties. This distinction is very well summarized in a citation reported by Broadwell [BM91], "*Stirring* [...] is a process of stretching of immaterial area. *Mixing* [...] is the process of diffusion of substance across immaterial surfaces. [...] Mixing depends on material properties such as diffusivities, whereas stirring is a purely kinematic aspect dependent on flow parameters. Indeed, it is possible to stir fluids that do not mix at all".

In practical configurations, the coherent structure as well as an increase in the Reynolds number promote the stirring effect, while the degree of homogenization depends solely on the diffusivities of the species considered. Hence, as also suggested by Coats [Coa96], the mixing of systems dominated by coherent structures cannot be modeled accurately with gradient-based techniques. As in most technical applications, the stirring effect of large structures will namely outperform the molecular diffusivity. The problem can become even more complex in the case of counter gradient diffusion processes which occur during combustion (Veynante et al. [VPDM96]).

Furthermore, the length scales of the coherent structures are much larger than the mixing layer thickness, at which scale a diffusion-like process takes place.

1.3.2 Mixing modeling

Because of the generation of large-scale coherent structures, turbulent mixing modeling is a complex task. The prediction of the mixing field in a practical combustor remains computationally heavy and requires experimental validation to accurately capture the mass transfer. Thus, low-order models of the mixing, describing the most relevant parameters of the flow, are of interest.

The field of chemical engineering is historically interested in the interaction between mixing and chemical reaction, generally of low order, and has developed tools based on single reactors like the plug flow reactor (PFR) and perfectly stirred reactor (PSR or WSR) to model the scalar mixing as well as chemical reactions [Fox03]. Tools were also developed to characterize the mean residence time distribution of those simple reactors as presented by Danckwerts [Dan52, Dan53]. Indeed, new commercial tools are based on the interconnection of a large number of single reactors (CHEMKIN from Reaction design). However, the reactor parameters (volume, residence time, mass transfer, etc.) must be calibrated, whether from computational fluid dynamics (CFD) or experimental measurement.

Some more basics models which describe the mixing in premixed combustors are reported in the literature:

1. Solution of 1D convection/diffusion equation: Chishty et al. [CBFY07, CY08]
2. Inter-connection of 3 reactors and 1D convection/diffusion equation: Ferro et al. [FPG01]
3. Lagrangian model and Langevin equation: Scarinci et al. [SF00, SFD04]
4. Analytical flow field model and Boussinesq hypothesis: Flohr et al. [FSP02]

5. Transport equation of mixture variance: Syed et al.[SRM07]

The previous models are mean flow models (items 1, 2, 3, 4, 5), some of which are based on the convection diffusion equation (1,2,5). Temporal time delay distributions are modeled with a Péclet number (1,2), spatial fluctuations derived from the shear stress field within the burner (4), and temporal and spatial fluctuations modeled with turbulent noise (3). Even if relatively simple, these models capture the dominant mixing mechanisms of premixed combustors quite well and can be used as reliable design tools. The complex coherent structures are not explicitly modeled, but their effect on the mixture quality can be captured through the calibration of the models. Therefore, an explicit model of the coherent fluctuations is not required to model the mixing quality in the case of very simple reactor networks.

1.3.3 Mixing in oscillating flows

Thermoacoustic instabilities may induce strong oscillation amplitudes of the velocity in the burner. Such oscillations generate oscillations in the fuel/air mixing composition and a question which needs to be answered is, whether such oscillations are able to have a positive effect on the RTD and mixing quality at the burner outlet.

Two parameters must then be considered: the frequency and the amplitude of the velocity fluctuations at the burner inlet. As shown in the theoretical work of Chishty [CY08] on a co-flow jet mixer, high-frequency pulsations (oscillation period lower than two times the mean burner residence time) are more likely to be damped at the burner outlet than low-frequency oscillations, as the frequency response of a premixer can be modeled as a low-pass filter. Furthermore it shows that an increase in the oscillation amplitudes leads also to an increase in the amplitude of the concentration fluctuations at the outlet and hence, to a worsening of the mixing quality[1]. Therefore, if a simple flow (e.g., a pipe flow) is considered, high-frequency forcing with moderate amplitudes may improve the mixing process.

[1] However, the *relative* temporal mixing efficiency of a premixer increases with forcing amplitude

However, if coherent fluctuations are involved, as it is the case in even simple jets, then an increase of the mixing quality may be achieved when the frequency of the oscillation and its phase are properly set. Such positive effects could be recorded in non-premixed flames [OHY09] and in swirl-inducing burners [PGW99] and may be obtained if active control strategies are followed. However, in case of self-excited thermoacoustic instabilities, the probability that the frequency of the instability matches that of the flow instability is very low. Hence, only high-frequency velocity fluctuations may have the potential to improve the mixing quality in standard premixed combustors.

1.4 State of the art of fuel injection designs

1.4.1 Experimental steps

The typical development steps of a burner are depicted in Fig. 1.7. As shown in the early sixties by Clarke et al. [CGH63], water flow measurements are well suited to derive information on the velocity field and passive scalar field of a combustion chamber. The high quality of the data and the low cost compared to reacting tests make them very attractive in the early design stages of a burner. Different burners with varying parameters can be tested to select the best configurations regarding, for example, the flow field or the fuel/air mixing profile. The best configuration can then be tested in an atmospheric combustor before being mounted into a multi-burner section. Eventually, the burner is implemented in a high-pressure test rig prior to final implementation into the full-scale engine.

Typical data obtained from cold flow test rigs are velocity and concentration profiles. However, only a few works have reported on the investigation of the residence time distribution in premixed combustors, and publications reporting on the interaction scalar/velocity field in such configurations are also rare. Therefore, a methodology will be presented in the next sections to increase the knowledge gained from cold flow measurements in the design process of a burner.

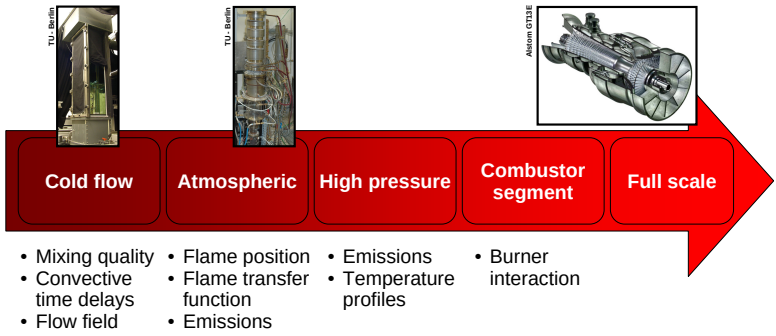

Figure 1.7: Burner Development Steps

1.4.2 Fuel injection in gas turbine burners

As aforementioned, the design of modern combustors must prevent the occurrence of thermoacoustic oscillations over a wide range of operating points and, at the same time, ensure good fuel mixing and flexibility. It is therefore interesting to compare how this is achieved in typical gas turbines. Figures 1.8 and 1.9 report some of the different techniques used by different gas turbine manufacturers to mix fuel and air prior to combustion.

All of the burners shown in Fig. 1.8 and Fig. 1.9 have two types of fuel injection in common: a pilot for startup and a premix fuel path for partial and full loads. Controlling the fuel split between the lines allows for control of the flame between the different operation regimes. Depending on the manufacturer, two and more stages can be used, the limitation still being the cost of such flexibility.

When taking a look at the injection types of most of the burners, the fuel is generally injected into the crossflow with a 90°angle. Most of the manufacturers modified the type of injection by integrating the fuel injectors inside the swirling vanes. The first hybrid burner generation of Siemens injected the fuel upstream of the radial vanes in co-flow, before the new crossflow injection was integrated into the swirling vanes. This injection type is used by all of the manufacturers except for Rolls Royce in its Trent combustor.

Turbine	NOx	Combustor	View of Burner and Injection
GE10			
DLN-1	25 ppm		
DLN-2	15 ppm		
DLN-3			
Siemens			
HR-3	< 25 ppm < 9 ppm achievable		
Mitsubishi			
DLN-2 (F eng., 1600K)	25 ppm		
DLN-3 (F eng., 1600K)	9 ppm (Target)		
DLN-4 (G eng., 1750K)	9 ppm (Target)		

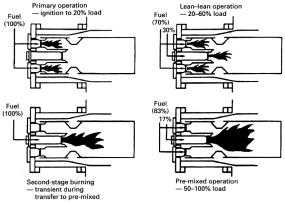

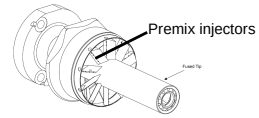

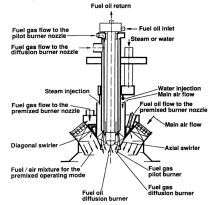

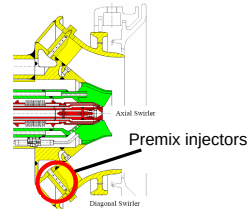

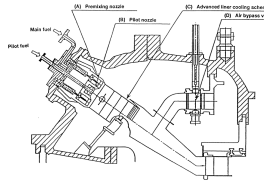

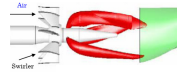

Original

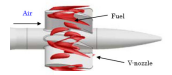

Modified

Figure 1.8: Illustration of the injection technologies and NO_x emissions achieved by the main heavy-duty gas turbine manufacturers (1) ([Moo97], [TNI+08], [BP08])

The mixing characteristics of such arrays of jets have been investigated for 60 years and allow, through reliable empirical correlations, good mixing at low manufacturing costs to be achieved. The implementation of such injectors is generally done without strong modifications from the 90°configuration, and few works have reported on the modification of the injection angle and shape of the injection holes. Still Stufflebeam [SKS99] reported that alterning between small (d=0.73 mm) and large (d=2.03 mm) holes also had a positive impact on the mixing quality of the burner for fuel injection momentum ratios ranging from 10 to 50, so that an improvement of the (passive) fuel injection design may still be achieved. The schematic of the combustor of PSM shown in Fig. 1.9 (middle row) indicates also that a modification of the fuel injection of the premix stage associated with a premixed pilot injection contributes to further reducing the NO_x emissions.

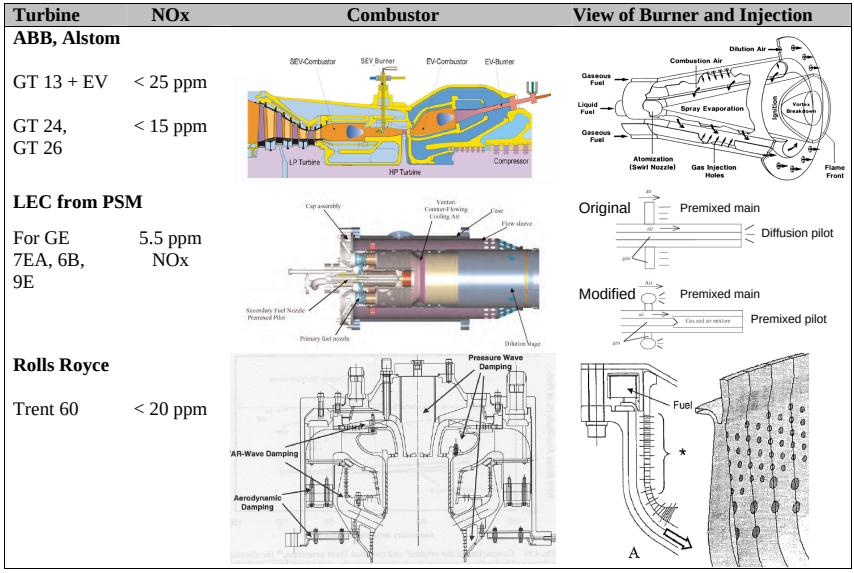

Figure 1.9: Illustration of the injection technologies and NO_x emissions achieved by the main heavy-duty gas turbine manufacturers (2) ([SFD04])

A complete redesign of the fuel injection concept has been performed by Scarincci [SFD04] who instead of injecting fuel into air suggests injecting air into fuel and implemented it on a Rolls Royce Trent gas turbine. A well stirred reactor is then achieved. This has the effect of minimizing the temporal equivalence ratio oscillations over a wide frequency range and, at the same time, achieving a very good mixing quality. The concept was successfully implemented into the land-based Trent engine (see Fig. 1.9). The drawback of such injection is its limitation to gaseous fuel, which is restricting regarding fuel flexibility (liquid and gas) proposed by other manufacturers with fuel in crossflow injections.

All of the combustors achieve low NO_x emissions with low pulsations, and the question which arises is, whether there is still a possibility of further increasing the degree of fuel/air homogenization in order to eventually further decrease the NO_x emissions, even if the part of the NO_x depending on the mixing quality may decrease with an increase of the engine pressure[BG07].

1.5 Optimization of crossflow fuel injections

1.5.1 Passive modifications

Figure 1.10(a) presents the type of injections which have already been investigated regarding the mixing of two gaseous mixtures. A lot of work has been performed by the NASA research group including the works of Holdeman [Hol83] and Liscinsky [LTVH92, LTH93, LTH95a], who tested different jet arrangements as well as shapes. Two parameters characterize most the mixing of crossflow jets: the jet momentum ratio and the orifice spacing ratio. Adjustment of these values from empirical correlations leads to the highest mixing improvement. Liscinsky also found that a change in the injector shape brings some, but rather marginal, improvement in the quality of mixing when compared to a round jet in cross flow. When a shape change is associated with an optimized fuel distribution, only a transverse slot injection (Fig. 1.10(b)) improves the mixing quality compared to an array of round jets.

Less work has been done on the impact of the injection angle on the mixing quality, as an inclination of the fuel injection with an angle smaller than 90° generally reduces the mixing quality for a given jet path length [Squ50]. However one may consider using different fuel injection angles to hypothetically increase the mixing quality.

1.5.2 Active forcing of the fuel injection

The impact of active forcing of a crossflow jet as a mean to increase the mixing quality has been recently investigated. The works performed by Hermanson et al. [HWJ98] , Johari et al. [JPTH99, Joh06] and Eroglu and Breidenthal [EB01] showed that full modulation with a square wave of single jets in crossflow can lead to substantial increase in the mixing quality. They identify the four parameters of jet to main flow velocity ratio, frequency of actuation, duty cycle and amplitude of forcing as critical for the control of the jet mixing. Hermanson noticed that for a fully modulated jet, short duty cycles (or injection times) strongly increase the jet penetration and vice-versa. Investigations on a similar configuration were performed

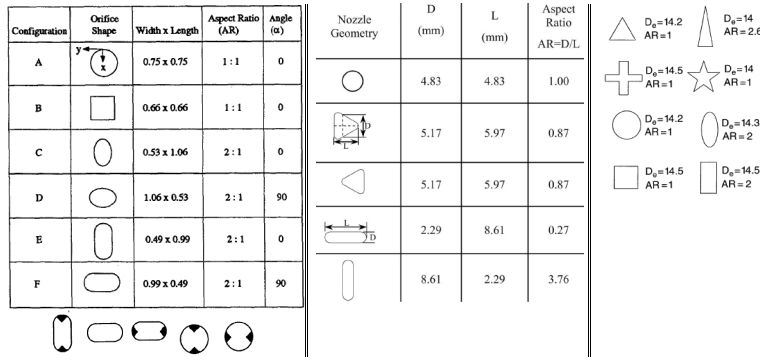

(a) Injection shapes tested by Liscinsky et al.[LTVH92, LTH95a] (left), Gutmark et al.[GIM08] (middle), and Mi et al.[MNL00] (right)

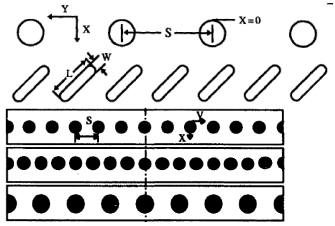

(b) Modified injector arrays [LTVH92, LTH93]

Figure 1.10: Passive modifications of crossflow fuel injectors

by Johari et al. [JPTH99] . The frequencies of interest range from 0.5 up to 5 Hz, corresponding to jet Strouhal numbers from 9 $\times 10^{-4}$ to 2.5 $\times 10^{-2}$. The nominal duty-cycles (dc) tested are equal to 50%, 30%, and 20%.

Their results confirm that low duty cycles increase the jet penetration strongly. This results in an increase of the degree of mixing of up to 50% for the best combination frequency/duty cycle. Similar results were obtained by Eroglu and Breidenthal [EB01] , who used also square wave actuation of a crossflow jet. They kept the duty cycle constant (dc=50%) and showed that the pulsing of the jet is more efficient for low jet to crossflow velocity

ratios with fully modulated flow rate. An optimal forcing frequency corresponding to a jet-based Strouhal number $St_j \approx 0.1$ was found. Some recent LES simulations carried out by Coussement et al. [CGSD10] limit the generality of these findings, as the gain in mixing quality depends also on the unmixedness parameter used for the quantification. They also find that sinusoidal forcing may be better suited for overall mixing enhancement than square wave modulation.

In real combustors, forcing of the fuel injection can lead to a positive decrease of the NO_x emissions [PGW99], suggesting that an increase of the mixing quality is obtained. However, there is until now no measurement performed to quantify the impact of periodical forcing of the fuel mass flow on the mixing quality at the outlet of a practical combustor. Most of the previous studies have been limited to single jet forcing and the effectiveness of such control methods in practical combustors still needs to be assessed.

1.6 Control of the fuel/air mixing

The optimization of a static injection configuration can be easily obtained for defined operating parameters of the burners. However, it is generally not possible to design a fuel injection configuration optimized for all of the operating conditions of an engine. Furthermore, the constraint of rapidly adjusting the power output of the turbine may also change the flame stability response. Other critical conditions, like the startup of the turbine, will require richer mixtures to stabilize the flame. For these reasons, all of the gas turbines are equipped with staged injections, as shown in Fig. 1.8 or in Fig. 1.9. These staged injections may be found inside a burner element or, as presented by Kokanovic et al. [KGTS06], may be applied to a group of burners inside a ring combustion chamber.

Full-scale tests allow for the fuel injection distribution which optimizes the combustor performance (i.e. reduce NO_x or CO emissions as well as pressure pulsations) to be determined while remaining within the safety margins of the engine. One can then consider open-loop control of the combustor. However, stochastic changes in the operating conditions (as variation of degree of humidity, ambient temperature, fuel composition, etc.) may move the default fuel distribution away from the optimal point

where NO_x and pressure pulsations are minimized. Therefore, an online feedback of the combustion parameters is needed to adjust the mixing profile. A closed-loop control is thus required.

Two types of closed-loop control may be considered: the first type requires no prior knowledge of the response of the combustor and can be used in the preliminary design stage to optimize the fuel injection profile. It may also be considered more like an optimizer than a controller. Evolutionary algorithms have been used to this end by Paschereit et al. [PSB03]. 16 independent injectors are used to fully control the mixing profile of the burner. Reductions in NO_x and pressure pulsations were achieved, but the time needed to obtain an optimal solution makes such control suitable more for design optimization than for real-time closed-loop control. Gradient based controller are much faster in optimization problems and were successfully used by Samuelson et al. [SM00]. In this work, fuel or air distribution was controlled in order to increase the combustion efficiency or reduce the NO_x emissions. The optimal injection was reached within 10 to 20 minutes, often limited by the measurement technique response time (in particular the emission sensor response). Gradient-based methods also mostly move stepwise on the field to optimize and the choice of the step size(often empirical) is critical to reaching an optimum point in a defined time. Hence smoother changes in the controller output may be needed to avoid abrupt changes in the combustor parameters.

The second type of closed-loop control concerns the optimization of predefined fuel injection maps as mentioned earlier. Here, the work of Kokanovic et al. [KGTS06] or Bulat et al. [BSMS07] provides a good insight into the advantages of fuel distribution adjustment compared to open-loop control. Their adjustments lead to strong decreases in NO_x emissions while avoiding high pulsation zones. The method presented by Kokanovic, which adjusts the fuel split depending on the monitored pressure pulsations and NO_x emissions can be applied within a single burner or for a group of burners in the combustor. The controller proposed by Bulat improves the dynamic response of the combustor as it is built from two controllers: one used to adjust the static fuel injection map, the second to adjust the fuel distribution during fast transient operations.

The possible remaining drawback of these controllers is that they depend on empirical models or, as in Kokanovic et al., on the use of statistical models like Gaussian processes. Physically based models are still needed to improve the modeling accuracy and increase the controller performance.

The aforementioned control strategies rely on slow changes in the mixing profile (frequency change of the order of magnitude of 0 Hz), and the mixing profile should be adjusted in order to avoid zones of instabilities and high NO_x emissions. To decrease or suppress combustion instabilities for one defined operating point and fuel distribution, the pulsating injection of fuel at a frequency related to the instability was successfully applied by many authors like Paschereit et al. [PGS00], Hatout et al. [HAG00], Cohen at al. [CSP01] among others. As thermoacoustic instabilities lead in most cases to an increase of NO_x emissions, as they induce temporal oscillations of the equivalence ratio, a stabilization generally leads to a reduction in NO_x emissions [CSP01] when lean mixtures are used. This active control strategy was already implemented successfully in gas turbines [HWJ+99]. However, because of its increased costs, such strategy is generally a transitional solution until passive modifications (as Helmholtz dampers) allow the unstable modes to be suppressed without active fuel modulation.

1.7 Objectives, methodology and outline of the thesis

The main objective of the present work is to control the NO_x emissions and pressure pulsations in a lean premixed combustor. The control should be achieved through adjustment of the fuel/air mixing profile inside the burner. To achieve the main goal, an original approach is applied which consists in gaining the most information from cold flow measurements possible for predicting the NO_x emissions and thermoacoustic behavior of the comsidered system. This new approach requires the completion of an additional goal, which is the validity of the cold flow modeling approach. A closed-loop control algorithm must then be developed to continuously adjust the fuel/air profile and stabilize the combustor, ensuring low NO_x emissions. Finally, the scalar mixing quality at the burner outlet must be improved through passive or active methods.

Figure 1.11 illustrates the methodology followed to characterize and model the mixing of the investigated burner. The first step of the investigations is performed with cold flow measurements in a water test rig. Both the mixing quality as well as the residence time distribution are characterized in these experiments with the help of a cold flow mixing model. The information on the flame position is used first to estimate the mixture quality at the flame location and then to derive the transfer function of the fuel/air ratio fluctuations reaching the flame. The latter can be used to predict the stability boundaries of the combustor.

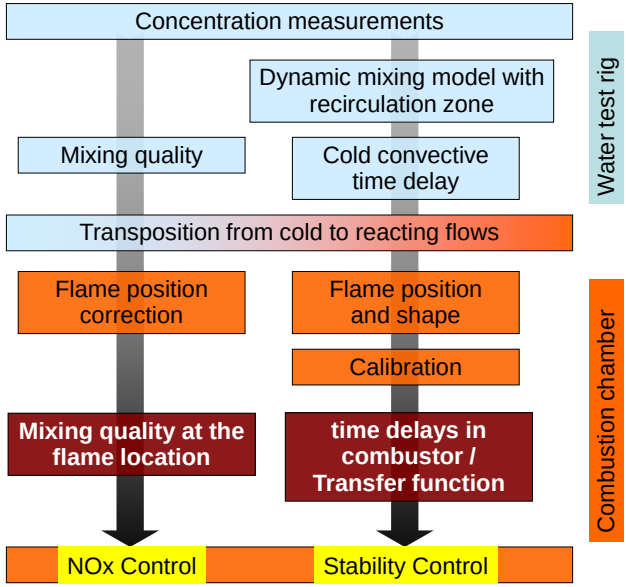

Figure 1.11: Strategy from cold to reacting flow to investigate, model and control NO_x emissions and pressure pulsations in a premixed combustor

The previous objectives are successively reported in the present work as illustrated in Fig. 1.12. The motivations as well as a literature review were already presented in the present chapter. Chapter 2 relates the theoretical background necessary for understanding of the basic physical mechanisms (mixing quality and mixing transfer function, NO_x emissions, acoustics and

heat release). The description of turbulent flows, swirling flows and their related coherent structures is provided. The basic equations describing the mixing in simple burner models is then performed, with the focus oriented on the passive scalar mixing. The practical realization of industrial mixers as well as the relevant parameters which determine the mixing quality are presented, followed by the equations used to transpose in the air the results obtained in water. A discussion about the physical differences between gaseous and aqueous mixing follows. The basics of combustion (laminar and turbulent flames, flame regimes, NO_x emissions formation pathways and experimental model) are then explained. Finally, the relevant acoustic equations are briefly described.

In Chapter 3, the basics of the fluorescence and chemiluminescence are described, as both principles are used in the two test rigs considered. The burner and its modified injectors as well as the water test rig and combustion chamber are then described. The measurement techniques used in both test rigs are then described. The thermoacoustic network model of the combustion chamber is also presented.

Starting with a thermoacoustic analysis of the combustor which justifies the use of the modified injection, Chapter 4 characterizes the standard injection for the combustor and shows that the modified injection developed is suited to control the pressure oscillations and NO_x emissions. The flow field as well as the passive scalar field of the burner are then shown to give an overview of the main mechanisms present in the burner.

The validation of the methodology from cold flow to reacting flow is the topic of Chapter 5. It is shown there that the flow field and dominant turbulent length scales are very similar, even in the presence of combustion. The chapter ends with an estimation of the combustion regime of one operating point in the Borghi diagram.

The flow field similitude being ensured, Chapter 6 draws the quantitative link between the cold flow mixture quality and the NO_x emissions. An estimation of the mixing quality at the flame is made possible when the experimental mixing quality model is associated with the flame position in the combustor. It is also shown that the chemiluminescence of the flame is an appropriate and fast surrogate measurement of the NO_x emissions.

Chapter 7 deals first with the modeling of the temporal mixing response (mixing transfer function MTF) of a staged fuel injection. A methodology which illustrates how the MTF can be recorded from high-speed laser-induced fluorescence is shown. A mixing network model is used to remove the influence of the recirculation zone on the response recorded at the burner outlet. A link between the cold flow MTF and the real flame transfer function is drawn with the help of flame visualization.

In Chapter 8, an extremum-seeking controller is implemented to control both the NO_x emissions and the pressure pulsations of the combustor. An extension of this controller with the knowledge gained from the cold flow measurements is then proposed.

Finally, the last part of the thesis, Chapter 9, deals with the development and testing of a new fuel injection concept to achieve better and faster fuel/air homogenization. The effect of the fuel injection modification and axial forcing on the mixing quality is reported. A promising self-oscillating device, a fluidic, exhibits the potential to further improve the scalar mixing quality in premixed burners.

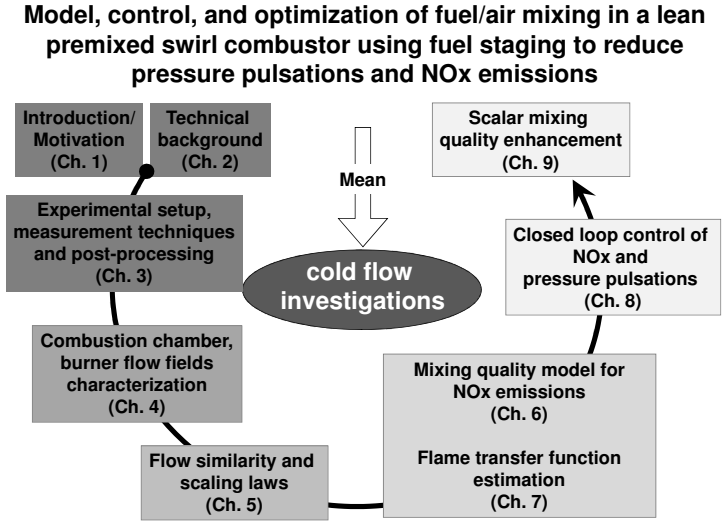

Figure 1.12: Schematic outline of the thesis

Chapter 2

Technical background

2.1 Turbulent flows

2.1.1 Phenomenologies

In the late 19th century, Lord Reynolds performed the first visualization of the turbulent flow regime, which differs strongly from laminar flow regime, in a simple channel. In laminar configuration the fluid flows in parallel layers without disruption between the layers; turbulent flows can be considered to be dominated by stochastic motion, which is the opposite of determined laminar flows. In this particular case, the energy brought to the fluid by the pressure gradient (necessary for bringing the fluid in movement) is first converted into a convection energy, which outweights the viscosity forces. A transfer of the kinetic energy in the mean velocity field $\overline{\boldsymbol{u}}(\boldsymbol{x})$ toward larege scale vortices (macro scale with integral length scale Λ^x_{uu}) takes place. These vortices break up into smaller vortices, and so on, down to the smallest scale called the micro scale l_k (or Kolmogorov scale), beyond which the dissipation process takes place and converts the kinetic energy in heat (Fig. 2.1).

Similar transfer mechanisms are valid for velocities or scalar properties (such as temperature or concentration) of a fluid and such process occur in all turbulent flows. The Reynolds number, ratio of dynamic to viscosity forces, is used to distinguish laminar from turbulent flows. It is built from a characteristic length D, a mean reference velocity U_0 and the kinematic

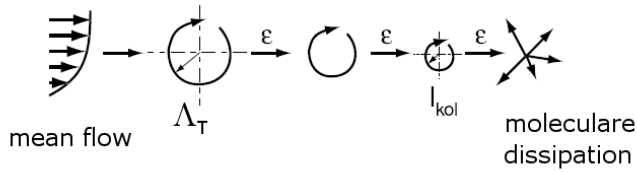

Figure 2.1: Energy transfer from the mean flow over the integral length scale Λ_T to the smallest length scale where molecular dissipation occurs (Kolmogorov length scale l_k) (from [Wäs08])

viscosity of the fluid ν. It reads

$$Re = \frac{U_0 D}{\nu} \,. \tag{2.1}$$

For example, the transition between laminar and turbulent flows takes place typically in pipe flows for Reynolds numbers of $Re \in \left[2.3 \times 10^3, 4 \times 10^3\right]$ and for most technical applications, a flow is considered to be turbulent when $Re > 4 \times 10^3$, a value which is more than 10 times smaller than the typical Reynolds number of today's gas turbine combustors.

2.1.2 Statistical description of turbulent flows

In turbulent flows, the instantaneous velocity field $\boldsymbol{u}(\boldsymbol{x}, t)$ (the bold notation states for a three-dimensional vector field, $\boldsymbol{x} = (x, y, z)$ and $\boldsymbol{u} = (u_i, u_j, u_k) = (u, v, w)$) can be split into the mean velocity field $\overline{\boldsymbol{u}}(\boldsymbol{x}, t)$ and a random, stochastic part $\boldsymbol{u}'(\boldsymbol{x}, t)$. This separation is called Reynolds decomposition and reads

$$\boldsymbol{u}(\boldsymbol{x}, t) = \overline{\boldsymbol{u}}(\boldsymbol{x}) + \boldsymbol{u}'(\boldsymbol{x}, t) \,, \tag{2.2}$$

where $\overline{(\cdot)}$ represents the temporal averaging operator, defined for statistically stationary turbulence as

$$\overline{\boldsymbol{u}}(\boldsymbol{x}) = \lim_{T \to \infty} \frac{1}{T} \int_0^T \boldsymbol{u}(\boldsymbol{x}, t) \, dt \,. \tag{2.3}$$

This results in the mean or expectation of the velocity field $\boldsymbol{u}(\boldsymbol{x}, t)$. The ensemble of the values taken by a random variable u from the velocity field $\boldsymbol{u}(\boldsymbol{x}, t)$ can be determined from a statistical analysis described by the so-called probability density functions (PDF). A probability density function of the variable u, f, is the derivative of the distribution function $F(U)$, which is the probability P of finding a value $u < U$:

$$F = P(u < U)\,, \tag{2.4}$$

where U is a sample space variable of the random variable u. The PDF f then simply reads

$$f(U) = \frac{dF(U)}{dU}\,. \tag{2.5}$$

The probability of finding the value u within the entire range of possible values is equal to unity and expressed as

$$\int_{-\infty}^{+\infty} f(U)\,dU = 1\,. \tag{2.6}$$

From the PDF f, the temporal statistical moments of order n are calculated according to the following expression

$$\overline{(u - \overline{u})^n} = \int_{-\infty}^{+\infty} (U - \overline{u})^n\, f(U)\,dU\,. \tag{2.7}$$

The first-order moment, with $n = 1$, is the averaged value, while the second-order moment, with $n = 2$, is called the variance and further denoted as σ^2, square value of the standard deviation σ. The same notation is valid when considering spatial variations. In this case, the temporal averaging operator can be replaced by the spatial averaging operator $\langle\cdot\rangle$.

If a finite number N of samples of a variable x are available, the average $\overline{x}$ is defined as

$$\overline{x} = \frac{1}{N}\sum_{i=1}^{N} x_i\,, \tag{2.8}$$

and the unbiased variance verifies

$$\sigma_x^2 = \frac{1}{N-1}\sum_{i=1}^{N}(x_i - \overline{x})^2 \,. \tag{2.9}$$

2.1.3 Length scales and energy cascade

2.1.3.1 Integral length scales

As illustrated in Fig. 2.1, if turbulent flows are dominated by stochastic motion, coherent structures are also generated by the flow. Hence, spatial locations close enough to one another will not take values independent from each other. Instead they will be correlated, and the degree of correlation will vary depending on the spatial ($d\boldsymbol{r}$) or temporal (dt) distance between the points. Such correlation is described mathematically by a generalized normalized correlation function (or correlation coefficient) R_{ij}, which reads

$$R_{ij}(\boldsymbol{x}, t, d\boldsymbol{r}, dt) = \frac{\overline{u_i'(\boldsymbol{x}, t) \cdot u_j'(\boldsymbol{x} + d\boldsymbol{r}, t + dt)}}{\sqrt{\overline{u_i'^2(\boldsymbol{x}, t)}}\sqrt{\overline{u_j'^2(\boldsymbol{x} + d\boldsymbol{r}, t + dt)}}} \,, \tag{2.10}$$

and verifies $-1 < R_{ij} < 1$. R_{ij} quantifies the degree of correlation between the turbulent velocity component u_i' measured at the coordinate $\boldsymbol{x}$ and at the instant t with the turbulent velocity component u_j' recorded at the location $\boldsymbol{x} + d\boldsymbol{r}$ at the time $t + dt$.

The integral macro scales of the flow are then obtained from the integration of the auto-correlation coefficient R_{ii}. The general definition reads

$$\Lambda_{u_i u_i}^{\boldsymbol{r},t}(\boldsymbol{x}, t) = \int_0^\infty R_{ii}(\boldsymbol{x}, t, d\boldsymbol{r}, dt)\, d\boldsymbol{r}\, dt \,. \tag{2.11}$$

When spatial length scales are considered, the temporal displacement is set to zero ($dt = 0$) and the macro length scale field in the direction defined by the vector $\boldsymbol{r}$, $\Lambda_{u_i u_i}^{\boldsymbol{r}}(\boldsymbol{x})$ is calculated. If planar spatial measurements are considered, with two velocity components recorded in two dimensions of the space, up to 4 integral length scales can be defined at each location: $\Lambda_{u_i u_i}^{x}(\boldsymbol{x})$, with $i = 1, 2$, are the longitudinal length scales if x is the

main flow direction. $\Lambda^{y}_{u_i u_i}(\boldsymbol{x})$, with $i = 1, 2$, are the transversal length scales. Otherwise, up to 9 typical length scales can be built into a three-dimensional flow. Similarly, the integral time scale $\Lambda^{t}_{u_i,u_i}$ can be calculated from Eq. 2.10 when setting the displacement to zero ($d\boldsymbol{r} = 0$).

With the Taylor hypothesis of frozen 2D turbulence, completed with the results of Wygnanski and Fielder, the link between $\Lambda^{x}_{u_i u_i}$ and $\Lambda^{t}_{u_i u_i}$ is drawn with the mean convective velocity $\overline{u_i}$:

$$\Lambda^{x}_{u_i u_i} = \overline{u_i}\Lambda^{t}_{u_i u_i}. \tag{2.12}$$

This means that from a pointwise measurement system with high temporal resolution, which allows $\Lambda^{t}_{u_i u_i}$ to be calculated, the spatial length scale is obtained by multiplying the latter with the averaged and local convective velocity $\overline{u_i}$. Unfortunately, this expression is generally not valid for complex three-dimensional and non-homogeneous turbulent flows, as the validity condition, which states that the velocity fluctuations are much lower than the mean flow velocity ($u'/\overline{u} << 1$), is generally broken.

2.1.3.2 Micro-length scales

The Taylor micro-scale is constructed from the Taylor expansion at the origin of the correlation function. The Taylor micro-scale is only an intermediate length scale between the integral and dissipation length scales and reads

$$\lambda_u = \left(\frac{2\overline{u'^2}}{\langle \left(\frac{\partial u'}{\partial x}\right)^2 \rangle} \right)^{0.5}. \tag{2.13}$$

In literature, the longitudinal Taylor micro-scale is often written as λ_f and the transversal Taylor micro-scale, as λ_g.

2.1.3.3 Dissipation length scales

The energy contained in the macro structures of the flow is transfered to smaller scales and so on, down to the smallest scales where the energy dissipates. The question of how this transfer takes place and down to which length scale has been answered using the theory of Kolmogorov [Kol41]. Three major hypotheses describe the (universal) behavior of turbulent

flows. From these hypotheses it is proved that for sufficiently high Reynolds numbers, the small-scale turbulent motion ($l << \Lambda^x_{uu}$) is statistically isotropic. In other words, for eddies of the size smaller than the integral length scales of the flow (typically $l < \frac{1}{6}\Lambda^x_{uu}$, [Pop00]), the directional information is lost and from here, the universal behavior of turbulent flows begins. This range is known as the *universal equilibrium range*. The parameters characterizing this domain are the transfer of energy, which, because of a statistical equilibrium, is equal to the dissipation rate ϵ, and the viscous dissipation, described by the kinematic viscosity ν. These two parameters allow the building of the characteristic length l_k, velocity u_k, and time τ_k scales, called the Kolomogorov scales. They are respectively equal to

$$l_k = \left(\frac{\nu^3}{\epsilon}\right)^{1/4} , \tag{2.14}$$

$$u_k = (\nu\epsilon)^{1/4} \text{ , and} \tag{2.15}$$

$$\tau_k = \left(\frac{\nu}{\epsilon}\right)^{1/2} . \tag{2.16}$$

The Kolmogorov length scales describe the smallest eddies existing in the flow, beyond which only molecular dissipation occurs. However, the dissipation process does not start at the length scale l_k but at higher length scales ($l > 60l_k$ [Pop00]), with a maximum close to the Taylor length scale λ_g. The Reynolds number Re_k at these Kolmogorov scales verifies

$$Re_k = \frac{u_k l_k}{\nu} = 1 . \tag{2.17}$$

The part of the kinetic energy contained in the flow at the different wave numbers $k = 2\pi/l$ is described by the turbulent kinetic energy spectrum $E(\kappa)$, which verifies

$$k_{l_1,l_2} = \int_{l_1}^{l_2} E(\kappa)\, d\kappa , \tag{2.18}$$

where k_{l_1,l_2} is the turbulent kinetic energy contained in the wavelength range $[l_1, l_2]$. Furthermore, it can be shown that the dissipation within

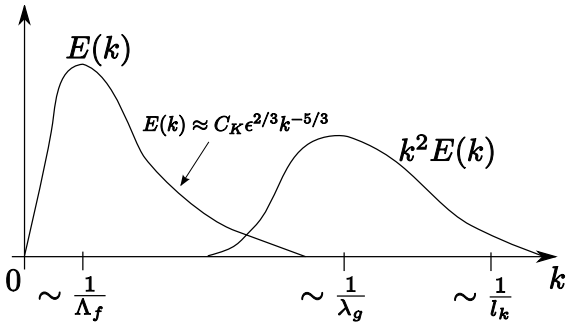

Figure 2.2: Turbulent kinetic energy spectrum $E(k)$ and dissipation spectrum $k^2E(k)$ of an isotrop turbulence with high Reynolds number Re. (From [BCB03])

that range verifies

$$\epsilon_{l_1,l_2} = \int_{l_1}^{l_2} 2\nu\kappa^2 E(\kappa)\, d\kappa\,. \tag{2.19}$$

For small wave numbers (i.e., large length scales close to Λ^x_{uu}), the dissipation is, therefore, much smaller than the turbulent kinetic energy. Furthermore, for sufficiently high Reynolds numbers, the range of the macro scales is much higher than the dissipation scales, so that a range exists where the viscosity merely influences the transfer process of energy from the large to the small scales. This transfer only depends on the dissipation rate and the energy spectrum verifies

$$E(k) \approx C_K \epsilon^{2/3} k^{-5/3}\,, \tag{2.20}$$

which is also called the Kolmogorov $-\frac{5}{3}$ spectrum. C_K is the Kolmogorov constant. This process is illustrated in Fig. 2.2, where the energy and dissipation spectra are presented.

An estimation of the dissipation rate ϵ can be obtained when looking at the energy of the large scales which must dissipate after the cascade process. The kinetic energy contained in these macro scales will solely depend on the turbulent velocity u'_{Λ^x} associated to the macro scale Λ^x (simplified

notation of Λ^x_{uu}), and so for the dissipation rate ϵ, which scales as

$$\epsilon \propto \frac{u'^3_{\Lambda^x}}{\Lambda^x} \,. \tag{2.21}$$

It is now interesting to compare the scales of two different fluids (water, index w and air, index a) used for investigations on one similar geometry (scaling ratio Λ^x_a/Λ^x_w). If Reynolds number similitude is ensured, the average Reynolds numbers between the two fluids are identical. This is also true for the turbulent Reynolds number, defined as

$$Re_t = \frac{u'_{\Lambda^x}\Lambda^x}{\nu} \,. \tag{2.22}$$

Hence, from the identity $Re_{t,a} = Re_{t,w}$, one can write

$$\frac{u'_{\Lambda^x,a}\Lambda^x_a}{\nu_a} = \frac{u'_{\Lambda^x,w}\Lambda^x_w}{\nu_w} \,. \tag{2.23}$$

In the same way, assuming that the proportionality factor in Eq. 2.21 is independent of the medium for geometrically similar setup, one also obtains

$$\frac{\epsilon_a\Lambda^x_a}{u'^3_{\Lambda^x,a}} = \frac{\epsilon_w\Lambda^x_w}{u'^3_{\Lambda^x,w}} \,. \tag{2.24}$$

Then, using Eq. 2.23 with Eq. 2.24 into Eq. 2.14 leads to the relationship between the Kolmogorov micro scales $l_{k,a}$ and $l_{k,w}$

$$l_{k,a} = l_{k,w}\left(\frac{\Lambda^x_a}{\Lambda^x_w}\right)^{0.5} \,, \tag{2.25}$$

which verifies that $l_{k,a} = l_{k,w}$ if the systems are geometrically identical ($\Lambda^x_a = \Lambda^x_w$). Hence, if the Reynolds similitude is conserved between two fluids used to investigate one setup, both the turbulent macro and micro scales are identical. This is a very practical consequence of the similarity theorem, also called Buckingham π-theorem.

This property is unfortunately not true for passive scalars (like concentration, temperature, etc.) added to the flow. In this case, the properties of the fluid, in particular the coefficient of diffusivity of a specie A in the

medium B, Γ_{AB}, play an important role and vary greatly between the fluids considered. The scale at which the molecular diffusion takes place is called the Batchelor scale, and is defined as

$$l_b = \left(\frac{\nu \Gamma_{AB}^2}{\epsilon} \right)^{1/4} . \tag{2.26}$$

It should be noted that in the case of the mixing of scalar fluid properties, the role of the diffusivity Γ_{AB} is similar to the role of the viscosity ν, which is responsible for the transfer (or diffusivity) of momentum within the fluid. Therefore, a dimensionless number, the Schmidt number, can be written as

$$Sc = \frac{\nu}{\Gamma_{AB}} \tag{2.27}$$

and Eq. 2.26 can be recast as

$$l_b = l_k / Sc^{0.5} . \tag{2.28}$$

For air flows, the Schmidt number verifies $Sc \approx 1$ while in aqueous solutions, typical Schmidt numbers are of the order $Sc \approx 10^3$. This means that the Batchelor scale is approximately equal to the Kolomogorov dissipation scale in the air, while in water it is approximately 30 times smaller.

To summarize this part, the typical length scales of the system considered ($Re \approx 4 \times 10^4$) are listed hereafter; details about the calculation can be found in Sec. 2.6 and Sec. 5:

	Λ_{uu}^x in m	l_k in m	l_b in m	τ_k in s
water	1×10^{-2}	3×10^{-5}	3.3×10^{-7}	1×10^{-3}
air	1×10^{-2}	3×10^{-5}	3×10^{-5}	3×10^{-5}

Table 2.1: Typical length and time scales of the flow field of the investigated burner for $Re \approx 4 \times 10^4$, preheated air temperature $T_{pre} = 423\,\mathrm{K}$

Table 2.1 reveals that the spatial resolution needed to resolve the Batchelor length scale in water is much higher than that in the air. The spatial scale of molecular mixing in water can only be resolved if a spatial resolution of

$6.7{\times}10^6\,\mathrm{m}^{-1}$ is achieved, which means that a camera with a standard resolution of $1000{\times}1000\,\mathrm{px}^2$ should be focused on a section of $0.15{\times}0.15\,\mathrm{mm}^2$ at most (!). This resolution constraint is approximately 30 times lower in the air.

However, the part of the micro scale scalar fluctuations in the the total unmixednes can be considered as negligible and does not need to be resolved in water. Indeed, similar to the velocity fluctuations, a spectrum of the turbulent scalar fluctuations ϕ'^2 can be measured, and a similar transfer of the fluctuating "energy" from the macro scales to the micro scales occurs, as illustrated in Fig. 2.3. The total quality of the mixture can be expressed, as shown by Baldyga [Bal89], as the sum of the mixing qualities (or concentration variances) of the inertial-convective range (length scales higher then l_k), the viscous-convective range (length scales between l_k and l_b), and viscous-diffusive range (length scales smaller than l_b). The relative part of the viscous-diffusive unmixedness in the total unmixedness of the mixture remains marginal so that only the inertial-convective and viscous-convective ranges can be considered.

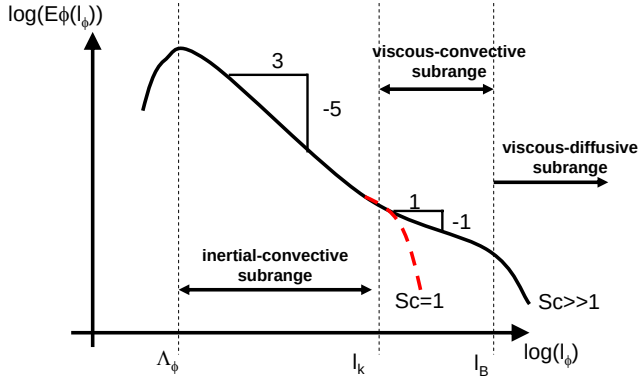

Figure 2.3: Spectrum of concentration variance in aqueous (solid) or gaseous (dashed) flows. From Baldyga and Bourne [BB99].

Furthermore, a macromixed system in water is not necessarily mixed at the molecular scale, i.e. micromixed; this is not the case in gaseous flows, as a consequence of the strong diffusivity. Hence, it is adequate to resolve the

inertial-convective subrange only when aqueous investigations are used to predict the mixing behavior of gaseous systems. This also means that the measurement system should resolve the whole cross section of the mixing channel to capture the large scale spatial inhomogeneities. In the present work, the optical measurement system has a spatial resolution of 10^4 px/m, giving a lowest resolved scale of 2×10^{-4} m, which is one order of magnitude higher than the Kolomogorov length scale l_k.

2.2 Swirling flows

In premixed combustion, flows with a high degree of swirl are typically used as hydrodynamic flame holders. The high degree of swirl in combination with a sudden area expansion generates a vortex breakdown, which then creates two recirculation zones. Between the recirculation zones and the main jet, i.e., in the shear layers of the flow, the velocities are sufficiently low to be on the order of magnitude of the turbulent flame velocity so that the flame can stabilize. This principle is used in the current setup and the following section presents the main flow field as well as dominant features of the flow at the outlet of the burner.

2.2.1 The burner and mean flow field

The burner used is an industrial standard swirl-inducing premixed burner, whose principle is depicted in Fig. 2.4. Two half-cones are radially shifted with respect to each other, creating two slots through which the air flows tangentially into the burner. The fuel, generally natural gas, as used in the present work, is injected into crossflow at the entrance of the inlet slots. The fuel then mixes with air inside the burner before reaching the flame, which can stabilize at the inner and outer shear layers. A complete description of the burner under running conditions can be found in Doebbeling et al.[DKP+94] or Sattelmayer et al.[SFH+92] .

Particle image velocimetry measurements (PIV) allow for characterization of the velocity field at the burner outlet. The axial mean velocity field is illustrated in Fig. 2.5 for the axial planes (xy) and (xz), the plane (xz) being defined by the inlet slots of the burner. The typical shape of a

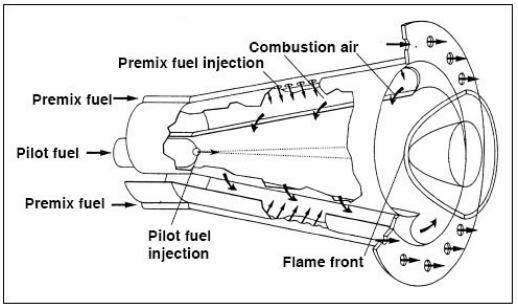

Figure 2.4: Principle of the swirl-inducing burner used in the present work [SFH+92]

conical-like jet flow surrounded by an internal recirculation zone (IRZ) and an external recirculation zone (ERZ) is recognizable. Moreover, the velocity field is not rotationnally symmetric, as the shape of the depicted iso-velocity lines vary between the two measurement planes. These results are important regarding the measurement of the fuel/air ratio at the burner outlet.

2.2.2 Swirl number

Swirling flows are characterized by the so-called swirl number S, which is a measure of the swirl intensity. The common definition of this number is based on the ratio of angular momentum flux $\dot{I}_\theta$ to axial momentum flux $\dot{I}_x$, as used by Gupta [GL85] or more recently Fritz [Fri03] and Kiesewetter [Kie05]. The general expression of S then reads

$$S = \frac{\dot{I}_\theta}{R\dot{I}_x} = \frac{\frac{1}{T}\int_0^T \int_0^R \int_0^{2\pi} \rho u_x u_\theta r^2 \, dr d\theta dt}{R\frac{1}{T}\int_0^T \int_0^R \int_0^{2\pi} \left(\overline{p}(r,\theta) - \overline{p}_\infty + \rho u_x^2\right) r \, dr d\theta dt}, \qquad (2.29)$$

where R is the characteristic radius used to make the ratio of the momentum fluxes dimensionless, p the static pressure, and p_∞ the pressure of the fluid at $r \to \infty$. Here, the velocity is expressed in cylindrical coordinates ($\boldsymbol{u} = (u, u_r, u\theta)$, axial, radial and azimuthal velocities). Splitting the instantaneous velocities into their mean and oscillating components and

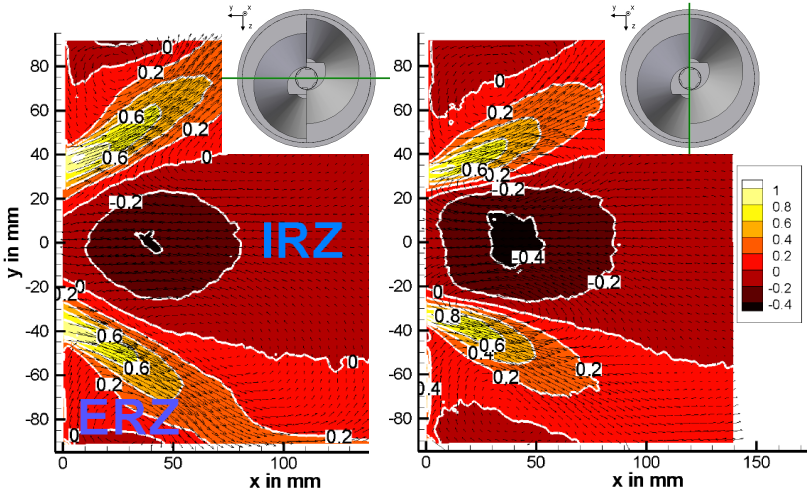

Figure 2.5: Contour plot of the axial velocity in m/s in the (xy) (left) and (xz) (right) measurement planes. Combustion chamber with d=200 mm, $U_0 = 0.5$ m/s. IRZ: Internal recirculation zone, ERZ: External recirculation zone.

averaging over time leads to the simplified definition

$$S_1 = \frac{\int_0^R \int_0^{2\pi} \rho \left(\overline{u_x u_\theta} + \overline{u'_x u'_\theta} \right) r^2 \, dr d\theta}{R \int_0^R \int_0^{2\pi} \left(\overline{p}(r,\theta) - \overline{p}_\infty + \rho \left(\overline{u_x^2} + \overline{u_x'^2} \right) \right) r \, dr d\theta}. \tag{2.30}$$

As the pressure term is experimentally difficult to measure, a second definition of the swirl number, S_2 can be built without the pressure term of Eq. 2.30. The normal and shear strain rates are also often neglected when compared to the values of the mean flow field [Fri03], so that if axisymmetry of the flow is assumed, a third simplified definition appears:

$$S_3 = \frac{\int_0^R \rho \overline{u_x} \cdot \overline{u_\theta} r^2 \, dr}{R \int_0^R \rho \overline{u_x}^2 r \, dr} \tag{2.31}$$

It is interesting to compare the three swirl number definitions on the present burner. The pressure term is first approximate from the radial pressure

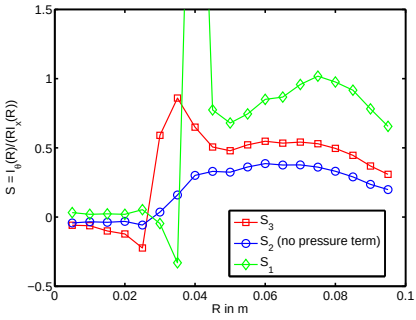

Figure 2.6: Swirl number as a function of the radius of integration for different swirl number definitions

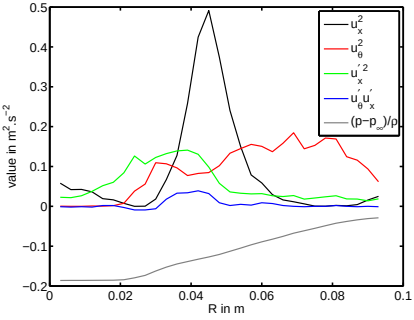

Figure 2.7: Comparison of the different terms of the swirl number definition

equation, which reads

$$p(R,\theta) - p_\infty = \int_{R=\infty}^{R} \rho \frac{\overline{u_\theta}^2}{r}\, dr\,, \tag{2.32}$$

where p_∞ is the pressure of the fluid at rest. Figure 2.6 shows the evolution of the three swirl numbers depending on the reference radius R. The azimuthal and axial velocities are measured with laser Doppler anemometry (LDA) performed in the measurement plane (xy) (perpendicular to the slots) at an axial location $x{=}D/4{=}20.5\,\text{mm}$ above the burner outlet for the 200 mm combustion chamber. It is clear that the different definitions induce considerable differences in the swirl numbers calculated ($S_2{=}0.32$ to $S_1{=}0.68$ for $R = 50\,\text{mm}$). This characteristic number is thus, dependent on both the swirl number definition as well as on the radius taken as reference. For a radius verifying $R \geq 50\,\text{mm}$, the swirl number remains either steady or presents a local minimum. Thus, this radius was chosen as the reference radius for swirl number calculations. Figure 2.7 compares the weight of the different swirl number definition terms depending on the radius of integration. It shows that the pressure term is more important than the normal and strain rates in the present case and should not be neglected. Thus, a swirl number of $S_1 = 0.68$ for the enclosed configuration was retained, confirming that a flow with strong swirling motion is used.

2.2.3 Coherent structures

The generation mechanisms of coherent structures in strong swirling flows was reviewed by Syred [Syr06]. In the typical flow field of premixed combustors, at least two different structures associated with each other are generally present: first, a so-called precessing vortex core (PVC) is generated close to the stagnation point of the internal recirculation zone. This vortex precesses around the flow axis as illustrated in Fig. 2.8, and so does the region of reverse flow. The direction of precession is strongly sensitive to the swirl number. This precessing motion initiates a helical secondary vortex which spreads radially and travels downstream of the flow. The winding of the helical structure, obtained when looking at a temporally frozen structure, is in most uncontrolled cases opposite to the precessing motion.

Coats [Coa96] discussed the general interaction between coherent structures and combustion. In the case of such a three-dimensional coherent structure, he points out that the effect of combustion on the structure depends strongly on the manner of introduction of the fuel. If a diffusion-like flame is used, the combustion will damp the helical structure, while if an almost perfectly premixed flame is used, the combustion may tend to increase the amplitude and rotation frequency. As such coherent structures are able to induce heat release fluctuations which may trigger combustion instabilities, they must be considered and their mechanisms understood.

Such coherent structures induce strong periodical velocity oscillations and the explicit formulation of these periodical oscillations with the so-called triple decomposition (Reynolds and Hussain [HR70]) is more appropriate in such cases

$$\boldsymbol{u}(\boldsymbol{x},t) = \overline{\boldsymbol{u}}(\boldsymbol{x}) + \tilde{\boldsymbol{u}}(\boldsymbol{x},t) + \boldsymbol{u}''(\boldsymbol{x},t)\,, \tag{2.33}$$

with $\tilde{\boldsymbol{u}}$ describing the coherent flow motion and $\boldsymbol{u}''(\boldsymbol{x},t)$, the non-coherent fluctuating motion.

Regarding the burner used in this work, the cold coherent structures were investigated by Paschereit et al. [PGW99] in a water test rig with help of planar LIF and LDA velocity measurements. Flame visualization performed in reacting flows helped to visualize the interaction of the structure

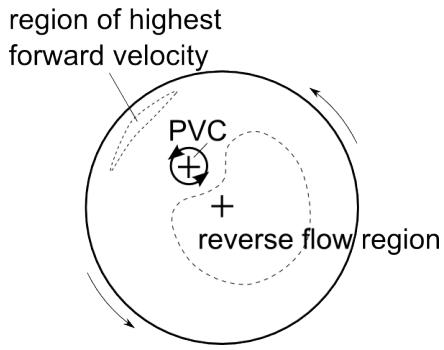

Figure 2.8: Cross-section of a swirling flow showing the precessing vortex core location relative to the rotation axis. The external arrow indicate the precessing motion of the three indicated regions. The direction of swirl may occur in both directions depending on the swirl number

with the combustion zone. The typical helical structure could be evidenced and will be fully characterized in the present work with high-speed measurement techniques.

2.3 Equations of turbulent flows

2.3.1 General equations

The motion of turbulent flows is described by the Navier-Stokes equations. The continuity equation reads

$$\frac{\partial \rho}{\partial t} + \nabla \cdot (\rho \boldsymbol{u}) = 0\,, \tag{2.34}$$

where ρ is the fluid density. For simplification $\boldsymbol{u} = \boldsymbol{u}\,(\boldsymbol{x}, t)$ is used in the following. The conservation of momentum reads

$$\frac{\partial \rho \boldsymbol{u}}{\partial t} + \nabla \cdot (\rho \boldsymbol{u}\boldsymbol{u}) = -\nabla p + \nabla \cdot \boldsymbol{\tau} + \rho \boldsymbol{g}\,. \tag{2.35}$$

The terms on the left-hand side of Eq. 2.34 and Eq. 2.35 represent the local rate of change and the convective term. On the right-hand side,

the pressure gradient is found. The term $\nabla \cdot \boldsymbol{\tau}$ represents the molecular transport due to viscosity and the term $\rho \boldsymbol{g}$ describes the volume forces acting on the flow (such as the forces due to buoyancy, neglected in the present work and in the following equations). $\boldsymbol{\tau}$ is the viscous stress tensor which, for a newtonian fluid, is

$$\boldsymbol{\tau} = \mu \left[2\boldsymbol{S} - \frac{2}{3}\boldsymbol{\delta} \nabla \cdot \boldsymbol{u} \right] , \tag{2.36}$$

and is built from the rate of strain tensor $\boldsymbol{S}$

$$\boldsymbol{S} = \frac{1}{2} \left[\nabla \boldsymbol{u} + \nabla \boldsymbol{u}^T \right] \tag{2.37}$$

and the rate of expansion tensor $\boldsymbol{\delta} \nabla \cdot \boldsymbol{u}$. If incompressible flows are considered, the latter parameter is zero and, assuming that ρ and the dynamic viscosity μ are uniform, the momentum equation simplifies to

$$\frac{D\boldsymbol{u}}{Dt} = -\frac{1}{\rho} \nabla p + \nu \nabla^2 \boldsymbol{u} , \tag{2.38}$$

where D is the substantial derivative in conservative form

$$\frac{D}{Dt} \equiv \frac{\partial}{\partial t} + \nabla \cdot \boldsymbol{u} . \tag{2.39}$$

If the instantaneous velocity field is decomposed, as in Eq. 2.33, and used in Eq. 2.35, then one can show that, after time averaging the equation and using the property of incompressibility, Eq. 2.35 reads

$$\frac{\bar{D}\overline{\boldsymbol{u}}}{\bar{D}t} = -\frac{1}{\rho} \nabla \overline{p} + \nu \nabla^2 \overline{\boldsymbol{u}} - \nabla \cdot \left[\overline{\tilde{\boldsymbol{u}} \tilde{\boldsymbol{u}}} + \overline{\boldsymbol{u}'' \boldsymbol{u}''} + \overline{\boldsymbol{u}'' \tilde{\boldsymbol{u}}} + \overline{\boldsymbol{u}'' \tilde{\boldsymbol{u}}}^T \right] , \tag{2.40}$$

where the operator $\frac{\bar{D}}{\bar{D}t}$ is the mean substantial derivative defined as

$$\frac{\bar{D}\overline{\boldsymbol{u}}}{\bar{D}t} \equiv \frac{\partial}{\partial t} + \boldsymbol{u} \cdot \nabla . \tag{2.41}$$

Considering the fact that the turbulent fluctuations are uncorrelated with the coherent motion, Eq. 2.40 simplifies to

$$\frac{\bar{D}\overline{\boldsymbol{u}}}{\bar{D}t} = -\frac{1}{\rho}\nabla\overline{p} + \nu\nabla^2\overline{\boldsymbol{u}} - \nabla\cdot\left[\overline{\tilde{\boldsymbol{u}}\tilde{\boldsymbol{u}}} + \overline{\boldsymbol{u}''\boldsymbol{u}''}\right] . \tag{2.42}$$

The last term on the right-hand side ($\overline{\boldsymbol{u}''\boldsymbol{u}''}$) characterizes the so-called Reynolds stress tensor, which appears alone in this equation if the coherent motion is not explicitly split from turbulent fluctuations. If the distinction is made, then a coherent Reynolds stress term ($\overline{\tilde{\boldsymbol{u}}\tilde{\boldsymbol{u}}}$) is added to the turbulent and conventional Reynolds stress term.

2.3.2 Scalar transport

Similar to the conservation of momentum, an equation of reacting scalar conservation can be formulated and reads

$$\rho\frac{\partial Z_i}{\partial t} + \rho\boldsymbol{u}\cdot\nabla Z_i = -\nabla\cdot(-\rho\Gamma_i\nabla Z_i) + \omega_i\,, \tag{2.43}$$

where Z_i is the mass fraction for the chemical species i, Γ_i is the binary diffusion coefficient of the species i building the (simplified !) diffusive flux term $\rho\Gamma_i\nabla Z_i$, and ω_i is the chemical source term. This formulation is useful when the kinetics of the reacting process should be taken into account.

If one then considers the evolution of a passive scalar $\phi\,(\boldsymbol{x},t)$ in an incompressible flow, Eq. 2.43 simplifies to

$$\frac{D\phi}{Dt} = \Gamma\nabla^2\phi\,. \tag{2.44}$$

Using again the triple decomposition of the passive scalar, one obtains an expression similar to Eq. 2.42, which reads

$$\frac{\bar{D}\overline{\phi}}{\bar{D}t} = \nabla\cdot\left(\Gamma\nabla\overline{\phi} - \overline{\tilde{\boldsymbol{u}}\tilde{\phi}} - \overline{\boldsymbol{u}''\phi''}\right) = \nabla\cdot\left(\Gamma\nabla\overline{\phi} - \overline{\boldsymbol{u}'\phi'}\right) . \tag{2.45}$$

In this equation, it appears that the coherent turbulent transport term plays a similar role in the turbulent diffusion of the scalar ϕ to that for the

diffusion of coherent turbulent Reynolds stress. The closure of Eq. 2.42 and Eq. 2.45 depends on the description of the coherent and turbulent fluxes. A well-known solution is to use the gradient-diffusion hypothesis, which reads for the turbulent diffusivity

$$\overline{\boldsymbol{u}'\phi'} = -\Gamma_t \nabla \overline{\phi}\,. \tag{2.46}$$

The effective diffusivity Γ_{eff} is then defined as the sum of the molecular and turbulent (and coherent) diffusivities and Eq. 2.45 becomes

$$\frac{\bar{D}\overline{\phi}}{\bar{D}t} = \Gamma_{eff} \nabla \cdot \nabla \overline{\phi}\,. \tag{2.47}$$

2.3.3 Scalar variance evolution

Regarding the mixing process, the evolution of the mixture PDF over the mixing path is generally of interest. This can be simplified in modeling the evolution of the scalar variance $\overline{\phi'^2}$, which characterizes the level of fluctuations, similar to the turbulent kinetic energy. Its conservation equation, assuming incompressible flow, can be written as (see also Pope [Pop00])

$$\frac{\bar{D}\overline{\phi'^2}}{\bar{D}t} + \nabla \cdot T_\phi = P_\phi - \epsilon_\phi\,, \tag{2.48}$$

where P_ϕ is the scalar-variance production

$$P_\phi = -2\overline{\boldsymbol{u}'\phi'} \cdot \nabla \overline{\phi}\,, \tag{2.49}$$

and ϵ_ϕ is the scalar dissipation

$$\epsilon_\phi = 2\Gamma \overline{\nabla \phi' \cdot \nabla \phi'}\,. \tag{2.50}$$

T_ϕ characterizes the flux of scalar variance as

$$T_\phi = \overline{\boldsymbol{u}'\phi'^2} - \Gamma \nabla \overline{\phi'^2}\,. \tag{2.51}$$

Equation 2.48 can be further simplified as shown by Syed et al. [SRM07]. If one assumes first that at high Reynolds numbers, the molecular diffusion

term $\Gamma\nabla\overline{\phi'^2}$ can be neglected. Then, if similar closure assumptions to the eddy viscosity model $k-\epsilon$ are used, Eq. 2.48 reduces to

$$\frac{\bar{D}\overline{\phi'^2}}{\bar{D}t} = \nabla\cdot\left(\frac{\nu_t}{\sigma_k}\nabla\overline{\phi'^2}\right) + 2\frac{\nu_t}{\sigma_k}\left(\nabla\overline{\phi}\right)^2 - c_{g2}\frac{\epsilon}{k}\overline{\phi'^2}\,, \tag{2.52}$$

where σ_k and c_{g2} are constants. The previous equation shows how the evolution of the scalar variance is also determined by the mean scalar profile $\overline{\phi}$. Over the mixing path, two things must be known: How can the variance be expressed as a function of the mean scalar profile? How does this variance evolve over the mixing length? To answer the first question, a balance at one axial location can be considered. For this, the temporal variation as well as the transport terms can be neglected compared to the production and dissipation terms and Eq. 2.52 can be simplified to

$$\overline{\phi'^2} = A_1\Lambda^x\left(\nabla\overline{\phi}\right)^2\,. \tag{2.53}$$

The variance of the scalar is, thus, proportional to the squared spatial gradient of $\overline{\phi}$ at each location in the combustor. This is especially true regarding the initial variance at the location of the fuel injection, $\overline{\phi}^{\prime 2}_{init}$, which will depend on the spatial fuel split $\left(\nabla\overline{\phi}\right)_{init}$.

The response to the second question, which deals with the evolution of the scalar variance along the mixing length, is obtained when a balance between the convective transport and the production term is built. A one-dimensional system is considered and the infinitesimal balance reads

$$\overline{u_x}\frac{d\overline{\phi'^2}}{dx} = -c_{g2}\frac{\epsilon}{k}\overline{\phi'^2}\,. \tag{2.54}$$

This expression, assuming that the terms u_x, ϵ, k remain unchanged along the mixing path, leads to the equation

$$\frac{\overline{\phi'^2}(x)}{\overline{\phi'^2}_{init}} = e^{-A_2/D_b x}\,. \tag{2.55}$$

The decay of the mixture variance within the burner therefore follows an exponential function, and its absolute value depends on the initial mixture

variance. The previous equations can be used to model the mixing quality evolution within the premixed combustor.

2.3.4 Response to temporal fluctuations (Mixing Transfer Function)

If the flow field in the swirl-inducing burner can be analytically described [FPB03, KST91], this description may vary if modifications are preformed in the geometry of the combustor. However, even if the flow field is strongly three-dimensional, a one-dimensional approach reveals some important characteristics of the response of the flow to axisymmetric perturbation, as is the case when combustion instabilities occur. Assuming a one-dimensional transport of a passive scalar ϕ, Eq. 2.47 can be recast as

$$\frac{\partial \phi}{\partial t} + U_0 \frac{\partial \phi}{\partial x} - \Gamma_t \frac{\partial^2 \phi}{\partial x^2} = 0\,, \tag{2.56}$$

U_0 being the mean bulk velocity inside the burner and Γ_t being the turbulent diffusion coefficient, the molecular diffusion coefficient Γ being neglected.

Made dimensionless with the (turbulent) Péclet number $Pe = U_0 L/\Gamma_t$, the normalized scalar $\phi^* \in [0, 1]$, the time $t^* = tU_0/L$ and the axial coordinate $x^* = x/L$, Eq. 2.56 reads

$$\frac{\partial \phi^*}{\partial t^*} + \frac{\partial \phi^*}{\partial x^*} - \frac{1}{Pe} \frac{\partial^2 \phi^*}{\partial x^{*2}} = 0\,. \tag{2.57}$$

The Fourier transformation of Eq. 2.57 for harmonic perturbations,

$$\mathcal{F}(\phi^{*\prime}(x^*, t^*)) = \hat{\phi^*}(x^*, iSt)\,, \tag{2.58}$$

can be used to obtain the burner mixing transfer function (MTF) between the burner inlet ($x^* = 0$) and outlet ($x^* = 1$). $St = fL/U_0 = f\tau_{ref}$ is the axial Strouhal number of the burner. The Fourier transformation of a

function f is defined here as

$$\mathcal{F}\left(f(t)\right) = \hat{f}\left(\omega\right) = \int_{-\infty}^{+\infty} f(t) e^{-i\omega t} dt\,. \tag{2.59}$$

With the harmonic boundary condition $\hat{\phi}(0, iSt) = \exp(iSt)$, the only solution which does not diverge for $St \to \infty$ is

$$\hat{\phi}(x^*, iSt) = \hat{\phi}(0, iSt) \exp\left(x^* \frac{Pe}{2}\left(1 - \sqrt{1 + 8\pi i St Pe^{-1}}\right)\right)\,, \tag{2.60}$$

and the mixing transfer function between $x^* = 0$ and $x^* = 1$ reads

$$MTF(iSt) = \exp\left(\frac{Pe}{2}\left(1 - \sqrt{1 + 8\pi i St Pe^{-1}}\right)\right)\,. \tag{2.61}$$

For comparison, the transfer function of the widely used well stirred reactor (WSR) was also calculated and reads

$$MTF_{WSR}(iSt) = \frac{1}{1 + 2\pi i St}\,. \tag{2.62}$$

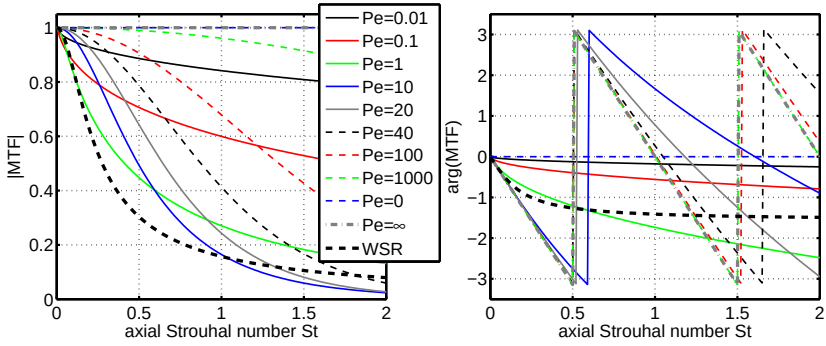

Figure 2.9: Amplitude (left) and phase (right) of the mixing transfer function (MTF) depending on the axial Strouhal number for different Péclet numbers. For comparison, the response of the well-stirred reactor (WSR) is depicted.

The amplitudes and phase plots of the mixing transfer function for different turbulent Péclet numbers are presented in Fig. 2.9. The results presented here can be also found in Chishty [CY08]. The general response of the premixer is that of a low-pass filter, with a cut-off frequency dependent on the Péclet number. Two extremal cases exist: if $Pe \to 0$, the convection is negligible and the diffusion of a perturbation at the inlet is transmitted immediately through the entire reactor. The response at the outlet gets closer to a dirac response without any mean convective time delay. The amplitude is, thus, maximized over the entire frequency range and the phase equals zero. If, on the contrary, $Pe \to \infty$, the convection dominates the mixing process. Here, the perturbations are convected almost unchanged toward the exit with a single time lag equal to the bulk residence time of the burner and the amplitude of the transfer function is also close to unity.

Péclet numbers of $Pe \in [5, 40]$ are typical for premixed swirl-inducing burners of gas turbines. For these values, the response for normalized frequencies higher than $St = 1.5$ is strongly dampened ($|MTF| < 0.2$) while it verifies $|MTF| > 0.5$ for $St < 0.5$. As typical residence times from the fuel injection down to the flame range from 5 to 10 ms, if concentration fluctuations are generated at the burner inlet, they will be strongly dampened at the burner outlet for $f > 200 - 100$ Hz. While this mechanism may not prevent the occurrence of combustion instabilities, it may limit the amplitude of limit-cycle oscillations.

When these transfer functions are converted back into an impulse response, the RTD is obtained and two integral values, the mean residence time $\overline{\tau^*}$ and the standard deviation $\sigma(\tau^*)$, can be calculated, as in Eq. 2.7. These properties are presented depending on the Pe number in Fig. 2.10. The value of the peak in the time delays, the most probable delay τ^*_{max}, is displayed as well. When $Pe \to 0$, the mean residence time decreases, while for $Pe > 1$, the mean convective time delay is constant and equal to unity. For $Pe < 100$, the peak of the most probable time delay is lower than the mean time delay. This is due to the tailing effect of the transition zone for moderate Pe numbers where the diffusion is not completely outperformed by the convective motion. The standard deviation of the RTD reaches a maximum for $Pe \in [0.1, 1]$ and decreases for lower or higher Pe-values,

which is consistent with the fact that the response at the outlet is close to a dirac response for $Pe \to 0$ and $Pe \to +\infty$.

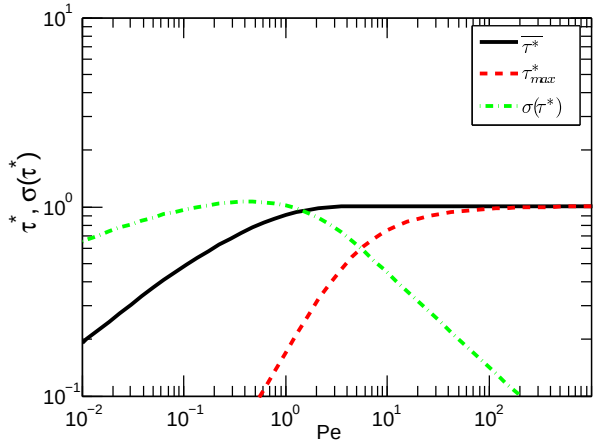

Figure 2.10: Evolution of the mean residence time $\overline{\tau^*}$, residence time at which the RTD presents a maximum τ^*_{max} and standard deviation of the residence time $\sigma(\tau^*)$

2.4 Jet in crossflow mixing

The previous section depicts the theoretical background necessary to describe the general behavior of spatial and temporal variations of the mixture quality in a premixed combustor. In the following, an analysis of the relevant factor for a technical mixer is presented. As shown in Fig. 2.4, a row of jets is used to inject the fuel upstream of the burner inlet slots. This injection is a typical jet in crossflow configuration which ensures appropriate mixing quality of the fuel/air mixture at the flame location.

Before looking at the effect of an array of jets, the mixing of one single jet must be considered. Such a configuration has been extensively investigated for more than 50 years and is still the subject of numerous research programs. The prediction of the jet trajectory, concentration decay, etc., are relevant topics for numerous industrial applications, such as mixing, cooling or pollutant dispersion. However, as remarked by Niederhaus [NCJ97],

"...the vast majority of the published work [on transverse jets] has focused on issues concerning the velocity field. Remarkably, there is a scarcity of research directed toward scalar transport or mixing, even though the majority of applications require knowledge of the transport of either mass or heat".

The first remarkable works dealing with the passive scalar mixing of jets in crossflow were made first by Holdeman [HW77] and then by Liscinsky [LTH95a, LTH95b]. Since then, some experimental and numerical investigations have been progressively closing the gap. Smith and Mungal [SM98], for example, conducted an extensive study on the scalar mixing characteristics of an air jet in crossflow. They investigated the jet structure, characteristic regions, and the decay of the concentration along the mixing path. Lee and Chu [LC03] used a Lagrangian integral approach to describe the mixing of buoyant and non-buoyant plumes and jets. Muppidi et Mahesh [MM05] performed DNS simulation of a jet in crossflow with an explicit definition of the upstream boundary layer of the crossflow. They identified that the jet trajectory is strongly dependent on the boundary layer thickness and these results were experimentally confirmed and completed by Gutmark et al. [GIM08]. In the following, the main features of a jet in crossflow are briefly described.

2.4.1 Jet mixing regions and structures

With slight differences, the literature reports two mixing regions regarding jets (inclined or non-inclined) in crossflow as illustrated in Fig. 2.11: a jet momentum dominated near field (MDNF), where the trajectory of the jet is marginally affected by the surrounding flow, and a main flow momentum dominated far field (MDFF), where the velocity of the jet narrows the velocity of the surrounding fluid. This description corresponds to the notation of Lee and Chu [LC03], who also introduced the length scale L_{mv} to separate the two zones:

$$L_{mv} = \frac{\sqrt{M_{v0}}}{U_a} \,. \tag{2.63}$$

$M_{v0} = u_j^2 \sin(\theta_j)\pi d_j^2/4$ is the vertical (kinematic) momentum flux of the jet at $y = 0$, and U_a, the bulk velocity of the main flow. For the momentum-dominated near field the jet penetration y verifies $y/L_{mv} \leq 1$, and for the momentum-dominated far field, $y/L_{mv} > 1$[1]. In a similar way, they define an integral length scale for a jet in co-flow

$$l_m^* = \frac{\sqrt{M_{j0}}}{U_a}\,, \tag{2.64}$$

with $M_{j0} = u_j(u_j - U_a)\pi d_j^2/4$, which is the excess momentum flux of the jet. They then define a strong jet (MDNF) when the relation $x/l_m^* \leq 10$ is valid, which means also that the excess velocity of the jet remains 70% higher than the entrainment velocity. According to typical injection mass flows of the burner used in the present work, this means that the jet would still be considered as strong after $x = 48$ mm ($u_j = 250$ m/s, $U_a = 30$ m/s, $d_j = 0.7$ mm). Hence, configurations with a low injection angle, or angles directed toward the exit plane of the burner are susceptible to generate a large decrease in the convective time delays of fuel. However, at the same time, a decrease of the convective time delays may reduce the mixing quality recorded at the burner outlet, as shown by Norster [Nor64] for simple jet configurations, so that an optimum regarding the mixing quality and the impact on convective time delays must be found.

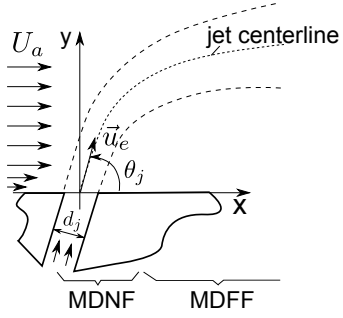

Figure 2.11: Jet mixing regions, from Lee and Chu [LC03]

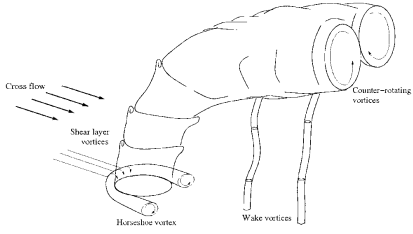

Figure 2.12: Vortical structures found in jet in crossflow, from Gutmark et al. [GIM08]

[1]Even if not explicitly mentioned, in case of fluids of two different densities, Eq. 2.63 should be multiplied by the square root of the densities ratio, $\sqrt{\rho_j/\rho_a}$

The structures which are generated by a jet in crossflow are quite complex and fully three-dimensional, as shown in Fig. 2.12. They involve four main structures [GIM08, CGSD10]: (1) the horseshoe vortex, due to the adverse pressure gradient in front of the injection hole, (2) the wake vortices, (3) the shear layer ring vortices, which is induced by a Kelvin-Helmholtz instability in the shear layer of the jet, and (4) the counter-rotating vortex pair (CVP), generated by the deflection of the jet, and which seems to be induced by the shear layer vortices. The latter structure dominates the far field mixing, even if it is generated in the near field of the jet.

2.4.2 Scaling laws

The evolution of the jet trajectory, velocity and concentration profiles, and velocity and concentration decays over the mixing length has been investigated numerically and experimentally. The jet centerline of inclined jets is generally approximated by a correlation reported by Lefebvre [Lef83]:

$$\frac{y}{d_j} = 0.82\sqrt{\frac{\rho_j u_j^2}{\rho_a U_a^2}}\left(\frac{x}{d_j}\right)^{1/3}\sin(\theta_j)\,. \tag{2.65}$$

The square root of the jet to crossflow momentum ratio $\sqrt{J} = \sqrt{\frac{\rho_j u_j^2}{\rho_a U_a^2}}$ is also referred to as r in the literature. Eq. 2.65 means that for geometrically similar configurations, as in the present work, the jet trajectory is solely dependent on J.

However, some variations in the constant and exponents are reported in literature and a perfect collapse of the curves does not occur when different setups are compared. Even in the case of a pure jet in crossflow ($\theta_j = \pi/2$), discrepancies in the normalization and exponent of the experimental curve of Pratte and Baines, $y/rd = A(x/rd)^m$, [PB67] are reported. Numerical investigations (Muppidi and Mahesh [MM05]) as well as experimental work (Gutmark et al.[GIM08]) point out that the boundary layer profile is responsible for these variations and has to be taken into account to formulate a global scaling law.

The decay of the velocity on the centerline u_m is also found to be a function of the parameter r:

$$\frac{u_m}{u_{j,0}} = B\left(\frac{x}{rd_j}\right)^n , \tag{2.66}$$

and a linear decay is observed in the far field ($n = -1$, [MNL00]). The decay of the concentration on the centerline C_m also verifies a similar scaling as

$$\frac{C_m}{C_0} = D\left(\frac{x}{rd_j}\right)^n , \tag{2.67}$$

with the difference being that the exponent n varies depending on the region considered. In the far field, $n = -2/3$ has been reported by Smith and Mungal [SM98] (jet in crossflow), Pan et al [PM01] (enclosed jet in crossflow in pipe), and Lee [LC03] (co-flowing jet). In the near field, the decay of the mean concentration seems more influenced by the geometry, going from -1.3 [SM98] to -0.45 [PM01].

The radial spreading of the concentration over the mixing length is important regarding the mixing quality downstream of the jet. The shape of the normalized average concentration $C(R)/C_m$ remains roughly close to a Gaussian function ([Lef83]) and reads

$$\frac{C(R)}{C_m} = \exp\left(-K_c\left(\frac{R}{x}\right)^2\right) , \tag{2.68}$$

where R is the jet radius in a plane orthogonal to the jet centerline. Lefebvre reported that for a co-flowing jet $Kc \approx 55$. With this latter scaling law, the concentration field $C(\boldsymbol{x})$ of a jet in crossflow is expected to be similar if the jet-to-crossflow momentum ratio is kept constant, and the previous equation can be used to roughly approximate the passive scalar field of the jet.

2.4.3 Mixing optimization of array of jets in crossflow

Depending on the goal of the technical system, numerous attempts have been made to influence the jet penetration, jet spreading, and entrainment

rate of such a "simple" configuration. They include passive as well as active measures, which are described in the following.

2.4.3.1 Jet shape

As mentioned in the introduction, numerous works have reported the influence of different jet outlet shapes on the flow and mixing properties for jets in crossflow. A review proposed by Gutmark and Grinsten [GG99] showed that, for subsonic flow, the changes in the hole shape have an impact on the streamwise mass flux and entrainment. In particular, the entrainment in the far field of rectangular or round tabbed jets is greatly enhanced compared to the non-tabbed jets which present marginal differences between each other. They also point out that the introduction of sharp edges in a nozzle increases the fine scale mixing, which can be used to reduce the coherent fuel/air mixture fluctuations. Unfortunately, no scalar measurement is available and, as pointed out by Nathan et al. [NMA+06], it is not straightforward to draw a conclusion regarding the scalar mixing quality from entrainment measurements.

On the contrary, the concentration measurements performed by Liscinsky in the near field of the jet ($x/d_j < 3$) [LTH95a, LTH95b] show that the different jet shapes tested marginally affect the mixing performance, even for tabbed jets. The trends obtained by extrapolating the results to higher mixing length do not change the main conclusions of the work, so in the end, a change in the jet shape is expected to have a marginal influence in the mixing quality at the burner outlet. Instead, the arrangement of the injectors is more critical to ensuring good fuel/air homogenization.

2.4.3.2 Passive injector arrangement

Regarding the quality of mixing, extensive experimental investigations of jets in enclosed crossflows have been conducted at NASA by Holdeman [HW77] and Liscinsky [LTVH92, LTH93]. They found that the relevant parameters influencing the mixing quality are the jet momentum ratio J as well as the hole spacing to channel height ratio S/H. The injection configuration leading to the best mixing quality is achieved for different

fuel injection arrangement when

$$\frac{S}{H} = \frac{C}{\sqrt{J}}\,, \tag{2.69}$$

with $C = 2.5$. This result is valid for a wide range of configurations ($J \in [6, 60]$, $H/d_h \in [4, 10]$, $S/d_h \in [2, 6]$).

Regarding the present investigated burner, the optimal hole spacing for given total gas and air mass flows can be obtained from the hole diameter d_h as

$$S = d_j \cdot \sqrt{2.5\frac{H\pi L_{sl}}{A_{sl}}} \cdot \sqrt{\frac{\rho_j(d_j, \dot{m}_g, n_h)}{\rho_{a,sl}(T_{pre})}} \cdot \frac{\dot{m}_a}{\dot{m}_g}\,, \tag{2.70}$$

with L_{sl} and A_{sl} being the slot length and area, respectively, ρ_j the density of the jet immediately at the outlet, $\rho_{a,sl}$ the density of air in the slot, n_h the number of holes on one slot, and $\dot{m}_a$ and $\dot{m}_g$ the mass flows of air and gas, respectively. For small changes of the actual geometry, as well as the standard operating points of the combustion chamber, which both ensure unchocked fuel injection, the density ρ_j can be considered to be constant, slightly larger than 0.661 kg/m^3. This equation solved for 3 operating points gives an optimal spacing S close to the design value of 4 mm (Tab. 2.2).

$\dot{m}_{air}$ in kg/h	$\dot{m}_{gas}$ in kg/h	T_{pre} in K	S in mm
220	7.1	298	3.57
220	7.1	423	3.89
220	7.1	623	4.29

Table 2.2: Estimation of the hole best spacing distance S using the operating conditions listed and the empirical correlation of Eq. 2.69

Hence, a marginal increase of the mixing quality is expected with a change of the spacing ratio. This correlation also predicts that the configuration of Stufflebeam [SKS99] called 15-U presents the best mixing characteristic compared to 5 other fuel shapes and distributions (the value H≈18 mm was estimated from drawings presented in different publications).

2.4.3.3 Pulsed jets

One possibility of further increasing the mixing of a jet with the surrounding flow is to actively control the jet momentum. Indeed, Johari [Joh06] reports that the concentration of turbulent puffs in water jets decays according to $(x/d)^{-3/4}$, compared to $(x/d)^{-2/3}$ for steady jets. Hence, if a mechanism is able to generate oscillations of the flow, an increase of the mixing quality may be obtained. Such increases of the mixing quality have also been reported in the review presented by Nathan et al. [NMA+06]. However, the authors point out that such oscillations are able to strongly increase the near field mixing while the far field may appear less affected by the active jet forcing. Therefore, tests must be performed to assess the effectiveness of such a method in the present complex configuration.

Hence, regarding previous works, an improvement of the mixing is not expected when the shape, or spacing ratio of the holes is varied. Instead, changes in the jet orientation and position or the use of active actuation of the jet are expected to bring some improvement to the mixing quality.

2.5 Water/air scalar mixing similitude

2.5.1 Key dimensionless numbers

One of the aims of the present work is to derive a model of the scalar mixing inside the burner from water tests. Key numbers for this are the Reynolds number Re and the jet to crossflow momentum ratio J between the fuel injections and the air flow. To allow for unsteadiness similitude, the Strouhal number St must be used. These numbers can be adjusted to ensure similarity between the different investigated configurations, as the jet trajectories scale with the parameter $\sqrt{J}d$. Indeed, when looking at the mixing of jets in crossflow, numerous works confirmed that a local velocity maximum, temperature maximum or concentration maximum [SM98] can be partly normalized by the parameter $\sqrt{J}d$ to ensure a similitude of the corresponding trajectories. As shown earlier, the Reynolds similitude allows the characteristic Reynolds numbers and associated turbulent

length scales between the two test rigs to remain constant. In particular, the turbulent Reynolds numbers Re_t and the Kolmogorov length scale are identical. Other numbers, such as the Schmidt number, are physically dependent on the system used and will differ between air and water.

2.5.2 Conversion from water to air

When setting the Reynolds and momentum ratio similitudes in the water test rig to combustion chamber conditions, it is not possible to ensure that the averaged well-mixed normalized dye concentration $C^*_{dye,\infty}$ in water or molar fraction $Y_{f,\infty}$ in air are identical for the two mediums. The notation C^* indicates that the concentration C is normalized by the concentration of the dye in the unmixed fuel injection piping (ensuring that $C^* \in [0, 1]$ in the whole domain). Hence, in order to use the quantitative concentration of water to predict the local mole fraction and equivalence ratio in air, a correction of the local concentration recorded in water $C^*_{dye}(\boldsymbol{x})$ must be applied.

As shown earlier, the jet trajectory matches between different setups if the momentum ratio J and inflow conditions are identical. The normalized concentration profiles $C(s,r)/C_m$ are expected to be similar [SM98], which means that for identical geometrical setups but two different mediums, the local normalized concentrations $C^*_f(\boldsymbol{x})$ recorded in air are proportional to the local normalized concentration in water $C^*_{dye}(\boldsymbol{x})$ according to

$$C^*_f(\boldsymbol{x}) = \frac{C^*_{f,\infty}}{C^*_{dye,\infty}} \times C^*_{dye}(\boldsymbol{x})\,, \tag{2.71}$$

where $C^*_{f,\infty}$ and $C^*_{dye,\infty}$ are the normalized concentrations of the perfectly homogenized gaseous fuel and water, respectively. Their values verify

$$C^*_{f,\infty} = \frac{Q_f}{Q_f + Q_{air}}\,, \tag{2.72}$$

and

$$C^*_{dye,\infty} = \frac{Q_{dye}}{Q_{dye} + Q_{water}}\,, \tag{2.73}$$

with Q_f being the total volume flow of fuel at the pressure and temperature set upstream of the flame and Q_{air}, the total volume flow of air at the same temperature. If isothermal mixing is considered, Eq. 2.71 can be transformed into

$$Y_f(\boldsymbol{x}) = \frac{Y_{f,\infty}}{C^*_{dye,\infty}} \times C^*_{dye}(\boldsymbol{x})\,, \tag{2.74}$$

where $Y_f = n_f/(n_{air} + n_f)$ is the mole fraction of fuel in the gaseous mixture. The ratio $\frac{Y_{f,\infty}}{C^*_{dye,\infty}}$ is the similitude ratio which depends on the operating conditions set in the combustor. Discrepancies in the mixing similitude will occur if the temperature difference between the jet and the main flow increases, as a consequence of the buoyancy forces.

Furthermore, the fuel distribution in the combustion chamber is generally expressed in terms of the fuel/air ratio (FAR) and then in terms of the fuel equivalence ratio ϕ. The latter is defined as

$$\phi = \frac{\dot{m}_f/\dot{m}_{air}}{(\dot{m}_f/\dot{m}_{air})_{st}} = \frac{FAR}{FAR_{st}}\,, \tag{2.75}$$

where the index $(\cdot)_{st}$ refers to the stoichiometric conditions of the combustion reaction. The local equivalence ratio $\phi(\boldsymbol{x})$ can be expressed as a function of the local mole fraction $Y_f(\boldsymbol{x})$ using the relationship linking the fuel mass flux $\dot{m}_f$, the fuel molar mass M_f, and the fuel mole flux $\dot{n}$: $\dot{m}_f = \dot{n}_f M_f$. The final expression then reads

$$\phi(\boldsymbol{x}) = \frac{Y_f(\boldsymbol{x})}{FAR_{st} M_{air}/M_f\,(1 - Y_f(\boldsymbol{x}))}\,. \tag{2.76}$$

This definition verifies that for pure fuel mixture ($Y_f(\boldsymbol{x}) = 1$), $\phi(\boldsymbol{x}) \to \infty$ and for a mixture free of fuel ($Y_f(\boldsymbol{x}) = 0$), $\phi(\boldsymbol{x}) = 0$. Combining then Eq. 2.71 and Eq. 2.76, the relationship between concentration in water and local equivalence ratio finally reads

$$\phi(\boldsymbol{x}) = \frac{\frac{Y_{f,\infty}}{C^*_{dye,\infty}} C^*_{dye}(\boldsymbol{x})}{FAR_{st}\frac{M_{air}}{M_f}\left(1 - \frac{Y_{f,\infty}}{C^*_{dye,\infty}} C^*_{dye}(\boldsymbol{x})\right)}\,. \tag{2.77}$$

Equation 2.77 can also be expressed as a function of the fuel mass fraction Z_f when using the transformation

$$Y_f = \frac{1}{1 + \frac{M_f(1-Z_f)}{M_{air}Z_f}} \,. \tag{2.78}$$

Depending on the operating points considered, a calibration map can be calculated to transpose the concentration C^*_{dye} into the equivalence ratio ϕ depending on the parameter $Y_{f,\infty}/C^*_{dye,\infty}$. The curves for different ratios $Y_{f,\infty}/C^*_{dye,\infty}$ are displayed in Fig. 2.13 with FAR_{st}=0.058147, $M_{air,dry}$ = 29 g/mol, and M_f = 16 g/mol. For a constant $C^*_{dye,\infty}$, an increase of the ratio $Y_{f,\infty}/C^*_{dye,\infty}$ leads to an increase of the local equivalence ratio ϕ and an almost linear relationship exists when $Y_{f,\infty}/C^*_{dye,\infty}C^*_{dye} < 0.05$.

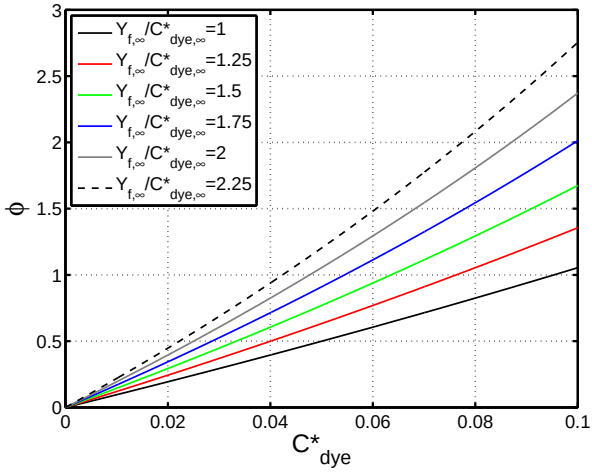

Figure 2.13: Conversion between concentration measured in water C^*_{dye} and the corresponding equivalence ratio ϕ in the combustion chamber as a function of the ratio $Y_{f,\infty}/C^*_{dye,\infty}$

How do the operating parameters such as equivalence ratio ϕ, preheat temperature T_{pre}, or fuel jet mass flux influence the ratio $Y_{f,\infty}/C^*_{dye,\infty}$? The answer can be found in Fig. 2.14 to Fig. 2.16. An increase in the preheat

temperature at a constant equivalence ratio ϕ reduces the momentum ratio J in the combustion chamber (Fig. 2.14). As a consequence, the dye volume flow in the water test rig has to be reduced for a set main volume flow (and Reynolds number) and the concentration of the perfectly mixed mixture $C^*_{dye,\infty}$ decreases, increasing the ratio $Y_{f,\infty}/C^*_{dye,\infty}$ (Fig. 2.15). An increase of ϕ in the combustion chamber leads, as expected, to an increase of the momentum, but has a negligible influence on the ratio $Y_{f,\infty}/C^*_{dye,\infty}$, which varies by less than 0.5% over the equivalence ratio range of interest. It should be noted that for the air mass flow considered ($\dot{m}_{air} = 220\,\mathrm{kg/h}$) and the ϕ range presented, the fuel is far from being choked, and this explains the weak variation of the isothermal lines observed in Fig. 2.15. If the fuel mass flux is increased through reduction of the total injection area or through a further increase of the total gas mass flow, the ratio $Y_{f,\infty}/C^*_{dye,\infty}$ increases, as shown in Fig. 2.16.

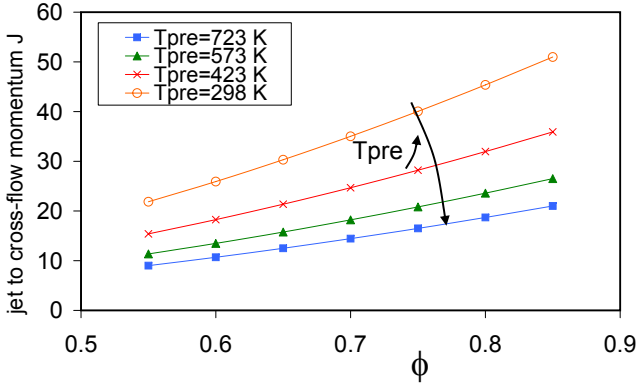

Figure 2.14: Evolution of the jet to crossflow momentum J depending on the equivalence ratio ϕ for different preheating temperatures. $d_j = 0.7\,\mathrm{mm}$, $\dot{m}_{air} = 220\,\mathrm{kg/h}$, standard swirl-inducing burner (62 gas holes).

The practical consequences for the investigations are the following:

- For a constant preheating temperature T_{pre} and equivalence ratio ϕ, the mixing properties of different total power can be described by one measurement in water as long as the mixing is independent of

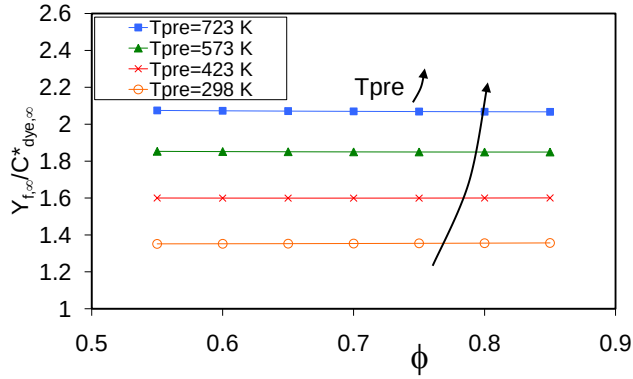

Figure 2.15: Evolution of the ratio $Y_{f,\infty}/C^*_{dye,\infty}$ depending on the equivalence ratio ϕ for different preheating temperatures. $d_j = 0.7\,\text{mm}$, $\dot{m}_{air} = 220\,\text{kg/h}$, standard swirl-inducing burner (62 gas holes).

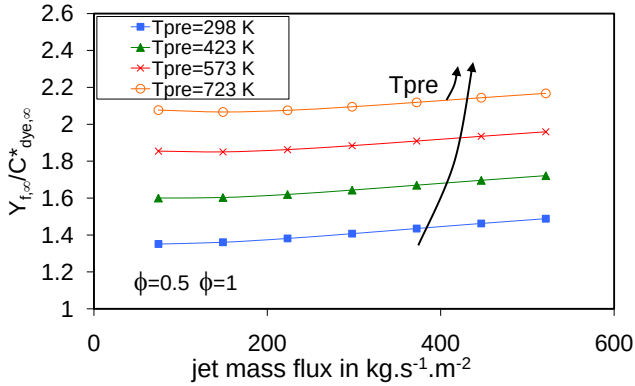

Figure 2.16: Evolution of the ratio $Y_{f,\infty}/C^*_{dye,\infty}$ depending on the fuel jet mass flux for different preheating temperatures. As indication, the equivalence ratio values $\phi = 0.5$ and $\phi = 1$ corresponding to the setup $d_j = 0.7\,\text{mm}$, $\dot{m}_{air} = 220\,\text{kg/h}$, standard swirl-inducing burner (62 gas holes) are displayed on the graphic.

the Reynolds number and the jet mass flux remains smaller than 150 $\text{kg.s}^{-1}\text{.m}^{-2}$.

- If the jet mass flux increases above 200 kg.s^{-1}.m^{-2}, then $C^*_{dye,\infty}$ must be decreased through a reduction of the injector mass flow in water.

2.5.3 Mixing quality evaluation

The mixture probability function will be obtained directly from the spatio-temporal concentration measurements. The mixing quality can then be calculated from the variance of the concentration fluctuations (σ^2), which is then normalized in various ways. Other parameters exist in literature and the interested reader is referred to the work of Wang [WK00]. In the present work, two different parameters are used. The first one is the *coefficient of variation*, defined as

$$s = \frac{\sigma(C^*)}{C^*_\infty} \tag{2.79}$$

and which depicts the ratio of the standard deviation of the concentration to the perfectly mixed concentration. The problem with this parameter is that it is not suited to compare the mixing efficiency of systems with different perfectly mixed concentrations C^*_∞. If such a comparison is needed, then the coefficient of variation should be normalized by its maximum value, obtained immediately after the start of the mixing process. This maximal variance of a binary mixture [PAOK04] reads

$$s_0 = \left(\frac{1 - C^*_\infty}{C^*_\infty} \right)^{0.5} . \tag{2.80}$$

A normalization of s by s_0 allows the mixing effectiveness of premixers using different perfectly mixed concentrations to be compared. In the case of the present burner, C^*_∞ ranges between $C^*_\infty \in [0.02, 0.06]$ and the resulting variation of s_0 is $s_0 \in [4, 7]$. The ratio $(s/s_0)^2$ give the second parameter, the so-called unmixedness parameter of Danckwerts [Dan52], which reads

$$U = \frac{\sigma^2}{\sigma_0^2} = \frac{\sigma^2}{C^*_\infty \left(1 - C^*_\infty\right)} , \tag{2.81}$$

where σ_0^2 is the variance immediately before the start of the mixing process (i.e. independant of the measurement position).

Depending on how the variance of the mixture σ^2 is calculated in Eq. 2.81, the spatial unmixedness U_x and the temporal unmixedness U_t are calculated. $U_x = \sigma_x^2/\sigma_0^2$ is obtained from the variance σ_x^2 of the temporally averaged concentration field $\overline{C^*}(i)$ recorded by the N_i pixels of a camera and which reads

$$\sigma_x^2 = \frac{1}{N_i - 1} \sum_{i=1}^{N_i} \left(\overline{C^*}(i) - C_\infty^* \right)^2 , \tag{2.82}$$

i being the index of the camera pixels. U_x can be considered as a measure of the macro-mixing and answers the question how good the two fluids are *in average* spatially mixed in the measurement plane. Temporal fluctuations, which typically dominate the mixing processes, are thus not taken into account. This is done by the parameter $U_t = \sigma_t^2/\sigma_0^2$ in which the variance σ_t^2 of all the concentrations recorded by the pixels of the camera is calculated as

$$\sigma_t^2 = \frac{1}{N_i N_t - 1} \sum_{i=1}^{N_i} \sum_{t=1}^{N_t} \left(C^*(i,t) - C_\infty^* \right)^2 , \tag{2.83}$$

where N_t corresponds to the number of snapshots recorded during one mixing run. U_t is more approriate to describe the mixing quality of technical systems as the spatial unmixedness is not able to capture temporal concentration fluctuations. However, both criteria together give a better understanding of the mixing mechanisms and are thus reported in the present work.

2.5.4 Discussion about the limitations of the water/air analogy

A direct comparison of the mixing process of identical setups in a gaseous and liquid setup is rare in literature. It is however important when quantitative results must be derived for a gaseous medium from liquid tests. Such a comparison has been performed on a single jet by Miller [MD91]. He measured the concentration fluctuation spectrum on the centerline of a single jet with point-wise spatially high-resolved LIF. The normalized scalar power spectra recorded show that in the low frequency range, the

scalar fluctuations increase with decreasing Reynolds number when a high Schmidt number ($Sc \approx 1000$) is considered. The spatial resolution was high enough and affected the results marginally when the Reynolds number was varied. When the total energy of the fluctuations, i.e. their variance, is plotted over the Reynolds number, it appears that it decreases with increasing Reynolds number for the case of high Schmidt number, Fig. 2.17. Similar measurements performed in gas ($Sc \approx 1$) show no Reynolds number dependency.

How these results can be quantitatively transfered to the actual swirl configuration remains an open question which would require quantitative investigations, but the general trends would be that (1) the unmixedness of water will generally over predict the unmixedness in the combustion chamber and (2) that an increase in the Reynolds number reduces the overestimation of the unmixedness relative to the gaseous conditions. As a typical Reynolds number of the present investigations is $Re \approx 3.5 \times 10^4$, a slight overestimation of the unmixedness recorded in water is expected.

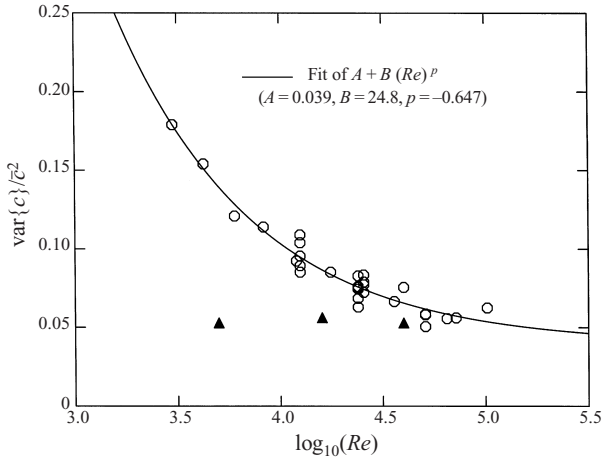

Figure 2.17: Normalized jet-fluid-concentration variance on the axis of a turbulent jet, as a function of jet Reynolds number (Miller 1991, [Mil91]). Circles: liquid-phase jets (Miller 1991); triangles: gas-phase jets (Dowling and Dimotakis 1990). Illustration taken from Dimotakis [Dim00].

2.6 Combustion

How the fuel reacts with the oxidizer depends on the technical application. Two ways of mixing reactants (non-premixed and premixed) can be combined with two types of flows (laminar or turbulent), leading to 4 types of technical flames. In the case of stationary gas turbines, the compactness of the flame, flow densities, and emission considerations impose the use of lean turbulent premixed flames (which is the case of the present burner), while for safety consideration, aircraft engines use non-premixed turbulent flames (Rich Quench Lean for example). Even if turbulent flames are used, the mechanisms of laminar flames must also be well understood, as turbulent flames are also considered to be a sum of more or less wrinkled laminar flames, which describe the complex flame front. In particular, the laminar premixed flame speed as well as the turbulent premixed flame speed are relevant parameters regarding the flame stabilization location.

2.6.1 Laminar premixed flames

How the flow properties of temperature, mass fraction, and reaction rate evolve across a laminar premixed flame is illustrated in Fig. 2.18. The fresh premixed reactants enter the flame with the velocity u_r and with a very low turbulence level (turbulent Reynolds number $Re_t < 1$). Through the action of diffusion, the reactants are preheated before the reaction effectively starts. Upon completing the reaction, the products reach the adiabatic flame temperature. A steady solution of the flame propagation problem exists only if the laminar flame propagation speed $S_{L,0}$ equals the reactant speed u_r.

A general formulation of the laminar premixed flame speed can be taken from [AOC96] and reads

$$S_{L,0}(p,T,\phi) = a\phi^b \exp\left(-c\left(\phi - d\right)^2\right)\left(\frac{T_{pre}}{T_0}\right)^e\left(\frac{p}{p_0}\right)^f, \tag{2.84}$$

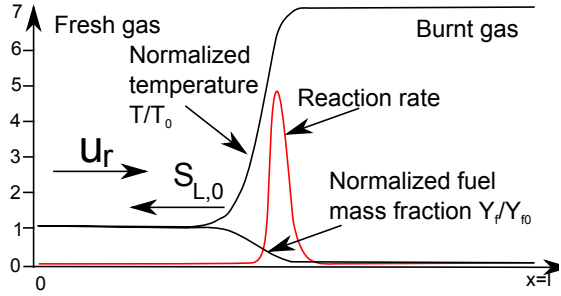

Figure 2.18: Typical evolution of the relevant parameters of a premixed flame across the flame front (from [PV05])

where a, b, c, d, e, f are constants which are obtained from the fitting of experimental data. Their values are valid for a particular fuel type completely premixed with air. The fitting of numerous experimental data for a methane-air mixture led to the following coefficients [AOC96]: $(a, b, c, d, e, f) = (0.6097, -2.554, 7.310, 1.230, 2.0, -0.5)$. The reference temperature and pressure are 300 K and 1 atm respectively. The exponents e and f show that temperature and pressure have opposite effects on the evolution of S_L.

2.6.2 Turbulent flames

When the inlet turbulence of fresh gas u' is further increased to satisfy $Re_t > 1$ the combustion regime changes from laminar to turbulent. This transition occurs simply when increasing the mass flux and hence the heat power of the combustion zone. The general consequence of an increased turbulence is a wrinkling of the flame front as turbulent eddies are transported through it. This leads to a stretching of the flame front which further increases the flame surface area and changes the local burning rate. The flame is then able to stabilize at inlet velocities which are higher than the laminar counterpart as well as in a wider range of velocities. The so-called turbulent flame velocity S_T is

$$S_T = \frac{A_T}{A_0} S_{L,0}\,, \tag{2.85}$$

where $\frac{A_T}{A_0} > 1$ is the ratio of turbulent flame area to laminar flame area.

There exists an impressive number of publications reporting a correlation of the turbulent flame velocity S_T with different system parameters. Lipatnikov [LC02] reviews and tests an large number of correlations used in literature. He summarizes that a suitable model of the turbulent flame speed should match the following trends:

- increase of S_T with an increase of turbulence u',
- increase of S_T and dS_T/du' by $S_{L,0}$,
- increase of S_T by pressure despite the decrease in $S_{L,0}$.

From his investigations he notices that three distinct models are able to capture these trends: The burning velocity model of Zimont, the turbulent velocity model of Peters and the coherent flame model (CFM). Another correlation often used because of its simplicity was reported by Kawanabe [KSTA98]:

$$S_T = S_{L,0}\left[1 + C\left(\frac{u^{'}}{S_{L,0}}\right)^n\right], \tag{2.86}$$

with the typical values for $C = 1.25$ and $n = 0.7$. When $u^{'} \gg S_L^0$, Eq. 2.86 simplifies to $S_T = Cu^{'}$ and the flame velocity fluctuations are independent of the laminar flame speed fluctuations.

2.6.3 Flame regimes

Depending on the mean flow field, turbulent characteristics, equivalence ratio distribution, and diffusive properties of the reactants involved, among others, the flame structure can vary greatly. The flame front can be localized in continuous thin reacting layers, be contained in small pockets or more spatially distributed, so that one can say that the combustion takes place in different regimes. These are summarized in the so-called "turbulent combustion diagrams" commonly named "Borghi" diagrams, even if such classification was performed earlier by Barrère [Bar74]. The diagram sorts the combustion regimes depending on the ratio of turbulent fluctuations to laminar flame velocity $u'/S_{L,0}$ and on the ratio of integral length

scale to the flame thickness Λ^x/δ_L. This classification is essential to build turbulent combustion models but gives more an order of magnitude information (due to the stochastic distribution of the parameters involved), than a precise location [PV05].

The base of these diagrams is the definition of the turbulent velocity u' which remains difficult to obtain experimentally. The RMS velocity of the fresh gas is generally used but, as pointed out by Poinsot [PV05], "has no theoretical basis in a premixed flame". The distinction between burnt and unburnt gas should be made (intermittency), but is difficult to obtain in complex turbulent flames. Furthermore, the RMS velocity recorded in swirling flow is a composition of coherent and turbulent motions. As pointed out by Lipatnikov [LC02] or from DNS simulations by Ulitsky [UC97], these macro scale motions may have a negligible contribution to the burning rate, as the stretching of the flame, which is responsible for local flame speed variations, occurs at smaller length scales. However, they may contain an important part of the turbulent velocity fluctuations (from 10 to 30% in thermoacoustically stable combustors). Thus, if the coherent motion does not contribute to the flame propagation, it should be removed from the calculated turbulent velocity. This justifies the use of proper orthogonal decomposition (POD) to remove this coherent part as presented in Sec. 5.

Three other dimensionless numbers, related to the two previous ones, characterize these combustion regimes: the Damköhler number, the Karlovitz number, and the turbulent Reynolds number, already defined in Eq. 2.22. The Damköhler number is defined for the largest eddies and corresponds to the ratio of their turbulent time scale to the chemical time scale:

$$Da = \frac{\tau_t}{\tau_c} = \frac{\Lambda^x S_{L,0}}{u' \delta_L} \,. \tag{2.87}$$

The Karlovitz number is related to the smallest eddies and is the ratio of the chemical time scale to the Kolmogorov time scale:

$$Ka = \frac{\tau_c}{\tau_k} = \left(\frac{\delta_L}{l_k} \right)^2 \,. \tag{2.88}$$

Both numbers can be expressed as a function of $u'/S_{L,0}$ and Λ^x/δ_L and thus define isolines with different slopes in the Borghi diagram:

$$\frac{u'}{S_{L,0}} = Da^{-1}\left(\frac{\Lambda^x}{\delta_L}\right), \tag{2.89}$$

$$\frac{u'}{S_{L,0}} = Ka^{2/3}\left(\frac{\Lambda^x}{\delta_L}\right)^{1/3}. \tag{2.90}$$

Finally, the turbulent Reynolds number (Eq. 2.22) is used to separate the laminar flame region from the turbulent flame region ($Re_t = 1$). This number can also be recast as

$$\frac{u'}{S_{L,0}} = Re_t\left(\frac{\Lambda^x}{\delta_L}\right)^{-1}, \tag{2.91}$$

and the following equality holds:

$$Re_t = Da^2 Ka^2\,. \tag{2.92}$$

To obtain these relationships, a Schmidt number of unity ($Sc = \nu/\Gamma = 1$) was assumed for all the gaseous elements and the flame thickness and characteristic time are defined as

$$\delta_L = \frac{\Gamma}{S_L}\,, \text{ and} \tag{2.93}$$

$$\tau_c = \frac{\delta_L}{S_{L,0}} = \frac{\Gamma}{S_{L,0}^2}\,. \tag{2.94}$$

The diffusion coefficient is calculated following the expression of Peters [PLV01]:

$$\Gamma = \frac{(\kappa/C_p)_{T_0}}{(\rho_u)_{T_{pre}}}\,, \tag{2.95}$$

where κ is the thermal diffusion coefficient, C_p the specific heat capacity, and ρ_u the density of the unburnt reactants. T_0 is the temperature of the inner layer which is assumed equal to 1500 K, and T_{pre} the temperature of the reactants.

The Kolmogorov length scale can also be defined from the integral length scale and the turbulent Reynolds number as

$$l_k = \frac{\Lambda^x}{Re_t^{3/4}} \,. \tag{2.96}$$

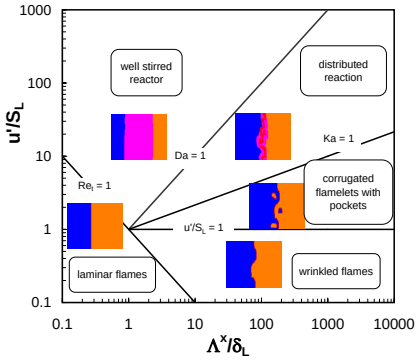

Figure 2.19: Borghi diagram (Peters [Pet86])

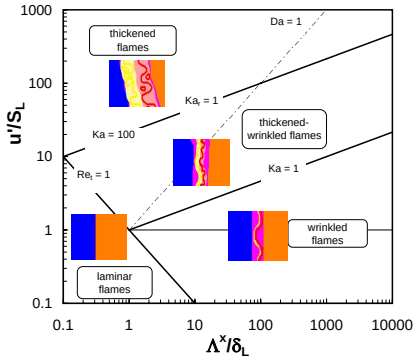

Figure 2.20: Modified turbulent combustion diagram from Peters [Pet99]

The different combustion regimes are depicted in the original Borghi diagram shown in Fig. 2.19. If the flame front thickness is much smaller than the Kolmogorov eddy scale l_k, then the flame front is seen as a continuum weakly wrinkled by the flow eddies. This regime is characterized by $\delta_L < l_k$ or $Ka < 1$ and $Da > 1$ and is called the "wrinkled flame regime" or "flamelet regime".

If the size of the flame front is further increased, through an increase in the relative turbulent fluctuations $u'/S_{L,0}$, while $Da > 1$ and $Ka < 1$, then the flame front becomes more wrinkled and may form pockets of fresh or burnt fuel. The "flame regime with pockets" or "corrugated flamelets" regime is reached.

Further increasing the turbulent fluctuations so that $Ka > 1$ and $Da > 1$ thickens the flame front and the "distributed reaction" zone or "thickened-wrinkled flame" is reached.

For $Da < 1$, the mixing time scale is much shorter than the combustion time scale and the combustion reaction is limited by the chemistry. The fuel and oxidizer are generally well premixed, decreasing their local concentration and consequently their chemical reaction rate. This is called the "well-stirred reactor" regime.

A distinction between the flame thickness δ_L and the reaction zone thickness δ_r ($\delta_r << \delta_L$) has been proposed by Peters [Pet99], building the Karlovitz number based on the reaction zone thickness:

$$Ka_r = (\delta_L/\delta_r)^2 . \tag{2.97}$$

If the flame thickness is smaller than or equal to the Kolmogorov eddies, then the small eddies will affect and wrinkle the reaction zone. Otherwise, only the diffusion layer will be affected. This transition occurs for $\delta_r = l_k$ and as for most premixed flames $\delta_L/\delta_r \approx 10$, the Karlovitz number of the reaction zone is equal to the Karlovitz number as $Ka_r = Ka = 100$. For $Ka > 100$, the "thickened flame regime" occurs, while for $1 < Ka < Ka_r$ we talk about the "thickened-wrinkled flame regime". This modification of the classification is depicted in Fig. 2.20.

Since the first classification, and with increase of the experimental and numerical tools to capture the flame properties locally, some variations of this classification have been performed. In particular, the effects of quenching, i.e., a decrease of the reaction rate to a negligible value, and flame-vortex interaction[PVC91] are now used. However, describing these mechanisms in detail is beyond the scope of the present work.

2.6.4 NO_x formation mechanisms

2.6.4.1 Classification of the formation mechanisms

Even if "clean" combustion should produce CO_2 and H_2O only, reactions building other chemical elements, like SO_2 or NO_x, take place. These by-products are harmful for the environment and have to be minimized before the exhaust gases are sent into the atmosphere. The most relevant by-products in gas turbine combustors are the NO_x molecules, as methane

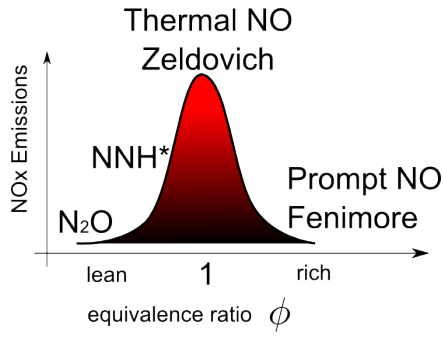

Figure 2.21: Dominant NOx formation mechanisms (From Joos [Joo06])

gases are mostly free of sulfur-bounde carbon molecules. The major parameter affecting NO_x formation is the flame temperature T_{fl}[SRM07], which is mainly controlled through the equivalence ratio ϕ and the preheating temperature T_{pre}. The equivalence mixing profile can locally change the temperature distribution within the flame. The residence time τ of the molecules in hot zones and finally the pressure p in the combustor are other major parameters which also have to be taken into account.

Five chemical mechanisms [Joo06] describe how NO_x are produced in combustors:

- Thermal NO_x (or Zeldovich)
- Fenimore Mechanism (also called prompt NO_x)
- Fuel NO
- N_2O routes
- NNH Radical

A simplified sketch showing which of the routes dominates the NO_x formation process is shown in Fig. 2.21, with the qualitative evolution of the NO_x plotted against the equivalence ratio. It shows that in lean

combustors with relatively low equivalence ratios ($\phi < 0.75$), the dominant routes should be the N_2O and NNH radical routes. However, all the chemical reactions involved show a great sensitivity to pressure and temperature within the ranges typical for gas turbines ($p \in [1, 30]$ bar and $T_{fl} \in [1700, 1900]$ K). This leads to a more complex behavior of the NO_x emissions than the one sketched in Fig. 2.21: indeed, as shown by Biagioli and Güthe [BG07] and Syed et al. [SRM07], an increase of the flame temperature leads to an increase of the ratio of NO_x emitted in the post-flame region to the NO_x emitted within the flame.

This observation led Biagioli and Güthe to order the formation mechanisms depending on their location relative to the flame position, characterized by a Damköhler criterion. The fast NO_x mechanism corresponds to the NO_x generated within the reaction zone (the "fast"[2] mechanism) and the slow NO_x mechanism corresponds to the NO_x generated in the post-flame region ("post-flame" mechanism). This contrasts with the standard definition of prompt and thermal NO_x as "fast" thermal NO_x can also be generated at the flame location, as a consequence of richer fuel/air mixture pockets.

Using these definitions, three main results are observed:

- The "fast" contribution is approximately three times less sensitive to fuel/air unmixedness, or adiabatic flame temperatur variation, than the "post-flame" NO_x. This is a consequence of the increase of the ratio $NO_{xpost-flame}/NO_{xfast}$ with the flame temperature.
- The sensitivity of "fast" and "post-flame" to unmixedness is weakly pressure dependent. Hence, the previous assertion is valid over a wide pressure range.
- The "fast" type contribution decreases as p increases ($NO_{xfast} \propto p^{-0.45}$) and the "post-flame" contribution decreases as p increases ($NO_{xpost-flame} \propto p^{0.67}$).

[2] the term "prompt" is originally used in [BG07], but replaced here by "fast" to avoid confusion with the rich "prompt" mechanism

The results of Biagioli and Güthe indicate further that the fuel/air unmixedness plays a more important role in increasing the NO_x emissions with increasing pressure. However, because of flame stability considerations, the perfect unmixedness is generally not achieved in a practical combustor. Regarding the operating conditions of the investigated burner (atmospheric, lean mixture $\phi \in [0.55, 0.7]$ and low preheat temperatures $T_{pre} \in [300, 423]\,\mathrm{K}$, leading to a T_{fl} range of $T_{fl} \in [1580, 1895]\,\mathrm{K}$), the "fast" NO_x will dominate the emissions even if the ratio $NO_{x post-flame}/NO_{x fast}$ increases with T_{fl}.

2.6.4.2 NO_x models

As the NO_x emissions should be predicted for a wide range of operating conditions, which is expensive to simulate, different empirical models are also used in literature to describe the NO_x emissions of gas turbines. The work of Lefebvre [Lef83] reports some of these correlations. They are mainly based on the assumption that the NO production is a function of

- dilution rate (present in gas turbines)
- residence time ($\propto L/U$)
- reaction rate ($\propto p^n \exp(B \cdot T)$)
- mixing rate ($\propto \Delta p/p$)

Tacina et al. [TLW08] recently used a model similar to the correlation of Lefebvre, in which 4 variables are included: the preheat temperature T_{pre}, the fuel air ratio ϕ, the pressure p and the relative pressure drop $\frac{\Delta p}{p}$.

$$EINO_x = A \exp\left(BT_{pre}\right) \phi^C P^D \left(\frac{\Delta p}{p}\right)^E \tag{2.98}$$

with A, B, C, D, E being positive empirical constants. Here the index EINOx represents the NO_x emissions normalized by the fuel mass flow. This expression gives a satisfying correlation but does not show an explicit influence of the fuel/air unmixedness. The latter is assumed to be dependent on the pressure loss coefficient. Increasing the pressure loss over the

burner also increases the energy dissipated inside the burner, which is favorable to the mixing and is expected to reduce the NO_x emissions. However, if variations of the fuel distribution are made in the burner (for example, by using a pilot flame), these changes are not captured by the model. The influence of the fuel/air mixing quality on NO_x emissions is strong and has been shown in literature by many authors [MTH+96, FSP02, SRM07]. Hence an appropriate correlation should take this parameter into account. A correlation which takes the mixing quality of the fuel with air into account and was validated for the burner used for the present investigations was reported by Alkabie [Alk00] and reads

$$NO_x = A_1 \exp\left(A_2 \phi_{\mathrm{PRZ}} \left(1 - s_{\mathrm{fl}}\right) + A_3 s_{\mathrm{fl}}\right) , \tag{2.99}$$

where ϕ_{PRZ} is the equivalence ratio of the primary recirculation zone, $s_{\mathrm{fl}} = \sigma/\overline{\phi}$ the unmixedness parameter, and A_1, A_2, and A_3 empirical constants. The problem which arises is the determination of the unmixedness parameter at the fuel location. Alkabie only used this parameter as a floating parameter which improves the data fit. Because of the generally complex flame shape and stabilization location, an experimental measurement of s_{fl} is namely difficult to obtain.

To estimate this unknown parameter, Syed et al. [SRM07] proposed a novel and simplified modeling approach. The overall NO_x emissions $\overline{NO_x}$ may be calculated from the mixture PDF f_Y weighted by the ideal NO_x formation rates $[NO_x]_{ideal}$ as

$$\overline{NO_x} = \int\int \left[NO_x\right]_{ideal} (Y,t)\, f\,(Y,t)\; dY\, dt\,. \tag{2.100}$$

A decomposition of the $[NO_x]_{ideal}$ between a time independent part ($[NO_x]_{fast}$) and a residence-time-dependent part ($[NO_x]_{post-flame}$) can be used to differentiate the "fast" and "post-flame" mechanisms. The NO_x formation rates can be simulated using, for example, the GRI 3.0 chemical kinetic scheme. During the first calibration step, the overall NO_x emissions are measured and the mixture PDF can be reconstructed, assuming a known distribution (like a beta-PDF), when Eq. 2.100 is inverted. The temporal dependency can also be removed if the NO_x are mostly of "fast" type, which was the case in their study.

However, to predict the NO_x emissions, a model able to predict the mixture PDF (or its corresponding variance) depending on the operating conditions and initial fuel/air distribution must be built. If the evolution of the mixture variance is described by Eq. 2.55, the flame position has to be determined to calculate the unmixedness at the flame location. This is achieved using the assumption that the scale of premixed combustion lies between the integral and Kolmogorov length scales.

Equation 2.55 can then be further extended to

$$\frac{s_{\text{fl}}}{s_0} = \exp\left(-ADa^{-3/2}\right) , \tag{2.101}$$

where s_0 is the initial unmixedness of the fuel distribution and A, a constant. The Damköhler number Da can be expressed depending on the operating parameters as

$$Da \propto T_{fl}^{-0.5} \left(\dot{m}_{air}/\rho_{air}\right) . \tag{2.102}$$

The only unknown in Eq. 2.101 for a determined fuel injection is the constant A. The latter is calculated from the calibration. The unmixedness at the flame can then be calculated (assuming a beta-probability density function and a known initial unmixedness s_0) and the resulting NO_x for various operating conditions obtained. The results obtained with this modeling approach match quite well with experimental results, even if a lot of assumptions are taken to obtain the final expression. It allows in particular for the fuel/air unmixedness impact on the NO_x emissions to be explicitely modeled. A change in the flame behavior (strong variation of the flame location or shape) still remains difficult to capture.

2.7 Acoustics

2.7.1 Wave equation and solutions

The wave equation for a fluid without mean flow is defined as

$$\frac{\partial^2 p'}{\partial t^2} - \overline{c}^2 \nabla^2 p' = 0 . \tag{2.103}$$

This equation is obtained from the conservation equation of mass, momentum and energy. The ideal gas law as well as the equation of state of the pressure are the two equations used to close the system of 5 unknowns (ρ, p, $\boldsymbol{u}$). The equations simplify when assuming first that the losses due to temperature and viscosity effect are negligible and second that the equation can be linearized when small pressure perturbation ($p'/p_0 << 1$) are considered. After substitution operations and using the definition of the sound velocity as $\overline{c} = \sqrt{\gamma RT}$, Eq. 2.103 is obtained.

In case of a fluid with mean flow $\overline{\boldsymbol{u}}$ (as in a combustor) and if a euclidian coordinate system is considered, the convective wave equation is obtained:

$$\left(\frac{\partial}{\partial t} + \overline{\boldsymbol{u}} \cdot \nabla\right)^2 p' - \overline{c}^2 \nabla^2 p' = 0\,. \tag{2.104}$$

If a one-dimensional system is further considered as well as harmonic perturbation of the pressure, p' can be expressed as the real part of its Fourier transformation and the temporal and spatial variables can be split giving the expression:

$$p'(x,t) = \Re\left\{\hat{p}(x,\omega)e^{(i\omega t)}\right\}\,. \tag{2.105}$$

Equation 2.104 then simplifies to

$$\left(1 - M^2\right)\frac{\partial^2 \hat{p}(x,\omega)}{\partial x^2} - 2Mik\frac{\partial \hat{p}(x,\omega)}{\partial x} + k^2\hat{p}(x,\omega) = 0\,, \tag{2.106}$$

with the wave number $k = \omega/\overline{c}$ and the Mach number $M = u/\overline{c}$. Equation 2.106 is also referred to as the convective Helmholtz equation. Because the pressure waves evolve harmonically in the system, solutions of the form $\hat{p}(x,\omega) = \exp(\lambda x)$ are investigated first. Using this assumption, the eigenvalues λ of Eq. 2.106 are

$$\lambda^{\pm} = \mp\frac{ik}{1 \pm M}\,, \tag{2.107}$$

and the solutions of Eq. 2.106 read

$$\hat{p}(x,\omega) = A^+(\omega)e^{\left(-ik^+x\right)} + A^-(\omega)e^{\left(+ik^-x\right)}\,, \tag{2.108}$$

with

$$k^{\pm} = \frac{k}{1 \pm M}. \tag{2.109}$$

The pressure oscillations are then

$$p'(x,t) = \left(A^{+}(\omega) e^{\left(-ik^{+}x\right)} + A^{-}(\omega) e^{\left(+ik^{-}x\right)} \right) e^{(i\omega t)}. \tag{2.110}$$

The solution for the acoustic velocity u' is obtained, assuming that it has the same expression as p' in Eq. 2.110. Using this time the convective momentum equation, which reads

$$\overline{\rho} \left(\frac{\partial}{\partial t} + \overline{\boldsymbol{u}} \cdot \nabla \right) u' + \nabla p' = 0\,, \tag{2.111}$$

replacing p' with the expression of Eq. 2.110 and identifying the coefficient of u' leads to the solution

$$u'(x,t) = \frac{1}{\overline{\rho c}} \left(A^{+}(\omega) e^{\left(-ik^{+}x\right)} - A^{-}(\omega) e^{\left(+ik^{-}x\right)} \right) e^{(i\omega t)}. \tag{2.112}$$

2.7.2 Influence of heat release on the wave equation

If heat is added to the acoustic system at a rate per volume $\dot{q}'$, it can be shown [BMP09] that the pure homogeneous acoustic equation becomes inhomogeneous as

$$\left(\frac{\partial}{\partial t} + \overline{\boldsymbol{u}} \cdot \nabla \right)^2 p' - \overline{c}^2 \nabla^2 p' = (\gamma - 1) \frac{\partial \dot{q}'}{\partial t}\,. \tag{2.113}$$

This equation is valid when the heat source is applied on the boundary of the considered acoustic domain so that the fluid can be considered as homogeneous within the boundary. In the particular case of a thin flame, this means that this equation can be applied just upstream or downstream of the flame. Equation 2.113 clearly shows the link between a heat source and the acoustic pressure, which is critical in assessing the stability of technical combustion systems, the particularity of these systems being that a

feedback mechanism exists so that the heat release fluctuations are dependent on the pressure fluctuations and not only a source of the acoustic oscillation.

Chapter 3

Experimental setup, measurement techniques, and post-processing

3.1 Fluorescence and Chemiluminescence

Most of the investigation performed used fluorescence or chemiluminescence principles. The present section gives an overview of the physical mechanisms underlying these principles.

3.1.1 Physical principle

Both measurement methods rely on the same principle, the excitation of one molecule from a low-energy state to an excited state of a higher energy level, but they differ in the way this excitation is generated. While the chemiluminescence is a luminescence emitted by molecules after a chemical reaction, the fluorescence is a luminescence resulting from the absorption of light at a shorter wavelength. The principle of the fluorescence is illustrated in Fig. 3.1.

When a molecule absorbs a photon of appropriate wavelength λ or frequency ν, it moves from its ground energy level Ψ_0 to an excited level Ψ_1. This process is called absorption and satisfies

$$\Delta E = E(\Psi_1) - E(\Psi_0) = h \cdot \nu = \Delta E_e + \Delta E_{vib} + \Delta E_{rot}\,, \tag{3.1}$$

where h is Planck's constant, ΔE_e the electronic transfer between the states Ψ_1 and Ψ_0, and ΔE_{vib} and ΔE_{rot} the transfer in vibrational and rotational levels. After a brief time (shorter than 10^{-9} s), the unstable molecule at

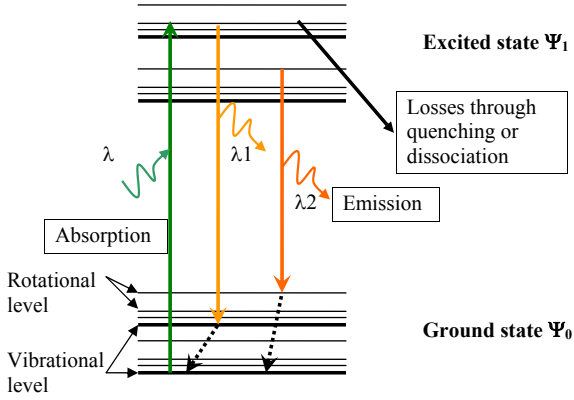

Figure 3.1: Fluorescence principle

this energy level falls back to its ground energy level, whether through quenching with other molecules or by emitting light with a shorter energy content (or higher wavelength). This second step is called emission and takes place for both fluorescence and chemiluminescence. The theory of quantum mechanics states that the energy levels of a molecule are not a continuum, but are quantified. This means for small molecules that light emission occurs at a discrete wavelength. Indeed, for small elements like OH radicals, a high-resolution spectrum of the light emitted shows single discontinuous peaks. For larger molecules, the number of energy levels is so high, that a continuum in the emission spectrum is generally observed.

The resulting emission spectra of chemiluminescence and fluorescence differ in that the emitted light spectrum from fluorescence has higher wavelengths than the absorbed one, while the chemiluminescence spectrum induced by combustion, for example, ranges from ultraviolet to infrared.

3.1.2 Formation mechanisms of OH* and CH*

The common mechanism for OH* production was proposed by Krishnamahari and Brodia in 1961 [KB61] an reads

$$CH + O_2 \rightarrow CO + OH^* \,. \tag{3.2}$$

The symbol "*" signifies the excited radical (in the previous equation the OH radical). Similar to the previous section, the radical has two different possibilities to again reach its ground state: through quenching with another molecule or with spontaneous emission of light, which gives

$$OH^* \rightarrow OH + h\nu\,. \tag{3.3}$$

The latter emissions can be recorded with suitable measurement techniques. The formation mechanisms of OH* are qualitatively and quantitatively well known, but the formation paths of CH* required more attention. This is due to the numerous reaction mechanisms involved in the formation of CH*, which are summarized in Fig. 3.2. The dominant reaction is that involving C_2H with O

$$C_2H + O \rightarrow CO + CH^*\,. \tag{3.4}$$

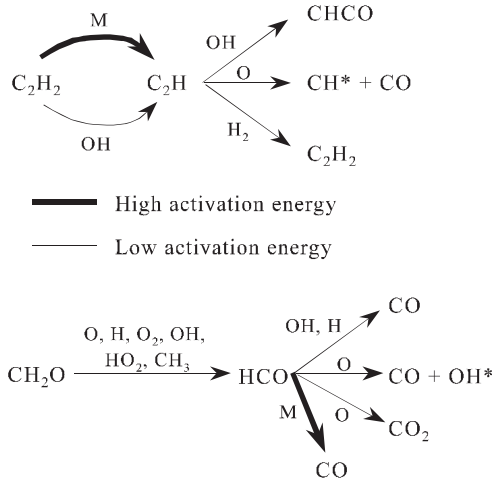

Figure 3.2: CH* and OH* chemiluminescence formation paths (from [Hab00])

3.1.3 OH*, CH*, CO_2* chemiluminescence

Since the first work on chemiluminescence in flames by Clark in 1958 [Cla58], numerous works have been performed to understand the generation of chemiluminescent species. In this first work, four major species (OH*, CH*, CO_2* and C_2*) were already identified and are still the major species used in combustion applications. These species have been investigated in order to estimate quantities like heat release, flame front location, fuel/air ratio, or NO_x emissions, and a brief summary of the main scientific findings are presented in the following.

3.1.3.1 Characterization of chemiluminescence response of a combustor flame

A typical chemiluminescence light spectrum of the flame of the investigated burner is shown in Fig. 3.3 with the four main species of interest. OH*, CH* and C_2* present sharp peaks centered around 308 nm, 431 nm, and 515 nm, respectively. The emissions of CO_2* are broad banded between 280 and 650 nm and constitute a non-negligible part of the total chemiluminescence emitted at the wavelengths of the three previous species. An increase of the equivalence ratio at constant preheat temperature strongly increases the amplitude of all the signals. Thus, OH* chemiluminescence was considered as a direct measure of the heat release in the first experiments. However, recent works by Haber [Hab00], Higgins et al.[HMLC01], Muruganandam et al. [MKO$^+$03], Schuermans et al. [SGM08], among others, have demonstrated that this is not the case for flames of standard burners. Following the work of Higgins [HMLC01], the chemiluminescence emitted by the species i, I_i, reads

$$I_i = k_i \dot{m}_{air} \phi^{\gamma_i} \,, \tag{3.5}$$

where k_i is a proportionality factor. The exponents γ_i satisfy $\gamma_{CH} > \gamma_{OH} > 1$ for lean mixtures ($\phi < 1$). The ratio I_{CH}/I_{OH} is, thus, a monotonically increasing function of the equivalence ratio for lean mixtures. The work of Muruganandam et al. [MKO$^+$03] shows, like Higgins earlier, that there is a weak effect of strain rate on CH* and OH* chemiluminescence. It also points out that the background emission of CO_2* must be subtracted when

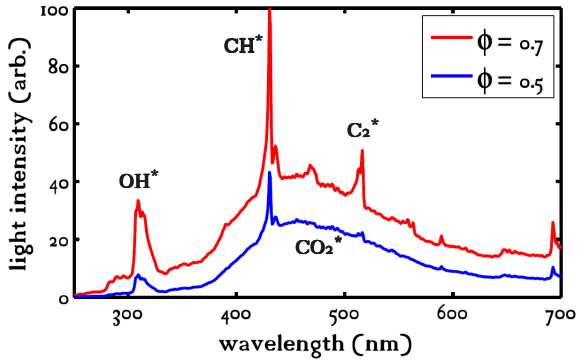

Figure 3.3: Wavelength spectra of a premixed lean flame (from [SGP+09])

recording the OH* and CH* emissions with band pass filters. In particular when going to higher pressures, the strength of the OH* and CH* peaks relative to the CO_2* background decreases strongly. The CO_2* should be, thus, subtracted if the real part of OH* emission at a defined wavelength has to be accurately recorded.

Further work of Lauer [LS08] shows that quantitative estimation of the local heat release on a complex 3D flame requires the combined use of a spectrometer and an intensified camera with a band pass filter. In the recent work of Schuermans et al. [SGP+09], the chemiluminescence properties are used to determine the flame transfer function of a burner under pressurized conditions. Using proper calibration, the coefficients of Eq. 3.5 differ for different species, like OH* and CH*, and can be used to improve the flame transfer function measurement compared to the use of one chemiluminescence signal only.

3.1.3.2 Chemiluminescence and NO_x emissions

As chemiluminescence emissions increase with the adiabatic flame temperature, it may be natural to use chemiluminescence in combustion diagnostics to monitor emissions. Samuelson et al. [SM00] demonstrated that in a

model combustor as well as in a gas turbine combustor, chemiluminescence of OH*, CH*, CO*, and CO_2* can be used to control the emissions of the combustors investigated by adjusting a fuel or air split. This method uses the property that in the case of inhomogeneous mixtures, local hot spots with high equivalence ratios are burnt with higher local temperatures and generate more chemiluminescence. Indeed, measurements performed in a combustor with different fuel distributions (and hence, mixing qualities) for a constant equivalence ratio ϕ show an increase of chemiluminescence emissions when the mixture quality worsens. Hence, to take the unmixedness effect into account, Eq. 3.5 should be extended with a function of the probability density function of ϕ instead of using the average equivalence ratio only (see also Chapter 6).

3.2 Burner and secondary fuel injections

In order to control the mixing profile within the burner, two staged injection lines are mounted just upstream of the standard injection row (see Fig. 3.4). Each of these staged injection lines is split into two independent injection chambers, an upstream (us) and a downstream (ds) injection chamber. The upstream injection chambers are connected together as well as the downstream injection chambers. The fuel repartition of the burner can be, thus, controlled over 3 independent fuel injectors (baseline, staged upstream injection and staged downstream injection).

In order to compare different operating conditions of the burner, two dimensionless parameters α and β characterize the fuel distribution. α describes the ratio premix gas to overall gas mass flow, and β characterizes the ratio upstream injection to total staged gas mass flow. They are defined as follows

$$\alpha = \frac{\dot{m}_{pre}}{\dot{m}_{all}} \quad \text{with} \quad 0 \leq \alpha \leq 1\,, \tag{3.6}$$

$$\beta = \frac{\dot{m}_{us}}{(1-\alpha)\dot{m}_{all}} \quad \text{with} \quad 0 \leq \beta \leq 1\,, \tag{3.7}$$

with $\dot{m}_{all} = \dot{m}_{pre} + \dot{m}_{us} + \dot{m}_{ds}$. $\alpha = 1$ corresponds to fully premixed injection (standard injection), $\beta = 1$ to the staged fuel totally injected

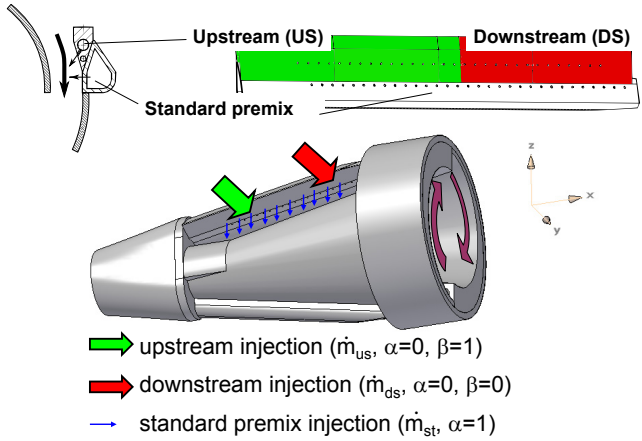

Figure 3.4: Sketch of the swirl-inducing burner with staged injection. Green: staged upstream injection (us); red: staged downstream injection (ds)

through the upstream injector, and $\beta = 0$ to the staged fuel totally injected through the downstream injector.

As shown in previous studies of Lieuwen [LTJZ01], a reduction or an increase of the time delays by at least 50% should be able to stabilize an unstable mode of the combustor (as long as no other mode is excited by the changes). As an increase of time delays would have meant injection of gas further upstream and, thus, higher geometrical modifications, the new staged injections were designed to reduce the convective time delays.

To this end, the fuel injection angles are designed with a value smaller than 90°. An illustration of the tested injection configurations is presented in Fig. 3.5. Four injectors were manufactured: the injector I00 was made of stainless steel for investigation in water and in the combustor while the injectors I01 to I03 were built with stereolithography for cold mixing investigations only. The upstream injection ports have each 16 injection holes of 0.7 mm diameter and the downstream ones, 14 for the injector I00 and 16 for the injectors I01 to I03. I01 and I02 are expected to have an impact on the mixing quality more than on the convective time delays, while the injection angle of 35°of I03 is expected to reduce the convective

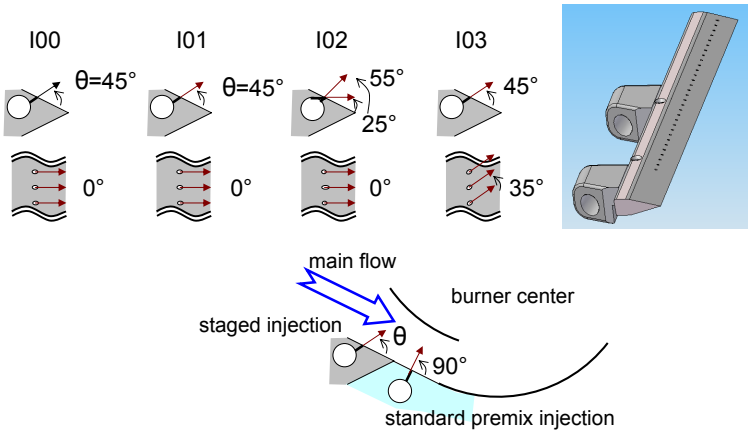

Figure 3.5: Staged fuel injector designs. All the injectors have the same hole spacing $S = 4\,\text{mm}$ and hole diameter.

time delays as the fuel is injected toward the exit of the burner. Because of a lower residence time, a decrease of the mixing quality is expected for this injection configuration.

In order to investigate the mixing process inside the burner, a model identical to the steel burner was built with perspex as well.

3.3 Cold flow investigations

Cold flow investigations were performed to characterize the scalar and vector flow fields. Standard measurement techniques like PIV, LDA, and LIF are used and described in the following section.

3.3.1 The water test rig

The water test rig used for the cold flow investigations is presented in Fig. 3.6. It consists of a measurement section of 400 x 400 mm, a main pump and two 3.5 m^3 tanks. The switching of the valve placed on the top of the tanks allows closed-loop (for PIV, LDA, measurements for example) or open-loop (for concentration measurement like LIF) operations to be set.

The volume flow (rotating wheel, SIGNET 8550) is measured at the outlet of the tank, before entering the pump. The measurement uncertainty of the rotating wheel is less than ± 2 %. The volume flow of the pump can be adjusted with an electric controller and the valve located downstream of the pump. If the pump frequency and level of tanks are properly set, oscillations in the volume flow smaller than ± 4% can be achieved. The overall error of the instanataneous volume flow remains, thus, within ± 4%.

A forcing mechanism can be mounted in the bypass of the pump or in the main piping to produce moderate to strong oscillations of the flow. After the water enters the test rig, two grids and a flow straightener smoothen the velocity profile before the flow enters the test section. The investigated burner is then fixed on a plate which can be mounted at an arbitrary position in the test section. Full optical access is ensured from the 4 sides as well as from the top. Water flows out of the test section over a effluent weir, back to the switching vane. Fluorescent dye is used for mixing investigations and different rotameters monitor the volume flow of dye injected through the different dye injection ports. The coordinate system of the burner mounted inside the water test rig is presented in Fig. 3.7.

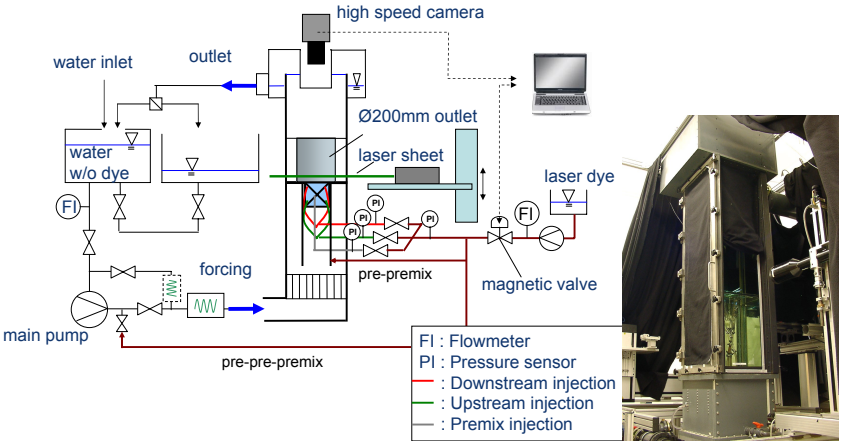

Figure 3.6: Flow chart and photo of the test rig

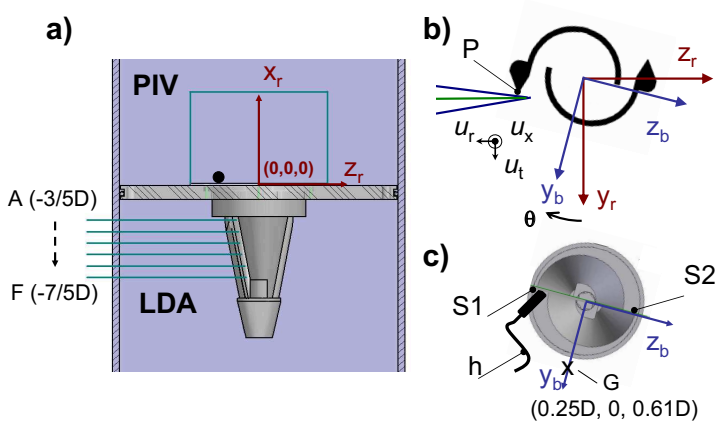

Figure 3.7: Coordinate systems used in the test rig. The index "b" stands for burner coordinate system, the index "r" stands for the test rig coordinate system. "h" is the hydrophone.

3.3.2 Hydrophone measurement

To perform phase average recording for LDA, LIF or PIV measurements, a reference signal is needed. A velocity or pressure probe can be mounted inside the flow field. As velocity measurement in water are very challenging, different probe types were tested: hot-film, hot-wire, and hydrophone. The diverse measurements showed that most velocity probes become damaged rapidly while the hydrophone can be used reliably in the test rig. To minimize the influence of the probe inside the flow field, the smallest hydrophone ($\oslash \approx 10\,\text{mm}$) proposed by Brüel & Kjaer is used (Type 8103, see Fig. 3.8). This sensor allows for recording sound and, hence, pressure fluctuations within the frequency range 0.1 Hz - 180 kHz.

Measurements were performed to investigate the response of the hydrophone to flow oscillations. The LDA measurement volume was first positioned close to the hydrophone sensor head, mounted at the burner outlet as shown in Fig. 3.7, and phase averaging of the recorded time signals was performed. Figure 3.8 shows that the oscillation of the hydrophone signal is inversely proportional to the velocity oscillations recorded with LDA (the phase averaging method is described in Sec. 3.5.2).

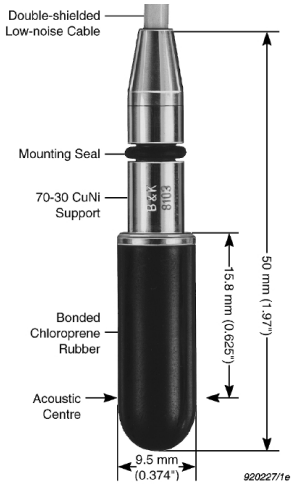

(a) Hydrophone Type 8103, documentation of Brüel & Kjaer

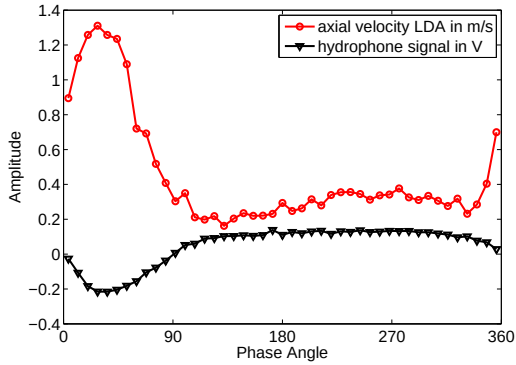

(b) Phase-averaged signals of LDA and hydrophone placed both at the burner oultet edge. The dominant structure showed a frequency of 4.2 Hz. The curves show that velocity and hydrophone signal are out of phase.

Figure 3.8: Characteristics of the hydrophone probe used in the water test rig

3.3.3 Laser Induced Fluorescence (LIF) for quantitative concentration measurements

3.3.3.1 Setup for LIF in water

Quantitative measurement of concentrations in water flow with tracer dyes is a well-established technique in fluid mechanics. First attempts to obtain the limitations of this measurement technique have been made by Guilbault [Gui73] and then Walker [Wal87], who investigated the response of diluted solution of fluorescein to different pH values, laser intensities, and concentrations. Since then, the technique has been further investigated to select appropriate dye/laser systems. The tracer dye chosen was rhodamine 6G, which is less sensitive to photobleaching [Cri97] and to temperature

changes, compared to its low-cost parent, rhodamine B. Photobleaching takes place when dye is unable to emit fluorescence after laser light exposure. As shown by Crimaldi [Cri97], photobleaching of rhodamine 6G may only be considered when using very low flow velocities ($\approx$ 1 cm/s). As the temperature of water changes over the time (through refilling or closed-loop tests), and as the dye consumption is relatively low, rhodamine 6G was, thus, preferred to other fluorescent dyes. As its absorption and fluorescence emission peaks are λ=526 nm and λ=555 nm respectively, the dye is very well suited to be excited by the 532 nm wavelength of Nd:YAG solid state lasers (see Fig. 3.9). The Schmidt number of the dye, measured in water, is approximately $Sc \approx 8.4 \times 10^3$ [Wal87].

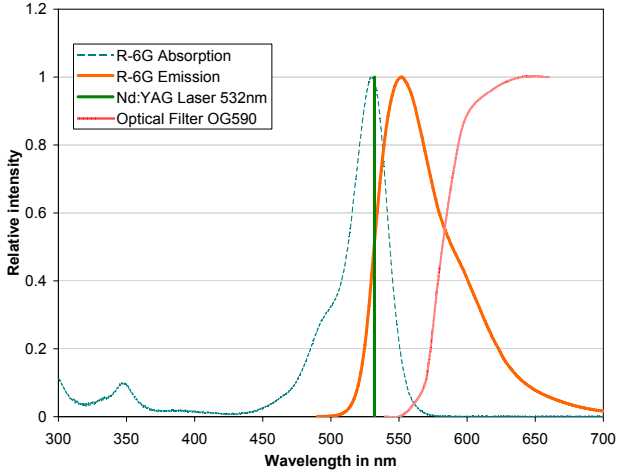

Figure 3.9: Absorption and emission spectra of rhodamin 6G [DFL$^+$98] compared with the transmission of the optical filter used in the LIF setup.

Different cameras are used to perform quantitative LIF investigations: a high-speed camera Photron PCI Fastcam 1024 performs the high-speed laser-induced fluorescence recordings (up to 1000 frame per seconds at a full resolution of 1024 x 1024 px^2), necessary to record the convective time delays of the burner and reduce the measurement time. The camera also allows the recording time to be reduced by two orders of magnitude compared to a standard low speed LIF system. This is a strong advantage

regarding the available measurement time of approximately 20 min in the open-loop configuration. The disadvantage of the camera is the CMOS sensor, which does not offer the quality of a CCD sensor regarding noise (non-cooled sensor) and resolution (10 bit converted in 8 bit instead of now standard full 12 bit for CCD cameras). An Imager QE of LaVision (1376x1040) is also used for the PIV/LIF investigations. A typical spatial resolution of 0.2 mm/px is, thus, achieved when the full combustion chamber section is recorded by the camera.

In order to record 2D images, a 1 mm thick laser sheet is generated with a 4 Watt CW-Laser (Polytec, Finesse, 532 nm, $\mathrm{RMS_{power}} < 0.5\%$), which excites the dye passing through the measurement plane. The emitted light is then filtered with a Schott OG590 optical filter and the resulting signal is recorded by the cameras.

3.3.3.2 Quantitative measurement principle

When passing through a medium filled of diluted dye at a concentration C, the intensity $I_L(b)$ of a laser beam will be attenuated along its path b through absorption of the light by the dye or other particles present in the flow. This phenomenon is shown through the response of the dye for different concentrations at different locations of the picture and for a single laser intensity in Figure 3.10. The linear response assumption is valid for concentrations $C^* \leq 0.08$ ($C \leq 3.2 \times 10^{-8}$ mol/l). Above this value, a decrease of the response due to light absorption is clearly visible. This attenuation along the beam path can be described with the Lambert Beer's law, defined as

$$I_L(b) = I_L(0)\, exp\left(- \int_0^b \left(\epsilon \cdot C(x) + \eta\right)\, dx \right), \tag{3.8}$$

where b is the beam path, ϵ the absorption coefficient of the dye used and η the absorption coefficient of the medium in which the dye is injected. The fluorescence signal emitted by the excited dye and recorded by a two-dimensional sensor $I_f(x, y)$ satisfies

$$I_f(x, y) = A(x, y) \cdot \Phi \cdot V \cdot I_L(x, y) \cdot C(x, y)\,, \tag{3.9}$$

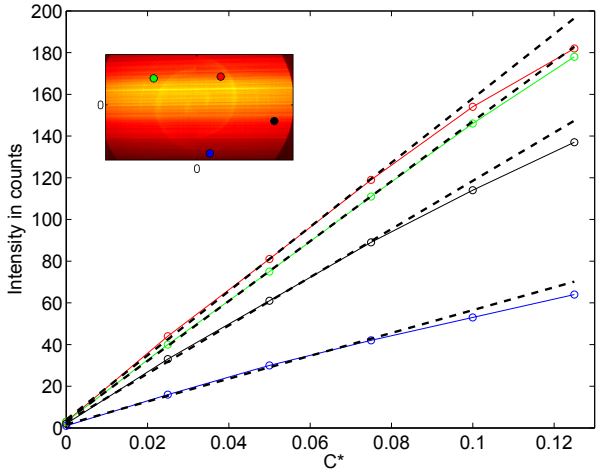

Figure 3.10: Linear relationship between intensity recorded by the camera and normalized concentration C* = C/(4×10^{-8}) mol/l

where $A(x, y)$ is a factor depending on the transmission of the optics, Φ the effective quantum yield of the dye and V the measurement volume. When the exponential term of Eq. 3.8 is low enough (i.e., low concentration, short beam path or short extinction coefficient), the laser beam attenuation does not need to be taken into account, and the fluorescence signal $I_f(x, y)$ is a linear response of the local concentration $C(x, y)$. A linear calibration allows the real concentration $C(x, y)$ from $I_f(x, y)$ to be determined. When the exponential term of Eq. 3.8 is no longer negligible, the absorption of the laser light must be taken into account and a ratiometric method, as presented by Pan [PM01], can be used. Such a correction method allows the influence of the parameters $\eta, A(x, y), \Phi, V$ to be suppressed, by dividing the recorded pictures with a picture of a known reference concentration C_{ref}. This is also an advantage for PIV/LIF investigations, where the seeding density may vary between different runs. After introducing the variable $\zeta(x) = 1 - \frac{C(x)}{C_{ref}}$, the local dye concentration is calculated as

$$\zeta(b) = 1 - \frac{I_f(b) - I_b(b)}{I_{f,ref}(b) - I_b(b)} \cdot exp\left(-\epsilon \cdot C_{ref} \cdot \int_0^b \zeta(x)\, dx\right), \qquad (3.10)$$

where I_b is a background image taken without any dye in the system but with the laser switched on. The post-processing requires only the knowledge of the reference concentration as well as those of the coefficient ϵ. The latter can be calculated with help of the mean pictures of two known concentrations satisfying $C_{ref,1} = a \cdot C_{ref,2}$. Equation 3.10 can be rewritten for each line i of the CCD sensor as

$$\epsilon_i C_{ref} x_i = \frac{1}{(1-a)} \cdot ln\left(a \cdot \frac{I_{ref,1,i} - I_{b,i}}{I_{ref,2,i} - I_{b,i}}\right), \tag{3.11}$$

where ϵ_i is the absorption coefficient calculated for one line of the sensor after a linear regression. When averaged over the lines of the CCD sensor, it gives a good approximation of the extinction coefficient. In the present case, the measurement gives $\epsilon_{rho6G} = 1.24 \times 10^7\,\mathrm{mol^{-1}m^{-1}}$ while the literature [DFL+98] reports $\epsilon_{rho6G} = 1.16 \times 10^7\,\mathrm{mol^{-1}m^{-1}}$, which corresponds to a difference of less than 7%.

3.3.3.3 Homogeneous concentration

Three ways of generating the homogeneous concentration $I_{f,ref}$ have been tested (see setup in Fig. 3.6): (1) closed-loop homogeneous concentration; (2) open-loop homogeneous concentration with injection of reference dye solution just downstream of the pump, (pre-pre-premix injection); (3) open-loop homogeneous concentration with injection of reference dye solution approximately 600 mm upstream of the burner, at the inlet of a pipe simulating the upstream section of combustion chamber (pre-premix injection). The methods required around 20, 5, and 1 minutes, respectively, to produce a homogeneous mixture.

To ensure good post processing, homogeneous reference concentrations were generated before each measurement run. As the open-loop measurement time with one tank is equal to 20 min at $8.55\mathrm{m}^3/\mathrm{h}$ and as the its refilling requires around 30 min, reducing the time needed to obtain the reference concentration is critical. Therefore, depending on the setup investigated, method 2 (pre-pre-premix) or 3 (pre-premix) was selected.

A comparison of the mixing efficiency of both methods was done and the measured averaged normalized concentration C^* as well as temporal unmixedness criterion U_t are listed in Tab. 3.1. The average of the homogeneous concentrations recorded vary little, indicating that the burner is properly sealed into the test rig. Because of its longer mixing length, the pre-pre-premix case shows a much better mixing quality than the pre-premix case. However, when compared to the standard premix injection, which is already well mixed, both homogeneous concentrations are more than two orders of magnitude better mixed than the standard burner injection. They can, thus, be equivalently used for the quantitative post-processing of the mixing pictures.

	pre-pre-premix	pre-premix	premix
$\langle\overline{C^*}\rangle$	0.03509	0.0356	0.03378
U_t	1.332×10^{-5}	2.9×10^{-5}	3.941×10^{-3}

Table 3.1: Comparison of the mixing quality of two homogeneous concentrations (pre-pre-premix and pre-premix) with a standard burner premix injection

Regarding the pre-pre-premix injection, the mixture is physically completely mixed and the unmixedness value is a measure of the noise of the measurement system. As mixing and measurement noise are statistically independent, the variance measured at the burner outlet can be defined as

$$\sigma^2_{tot} = \sigma^2_{mixing} + \sigma^2_{noise}\,. \tag{3.12}$$

In pre-pre-premix conditions, one can assume that $\sigma^2_{tot} = \sigma^2_{noise}$. This value can be used to determine how strongly the measurement of a typical mixing quality is affected by the noise of the measurement system. For the standard premix injection, the ratio of the variances $\sigma^2_{noise}/\sigma^2_{tot}$ is equal to 33, so that the noise of the measurement system can be considered as negligible regarding the mixing qualities recorded for standard injection of the burner.

3.3.3.4 Measurement accuracy

The rotameters of the test rig (Georg Fisher) were calibrated using a chronometer and a bucket. For very low volume flows set, the measured volume flows were superior by 30% to the set values. The error decreases exponentially with increasing volume flow but measured values remain 4 to 5% higher when the maximum of the scale is reached.

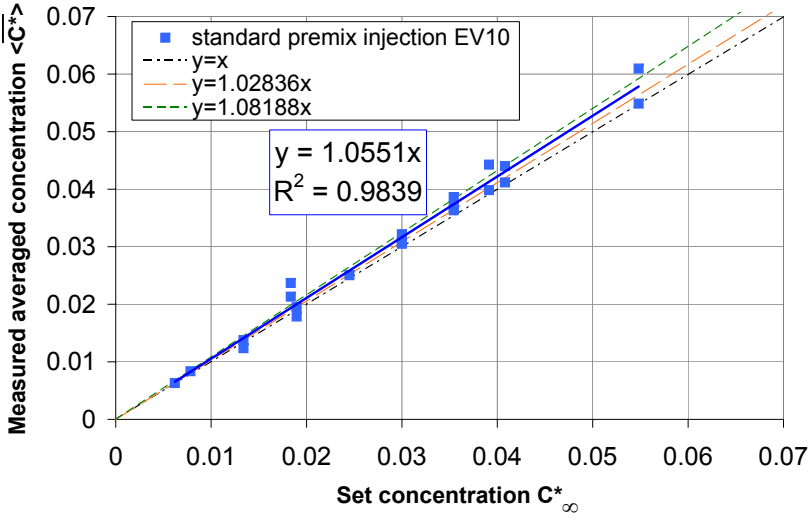

Figure 3.11: Comparison of the accuracy of concentration measurements in the water test rig. The set concentration is the theoretical concentration set with the dye and main volume flows, the measured concentration is recorded by the camera and post-processed with absorption correction for a standard premix injection of the burner. The homogeneous concentrations are performed in pre-pre-premix mode. The 95% confidence interval limits are plotted on both sides of the regression curve.

After correction of the volume flows with the experimental calibrations, the accuracy of the LIF measurement technique can be calculated from reference concentrations taken during different measurement campaigns.

The measured concentration with respect to the set concentration is displayed in Fig. 3.11. A linear fit with a confidence interval of 95% gives the results $\langle \overline{C}^* \rangle / C^*_{set} = 1.0551 \pm 0.0268$. A 5% bias appears in the measured data, which is due to small leckage around the burner fixation plate. This leads to a smaller water flow through the burner than the total volume flow measured upstream of the pump, and explains the higher concentrations recorded than the ones set. However, this error can be compensated for when the momentum ratio is calculated from the recorded concentration and not from the set volume flows.

3.3.3.5 Influence of mean flow on fluorescence intensity

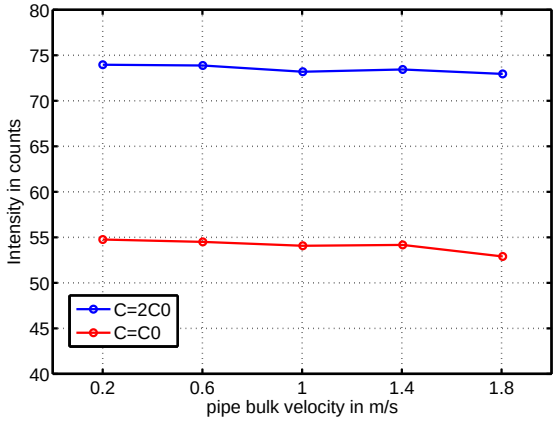

Figure 3.12: Impact of pipe bulk velocity on fluorescence intensity for homogeneous concentrations. $C0 = 8 \times 10^{-9}$ mol/l.

Wang [WK00] pointed out that the mean flow velocity may have an impact on the recorded fluorescence intensity of the system Argon-Ion Laser/Fluorescein. To verify this on the present LIF system, tests were conducted in a pipe of 40 mm in diameter. The pipe bulk velocity was selected within the range occurring in the mixing experiments of the burner. Figure 3.12 shows that an increase in the mean velocity of the pipe leads to a slight decrease in the mean intensity of around 1% per m/s. Hence, the influence of

the velocity on the measured concentration can be considered to be negligible and the measurement technique is a pure concentration measurement technique.

3.4 Reacting flow investigations

3.4.1 The combustion chamber

´ Reacting tests were performed in a cylindrical atmospheric combustion chamber of 200 mm diameter which had full optical access to the flame (Fig. 3.13 and Fig. 3.14) thanks to a silica glass cylinder of 300 mm height. The temperature of the main air flow T_{pre} is controlled by a preheater mounted upstream of the burner. A resonance tube can be mounted downstream of the combustion chamber to amplify a combustion instability corresponding to a 1/4 wave mode oscillation (bulk oscillation mode). An extensive description of the test rig can be found in Albrecht et al. [ABB+06] .
The signal of microphones or photomultipliers are recorded on 16-bit data acquisition cards from National Instruments (NI PXI-6143 S-Series mounted in NI PXI-1031). Routines written in LabVIEW are used to save the data.

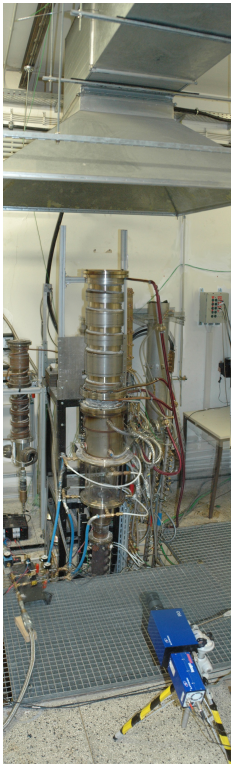

Figure 3.13: Photograph of the combustion chamber

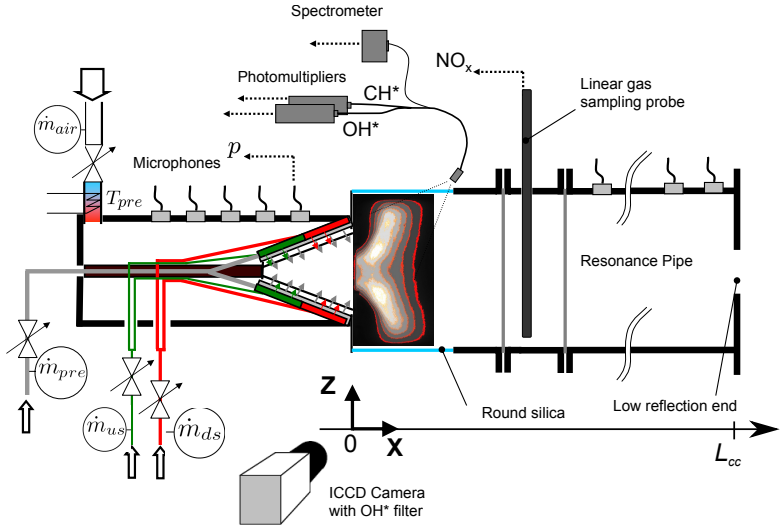

Figure 3.14: Schematic of the combustion chamber with mounted staged fuel injection

3.4.2 Measurement techniques

3.4.2.1 Exhaust gas analysis

A water-cooled finger probe extracts a small volume flow of the exhaust gas of the combustor (ca. 60 l/min) downstream of the flame. The gas is pumped through a heated piping system (140°C) to the exhaust gas analyzer built from 4 modules manufactured by ABB. It allows for analysis of NO and NO_2, CO and CO_2 as well as the rest of the oxygen O_2. The description of the modules as well as their measurement ranges are listed in Tab. 3.2 and further information is available in [BS09]. To allow for a comparison of the NO_x values of different operating points, the wet measurements are corrected to a dry basis and normalized at 15 % O_2as

$$NO_{x,15\%O_2} = NO_{x,meas,dry} \frac{21 - 15}{21 - [O_2]_{meas}}, \tag{3.13}$$

with $[O_2]_{meas}$ being the remaining oxygen after the combustion. Two different exhaust probe hole arrangements were designed and manufactured in-house, one with equidistant holes, the second with a surface averaged hole profile. The emissions measured by the two probes were very similar so that the composition of gas at the measurement location (660 mm downstream of the burner dump plane) can be considered as perfectly mixed and independent of the arrangement of the probe's holes.

Molecule	Module	Measurement range	Type of measurement
NO, NO_2	Limas 11 HW	$0 \cdots$ 20 ppm	UV absor., wet gas
CO_2	Uras 14	$0 \cdots$ 15 Vol %	IR absor., dry gas
CO_{low}	Uras 14	$0 \cdots$ 200 ppm	IR absor., dry gas
CO_{high}	Uras 14	$0 \cdots$ 1000 ppm	IR absor., dry gas
O_2	Magnos 106	$0 \cdots$ 25 Vol %	IR absor., dry gas

Table 3.2: Exhaust gas analysis of the combustion chamber

3.4.2.2 OH*/CH* - Chemiluminescence and spectrometry

As the intensity of the chemiluminescence is weak, the light intensity collected has to be amplified by so-called phototubes. The chemiluminescence of the flame is recorded, whether global and time resolved with multiple photomultipliers equipped with filters or spatially resolved at a low time resolution (up to 6 Hz) with the intensified CCD (ICCD) camera.

Photomultipliers of the type H5784-04 of Hamamatsu are used. A filter corresponding to the wavelength of interest can be mounted on their front side. The light received by the photomultipliers is transmitted through an optic fiber arrangement which ensures that the whole flame is located in the field of view of the fiber optic and that each photomultiplier receives the same amount of light from the same region. A description of the complex fiber bundle may be found in [GMPS09]. Because the flame stabilizes either partly inside or completely outside of the burner depending on the fuel injection profile or the equivalence ratio [Bia06], the end cap of the fiber optic is mounted at the end of the silica segment and inclined by 45° toward the burner. The numerical aperture of the fiber optic (NA=22) ensures that the fiber records the light from a cone with a diameter of approximately

120 mm at the burner outlet ensuring that almost all of the light emitted by the flame is collected. The photomultiplier signals are amplified and low-pass filtered by DISA 55D26 signal conditioners. Before any processing, the background signal measured without flame is recorded and subtracted from the instantaneous signal.

The ICCD camera is a combination of an intensifier (Intensified Relay Optic, IRO) and a CCD camera (Imager QE of LaVision). The IRO is a purely optical intensifier using the same principle as a photomultiplier. The electrons multiplied through a micro-channel plate are projected on an high-sensitivity phosphor shield (P24, decay time of 4 ms) which produces the image recorded by the CCD sensor. The shutter time was set to 100 μs and the gain set to 90. These settings offer a good compromise between a good illumination and the instantaneous capture of dynamic phenomena of up to 250 Hz (angular resolution of the pictures of 9°). A silica UV-lens (Pentax 7838-UV, F/3.8 to F/16) allows recording of light of wavelengths from 250 nm to 1200 nm and above. The lens is mounted between the filter holder and the IRO.

The Signal to Noise Ratio (SNR) of the pictures was estimated to be typically $\mathrm{SNR}_{single} \approx 0.52$ for single images and $\mathrm{SNR}_{average} \approx 3.1$ for an average picture made of 35 snapshots (see Dussault and Hoess [DH04] for calculation method and Lacarelle et al. [LLB+10] for more details). This SNR varie depending on the local intensity recorded, being higher when high-intensity events are recorded and vice versa. This theoretical calculation points out that the OH* signal remains extremely noisy and that interpretation of single snapshots is possible, but must be done with caution. Only averaged pictures show a sufficient SNR (even if very low) to lead to a non-ambiguous interpretation of the recorded structures.

The different filter types used on both the photomultipliers or ICCD camera are listed in Tab. 3.3.

A comparison of the OH* and CH* pictures of the flame for a lean mixture ($\phi = 0.555$) is shown in Fig. 3.15. The general flame shape is the same for both filters. Slight differences appear when considering the positions of the radially integrated maxima (difference of 30 pixels equivalent to 6 mm) or center of gravity but no general trend could be observed when considering

Signal recorded	Filter wave length	Apparatus
OH	312 ± 2 nm	ICCD camera
CH	431 ± 2.4 nm	ICCD camera
OH	308.2 ± 11.2 nm	Photomultiplier
CH	431 ± 4.3 nm	Photomultiplier

Table 3.3: Filters used for chemiluminescence investigations

other operating points. Even if the OH* radical is reported to have a much longer lifetime after the reaction zone than the CH* radical, it seems that no difference is visible in the flame shape, presumably because of the strong recirculation of exhaust gas. Therefore, as the CH* signal is much weaker, the OH* signal was used to determine the flame characteristics such as flame position and width.

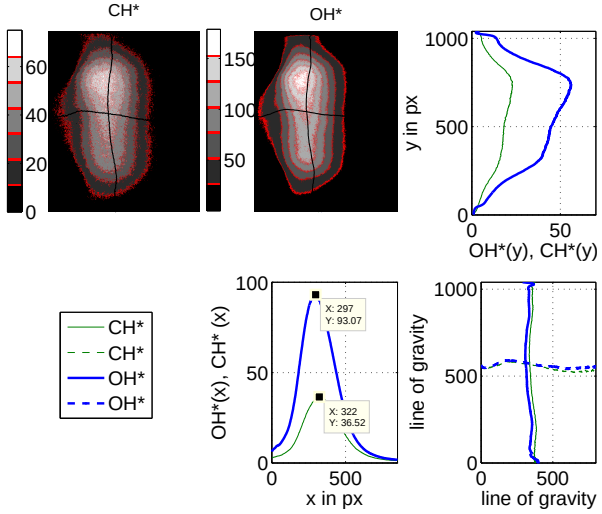

Figure 3.15: Comparison of OH* and CH* chemiluminescence for a lean mixture at ϕ=0.55 showing marginal differences in the flame shape recorded with both filters. Top right: average of the axially integrated OH* and CH* pictures. Bottom middle: average of the radially integrated OH* and CH* pictures. Bottom right: center of gravity of the OH* and CH* pictures.

The photomultipliers are well suited to record the chemiluminescence released by the flame with a high temporal resolution, but as shown is the spectra in Fig. 3.3, they are not suited for differenciating the sources of chemiluminescence. To circumvent this problem, a Peltier cooled spectrometer of Ocean Optics records the light spectrum of the flame. Through the fiber bundle, the same field of view as for the photomultipliers is ensured. As the quality of the spectrum was more relevant than a fast acquisition, the spectra were integrated over 2 s and an average spectrum from 10 records was taken for each point reported.

3.4.2.3 Microphones and flame transfer function measurements

Pressure probes To record the acoustic velocity fluctuations in the test rig, the Multi-Microphone Method (MMM) [PSPM02] was used. An extensive description of the method as well as of the measurement probe can be found in [Bot08] and the main points are summarized here. First of all, the pressure probes used are 1/4" condenser microphones (G.R.A.S. 40BP with pre-amplifiers 26AC). They are mounted in water-cooled microphone holders with a 1 mm outlet hole to prevent damages from high temperatures, in particular downstream of the flame. Because the water contained in the hot gases should not condense on the microphone membrane, the temperature was set to 333 K.

The microphones are calibrated in terms of amplitude and phase relation in a calibration tube of 200 mm diameter, which is equipped with a loudspeaker at one end and a low-reflecting termination on the other end to avoid acoustic nodes at the microphone position. They are mounted circumferentially at one axial location. A reference microphone, wall flush-mounted and thus recording the pressure oscillations inside the tube, is fixed at the same position. The latter is absolutely calibrated with a pistonphone (Brüel & Kjaer Type 4228) at 124 dB and 250 Hz, and the other microphones are calibrated relatively to the reference microphone.

Multi-Microphone Method (MMM) Up to 5 microphones can be mounted upstream and downstream of the burner, ensuring a good accuracy of the MMM measurements. A least square regression method is used to calculate the unknown amplitudes of the traveling waves $A^+(\omega)$ and

$A^-(\omega)$ from Eq. 2.110 and Eq. 2.112. Because of its ease, the frequency domain of Eq. 2.110, Eq. 2.108 will be used. Eq. 2.108 expressed for N microphones located at the axial positions $x_1 \dots x_N$ leads to the system of equations

$$\begin{bmatrix} \hat{p}(x_1,\omega) \\ \hat{p}(x_2,\omega) \\ \vdots \\ \hat{p}(x_N,\omega) \end{bmatrix} = \begin{bmatrix} e^{-ik^+x_1} & e^{+ik^-x_1} \\ e^{-ik^+x_2} & e^{+ik^-x_2} \\ \vdots & \vdots \\ e^{-ik^+x_N} & e^{+ik^-x_N} \end{bmatrix} \begin{bmatrix} A^+(\omega) \\ A^-(\omega) \end{bmatrix} . \tag{3.14}$$

With the definition

$$\mathbf{H} = \begin{bmatrix} e^{-ik^+x_1} & e^{+ik^-x_1} \\ e^{-ik^+x_2} & e^{+ik^-x_2} \\ \vdots & \vdots \\ e^{-ik^+x_N} & e^{+ik^-x_N} \end{bmatrix} \tag{3.15}$$

and using the Moore-Penrose pseudo-inverse of a matrix defined as $\mathbf{H}^+ = \left(\overline{\mathbf{H}}^{\mathrm{T}}\mathbf{H}\right)^{-1}\overline{\mathbf{H}}^{\mathrm{T}}$, where the operator $\overline{(\cdot)}$ is the complex conjugate, $(\cdot)^{\mathrm{T}}$, the transpose operator, and $(\cdot)^{-1}$, the inverse operator, one obtains the solution for the coefficient $A^+(\omega)$ and $A^-(\omega)$:

$$\begin{bmatrix} A^+(\omega) \\ A^-(\omega) \end{bmatrix} = \mathbf{H}^+ \begin{bmatrix} \hat{p}(x_1,\omega) \\ \hat{p}(x_2,\omega) \\ \vdots \\ \hat{p}(x_N,\omega) \end{bmatrix} \tag{3.16}$$

$A^+(\omega)$ and $A^-(\omega)$ are solutions of Eq. 3.14 in the least square sense. As for every regression method, the residual resulting from the fitting should be minimized and remain lower that 5%, which was the case for the measurements presented here. One uncertainty source is the determination of the local temperature T, which has a direct effect on the averaged density $\overline{\rho}$ as well as the acoustic sound velocity $\overline{c}$. This is particularly true downstream of the flame where axial as well as even more radial temperature gradients take place, due to the cooling effect of the walls.

The determination of $A^+(\omega)$ and $A^-(\omega)$ allows the velocity fluctuations $\hat{u}(x,\omega)$ to be calculated at any axial location in the test section. For the tests considered, the burner outlet ($x = 0\,\mathrm{mm}$) was chosen as the reference plane for the acoustic fluctuations.

Flame transfer function The flame transfer function (FTF), is the response of the heat release of the flame to acoustic pulsations. It is defined as

$$FTF(\omega) = \frac{\hat{\dot{Q}}'(\omega)/\overline{\dot{Q}}}{\hat{u}'(\omega)/U_0}\,, \tag{3.17}$$

with $\dot{Q}$ being the global heat release rate, $\hat{\dot{Q}}'(\omega)$ the Fourier transform of its temporal fluctuations, U_0 the mean bulk velocity in a reference plane, generally located upstream of the flame, and $\hat{u}'(\omega)$ the Fourier transform of the acoustic fluctuations at the same location.

Technically, an optical measurement of the heat release fluctuations requires the use of different chemiluminescence signals [SGP+09]. Here however, only the CH* chemiluminescence signal will be used to obtain a surrogate measurement of the heat release fluctuations. The flame transfer function can also be measured from pure acoustic measurements which avoid to use optical signals. The method is described for example in [PP98].

As shown in Sec. 3.4.3, the flame transfer function is a key element to assess for the stability of a combustion system. In general, the response of the flame also depends on the amplitude of forcing, low amplitudes corresponding to the linear regime, while high forcing amplitudes correspond to the non-linear regime followed by a saturation regime. The attempt to account for the sensitivity of the flame response to varying acoustic-forcing amplitudes is a recent field of research in and of itself [NDSC08] and will not be mentioned further. It was only ensured that the acoustic forcing of the flame remained low enough so that the flame was maintained in the linear regime. The amplitude of acoustic forcing is depending on the forcing frequency in the test rig for a defined loudspeaker voltage, in particular close to resonant frequencies, which induce strong velocity fluctuations. The FTF was, thus, recorded from mono-frequent forcing, and the loudspeaker voltage was adjusted for each frequency so that the velocity fluctuations satisfied $u'/\overline{u} < 0.07$.

Signal processing To calculate the flame transfer function, the chemiluminescence and pressure signals are cross-correlated with the excitation signal. The cross-spectra are then calculated with Welch's method with 50% overlap to reduce the spectrum noise. With the cross-spectra of the pressure signals, the cross-spectrum of the velocity fluctuations is calculated. The ratio of the spectra of the cross-correlated chemiluminescence fluctuations to the velocity fluctuations then compose the chemiluminescence transfer function, surrogate of the flame transfer function.

3.4.3 Thermoacoustic network model

The previous measurement technique is then used to determine the so-called transfer matrices of the combustion chamber elements. Such a technique has been developed by Munjal [Mun87] to characterize the acoustic response of mufflers and ducts, and was extended to analyze the stability of combustion systems by Paschereit and Polifke [PP98], Paschereit et al. [PFS01] or Schuermans [Sch03]. In particular, an extensive description of the modeling task is given in the last reference. Here, a summary of the elements used to describe the combustor is given. The combustion chamber can be modeled as a network of one-dimensional acoustic elements as illustrated in Fig. 3.16.

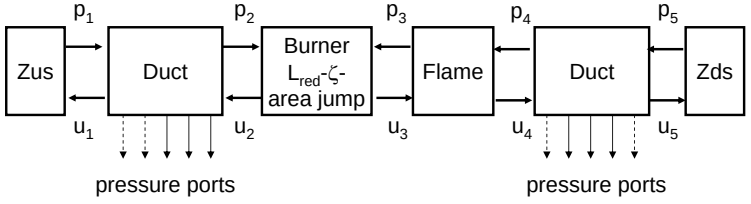

Figure 3.16: Thermoacoustic network of the combustor

Each element of the network is characterized by a transfer matrix which describes the evolution of the acoustic pressure and velocity downstream of the element depending on the upstream state and the source terms within

the element. The transfer matrix notation reads

$$\begin{bmatrix} \frac{\hat{p}}{\rho c} \\ \hat{u} \end{bmatrix}_{downstream} = \begin{bmatrix} T_{11}(\omega) & T_{12}(\omega) \\ T_{21}(\omega) & T_{22}(\omega) \end{bmatrix} \cdot \begin{bmatrix} \frac{\hat{p}}{\rho c} \\ \hat{u} \end{bmatrix}_{upstream} + \begin{bmatrix} \frac{\hat{p}}{\rho c} \\ \hat{u}\,, \end{bmatrix}_{source} . \quad (3.18)$$

The source term is different from $\mathbf{0}$ for elements like a flame or a loudspeaker. The main elements of the system are briefly described in the following.

Upstream impedance Because of the complex geometry of the upstream section (flexible inlet pipe, preheater, and 90° elbow), the upstream acoustic impedance $\mathcal{Z}$ is directly measured with the MMM. Its definition reads

$$\mathcal{Z}(\omega, x) = \frac{\hat{p}(\omega, x)}{\hat{u}(\omega, x)\boldsymbol{n_u} \cdot \boldsymbol{n_b}}\,, \quad (3.19)$$

where $\boldsymbol{n_u}$ is the direction of propagation of the acoustic wave and $\boldsymbol{n_b}$, the inward normal to the system boundaries.

Pipe with mean flow The transfer function of a straight round pipe between an upstream and a downstream position with a distance of $x_2 - x_1 = L$ and a mean flow without losses can be derived as

$$\boldsymbol{T} = \frac{1}{2} \begin{bmatrix} e^{(-ik^+L)} + e^{(ik^-L)} & e^{(-ik^+L)} - e^{(ik^-L)} \\ e^{(-ik^+L)} - e^{(ik^-L)} & e^{(-ik^+L)} + e^{(ik^-L)} \end{bmatrix} . \quad (3.20)$$

Burner A critical element of the thermoacoustic model is the burner which exhibits a quite complex flow with pressure loss. The simplified transfer matrix expression of a compact element with losses can be derived from the unsteady isothermal mass and momentum equations with a pressure loss term, as derived by Paschereit and Polifke [PP98]:

$$\boldsymbol{T} = \begin{bmatrix} 1 & M_u \left(1 - \zeta - \left(\frac{1}{AR}\right)^2\right) - i\frac{\omega}{c} L_{red} \\ 0 & \frac{1}{AR} \end{bmatrix} . \quad (3.21)$$

AR is the ratio of the downstream duct area to the upstream duct area $AR = \frac{A_3}{A_2}$, L_{red} is the reduced length of the burner, and ζ the hydraulic pressure loss coefficient. To achieve a better identification of the burner

transfer matrix parameters with experimental data, an adjustment of the reference plane was implemented, as proposed by Paschereit et al. [PFS01].

Acoustic flame model As written for Eq. 2.113, a closure is needed to express the source term of the flame in the combustor. The $n-\tau$ model reported by Crocco and Cheng [CC56] is an analytical formulation which states that the velocity jump induced by the flame is expressed as

$$u_4'(t) = u_3'(t) + n u_3'(t)(t-\tau)\,. \tag{3.22}$$

The time delay τ expresses the observed time delay existing between the fluctuations upstream and downstream of the flame. n is the so-called interaction index. Both parameters can be obtained from a fit of the measured data. This formulation was useful to describe the main behavior of combustion instabilities, but remains an empirical model. A physical model of the flame transfer function can be derived using the mass, momentum, energy, and state conservation equations across a flame sheet. The well-known Rankine-Hugoniot equations can be obtained, which describe the pressure, density, and temperature jumps across the flame. After a reformulation corresponding to the transfer matrix approach, the transfer matrix of the flame is obtained as

$$\boldsymbol{T}_{fl} = \begin{bmatrix} \frac{(\overline{\rho}c)_3}{(\overline{\rho}c)_4} & -\frac{(\overline{\rho}c)_3}{(\overline{\rho}c)_4}\left(\frac{T_4}{T_3}-1\right) M_3 \left(1+\frac{q'/\overline{q}}{u_3'/\overline{u}_3}\right) \\ -\left(\frac{T_h}{T_3}-1\right)\gamma M_u & 1+\left(\frac{T_4}{T_3}-1\right)\frac{\dot{q}'/\overline{\dot{q}}}{u_3'/\overline{u}_3} \end{bmatrix}. \tag{3.23}$$

Experimental measurements of the flame transfer matrix from the acoustic method showed that the elements T_{12} and T_{21} of the flame transfer matrix can be neglected [Sch03] in the present burner. This is also a consequence of the very small Mach number. The ratio of the characteristic impedances $\frac{(\overline{\rho}c)_3}{(\overline{\rho}c)_4}$ can also be expressed as a function of the temperatures upstream and downstream of the flame so that Eq. 3.23 may be simplified as

$$\boldsymbol{T}_{fl} = \begin{bmatrix} \sqrt{\frac{T_4}{T_3}} & 0 \\ 0 & 1+\left(\frac{T_4}{T_3}-1\right)\frac{\dot{q}'/\overline{\dot{q}}}{u_3'/\overline{u}_3} \end{bmatrix}. \tag{3.24}$$

Downstream reflection coefficient The downstream reflection coefficient was modeled using the exit impedance formulation proposed by Schuermans et al. [SBFP04] as

$$\mathcal{Z}_{exit} = i\omega \frac{L_{cor}}{c_{end}} + D \left(\frac{r\omega}{2c_a} \right)^2 \frac{\rho_a c_a}{\rho_{end} c_{end}}, \tag{3.25}$$

with $L_{cor} = 0.61\,r$ and D a damping coefficient which takes into account the changes in the geometry with respect to the original unflanged end of the downstream duct. r is the radius of the downstream duct and ρ_a and c_a the density and sound speed of the ambient air.

3.5 Velocity measurement techniques

3.5.1 Particle image velocimetry (PIV)

PIV measurements are performed in the two test rigs with a low-speed PIV system (Continuum Nd:YAG Laser, 20mJ per pulse, acquisition with a PCO Sensicam, 1280 x 1024 px^2, 4 image-pairs per seconds). Seeding of water is achieved with $\varnothing$ 5 μm spherical silver coated particles, seeding of air is done with oil ($\varnothing$ 0.8 μm, Merck) for the non-reacting investigations and with silicon dioxide (SiO_2) for reacting investigations. The post processing is performed with the software VidPIV produced by ILA GmbH.

To reduce the influence of reflections on the cylinder walls, the average of all the pictures is subtracted from each single snapshot. The resulting pictures are then processed in 32 x 32 px^2 interrogation areas with a 50 % overlap. The interrogation areas are cross-correlated and a local median filter is used to eliminate spurious vectors. The eliminated data are replaced via interpolation from adjacent interrogation areas. The resulting vector field is used for an adaptive cross-correlation of the data, spurious data are filtered again and adaptive cross-correlation in 16 x 16 px^2 interrogation areas is reapplied. The percentage of spurious vectors never exceeded 2 % in the water investigations.

The quality of combustion chamber data, in particular those for the reacting flow, is much lower than the water test rig measurements. In the air,

non-homogeneous seeding density, optical reflexions of the cylindrical wall, agglomeration of seeding on the combustor wall as well as the low signal recorded led to significantly more velocity outliers and, hence, a higher error for single velocity estimation than in water (±16% against ±7.7%, calculation method defined in [ITT08]). In fact, because of the smoothing effect of the PIV interpolation, the velocities are more underestimated so that the turbulent quantities of the combustion chamber will be underpredicted. On the contrary, higher volume flow oscillations will slightly increase the degree of turbulence in the water test rig, but will remain closer to the real degree of turbulence.

3.5.2 Laser Doppler anemometry (LDA)

A two component LDA system manufactured by Dantec (Model No 5500A-00 with BSA F60) was used in the water test rig. The positioning of the LDA measurement volume is ensured by a traversing system and positioning correction due to the different refraction indexes (air/glass and glass/water) is applied if necessary. As shown in [FKS00], if the axial velocity component is not influenced by the round combustion chamber (except for a constant position shift), the azimuthal component may be affected by the variation of the incident angle of the laser beam with the round surface. However, if the angle remains below 6°, close to the actual value of 7°, then the changes in the interference pattern are negligible. Using the small incident angle assumption, the axial and azimuthal measurement volume position can also be considered to be coincident.

To reduce the bias error, the velocities recorded are weighted with their transit time before statistical momentums are calculated. For the phase-averaged measurements presented in Sec. 4.3.2.3, this correction is not necessary and the collecting mode "sample and hold" of the bursts is set for the bursts (2 ms dead time between two valid bursts, i.e., maximal data rate of 500 Hz). To increase the data rate, the two velocity measurements are non-coincident. Data rates ranging from 100 Hz up to 500 Hz are achieved, depending on the location of the measurement probe. These values are sufficient to obtain a good resolution of the dominant frequencies of interest below 10 Hz.

As the flow is strongly dominated by a helical structure, the triple decomposition of Eq. 2.33 is used on the LDA time signal. The velocity samples acquired are phase sorted with respect to the filtered reference signal (the hydrophone), with a phase resolution of 1° (resulting in 360 bins). About 15,000 valid samples for each measurement point are taken. The mean phase-averaged profile is obtained by fitting a Fourier series to the bin-averaged profile, as described by Sonnenberger [SGE00]. Five harmonics are used and ensure a higher stability of the obtained profile against measurement outliers. The formulation of the Fourier estimation of the mean phase averaged velocity $\tilde{u}_{F,t}(\phi)$ (here for the azimuthal velocity) is therefore,

$$\tilde{u}_{F,t}\left(\phi\right) = \overline{u}_t + \sum_{m=1}^{5} a_m cos\left(2\pi m f_0 \phi\right) + b_m sin\left(2\pi m f_0 \phi\right) \ , \tag{3.26}$$

where $\overline{u}_t$ is the mean velocity at the considered point, ϕ the phase angle, f_0 the dominant frequency, a_m and b_m the Fourier coefficients of the mth harmonic. To allow for a direct comparison of the amplitude and phase shift relationship between the measurement points and the hydrophone signal, Eq. 3.26 is reformulated as

$$\tilde{u}_{F,t}(\phi) = \overline{u}_t + \sum_{m=1}^{5} \left|\tilde{u}_{t,m}\right| cos\left(2\pi m f_0 \phi + \angle \tilde{u}_{t,m}\right) \ , \tag{3.27}$$

with $\tilde{u}_{t,m} = a_m - i b_m$. The same processing is applied to the hydrophone signal because the hydrophone data are sampled with a valid burst of the streamwise velocity and not continuously sampled. Figure 3.17 confirms the effectiveness of the Fourier estimation in comparison to the bin-averaging method. The temporal signal was recorded at the position G at the burner outlet for the unforced flow (see position in Fig. 3.7). The left plot in Fig. 3.17 shows the phase-sorted samples of the azimuthal component u_t and the resulting bin averaging. It proves the strength of the random component u'_t relative to the coherent motion $\tilde{u}_t$, the coherent fluctuation representing 10 to 20% of the total velocity fluctuations. The Fourier estimation on the right plot smooths the bin-averaged profile and allows for a

better estimate of $\tilde{u}_t(\phi)$ to be obtained. It is also noticeable from Fig. 3.17 that the phase averaged signal at the burner outlet is not sinusoidal but qualitatively reproduces the signal obtained in other experimental configurations [Syr06].

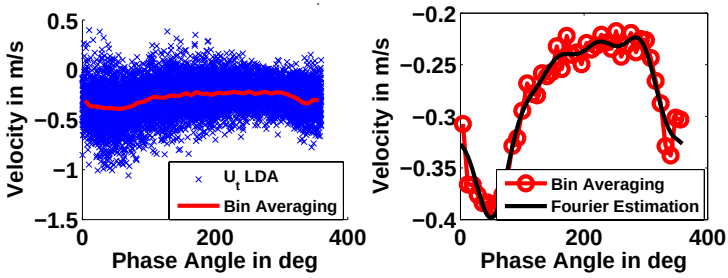

Figure 3.17: Scatter plot of the azimuthal velocity u_t, bin averaging of the velocity (left) and comparison of the bin averaging with the Fourier estimation of the bin averaged velocity (right), $\tilde{u}_{F,t}$ for the unforced flow.

Temporal spectra are also calculated from the LDA time signals. Because of the randomly acquired data, which cannot be used directly for FFT analysis, the acquired data are equally resampled with the mean sampling time of the time series [RM00]. The power spectrum is then calculated with the function pwelch in Matlab, and to reduce the noise, the whole time signal is split into periods of 7 sections and the resulting spectra averaged together.

3.6 PIV/LIF Measurement

A combined PIV/LIF measurement system is used to characterize the unsteady flow field and particularly the interaction between scalar and velocity fields. A diagramm of the system is presented in Fig. 3.18. Before entering the measurement section, the laser beam passes through a continuously stirred cell filled with a rhodamine 6G reference concentration. The measurement area, which contains more than half the outlet diameter and the reference cell, is recorded by two cooled CCD cameras. A band pass interference filter centered around 532 nm is mounted between

the objective and the PIV camera (PCO Sensicam) while a high pass filter OG590 is fixed on the LIF camera (Imager QE). The overlapping of the two cameras is adjusted with a spatial precision of ±2 pixels (± 0.2 mm). The oscillations of the reference cell global intensity are proportional to the laser power oscillations and used in the post-processing to correct the concentration pictures. For the measurement presented here, 500 PIV/LIF snapshots are recorded and processed with VidPIV for the PIV snapshots. The LIF snapshots are post-processed with the same routine as described in Sec. 3.3.3.2.

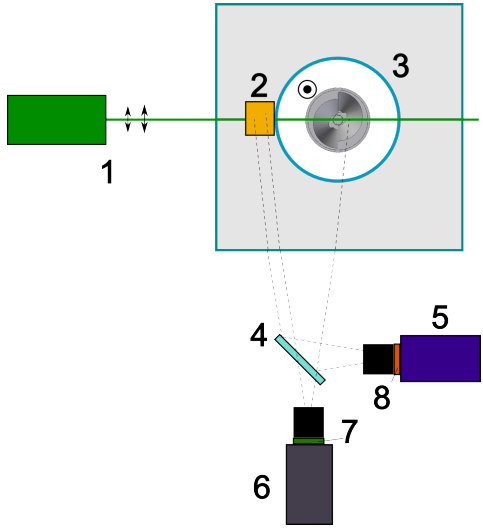

Figure 3.18: PIV/LIF System: 1-Nd:YAG Laser (532 nm) + lenses to generate 1.5 mm laser sheet. 2-reference cell. 3-Burner mounted into 200 mm cylinder inside the square test rig. 4- 50-50 splitter plate. 5-LIF Camera. 6- PIV Camera. 7- 532 nm bandpass filter. 8- OG590 filter.

3.7 Proper Orthogonal Decomposition (POD)

Proper orthogonal decomposition (POD) is used to extract the dominant modes contained in the flow field from a series of snapshots. Spatial or temporal modes can be extracted depending on the data set available. Datasets

with high temporal resolution (from hotwire array for example) allow temporal modes to be extracted, while datasets with high spatial resolution (from PIV for example) allow spatial modes to be characterized. The resulting dominant modes describe the coherent structures which dominate the flow field. In the present thesis, spatial modes calculated from PIV data are shown. The general decomposition of the turbulent velocity field of Eq. 2.2 reads:

$$\mathbf{u}(\mathbf{x},t) = \overline{\mathbf{u}}(\mathbf{x}) + \sum_{i=1}^{N} a_i(t)\mathbf{u}_i(\mathbf{x}), \tag{3.28}$$

where $\overline{\mathbf{u}}(\mathbf{x})$ denotes the ensemble average of $\mathbf{u}(\mathbf{x},t)$, $\mathbf{u}_i$ is a POD mode, a_i its respective amplitude, and N is the number of modes used for the decomposition. $\mathbf{u}_i$ are also referred to as the basis functions of the flow field. The aim of the POD is to find a set of empirical basis functions which should represent the flow in an optimally compact fashion. Mathematically, this leads to solving the eigenvalue problem

$$\int_{\Omega} \overline{\mathbf{u}'(\mathbf{x},t) \otimes \mathbf{u}'(\mathbf{x}',t)}\mathbf{u}_i(\mathbf{x}')d\mathbf{x}' = \lambda_i \mathbf{u}_i(\mathbf{x})\,, \tag{3.29}$$

where Ω is the flow domain considered. λ_i are the eigenvalues corresponding to the eigenfunctions (modes) $\mathbf{u}_i$, $\overline{\mathbf{u}'(\mathbf{x},t) \otimes \mathbf{u}'(\mathbf{x}',t)}$ is the two-point space-time correlation tensor ($\otimes$ is the dyadic product). The eigenvalues λ_i represent the contribution of the mode i to the mean turbulent kinetic energy (TKE). The modes are ordered by decreasing energy contribution (optimality condition). The time coefficients can be obtained by taking the inner product of the instantaneous snapshot $\mathbf{u}(\mathbf{x},t)$ with the considered mode as

$$a_i(t) = \int_{\Omega} \mathbf{u}'(\mathbf{x},t)\mathbf{u}_i(\mathbf{x})d\mathbf{x}\,. \tag{3.30}$$

In the present study, the decomposition is obtained with the methods of the snapshots of Sirovich. Further details can be taken from [HLB98]. The method was applied to the velocity and chemiluminescence pictures.

Chapter 4

Combustion chamber and burner flow field characteristics

This chapter with help of the thermoacoustic model justifies the use of the fuel staging as a mean of controlling thermoacoustic instabilities. The theoretical model is validated with experimental data recorded with the modified fuel injector I00. Furthermore, an overview of the flow and passive scalar fields is given to illustrate the main mixing mechanisms taking place inside the burner.

4.1 Thermoacoustic behavior

4.1.1 Acoustic measurements and model

The thermoacoustic network was used to investigate the capacity of a modified distribution of fuel residence time to control the thermoacoustic instabilities in the combustor. The comparison between the model and measurements for the phase of the elements of the burner transfer matrix is shown in Fig. 4.1 and demonstrates the very good agreement of the model with the experimental data. Qualitatively similar results were observed for the amplitude of the element of the transfer matrix which, for brevity, are not shown here.

An estimation of the pressure spectrum in the combustor can be obtained by solving the linear system

$$\boldsymbol{S}\boldsymbol{r} = \boldsymbol{q}\,, \tag{4.1}$$

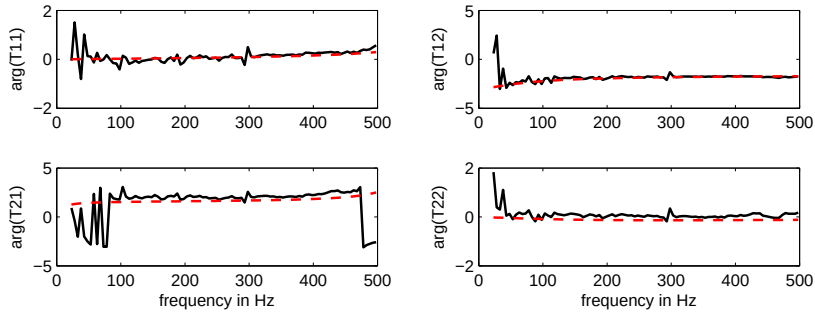

Figure 4.1: Measured (solid) and modeled (dashed) phase of the burner transfer matrix elements for the operating conditions $\dot{m}_{air} = 200\,\mathrm{kg/h}$ and $T_{pre} = 293\,\mathrm{K}$.

where $\boldsymbol{S}$ is the matrix of the interconnected elements of the acoustic system, $\boldsymbol{r}$ is the state vector pressure and velocity fluctuations defined as

$$\boldsymbol{r} = \begin{bmatrix} \frac{\hat{p}_1(\omega)}{\rho_1 c_1} \\ \hat{u}_1(\omega) \\ \vdots \\ \frac{\hat{p}_N(\omega)}{\rho_N c_N} \\ \hat{u}_N(\omega) \end{bmatrix}, \tag{4.2}$$

and $\boldsymbol{q}$ the vector of the acoustic sources of the system. Equation 4.1 is then solved for each frequency of interest and the transfer function of pressure and velocity fluctuations at every location implemented in the matrix can be extracted. As an example, the pressure spectrum simulated for a microphone located at $x = 1.037\,\mathrm{m}$ downstream of the burner is shown in Fig. 4.2. The forcing was performed upstream of the burner and the pressure signal of a microphone mounted upstream of the burner ($x = -541\,\mathrm{mm}$) was used as a source for the system. The locations of the pressure peaks are relatively well captured, even if some slight deviation in the peak frequencies can be observed. The deviations are greater with respect to the amplitude of the pressure spectrum. However, for stability analysis, i.e., answering the question of whether the undamped system may become unstable or not, the phase information is more important. Except in the very-low frequency

range, the agreement is relatively good.

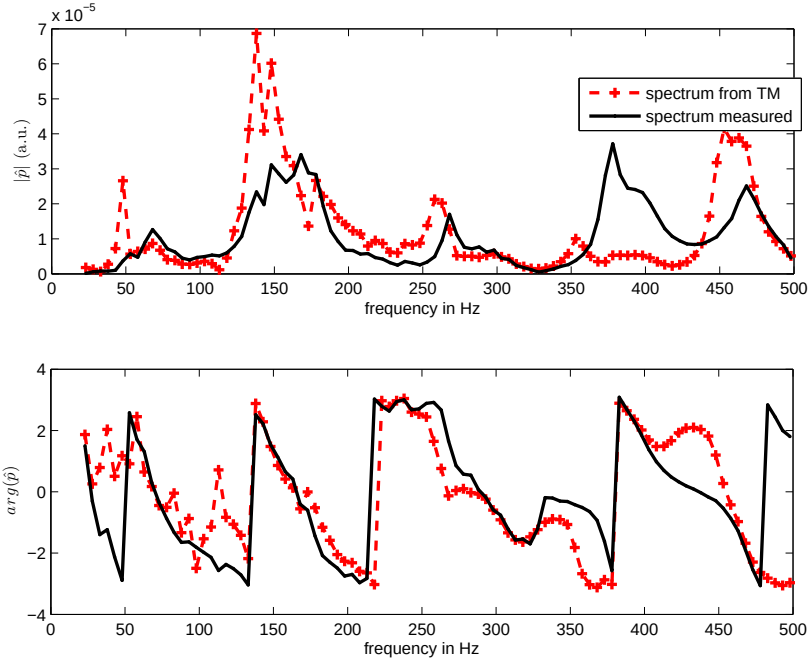

Figure 4.2: Measured (solid) and modeled (dashed) pressure spectrum recorded 1.037 m from the burner exit plane (L_{cc}=1.5 m, 200 mm outlet) showing a good agreement for both the pressure amplitude (top) and the phase (bottom). Operating conditions $\dot{m}_{air}$ = 200kg/h and T_{pre} = 293 K

4.1.2 Stability analysis

Without any acoustic source, the system will remain stable, i.e., no resonance phenomena can take place. If an acoustic source generates acoustic waves at a frequency close to that of a system mode, then a resonance can occur which will lead, in the case of the present combustor, to a standing wave pattern of the pressure distribution at the given resonance frequency. In a combustion system, the heat release fluctuations will act as a loudspeaker, but the amplitude of acoustic fluctuations which can be achieved

is much larger and one can then talk about thermoacoustic instabilities. To describe the interaction of the flame with the acoustic field of the combustor, the analytical flame model of Schuermans et al. [SBFP04] is used to model the T_{22} element of the flame transfer matrix (Eq. 3.23). Its expression reads

$$T_{22} = \frac{\hat{u}_4}{\hat{u}_3} = 1 + \left(\frac{T_4}{T_3} - 1\right)\left(e^{-i\omega\tau_t}e^{-0.5\omega^2\sigma_t^2} - e^{-i\omega\tau_\phi}e^{-0.5\omega^2\sigma_\phi^2}\right), \quad (4.3)$$

where τ_t and σ_t are the mean turbulent time delay and standard deviation, respectively, and τ_ϕ and σ_ϕ the mean fuel convective time delay and standard deviation, respectively. This definition is only valid when a technically feasible flame with a choked fuel injection is considered. If the fuel injection is not choked, then the last term of Eq. 4.3 would vary slightly in amplitude and phase and the element T_{21} of the flame transfer matrix (Eq. 3.24) would not be equal to zero. If a perfectly premixed flame is considered, the contribution of the fuel convection of Eq. 4.3 drops toward zero, as the convection time increases toward infinity.

To investigate the impact of changes in the convective time delays or more generally in the RTD on the system stability, the convective time delay is expressed as $\tau_\phi = \tau_{xL} + \tau_t$ and $\sigma_\phi^2 = \sigma_{xL}^2 + \sigma_t^2$. This definition splits the total convective time delay into a purely convective part, which takes place, for example, inside the burner, down to the position $x = xL$, very close to the burner outlet, and another part which is a function of the flame location at the burner outlet. The proposed model assumes that the equivalence ratio fluctuations at the burner outlet travel with the same velocity and over the same distance as the purely turbulent fluctuations from Eq. 4.3. This is not necessarily the case in real burners, as the vortex speed may be lower than the mean flow speed. However, it satisfies the relationship $\tau_t < \tau_\phi$ which could be experimentally measured on a similar burner [SBFP04].

The stability analysis of the system is performed by analyzing the eigenvalues of the resulting system matrix. The influence of the variation of the mean convective time delay and its relative spreading on the stability boundaries of the long combustor are shown in Fig. 4.3. The plot on the left represents the expected frequency (the real part of the eigenvalue) while

the one on the right displays the growth rate of the eigenvalue (imaginary part of the eigenvalue). A negative growth rate indicates an unstable mode of the system. In these plots, the convective time delay is normalized by the mean bulk residence time in the burner, for the operating condition considered (OPA, $(\dot{m}_{air}, \phi, T_{pre})$=(220 kg/h, 0.555, 423 K)), $\tau_{xL,ref} = 0.00479$ s, and the values of the turbulent parameters are constant and equal to $\tau_t = \tau_{ref} = 0.00479$ s and $\sigma_t/\tau_t = 0.3$. The resulting mean total convective time delay τ_ϕ is then equal to the time delay obtained from FTF measurements at these operating conditions.

The results show that a decrease in the convective time delays $\tau_{xL}/\tau_{xL,ref} < 1$ or/and an increase in the spreading of the distribution are beneficial for the combustor stability. Hence a reduction in the convective time delays is expected to have a stabilizing effect on the combustor for the present geometry if the flame position remains unaffected by fuel distribution changes. The latter is not true in general and in particular in the burner investigated. For this reason, a simulation was performed with a shorter turbulent time delay ($\tau_t = \tau_{ref}/2$). The results produced a similar trend.

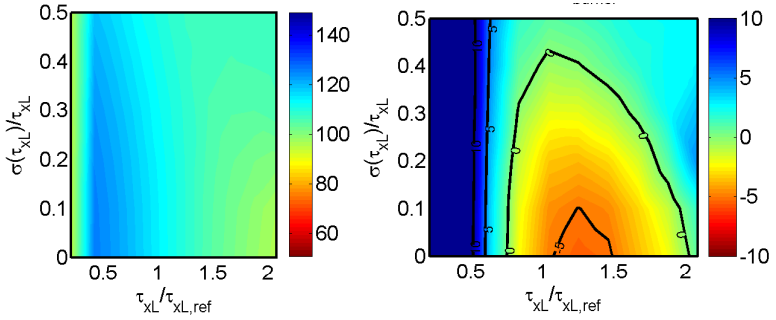

Figure 4.3: Stability map of the combustion chamber (L_{cc}=1.57 m, 200 mm outlet) showing the effect of adjusting the convective time delay and its spreading on the combustor stability. Left picture: frequency in Hz of the quarter-wave mode. Right picture: growth rate of the mode; a negative value indicates an unstable system. Operating point A: $\dot{m}_{air} = 220$kg/h, $\phi = 0.555$, $T_{pre} = 423$ K.

Regarding the short combustion chamber, however (L_{cc}=0.66 m), a decrease in the mean convective time delay will worsen the combustor stability

(Fig. 4.4). This is consistent with the increase in the resonance frequency of the system. Furthermore, if the spreading of convective time delay is in general beneficial for the stability of the combustor, the results obtained with the short combustor indicate that an increase in the convective time delay spreading may have a negative effect on the stability of the combustor ($\tau_{xL}/\tau_{xL,ref} \in [1.2, 2]$), with a risk that the system becomes unstable.

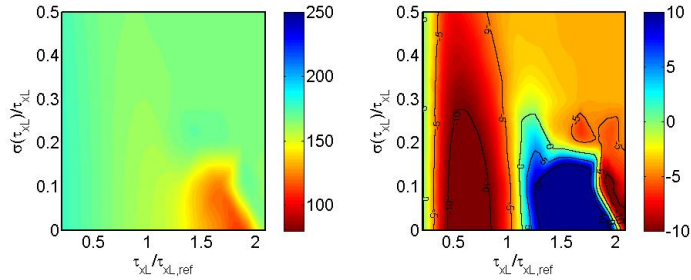

Figure 4.4: Stability map of the combustion chamber (L_{cc}=0.66 m, 200 mm outlet) showing the effect of adjusting the convective time delay and its spreading on the combustor stability. Left picture: frequency of the quarter-wave mode. Right picture: growth rate of the mode; a negative value indicates an unstable system. Operating point A: $\dot{m}_{air} = 220$kg/h, $\phi = 0.555$, $T_{pre} = 423$ K.

These results confirm that optimal fuel injection is mostly dependent on the boundary conditions of the system.

4.2 Combustion control using staged injection

4.2.1 Characterization of the standard burner

The response of the burner with the mounted secondary injector I00 (see geometry in Fig. 3.5) is presented at this stage using the standard fuel injection only ($\alpha = 1$) for different operating conditions. Figure 4.5 and Fig. 4.6 illustrate the pressure pulsations and NO_x emission maps as a function of

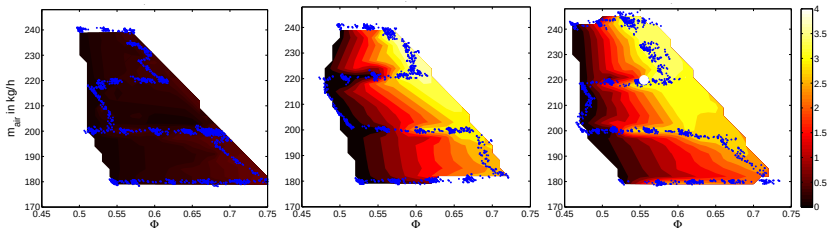

Figure 4.5: RMS value of the pressure pulsations (a.u.) for the standard burner injection with resonance pipe (L_{cc}= 1.57 m) at three preheating temperatures T_{pre}=295.5 K, 360.5 K, 423 K (from left to right). The operating point A is marked with a white circle.

the equivalence ratio ϕ and the combustor air mass flow $\dot{m}_{air}$ at three preheating temperatures. The combustor is equipped with a resonance tube (L_{cc}=1.57 m) and the pressure oscillations are recorded at x=-411 mm. The air mass and fuel mass flow rates are varied while the preheating temperature remains constant. The points in blue depict the effectively recorded points as pressure and NO_x emissions are continuously recorded while the fuel and air mass flows are continuously varied.

Whereas the combustor is stable with the lowest preheating temperature, it becomes unstable when the temperature is increased to $T_{pre} = 360.5$ K or $T_{pre} = 423$ K. The high pressure pulsations of the operating point A, which was simulated in the previous section and which is marked with a white circle in Figure 4.5 and Fig. 4.6, confirms the results of the simulation, which predicted an instability. When the combustor is unstable, an increase of the equivalence ratio augments the amplitude of the pressure pulsations, as a result of the increase of the heat release fluctuation amplitude, as predicted by the wave equation with heat release Eq. 2.113. For all the unstable points, the dominant frequency is close to 100 Hz, corresponding to the 1/4 wave mode of the downstream side of the combustor. Furthermore, lean mixtures produce, as expected, less NO_x emissions. However, when strong pressure pulsations take place, as it is the case when the preheat temperature is increased from $T_{pre} = 295.5$ K up to $T_{pre} = 360.5$ K, NO_x emissions increase.

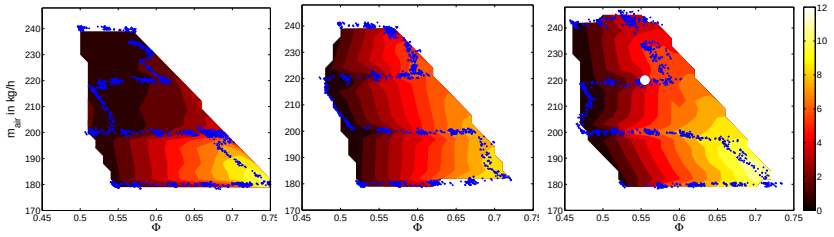

Figure 4.6: NO_x emission map (in ppm, dry, 15% O_2) of the standard burner injection with resonance pipe (L_{cc}= 1.57 m) at three preheating temperatures T_{pre}=295.5 K, 360.5 K, 423 K (from left to right). The operating point A is marked with a white circle.

4.2.2 Staged injection : control of an unstable case

The unstable operating point A, defined with the triplet ($\dot{m}_{air}, \phi, T_{pre}$)= (220 kg/h, 0.555, 423 K), with the long combustor, was selected and the effect of a variation of the fuel distribution (α,β) on pressure pulsations and NO_x emissions is shown in Fig. 4.7. Clearly, the changes in the fuel distribution allow the combustor to stabilize when $\alpha \to 0$, i.e., when the staged injection becomes dominant. The results are even better when $\beta \to 0$, i.e. when the fuel is injected closer to the burner outlet, resulting in shorter fuel convective time delays. This corresponds to the behavior predicted by the thermoacoustic simulation. The power spectra of the unstable and stabilized cases presented in Fig. 4.8 confirm that the instability completely disappears when the fuel injection is properly set.

As shown in Fig. 4.7, there is a small correlation between the pressure amplitude and NO_x emissions. A strong decrease in NO_x emissions occurs when the combustor is stabilized, in particular when moving from the upper-right corner to the lower-left corner of the map. The axial Strouhal number of the instability ranges from St=0.42 for a bulk velocity of 15 m/s to St=0.8 for a bulk velocity of 8 m/s. Assuming a Péclet number of $Pe \approx 40$, the one-dimensional mixing model presented in Sec 2.3.4 indicates that the relative temporal fluctuations of the spatially averaged concentration at the burner outlet will remain high ($\approx$ 50% of the fluctuation amplitude at the inlet). Furthermore, the work performed by Chishty [CY08] indicates that though the pulsation amplitude may damp

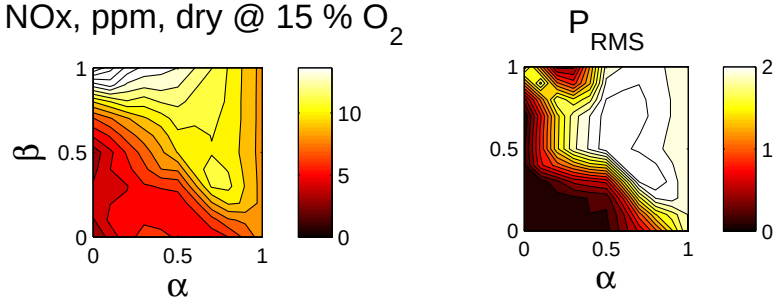

Figure 4.7: Impact of the fuel distribution on the NO_x emissions and pressure pulsations in the combustion chamber (fuel injector I00 combined with standard injector, operating point A, L_{cc}= 1.57m)

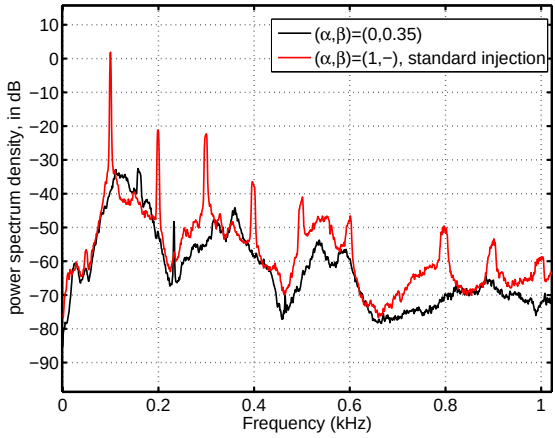

Figure 4.8: Spectrum of the unstable standard injection compared with the stable injection (α, β)=(0,0.35) (fuel injector I00 combined with standard injector, operating point A, L_{cc}= 1.57m)

the relative FAR fluctuations, the absolute amplitude of the fluctuations always increases with increasing velocity fluctuation amplitude. The total unmixedness reaching the flame then increases and so do the NO_x emissions. This explains the positive effect of a stabilization of the combustor

on the unmixedness and resulting NO_x emissions when such low instability frequencies are involved.

4.2.3 Performance of the staged injection with stable combustor

The ability of the injector I00 to stabilize the combustor and produce low NO_x emissions has thus been assessed for one operating point with one combustor geometry. Now, the quality of the new injection with respect to the NO_x emissions must be compared to the one of the standard injection in a stable combustor. The short combustor was used (L_{cc}=0.66 m) and low pressure pulsations were ensured through the use of an unsealed combustion chamber. The results presented in Fig. 4.9 show that the injection (α,β)=(0,0.5) results in slightly higher NO_x emissions than the standard fuel injection. Nevertheless, this small NO_x penalty is compensated by the possibility of stabilizing the combustor. Furthermore, it is expected that slight modifications of the injector design may be able to bring the NO_x emissions back to the level of the standard fuel injection. Finally, the map of the mean OH* chemiluminescence of the flame recorded with the photomultiplier suggests that the chemiluminescence signal may be used to monitor the NO_x emissions.

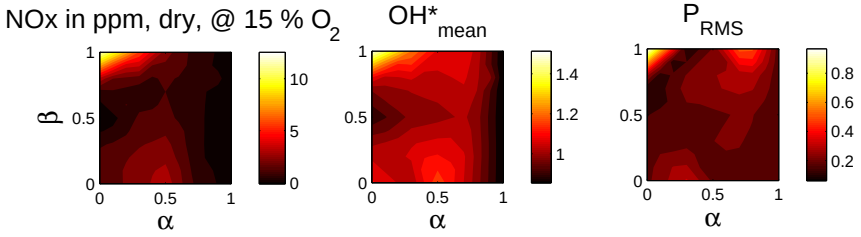

Figure 4.9: Emission, mean OH* chemiluminescence and stability map (fuel injector I00 combined with standard injector, operating point A, L_{cc}=0.66 m but unsealed combustion chamber to suppress 1/4 wave mode)

The possibility of controlling the pressure pulsations and NO_x emissions without strong NO_x penalties has been already demonstrated here. However, a better understanding of the mechanisms occurring in the combustor is needed to model and predict the behavior of the test rig. This starts with a characterization of the flow and additional scalar fields of the burner presented in the next section.

4.3 Flow and scalar fields

4.3.1 Characterization of the standard burner flow field

4.3.1.1 Flame shape

The mean velocity field at the burner outlet, presented in Sec. 2.2.1 exhibits a strong non-axisymmetric shape. This asymmetry induces an asymmetry in the flame shape as shown by the average OH* chemiluminescence image recorded from two viewing angles with respect to the burner (Fig. 4.10). The flame structure is even highly three-dimensional, with a side which dominates the heat release. Similar flame shapes have been obtained by other authors from visualization of the same burner type [GS07] and confirm that a full characterization of the reacting flow would require measurements in different streamwise planes.

4.3.1.2 Cold flow structure

Swirling flows with strong recirculation zones exhibit strong coherent structures which affect the turbulent flow field and subsequently the heat release. In this section, LDA and PIV measurements performed at the burner outlet to capture and quantify the coherent motion are described. For these measurements the outlet area is equal to the water test rig cross-sectional area of 400 x 400 mm^2. First, PIV measurements triggered by the hydrophone signal are performed as described in Sec. 3.5.1. The data is expressed as the azimuthal vorticity Ω defined as

$$\Omega = \frac{\partial u_x}{\partial r} - \frac{\partial u_r}{\partial x} \tag{4.4}$$

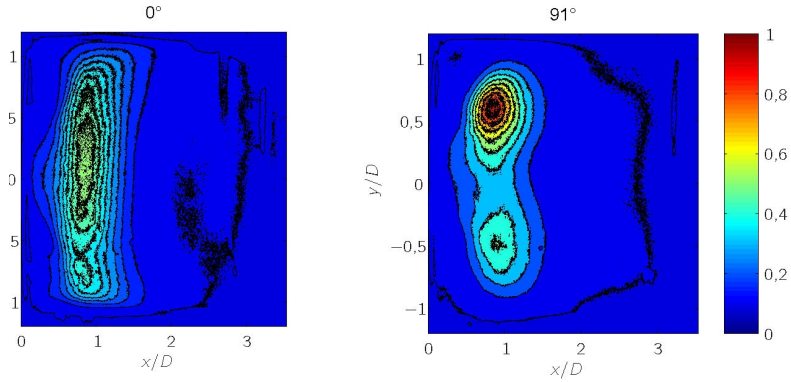

Figure 4.10: Normalized and averaged OH* chemiluminescence images of the standard fuel injection for two viewing angles of the camera (0 and 91 degrees in the left and the right images respectively) showing the non-rotational symmetry of the flame as well as an asymmetry in the heat release distribution. The angle corresponds to the angle between the camera viewing axis and the slot plane of the burner.

with r being the radius from the flow centerline. This definition is suitable for the characterization of rotational systems, as a rotational structure centered on r/D=0 will have the same vorticity sign (and hence the same color in the color plots) in the positive ($z_b/D > 0$) and negative ($z_b/D < 0$) half-axial planes.

Four of the eight phase angles acquired, which are presented in Fig. 4.11, clearly depict the streamwise evolution of a helical structure. Indeed, the image at a phase angle of 0° appears to be the axially symmetric reflection of that at a phase angle 180°. This helical structure is composed of two counter rotating vortices which evolve downstream as the phase angle increases. Measurements performed with the LDA shows that the normalized frequency of the helical structure meets the condition $St \approx 1$. As the helical structure could be detected at the burner outlet, the question of what happens in the slot needs to be answered.

To this end, LDA measurements are performed at slot 1 at the axial positions illustrated in Fig. 3.7. Then, the complete system hydrophone/burner is rotated by 180° allowing access to the second slot. The power spectrum

densities presented in Fig. 4.12 show that an oscillation at the same frequency is present within the slots. This oscillation can be found back near the burner apex (x_E/D=-1.2). Further, the local relative amplitude of the coherent azimuthal velocity oscillation $\tilde{u}_t/\overline{u}_t$ in both slots is plotted as a function of axial position. The relative amplitude of the fundamental frequency is calculated from the amplitude of the FFT peak divided by the mean azimuthal velocity (Eq. 3.27). This amplitude increases as a fourth power of the axial position, but still remains lower than the amplitude observed in the shear layer at position G ($x/D \approx 0.2$).

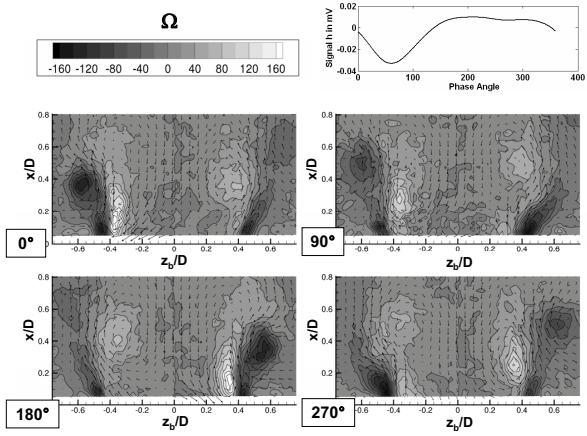

Figure 4.11: Phase-averaged color plots of the azimuthal vorticity Ω (in s^{-1}) in the (x_b,z_b)-plane of the unforced flow which provides evidence of the natural helical mode. Four phases of the hydrophone signal (top right) are used to trigger the acquisition. The arrows represent the velocity vectors. Unconfined flow

The evolution of the phase shift $\angle\varphi$ between the azimuthal velocities in the two slots and the hydrophone is shown in Fig. 4.13. A phase shift of about 180° is visible, confirming the helical nature of the oscillations in the burner slots. This plot also allows the axial wave length λ of the instability inside the burner to be calculated, and this is estimated to be $\lambda = 2.25D$. As a consequence of the velocity decrease downstream of the dump plane, this wavelength decreases down to $0.5D$ at the burner outlet (Fig. 4.11, 90°angle) before the structure breaks up.

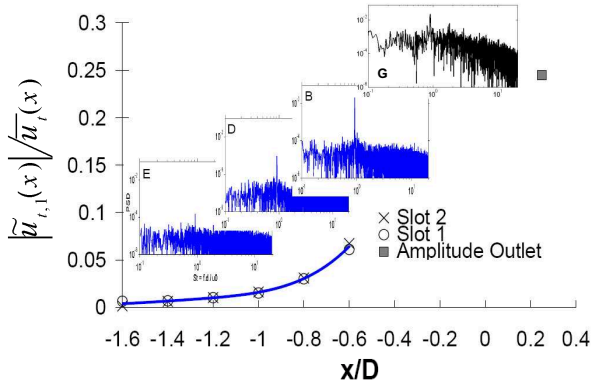

Figure 4.12: Relative oscillation amplitude of the natural frequency for u_t over the axial position for the unforced flow. Spectrum of the signal at the different locations ($x_E/D = -1.2$, $x_D/D = -1$, $x_B/D = -0.6$ and shear layer G) are shown. A fourth-order polynomial fits the amplitudes of slots 1 and 2, unconfined flow

The sign of the helical mode is determined by introducing a second hydrophone probe. One hydrophone (h_2) is fixed over slot one, while the angle β of the other hydrophone (h_1) is varied around the circumference of the burner (see Fig. 4.14). The cross-correlation $R_{h_1h_2}$ of the two signals gives the resulting time lag and hence phase lag $\angle_{h_1h_2} = \angle_{h_1} - \angle_{h_2}$ as a function of the angle β. Figure 4.14 shows that both angles have the same sign and, given the definition of $R_{h_1h_2}$ (Eq. 2.10), this means that the signal h_1 precedes the signal h_2 when $\beta \in [0, 180]$ and follows h_2 when $\beta \in [-180, 0]$. The helix is rotating in the same direction as the swirling motion, which is negative when looking at the coordinate system in Fig. 4.14 (left handed). Because the helical structure is traveling downwards with increasing phase angle in Fig. 4.11, the winding of the helix is right handed. The sign of the resulting mode is then positive (m=1), confirming the results of the LES simulation on a geometrically similar burner model reported by Duwig et al. [DFL+07]. The final wave equation of the helix reads

$$\varphi_{hel}\,(x, \theta, t) = (kx + m\theta - \omega t)\ , \tag{4.5}$$

with $k = 2\pi/(2.25D)$, $m = +1$, and $\omega = 2\pi St_n U_0/D$ [FHS06].

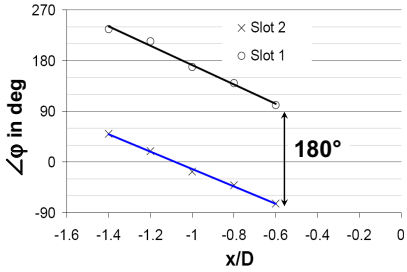

Figure 4.13: Phase relationship between the tangential velocity u_t and the hydrophone signal h within the slots 1 and 2 of the burner as a function of the axial position x/D for the unforced flow, unconfined flow

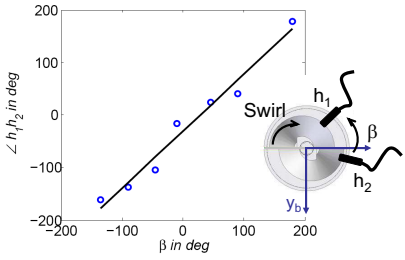

Figure 4.14: Phase difference recorded by the two hydrophones with variation of their relative angle β, indicating that the structure rotates with a swirling motion, unconfined flow

Various different mechanisms may be responsible for the oscillations encountered in the slot, either associated with the local effect of the helical structure on the local pressure loss in the slot or the change in nature of the flow from supercritical to subcritical [LFG+09]. The main fact is that these oscillations induce velocity fluctuations which may, as shown later, lead to concentration fluctuations at the burner outlet and influence the mixing quality.

4.3.2 Burner flow and scalar fields with staged injection

4.3.2.1 Burner flow field with modified injections

The influence of the different burner models and of the staged injector I00 on the flow field has to be quantified. Figure 4.15 compares the mean axial and tangential velocity profiles of the two burners (one in perspex; one in steel, with a short lance) used during the mixing and velocity experiments in the water test rig. The axial and tangential velocities of the steel (blue and ○) and perspex (black and +) burners are very similar, with slight

differences in the central recirculation zone, confirming that the model and the original steel burners are almost identical regarding the velocity field they generate. The perspex burner is thus a good replication of the standard steel burner. When the staged injector I00 is added upstream of the slots of the steel burner (red and □), it increases the maximum axial velocities by approximately 15% and slightly widens the internal recirculation zone. The general velocity field is close to the standard velocity field, so that the influence of the staged injector I00 can be considered marginal.

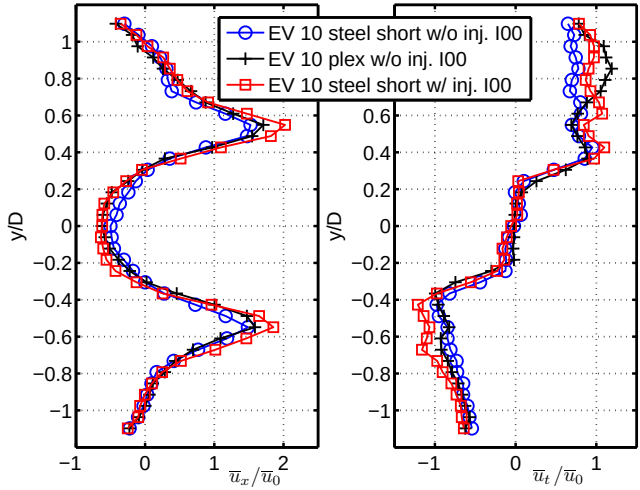

Figure 4.15: Radial velocity profiles ($x = 0.25D$) of the axial and tangential mean velocities $\overline{u}_x$ and $\overline{u}_t$ for the short stainless burner, the short stainless burner with staged injector I00, and the plexiglass model, $Re = 3.5 \times 10^4$. LDA data, outlet diameter 200 mm, no fuel injection.

Further measurements also showed that the mean and turbulent flow fields are weakly dependent of the Reynolds number for $Re > 20 \times 10^3$, thus ensuring the transferability of results to other operating conditions.

4.3.2.2 Scalar mixing at the burner outlet

By changing the fuel distribution within the burner, the mixing profile at the burner outlet varies strongly. Figure 4.16 illustrates these variations when the fuel injection is modified from fully upstream (α, β)=(0, 1) to mostly downstream (α, β)=(0, 0.17). Using an upstream dominated fuel injection enriches the central zone of the burner while injection downstream enriches the outer zone. The global probability density function (i.e., the PDFs presented are not the PDFs of the time-averaged images shown in Fig. 4.16 but are generated from all the instantaneous images of the mixing process) shown below the averaged images fit relatively well with a beta-function, which is typically used to model binary mixing processes.

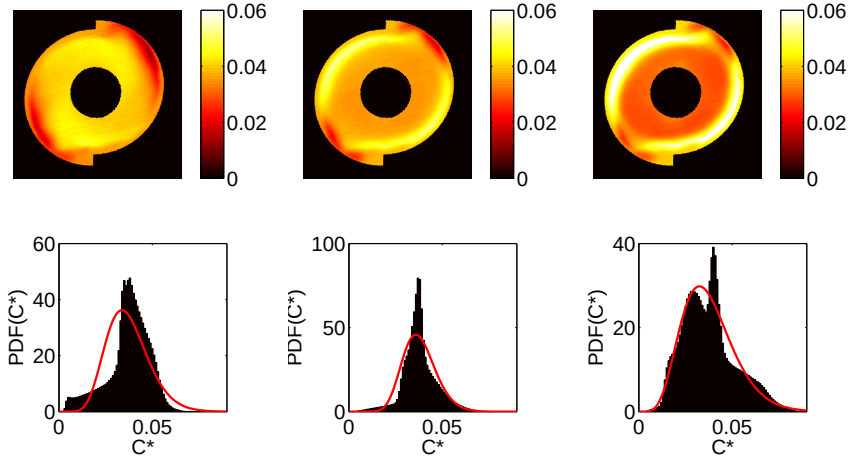

(a) (α, β)=(0,1) (b) (α, β)=(0,0.5) (c) (α, β)=(0,17)

Figure 4.16: Top: Normalized concentration $C*$ for different injection configurations recorded with HS-LIF at $x = 5\,\text{mm}$. A filter (black zones) is applied to exclude the recirculation zones from the processing. Bottom: Corresponding global probability density function with beta-function fit.

With Eq. 2.77, the equivalence ratio PDFs are obtained (Fig. 4.17). They show that the equally distributed injection deviates considerably from the ideal mixture. In particular, premixing at the burner outlet is not complete and some improvement of the mixture quality may be achieved.

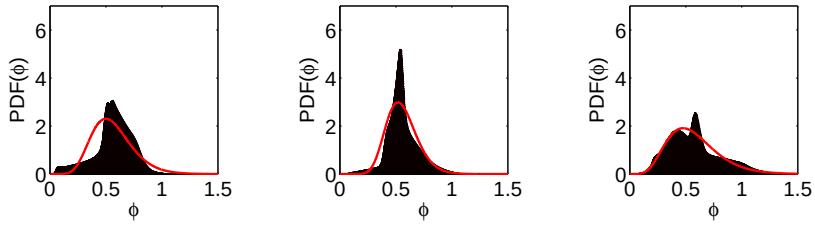

(a) (α, β)=(0,1) (b) (α, β)=(0,0.5) (c) (α, β)=(0,17)

Figure 4.17: Corresponding global probability density function of the equivalence ratio ϕ. Operating point A. The red curve corresponds to the transformation of a beta function fitting performed with the fuel mole fraction Y_f.

4.3.2.3 Helical structure and scalar mixing

The velocity fluctuations induced by the helical structure at the slot entrance induce coherent oscillations in the scalar mixing field. The change of the fuel distribution not only allows the spatial fuel repartition to be adjusted before it reaches the flame, but, combined with the helical velocity fluctuations, may also enhance or damp the temporal scalar fluctuations. Figure 4.18 shows the impact of four fuel distributions on the temporal oscillations of the spatially-averaged concentration at the burner outlet. The dominant peak occurs at twice the rotation frequency of the helical structure, which is a consequence of the π rotational invariance of the burner. When extreme injection is used, the fluctuation amplitude of the spatially-averaged concentration recorded at the burner outlet is maximal, reaching a relative oscillation amplitude of 5.7% for the distribution (α, β)=$(0, 1)$, while it is strongly damped down to 1.3% when the

distribution (α, β)=$(0, 0.5)$ is used. Without the staged injection, a relative oscillation amplitude of just 0.57% is achieved. Even if relatively low, these oscillations may be able to trigger combustion instability. In particular, it should be noted that the local concentration fluctuations can be much higher close to the slots.

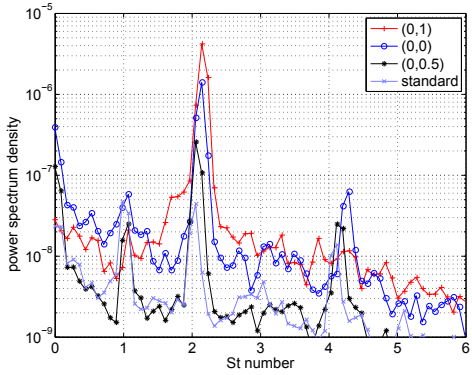

Figure 4.18: Influence of the fuel distribution on the power spectrum of the spatially-averaged concentration fluctuations $\langle C^* \rangle'$ recorded 5 mm downstream of the burner outlet with HS-LIF (C^*_∞=0.035)

The use of the simultaneous PIV/LIF measurement technique allows the interaction between the scalar and velocity fluctuations to be quantified. For the upstream staged injection $(\alpha, \beta) = (0, 1)$, the analysis of the normalized radial $\overline{v^{*\prime} C^{*\prime}} = \overline{v' C'}/(U_0 C_\infty)$ and axial $\overline{u^{*\prime} C^{*\prime}} = \overline{u' C'}/(U_0 C_\infty)$ turbulent scalar transport terms presented in Fig. 4.19 and Fig. 4.20 respectively clearly shows that the velocity and concentration oscillations correlate strongly at the burner outlet. The results show qualitatively the same trends observed with a large eddy simulation performed by Flohr at al.[FSP02] : the radial scalar flux is directed toward the center of the flow for small radial positions ($r = |y/D| < 0.35$) and toward the outer wall for higher radial values ($0.45 < r = |y/D| < 0.35$). The turbulent axial flux is directed in the downstream x-direction on the inner and outer sides of the conical jet.

The consequences of these results for the modeling of the mixing inside the burner are multiple. Not only the turbulence but also the coherent motion

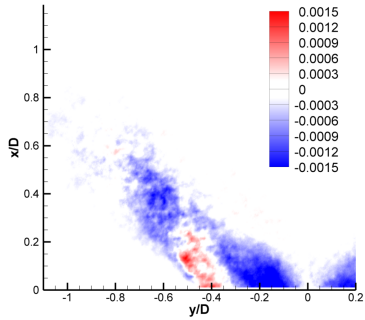

Figure 4.19: Dimensionless radial scalar flux $\overline{v^{*\prime}C^{*\prime}}$ taken in an axial plane perpendicular to the slot plane at the burner outlet. Upstream injection $(\alpha, \beta) = (0, 1)$.

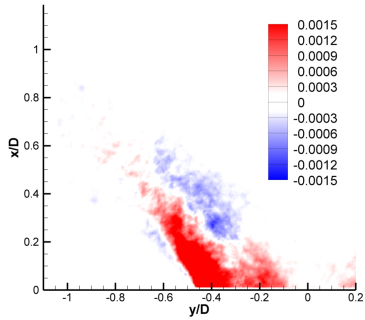

Figure 4.20: Dimensionless axial scalar flux $\overline{u^{*\prime}C^{*\prime}}$ taken in an axial plane perpendicular to the slot plane at the burner outlet. Upstream injection $(\alpha, \beta) = (0, 1)$.

should be modeled, especially if one is interested in statistical moments of an order higher than two. The presence of these coherent oscillations will greatly contribute to an increase in the fuel/air unmixedness when compared to mean field scalar models, due to the increased temporal fluctuations. This may be important when trying to obtain a model of the emissions or combustor stability with a temporal resolution close to that needed to describe the coherent motion. However, in the present work the aim is to control combustion with frequencies more than one order of magnitude lower than the helical oscillation frequency. Therefore, a mean field mixing model with a mixture probability density function should be well suited to characterizing the changes induced by slow changes in the mixing profile. The impact of the coherent motion on the mixing profile or the residence time may thus be corrected a posteriori to improve the accuracy of the results. Accordingly, we go on to develop a mean flow mixing model of the burner to characterize the convective time delays as well as the mixing quality changes. Prior to this, however, the possibility of using cold flow measurement to predict the combustion behavior must be assessed.

Chapter 5

Flow similarity and scaling laws

5.1 Burner flow similarity in air and water

5.1.1 Mean and turbulent flow fields

Before quantitative information is extracted from measurements with the water test rig to predict the reacting flow behavior, it is necessary to ensure that the water and non reacting air test rigs deliver similar results. First of all, both test rigs must present the same flow field and consequently similar velocity profiles. This is demonstrated by the axial velocity profiles shown in Fig. 5.1 and radial velocity profiles of Fig. 5.2. These figures compare measurements performed in water (Re=3.9 $\times$ 10^4), and in air without preheating (Re=4.8 $\times$ 10^4) using SiO_2 oil droplets as a seeder and with preheating (Re=3.9 $\times$ 10^4) using solid particles SiO_2 for seeding. The velocity profiles of the three cases match very well, confirming also that for the investigated range the flow is weakly Reynolds-number dependent. The slight differences appearing in the mean velocities can be explained by some small geometrical differences between the two test rigs and the strong light reflections in the air rig, even though background correction is used. The degree of turbulence Tu of the measurements taken in water is greater than in the combustion chamber (Fig. 5.3). This discrepancy is mainly due to the higher degree of turbulence of the water test rig, which showed higher mean flow fluctuations ($\pm$3-4% versus less than $\pm$1% in the air rig).

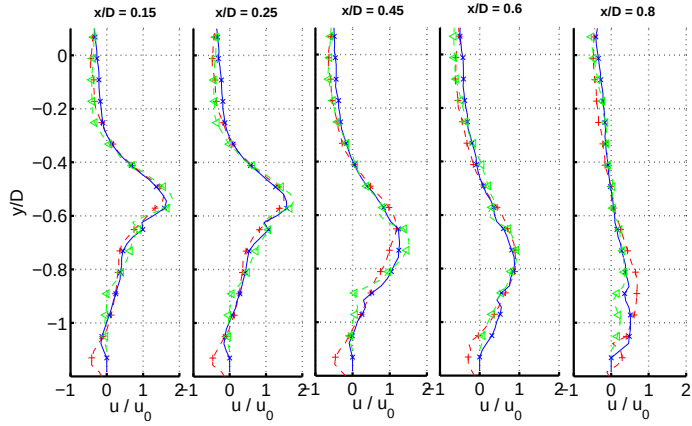

Figure 5.1: Half-plane axial velocity line plots at 5 axial positions. PIV measurements in water (+, Re=3.9 × 10^4) and in air with oil seeding (×, Re=4.8 × 10^4), with SiO_2 seeding (◁, Re=3.9 × 10^4).

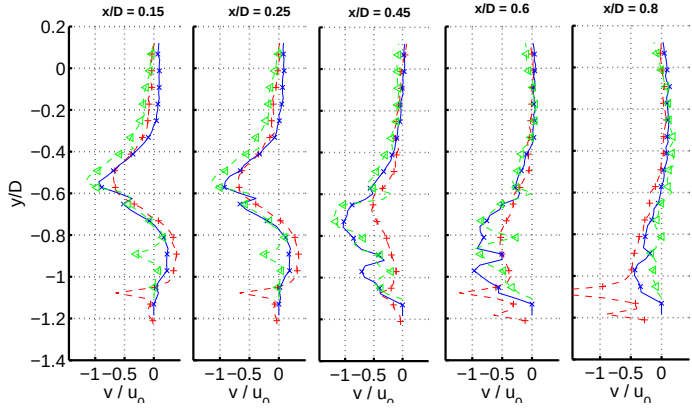

Figure 5.2: Half-plane radial velocity line plots at 5 axial positions. PIV measurements in water (+, Re=3.9 × 10^4) and in air with oil seeding (×, Re=4.8 × 10^4), with SiO_2 seeding (◁, Re=3.9 × 10^4).

5.1.2 Scalar mixing

To compare the scalar mixing between the test rigs, quantitative Mie scattering measurements are performed at the burner outlet in the combustor,

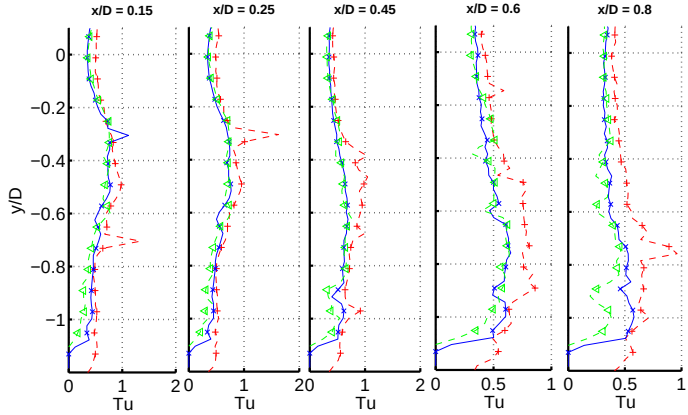

Figure 5.3: Half-plane degree of turbulence $Tu = 1/u_0\sqrt{(u_x'^2 + u_r'^2)/2}$ line plots at 5 axial positions. PIV measurements in water (+, Re=3.9 × 10^4) and in air with oil seeding (×, Re=4.8 × 10^4), with SiO_2 seeding (◁, Re=3.9 × 10^4).

in a similar way to the LIF experiments. The liquid seeding (oil droplets of DEHS, ⌀ ≤ 1μm) is added whether to the fuel injection line to assess the mixing at the burner outlet or well upstream of the burner in the main flow to record the homogeneous picture. For these experiments, the methane of the fuel injection was replaced by air. According to the data sheet, the seeding mass added to the gas is negligible and the jet-to-crossflow momentum is calculated from pure air mass flow.

To ensure a sufficient signal-to-noise ratio, the exposure time of the camera in the combustion chamber is identical to the exposure time in the water test rig. However, as the velocities differ by a factor of more than 15, the ratio of exposure time τ_{cam} to the mean residence time of the flow in the laser plane, τ_{flow}, is much higher in the air than in the water ($\tau_{cam}/\tau_{flow} = \Delta t_{shutter}(u_0/\Delta x_{Laser}) \approx 56$ in the combustion chamber and $\tau_{cam}/\tau_{flow} \approx 1.8$ for the water test rig measurements). This leads to a strong smearing of the temporal fluctuations for the recordings performed in the air and means that only the average concentration profiles can be compared.

The normalized average concentrations recorded at the burner outlet for

the upstream fuel injection for the two test rigs are displayed in Fig. 5.4. To allow for a direct comparison, the concentrations are normalized by their perfectly mixed concentration $Y^*_{f,\infty}$ and C^*_∞ respectively. The spatial fuel distribution is similar in the two test rigs with slight variations in the position of the extremes of concentration. The mixing processes in water and air are thus qualitatively similar as expected. However, the advantage of a LIF measurement over the Mie scattering technique is clear as the boundaries of the burner do not interfere with the results in the water test rig.

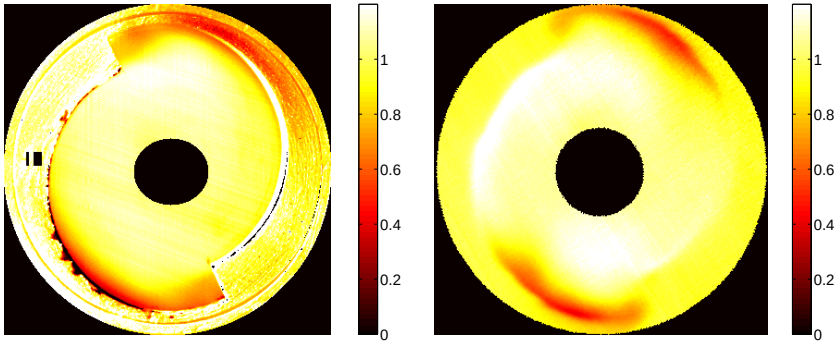

Figure 5.4: Concentration slices at the burner outlet ($xL = 5\,\text{mm}$) in the combustion chamber (left, $\overline{Y}^*_f(i)/Y^*_{f,\infty}$, Mie scattering) and in the water test rig (right, $\overline{C}^*(i)/C^*_\infty$, HS-LIF) for the upstream injection with injector I00, (α, β)=$(0, 1)$ and identical jet-to-crossflow momentum ratio (J=17).

Given that the long relative camera exposure time, as well as the high level of local noise due to reflections in the air, do not allow the global mixture PDF in the combustion chamber to be captured, it is difficult to answer the question concerning the similitude of the mixing qualities in air and water. Therefore, an analogy with the measurements of Miller [Mil91] is used. For this, the mixing quality at the outlet of the burner in the water test rig is investigated for different Reynolds numbers, holding the jet-to-crossflow momentum constant. The resulting curve presented in Fig. 5.5 shows a very small increase in the mixing quality (or decrease in the normalized variance of the concentration fluctuations) with the Reynolds number. The slope

of the curve is approximately equal to the slope of the curve obtained by Miller (red double arrow), which indicates that the mixing quality is almost independent of the Reynolds number and of the medium considered. This also suggests that the mixing quality is quantitatively similar in air and in water in the present configuration.

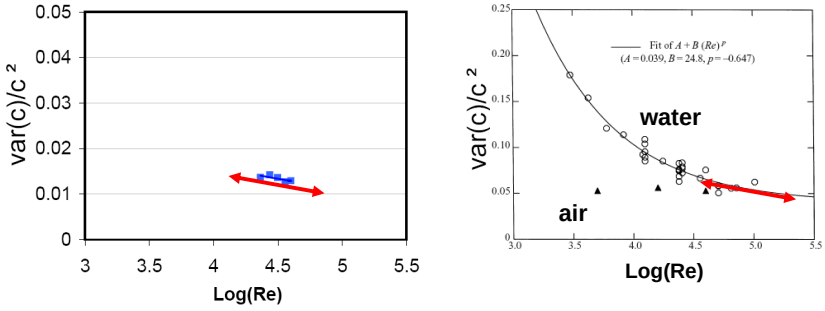

Figure 5.5: Dependence of the normalized scalar variance on the Reynolds number recorded at the burner outlet and at x=5 mm in the water test rig (left). Comparison with the data of Miller taken from [Dim00] (right). See also Fig. 2.17.

5.1.3 Influence of combustion on the mean flow field

A further step consists in determining how strongly the flame influences the flow field. Images of the flame were recorded with the ICCD camera equipped with the OH* bandpass filter. The average emissions of three fuel distributions obtained with the injector I00 are presented in Fig. 5.6. Figures 5.7 to 5.9 illustrate the influence of the fuel distribution and hence of the flame location on the velocity field in the (xy)-plane of the burner. Figure 5.7 displays the velocity field in a two-dimensional plane while Fig. 5.8 identifies the location of the recirculation zone with the isoline of the axial velocity $u = 0$. Finally, Fig. 5.9 shows the axial and radial velocity profiles at selected streamwise locations.

When compared with the cold case of Fig. 5.7(d), combustion with the standard injection does not strongly affect the main features of the flow which are position and width of the recirculation zone and shear layer location.

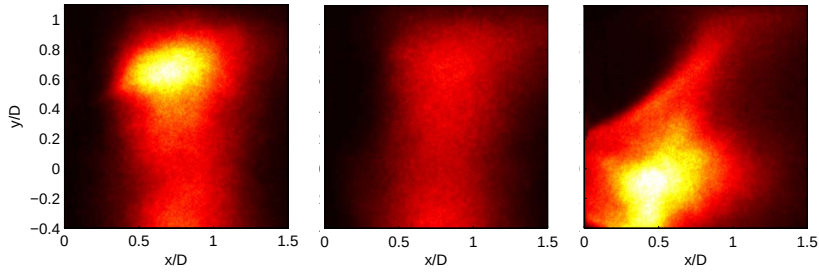

(a) $(\alpha, \beta) = (0, 0)$ (b) $(\alpha, \beta) = (0, 0.5)$ (c) $(\alpha, \beta) = (0, 0.75)$

Figure 5.6: Average OH* chemiluminescence pictures recorded for three fuel distributions, OPA and injector I00

As shown in Fig. 5.9, the velocity profiles of the reacting and cold flows are almost identical immediately downstream of the burner outlet plane (until $x/D < 0.4$). Changing the fuel injection leads to some changes in the flow field: an injection of fuel mostly downstream (injection (α, β)=$(0, 0)$ on Fig. 5.7(a) and Fig. 5.6(a)) slightly widens the IRZ, but the flow field remains fairly similar to the baseline injection; on the contrary, fuel injection located mainly upstream (see Fig. 5.7(c) and Fig. 5.6(c)) leads to an anchoring of the flame inside the burner, widens the angle of the conical jet, and increases the recirculation zone maximal diameter to $1.6D$ (compared to $0.8D$ in the other cases), but also reduces the intensity of recirculation of hot gases in the IRZ. This results in a lower mixing rate of fresh gas and air mixture with the exhaust gas, leading in turn to a higher equivalence ratio at the flame front compared to a flame stabilized at the burner outlet. This flame may thus produces higher NO_x emissions.

Although the calculated degree of turbulence Tu is physically meaningless as no distinction is made between burnt or unburnt gas [PV05], it can be used to qualitatively compare the different injection locations. Figure 5.10 shows that for all the configurations, the turbulent fluctuations are maximal in the inner shear layer of the flow. Consistent with the lower velocities recorded in the inner recirculation zone, the turbulence is lower for the upstream injection (α, β)=$(0, 0.75)$ than for the other cases down to x/D

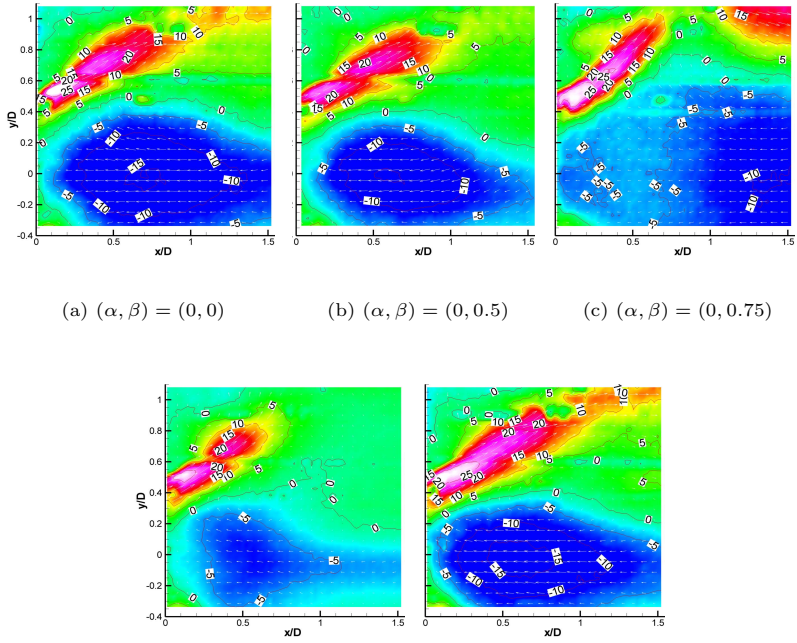

(a) $(\alpha, \beta) = (0, 0)$ (b) $(\alpha, \beta) = (0, 0.5)$ (c) $(\alpha, \beta) = (0, 0.75)$

(d) Cold (e) $(\alpha, \beta) = (1, 0)$

Figure 5.7: Mean velocities in m/s measured with PIV in the (xy)-plane for different fuel injection distributions, 250 snapshots taken for each case, OPA and injector I00

$= 0.7$. When the flame stabilizes outside, the turbulent fluctuations of the reacting flow are similar to ones of the non-reacting case. Above $x/D \geq 1$, this intensity is almost independent of the radius.

5.1.4 Coherent structures and combustion

If the average and turbulent flow fields are similar when the flame stabilizes at the burner outlet, the same behavior is expected for unsteady coherent structures. To investigate this, POD analysis of the PIV snapshots is carried out and the resulting modes of the axial velocity are shown

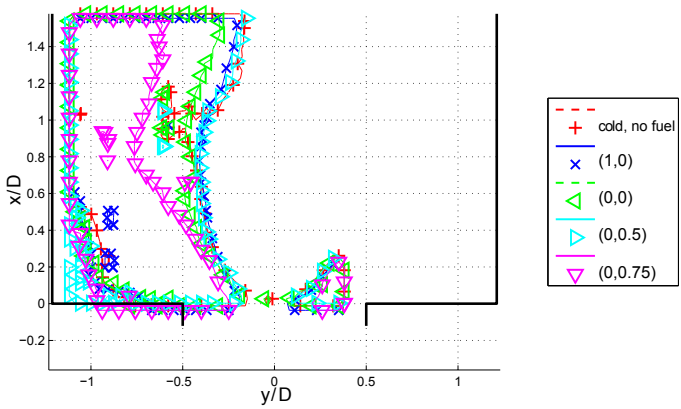

Figure 5.8: Isoline $u = 0$ for the cold (cold, no fuel) and reacting cases (4 other cases) of Fig. 5.7

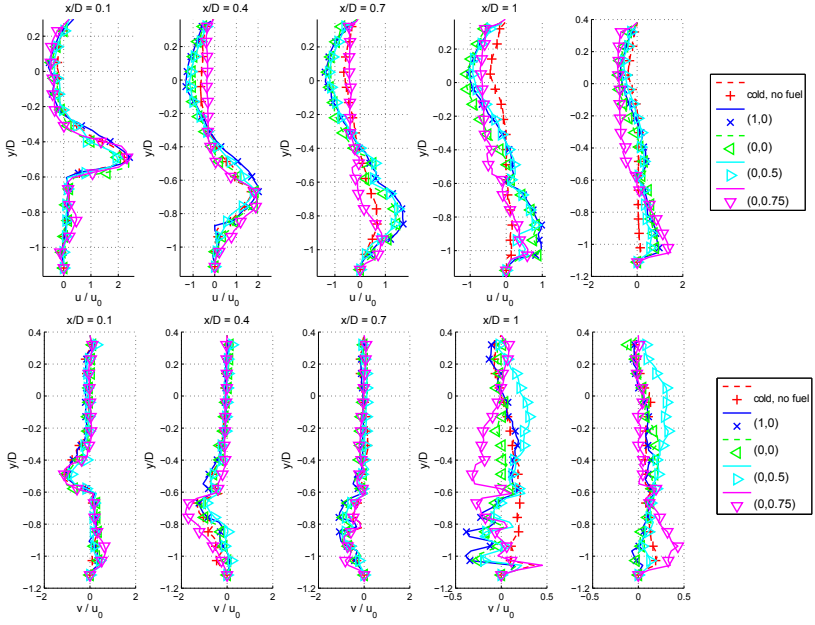

Figure 5.9: Normalized axial (top) and radial (bottom) velocities for the cases of Fig. 5.7.

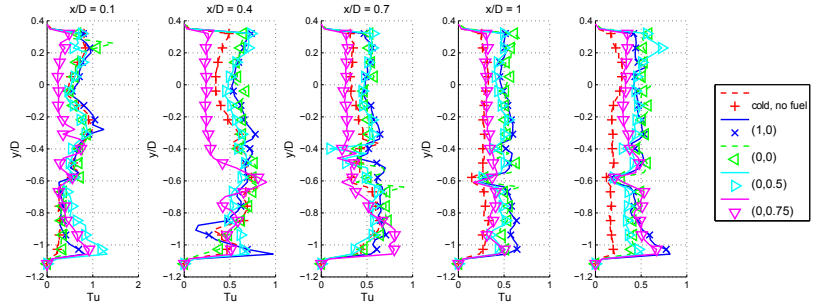

Figure 5.10: Degree of turbulence Tu for the cases illustrated in Fig. 5.7.

in Fig. 5.11. The 6 modes of the non-reacting case and 3 reacting cases corresponding to 3 different fuel injections are represented with a normalized black-and-white scale. Furthermore, the relative energy content (the normalized eigenvalues) of the modes is shown in Fig. 5.12. The field of view of the snapshots is cropped at $x = 70\,\text{mm}$.

It is evident, considering the POD mode shapes, that when the flame stabilizes outside the burner (Fig. 5.11(b) and 5.11(c)), the structures are very similar to the non-reacting cases (Fig. 5.11(a)). The first two modes correspond to the helical structure (antisymmetry with the centerline of the flow) and remain practically unchanged when combustion takes place. Mode 3 remains almost unchanged, while though modes 4 to 6 are less pronounced for the reacting cases, they present strong similarities with modes 4 to 6 of the non-reacting case. Analysis of the radial component of the POD (not shown here) revealed that these lower-energy structures are symmetric and correspond to the vortex shedding created by the dump plane. On the contrary, when the flame stabilizes inside the burner, the coherent mode shapes almost disappear just by the burner outlet and only some minor structures are visible in the shear layer of the flow field. Unfortunately, the chosen camera field of view does not allow to answer the question whether the structure are axisymmetric or not.

As shown in Fig. 5.12 the energy content of the modes is quite similar for the different configurations. Depending on the injection considered, some

modes are slightly damped when compared to the non-reacting cases ($N >$ 3 for the injection (1,0), N=1 and $N >$7 for the injection (α, β)=$(0, 0)$). On the other hand, for the flame anchored inside the burner, the energy content of the modes identified is much lower, confirming the damping effect of this type of flame. These POD results from PIV snapshots thus provide a new insight into the phase-averaged images of the flame OH* chemiluminescence which also revealed the helical structure of the flow field [LLB$^+$10] (Fig. 5.14).

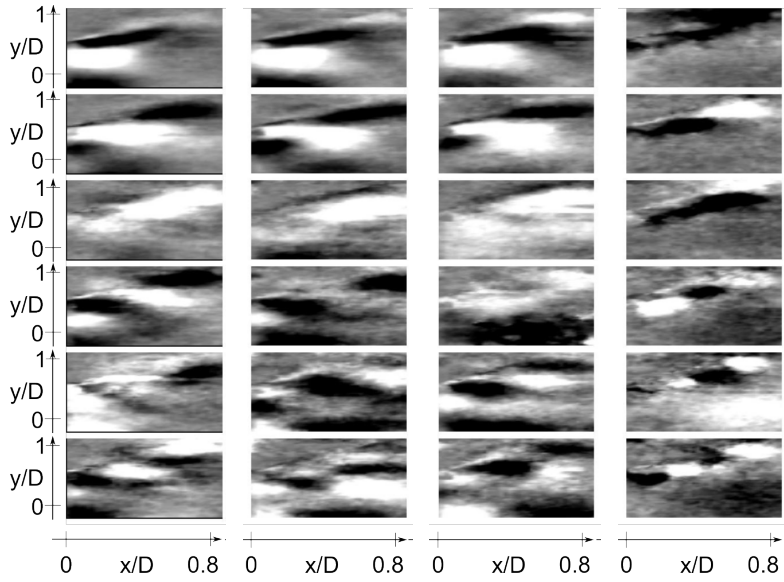

(a) Non reacting (b) (1,0) (c) (0,0) (d) (0,0.75)

Figure 5.11: POD modes of the axial velocity in non-reacting preheated flow (left), reacting standard premix injection (second), reacting downstream injection (third), and reacting upstream injection (right). Modes 1 to 6 from top to bottom.

The similarity of the non-reacting and reacting flow fields is thus mostly dependent on the flame position. When the flame stabilizes at the burner outlet, the dominant helical structure of the flow remains present in the

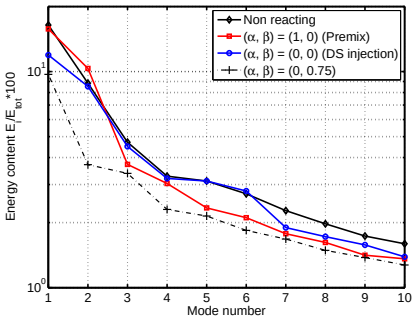

Figure 5.12: Turbulent kinetic energy of the axial velocity of the modes shown in Fig. 5.11

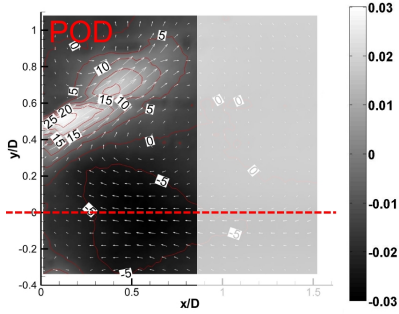

Figure 5.13: Region of interest of the POD modes and corresponding legend of Fig. 5.11

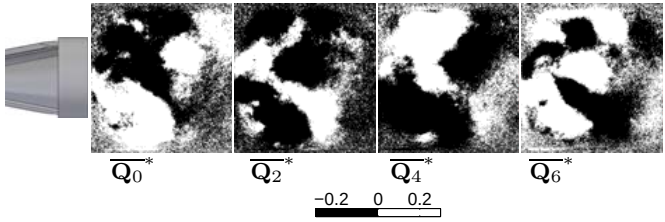

Figure 5.14: Phase-averaged images of the local relative OH* chemiluminescence oscillations at the outlet of the swirl-inducing burner revealing a flapping motion orthogonal to the flow direction, a consequence of the 3D rotating helical structure, operating point A.

flame and its energy content is almost identical to the cold flow case. Cold flow measurements performed just upstream of the flame are thus expected to capture well the flow characteristics upstream of the flame. On the contrary, non-negligible variations between non-reacting and reacting flows occur if the flame is anchored inside the burner.

5.2 Toward the Borghi diagram

The flame of industrial gas turbine burners is characterized by high turbulent Reynolds numbers ($Re_T > 1000$), low Damöhler numbers ($Da < 10$), and Karlowitz numbers higher than 10 [GSJ07]. Predicting the combustion regime of a burner is essential for the choice of numerical models and this is attempted in this section. The main goal is to show that this can be (at least partly) achieved using the non-reacting measurements.

To achieve this, the integral length scales of the burner flow field are estimated from the water test rig with help of PIV and LDA in the (xy)-plane (perpendicular to the slot plane). The PIV results presented are taken immediately after the LDA results to decrease the sources of error. The overlapping of the two measurement planes is achieved with an error of less than 0.5 mm. The axial (Λ^x_{uu}, Λ^x_{vv}) and radial (Λ^y_{uu}, Λ^y_{vv}) length scales are measured with PIV, the axial (Λ^t_{uu}) and azimuthal ($\Lambda^t_{u_t,u_t}$) temporal time scales with LDA. The volume flow through the burner is set to 8.55 m^3/h ($Re = 3.5 \times 10^4$).

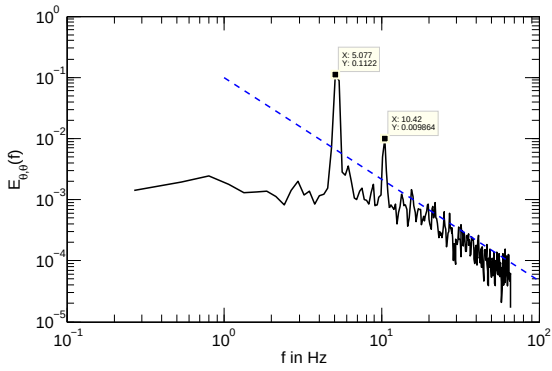

Figure 5.15: The energy spectrum $E_{t,t}$ of the tangential velocity in the shear layer flow ($\boldsymbol{x} = (10, 30, 0)$ mm). The dotted line indicates the -5/3 decay of the inertial range. Perpex burner without additional injector, water volume flow set to 8.55 m^3/h.

5.2.1 Temporal length scales from LDA

A typical LDA spectrum of the tangential velocity recorded in the shear layer at the outlet of the burner ($\boldsymbol{x}$=(10, 30, 0) mm) is shown in Fig. 5.15. The spectrum clearly shows the dominant frequency of the coherent structure around 5.1 Hz as well as its second harmonics around 10.4 Hz. These frequencies are present in most of the region downstream of the dump plane. When normalized, they correspond to the frequency of the helical structure observed in the previous section ($St \approx 1$). At the cut off frequency of 65 Hz, the spectrum is still in the inertial range and the dissipation range cannot be captured because the sampling rate is too low. Sampling rates at least two orders of magnitude higher can be obtained but only in air flows, which for LDA measurements in the inertial range are more suitable than water flows.

Historically, there are a range of approaches to calculating the integral length scales and different methods are generally employed depending on the nature of the flow (isotropic turbulence or dominated by coherent structures). Among the different methods, one can list:

1. assessment of the limits of the energy spectrum ($\Lambda^t_{uu} = \lim_{f\to 0} E_x(f)/(4u')$),
2. integration of the correlation function to ∞, to the first zero crossing or to the first minimum,
3. evaluation of maximum of the product $fE(f)$,

The length scales obtained should be independent of the method used to calculate them. However, a strongly periodic signal leads to some difficulties with the calculation of these integral scales. As shown in Fig. 5.16, integration of the correlation function up to the first zero crossing (dashed and $\times$) or up to its first minimum (dashed and $\square$) produces differences of more than 50% in the resulting time scale. This deviation is a consequence of the strong dominant frequency present in the signal and its harmonics. Therefore, signal processing is needed to avoid these discrepancies.

The resampled values of the LDA time signals used for the autocorrelation calculation are previously filtered in the frequency domain [SJMS01]: thereby, the dominant peaks of the helical structure and of its 2nd and 3rd harmonics are removed from the signal[1]. The filtered signal is then transformed back into the time domain. That way, an estimation of the pure turbulent motion u'' (see Eq. 2.33) is obtained and the length scales are calculated following Eq. 2.11. Having removed the coherent velocity fluctuations, the two previous methods then give very similar results (solid and $\times$ or solid and $\square$ in Fig. 5.15). As it produces fewer outliers, the method of the integration to the first minimum was selected as the method to calculate the integral length and integral time scales.

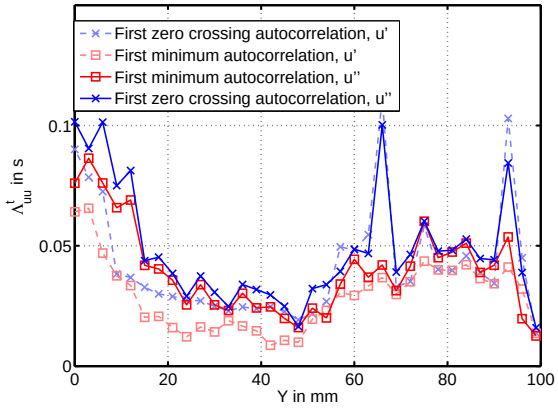

Figure 5.16: Comparison of the integral time scale Λ^t_{uu} at the axial position x=20.5 mm (z=0) calculated with two methods applied to the coherent and turbulent fluctuations u' (light colors) or on the purely turbulent fluctuations u'' (dark colors). Perpex burner without additional injector, water volume flow set to 8.55 m^3/h.

Figure 5.17 shows the time scales of the axial Λ^t_{uu} and azimuthal velocities $\Lambda^t_{u_t u_t}$. For both components, the radial and axial variations of their values are similar, with extreme values being less pronounced for the azimuthal temporal scale than for the axial one. Close to the region where $u(\boldsymbol{x})$ is

[1] This results in an non-physical spectrum with unresolved frequencies. To avoid this, it is possible to use a fit of the energy spectrum without taking the frequency range of the dominant oscillations into account.

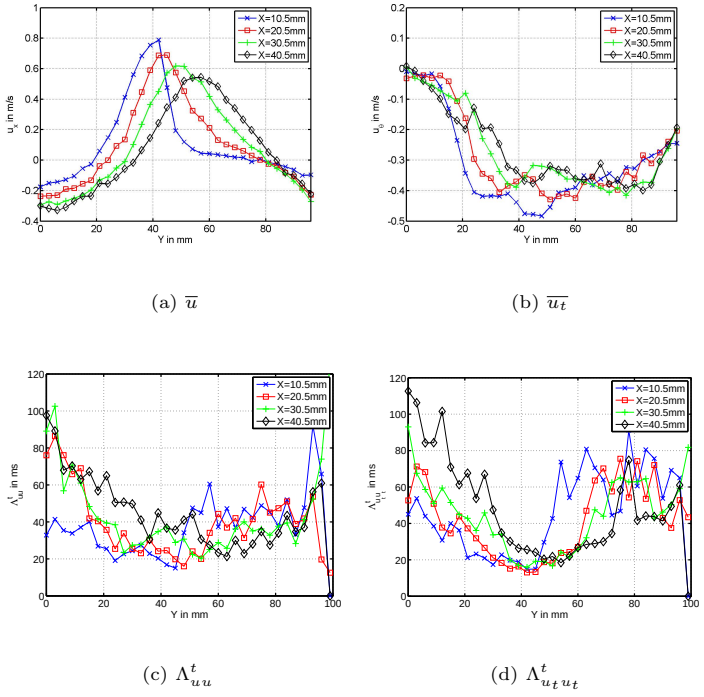

(a) $\overline{u}$ (b) $\overline{u_t}$

(c) Λ^t_{uu} (d) $\Lambda^t_{u_t u_t}$

Figure 5.17: Radial profiles of the axial and tangential mean velocities (Fig. 5.17(a) and 5.17(b)) as well as of their respective integral temporal scales Λ^t_{uu} and $\Lambda^t_{u_t u_t}$. Water test rig LDA data taken at 4 axial locations

maximal and positive, the time scale reaches a minimum, as a consequence of the high mean intensity of the convective motion and turbulent fluctuations. When the velocity decreases, whether radially or axially, an increase in the integral time scale is observed, reaching a maximum at the centerline of the flow. In the region relevant for flame stabilization, close to the points where $u = 0$, the typical values are $\Lambda^t_{uu}, \Lambda^t_{u_t u_t} \in [20, 40]$ ms.

5.2.2 Spatial length scales from PIV

A similar method can be applied to the PIV snapshots to extract the turbulent length scales. The four turbulent length scales are first calculated from the instantaneous fluctuation velocity u' and the integration of the autocorrelation function up to the first zero crossing. The spatial resolution of the PIV measurements in the water test rig is approximately 1.07 mm/vector, which is sufficient to resolve the macro scales, and 450 snapshots are used for the statistical analysis.

The correlation calculated at one location should be theoretically independent of the direction of the integration, i.e., $R_{ii}(\boldsymbol{x}, d\boldsymbol{r}) = R_{ii}(\boldsymbol{x}, -d\boldsymbol{r})$. As the measurement area is limited by the camera field of view and object boundaries, the values of the correlations become less accurate when the point $\boldsymbol{x}$ is close to a boundary and when the integration is performed toward the domain boundary. For this reason, the length scales are calculated in both directions, giving $\Lambda^{+,\boldsymbol{r}}_{u_i u_i}(\boldsymbol{x})$ and $\Lambda^{-,\boldsymbol{r}}_{u_i u_i}(\boldsymbol{x})$, with $\boldsymbol{r}$ a unit vector of the direction considered. A simple weighting correction proposed by Wäsle [WWRS06] is then applied as

$$\Lambda^{\boldsymbol{r}}_{u_i u_i}(\boldsymbol{x}) = \left(1 - \frac{(\boldsymbol{x} - \boldsymbol{x}_{min}) \cdot \boldsymbol{r}}{l_{\boldsymbol{r}}}\right) \Lambda^{+,\boldsymbol{r}}_{u_i u_i}(\boldsymbol{x}) + \frac{(\boldsymbol{x} - \boldsymbol{x}_{min}) \cdot \boldsymbol{r}}{l_{\boldsymbol{r}}} \Lambda^{-,\boldsymbol{r}}_{u_i u_i}(\boldsymbol{x}) \,, \tag{5.1}$$

with $l_{\boldsymbol{r}} = (\boldsymbol{x}_{max} - \boldsymbol{x}_{min}) \cdot \boldsymbol{r}$ being the distance between two boundaries of the domain in the direction $\boldsymbol{r}$.

The resulting four length scales are presented in Fig. 5.18, with the isoline u=0 depicted in white for clarity. The length scales evolve in different ways. The axial length scale $\Lambda^x_{uu}(\boldsymbol{x})$ takes high values in the immediate vicinity of the burner outlet ($\Lambda^x_{uu}(\boldsymbol{x}) \approx 30\,\text{mm}$), and decays rapidly to be more homogeneously distributed for axial positions $x > 40\,\text{mm}$ ($\Lambda^x_{uu}(\boldsymbol{x}) \approx 20\,\text{mm}$). The corresponding radial length scale $\Lambda^y_{uu}(\boldsymbol{x})$ has values in the range $\Lambda^y_{uu}(\boldsymbol{x}) \in [5, 12]\,\text{mm}$, the highest values being reached in the inner shear layer region. The ratio $\Lambda^x_{uu}(\boldsymbol{x})/\Lambda^y_{uu}(\boldsymbol{x})$ is close to 2, which is a typical value in case of isotropic turbulence [Fie03]. On the other hand, the length scales of the radial velocity component exhibit relatively high values not only at the burner outlet ($\Lambda^x_{vv}(\boldsymbol{x}) \approx 15\,\text{mm}$, $\Lambda^y_{vv}(\boldsymbol{x}) \approx 25\,\text{mm}$), but also in the recirculation zone ($\Lambda^x_{vv}(\boldsymbol{x}) \approx 30\,\text{mm}$), possibly because of

the precessing motion induced by the vortex core. Within the positive axial velocity zone, and for axial location $x > 40\,\mathrm{mm}$, their values range between $\Lambda^x_{vv}(\boldsymbol{x}) \in [7,\, 12]\,\mathrm{mm}$ and $\Lambda^y_{vv}(\boldsymbol{x}) \in [10,\, 17]\,\mathrm{mm}$.

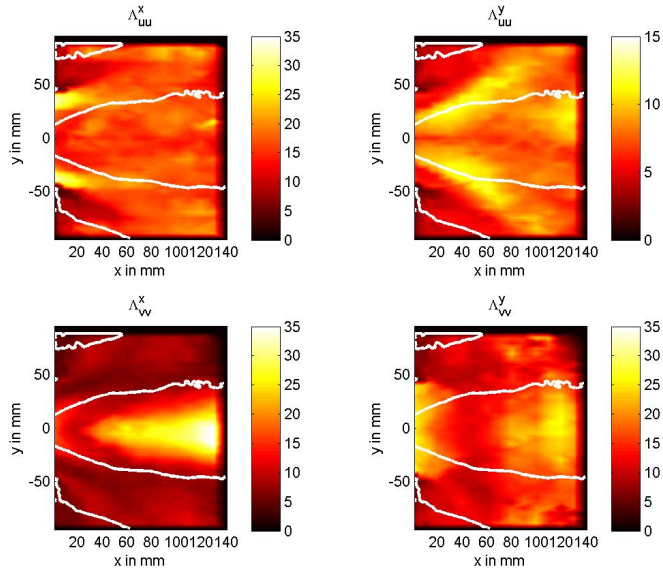

Figure 5.18: Spatial length scales calculated directly from the fluctuating velocity field $\boldsymbol{u}'(\boldsymbol{x})$.

The high values of the length scales visible at the burner outlet are clearly a consequence of the helical structure which dominates the fluctuation flow field at this location. As suggested from numerical simulations, such coherent structures may not have a strong influence on the flame propagation [UC97, LC02], and it may be more appropriate to describe the turbulent characteristics without the dominant coherent fluctuations. This can be obtained with help of the POD analysis.

If the POD is used to calculate the coherent fluctuations of N_c modes from N available modes as

$$\tilde{\boldsymbol{u}}_{N_c}(\boldsymbol{x}, t) = \sum_{i=1}^{N_c} a_i \boldsymbol{u}_i(\boldsymbol{x})\,, \tag{5.2}$$

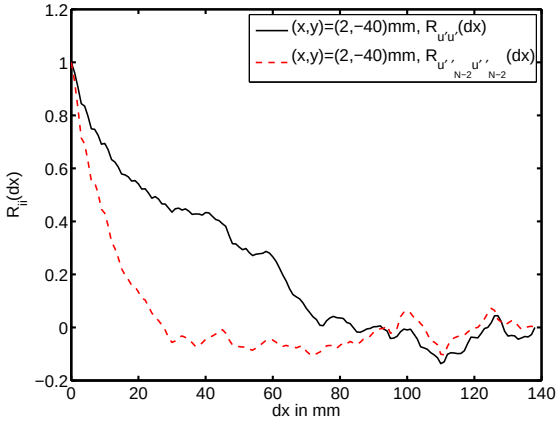

Figure 5.19: Correlation function of the turbulent axial velocity $R_{u'u'}$ and from POD and triple decomposition calculated turbulent axial velocity $R_{u''u''}$ calculated at the point $(x, y) = (2, -40)$ mm

then the stochastic fluctuation $\boldsymbol{u}''_{N-N_c}$, used to calculate the length scale, is linked to the total fluctuation $\boldsymbol{u}'$ as

$$\boldsymbol{u}''_{N-N_c}(\boldsymbol{x}, t) = \boldsymbol{u}'(\boldsymbol{x}, t) - \tilde{\boldsymbol{u}}_{N_c}(\boldsymbol{x}, t)\,, \tag{5.3}$$

and the triple decomposition of Eq. 2.33 reads

$$\boldsymbol{u}(\boldsymbol{x}) = \overline{\boldsymbol{u}(\boldsymbol{x})} + \tilde{\boldsymbol{u}}_{N_c}(\boldsymbol{x}, t) + \boldsymbol{u}''_{N-N_c}(\boldsymbol{x}, t)\,. \tag{5.4}$$

The question which now arises is which value the parameter N_c should take? Accordingly, two values $N_c = 2$ and $N_c = 8$ are tested. For $N_c = 2$, only the two highest energy modes are taken into account and these represent approximately 16% of the total turbulent kinetic energy (TKE). With $N_c = 8$, the modes with TKE contributions higher than 2% are considered as coherent motion and together these represent 33.6% of the total TKE. The impact of this correction on the correlation function is illustrated in Fig. 5.19 for the point $\boldsymbol{x} = (2, -40)$ mm. The filtering approach clearly leads to an earlier zero-crossing of the function and much smaller length scales are obtained.

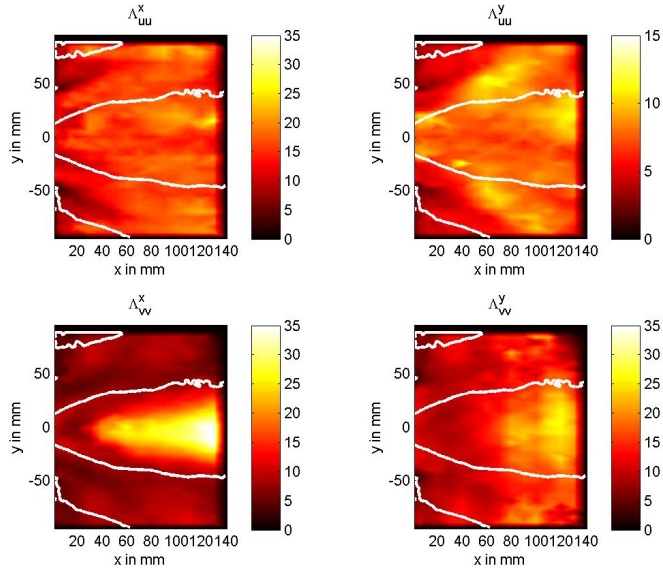

Figure 5.20: Spatial length scales calculated directly from the turbulent velocity field $\boldsymbol{u}''_{N-2}(\boldsymbol{x}, t)$ (2 first dominant modes subtracted).

The length scales calculated from $\boldsymbol{u}''_{N-2}(\boldsymbol{x}, t)$ and $\boldsymbol{u}''_{N-8}(\boldsymbol{x}, t)$ are shown in Fig. 5.20 and Fig. 5.21, respectively. When $N_c = 2$, the high values of the length scales located in the vicinity of the burner are strongly damped, and increasing N_c to 8 further reduces the length scales obtained. For example, while for the axial length scale $\Lambda^x_{uu} \approx 15\,\text{mm}$ at $\boldsymbol{x}$=(40, 40) mm with N_c=2, this value decreases to $\Lambda^x_{uu} \approx 7\,\text{mm}$ for N_c=8. In the flame region ($30 < x < 90$, $u > 0$), $\Lambda^x_{uu} \in [13, 16]\,\text{mm}$ for N_c=2 and $\Lambda^x_{uu} \in [7, 13]\,\text{mm}$ for N_c=8. Hence, it can be seen that the length scales depend on the number of modes used to extract the coherent fluctuations.

A consequence of this filtering is also a reduction of the stochastic fluctuations, as shown in Fig. 5.22. In this figure, the total fluctuation velocity which characterizes the mixing regime of the burner is calculated as

$$u''_{N-N_c,tot} = \sqrt{\frac{1}{3}\left(2{u''_{N-N_c}}^2 + {v''_{N-N_c}}^2\right)}, \tag{5.5}$$

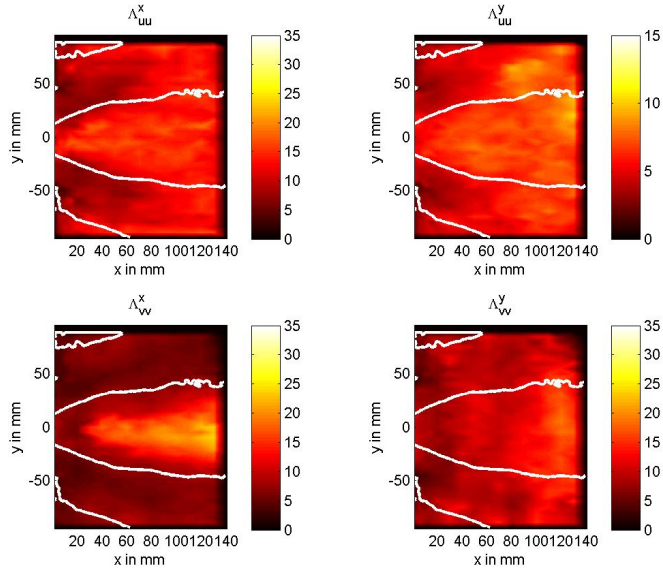

Figure 5.21: Spatial length scales calculated directly from the turbulent velocity field $\boldsymbol{u}''_{N-2}(\boldsymbol{x}, t)$ (8 first dominant modes subtracted).

assuming that the azimuthal velocity, not recorded by the PIV, is approximately equal to the axial velocity component [Wäs08]. As shown by the velocity profiles in Fig. 4.15, this may slightly overestimate $u''_{N-N_c,tot}$ in the shear layer region but strongly underestimate it at high radial locations $y/D > 0.75$. Nevertheless, when POD filtering is used, the filtered fluctuation velocity $u''_{N-8,tot}$ presents much lower values than the unfiltered fluctuation velocity $u' = u''_{N-0,tot}$, in particular in the shear layer immediately next to the burner outlet. This is an expected consequence of the removal of 33.6% of the TKE.

If the length scales and turbulent velocities decrease, the turbulent mixing time $\tau_t = \Lambda^x_{uu}/u''_{N-N_c,tot}$ calculated for $N_c = 0$, 2, and 8 and shown in Fig. 5.23 appears to be marginally dependent on the filtering procedure of the snapshots, as both values Λ^x_{uu} and $u''_{N-N_c,tot}$ decrease when filtering is applied. It slightly decreases in the region of high positive velocities when

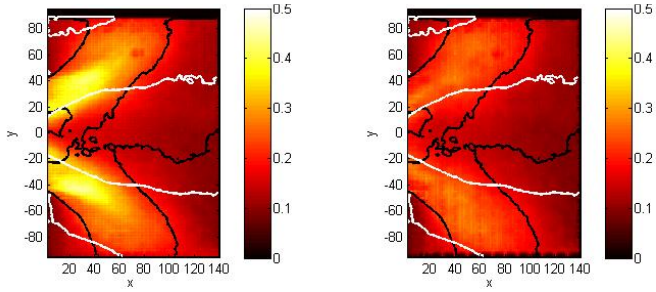

Figure 5.22: Comparison of the total fluctuation velocity $u'(\boldsymbol{x})_{tot}$(left, no POD modes filtered out) with the total turbulent fluctuations $u''_{N-N_c,tot}$ (right, 8 POD modes filtered out).

8 POD modes are used to filter the data. Further downstream, the changes are less pronounced as the POD mode structures are mostly located at the burner outlet and in the shear layers. With 8 POD modes filtered the turbulent mixing time is lowest in the high-shear and high-velocity regions ($\tau_t \in [30,\, 70]$ ms) and increases up to 120 ms in the recirculation zone.

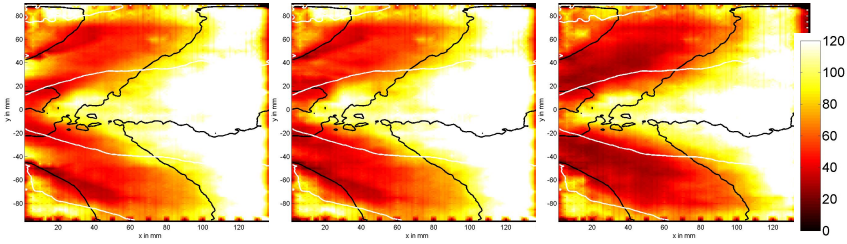

Figure 5.23: Turbulent mixing time τ_t in ms calculated from $u''_{N,tot}$ (left), $u''_{N-2,tot}$ (middle, 2 POD modes filtered), and $u''_{N-8,tot}$ (right, 8 POD modes filtered). The white and black lines represent the $u = 0$ and $v = 0$ isolines respectively.

The results described above show that the method presented is able to select the coherent fluctuations which may interact the most with the combustion, and that the results vary greatly depending on the cut-off mode selected. This implies that it is necessary to determine precisely which scale should be removed from the analysis. This problem is, however, beyond

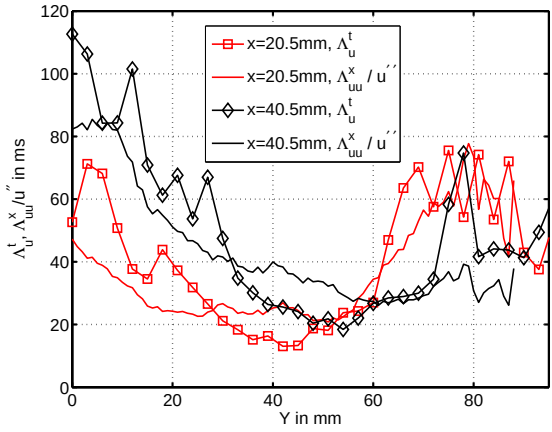

Figure 5.24: Comparison of the turbulent time scale measured directly with LDA (Λ_u^t) and indirectly with PIV (Λ_{uu}^x/u'') at the axial positions $x = 20.5\,\text{mm}$ and $x = 40.5\,\text{mm}$

the scope of the present work. Therefore, this value was set at N_c=8, so that all the strong coherent structures are removed for the scale analysis. In the region which is relevant for the combustion ($x \in [30,\ 90]\,\text{mm}$, $u > 0$), the turbulent mixing time lies in the range $\tau_t \in [30,\ 70]\,\text{ms}$. In the same region, u''_{tot} is within the range $u''_{tot} \in [0.19,\ 0.23]\,\text{m/s}$ and the spatial axial length scale Λ^x_{uu} within $\Lambda^x_{uu} \in [7,\ 13]\,\text{mm}$.

Finally, the integral time scales of the LDA measurement can be compared with the time scales obtained from the PIV. In other words, we can now ask whether the equality

$$\Lambda_u^t \stackrel{?}{=} \Lambda_{uu}^x/u'' \tag{5.6}$$

is satisfied? Figure 5.24 shows a comparison of the time scales at different axial locations. Though the time scales measured with LDA (□ and ⋄) are lower in the high positive velocity region than those derived from PIV (*solid*) and higher in the back flow regions, the values are in general similar. Notably, even though the methods of calculation are very different, an acceptable agreement between the two measurement techniques is obtained.

5.2.3 Characteristic scales in the combustion chamber

The same processing is applied to the combustion chamber data for the non-reacting and the reacting standard premix injection configurations. The 8 first POD modes of the flow are filtered out of the instantaneous snapshots. To compare the turbulent velocity fluctuations and characteristic times between the two test rigs, the data were normalized with the mean bulk velocity and residence time in the burner ($u_0 = 0.45\,\mathrm{m/s}$ and $\tau_0 = 0.1467\,\mathrm{s}$ in water, $u_0 = 14\,\mathrm{m/s}$ and $\tau_0 = 4.79 \times 10^{-3}\,\mathrm{s}$ in the combustion chamber). As previously mentioned, the statistical values of the combustion chamber results did not fully converge and were of worse quality than the non-reacting flow results. Still, the characteristic scales presented in Fig. 5.25 demonstrate a good similitude even in the presence of flame, in particular just at the outlet of the burner. The results of the cold flow measurements can thus be used to estimate the position of the combustion in the Borghi diagram.

5.2.4 The Borghi diagram

The results presented above can be used to locate the combustion regime on the Borghi diagram. Certain scales do not change between the water and air experiments; for example, the integral length scale, as the geometry remains the same. Others, which are dependent on the fluid properties, vary strongly but can be estimated from the velocities and integral scales of the fluid. An attempt is made in the following to locate the operating point A on the Borghi diagram.

With the previous results, the borders of a flame fully premixed and with the temperature of the reactants set at $T_{pre} = 423\,\mathrm{K}$ satisfy

$$\frac{u''}{S_L} = \frac{[5.85 \ldots 7.08]}{0.195} \in [29.97 \ldots 36.26] \tag{5.7}$$

$$\frac{\Lambda^x_{uu}}{\delta_L} = \frac{[0.007 \ldots 0.013]}{4.76^{-4}} \in [14.72 \ldots 27.33]\,, \tag{5.8}$$

and these borders are depicted in Fig. 5.26. The laminar flame speed is calculated from the correlation described in Abu-Orf [AOC96] while the flame

thickness δ_L is calculated from equations Eq. 2.93 to Eq. 2.95. The region enclosed by the yellow rectangle represents the possible range of local values assuming ideal premixing. Following the classification of Peters [PLV01], the flame is then located in the thickened-wrinkled flame regime.

However, a real flame is seldom perfectly premixed (due to technical limitations), so that a variation of the equivalence ratio should be taken into account. When assuming a range of equivalence ratios between $\phi \in [0.4 \ldots 0.7]$, the relevant region of the Borghi diagram widens to the red rectangle shown in Fig. 5.27.

Furthermore, Vanoverberghe [Van04] noticed that in swirling flows with a recirculation zone part of the incoming reactant flow is heated up by the combustion products. This increase in temperature leads to an increase in the laminar flame velocity as well as a reduction of the flame thickness through an increase in diffusion. If an increase in the reactant temperature from 150°C to 300°C is assumed, the relevant region of the Borghi diagram increases further to that indicated by the dark red rectangle in Fig. 5.27. Nevertheless, the flame remains mostly in the thickened-wrinkled flame regime.

5.3 Conclusion on the similitude air/water

This chapter has shown that the mean velocity and passive scalar fields are similar in non-reacting and reacting conditions as long as the flame is anchored downstream of the burner. Otherwise, a complete change in the flow field takes place, which makes it difficult to predict the behavior of the combustor from non-reacting experiments. A method based on proper orthogonal decomposition filtering has been proposed to extract the turbulent integral length and time scales of the flow field without the influence of the helical flow structure. A comparison of these length scales has shown that they are similar in reacting and non-reacting conditions. Finally, the non-reacting experiments have been used to estimate the location of the combustion regime of the burner on the Borghi diagram.

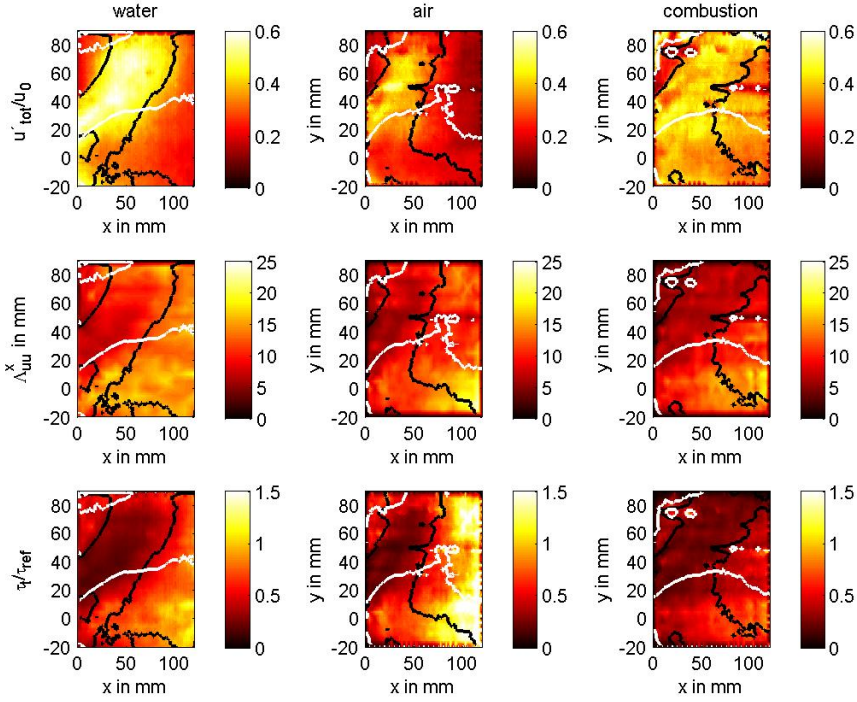

Figure 5.25: Comparison of the turbulent scales of water, air and air with combustion (columnwise, from left to right) with the 8 dominant POD modes filtered out of the snapshots. From top to bottom: normalized turbulent velocity $u''_{N-8,tot}/u_0$, integral length scale Λ^x_{uu} in mm, normalized turbulent time τ_t/τ_0. setup combustion: OPA, injector I00, (α, β)=$(1, -)$, L_{cc}=0.66 m.

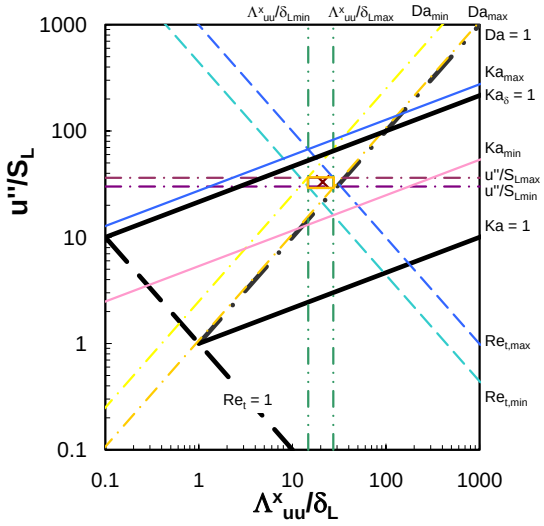

Figure 5.26: Borghi diagram of the swirl-inducing burner for operating point A, $(\dot{m}_{air}, \phi, T_{pre})$=(220 kg/h, 0.555, 423 K), assuming perfect premixing. The yellow rectangle highlights the region involved.

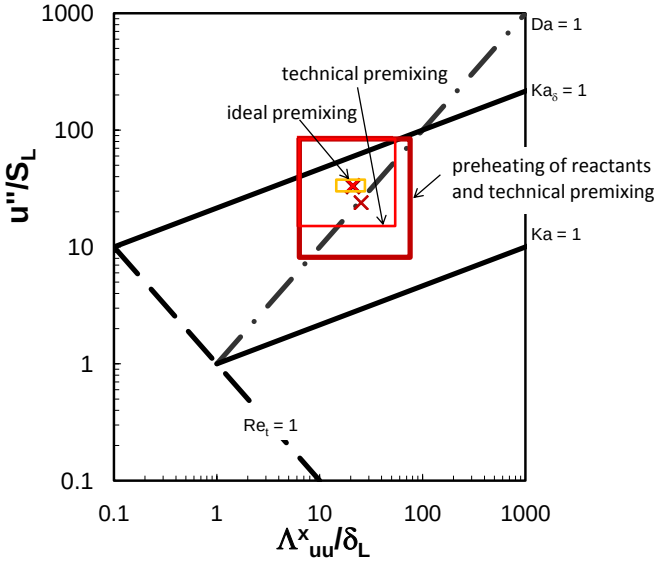

Figure 5.27: Borghi diagram of the swirl-inducing burner for operating point A considering technical limitations on premixing with or without preheating of the reactants

Chapter 6

A quantitative link between mixture PDF and NO_x emissions

The previous section showed that the non-reacting and reacting flows present strong similarities. We now go on to explore the relationship between the mixing quality measured in cold flow experiments and the NO_x emissions under reacting conditions. For these investigations, fuel is injected through injector I00 only ($\alpha = 0$).

6.1 Experimental scalar mixing model

6.1.1 Identification of the experimental mixing model

The mixing quality of the burner is recorded in an axial cross-section 5 mm downstream of the burner outlet. Typical average concentration images have already been shown in, for example, Fig. 4.16. The measured coefficient of variation of the dye/water mixture is denoted by $s_{x=5mm}$ and is equal to $s_{x=5mm} = \sigma_t\left(C^*\right)/C^*_\infty$. Figures 6.1 and 6.2 depict the evolution of $s_{x=5mm}$ as a function of the Reynolds number and of the parameters J_{eq} and β respectively. J_{eq} corresponds to the jet-to-crossflow momentum calculated for an evenly distributed injection of fuel (β=0.5). As shown in the previous section (Fig. 5.5), a very weak Re-dependency of $s_{x=5mm}$ is present in water experiments if the momentum ratio J_{eq} is kept constant. This weak Reynolds number dependency suggests that the air and water mixing qualities should be quantitatively very similar. However, as

no information on the evolution of the mixing quality in the air is available, the Reynolds number dependency is still taken into account in the experimental mixing model.

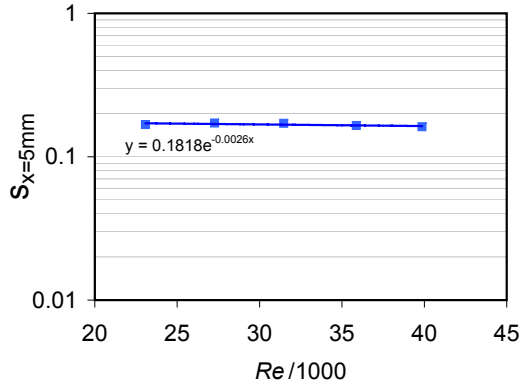

Figure 6.1: Dependency of the unmixedness parameter $s_{\mathrm{x=5mm}} = \sigma_{\mathrm{t}}\left(C^*\right)/C^*_{\infty}$ on Reynolds number Re, holding J_{eq} constant. Measurements in water for the standard fuel injection. ($\alpha = 1$), Re=Re_{ref}=3.59×10^4

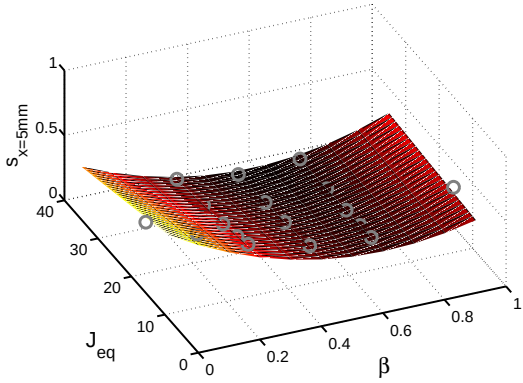

Figure 6.2: Dependency of the unmixedness parameter $s_{\mathrm{x=5mm}}$ on the fuel distribution parameter β and equivalent momentum ratio J_{eq}.

Figure 6.2 shows that the mixing quality is strongly dependent on the fuel distribution β, but less on the momentum J_{eq}. The minimum is achieved for values close to $\beta \approx 0.65$ and an increase in J_{eq} leads to a decrease in

the unmixedness, except for values of β close to 1. The dependence on β is well approximated by a second-order polynomial and the dependence on J_{eq} is mainly linear.

As the Re-number has a small effect on the mixing quality when compared to two other parameters, the general expression of the unmixedness $s_{\mathrm{x=5mm}}$ is defined as

$$s_{\mathrm{x=5mm}}\left(Re, J_{\mathrm{eq}}, \beta\right) = f\left(Re\right) + g\left(J_{\mathrm{eq}}, \beta\right) \,, \tag{6.1}$$

where the function f is a small linear correction of the main function g. Regarding the results presented in Fig. 6.1 and in Fig. 6.2, $s_{\mathrm{x=5mm}}$ can be modeled by the following function

$$\begin{aligned} s_{\mathrm{x=5mm}} = & \underbrace{A_0\left(\exp\left(A_1 Re\right) - \exp\left(A_1 Re_{\mathrm{ref}}\right)\right)}_{\mathrm{f}} \\ & + \underbrace{\left(B_1\beta + B_2\right) J_{\mathrm{eq}} + \left(C_0\beta^2 + C_1\beta + C_2\right)}_{\mathrm{g}} \,, \end{aligned} \tag{6.2}$$

where A_{i}, B_{i}, and C_{i} are the parameters of the functions f and g, and $Re_{\mathrm{ref}} = 3.59 \times 10^4$ is the reference Reynolds number at which the function g is measured. These parameters are fitted to experimental data and are summarized in Tab. 6.1.

A_0	A_1	B_1	B_2	C_0	C_1	C_2
-0.18	-2.6E-6	1.1E-2	-8.9E-3	9.8E-1	-1.5	0.72

Table 6.1: Fitting parameters of Eq. 6.2

6.1.2 Influence of the fuel distribution of the flame position

To characterize the impact of the flame on the flow field, measurements are performed in reacting flow for different fuel-injection configurations. Figure 6.3 presents the impact of different fuel distributions on the flame position x_{fl} for a range of operating conditions. If enough fuel is injected

through the downstream region, ($\beta < \beta_{\text{lim}}$), the flame is anchored at the burner outlet. Higher values of β lead to an anchoring of the flame inside the burner, due to the rich mixture zone located at its apex. The resulting flame is close to a diffusion flame, mostly stabilized in the inner shear layer of the flow. This leads to a radially more compact flame, which also produces high NO_x emissions. The value β_{lim} at which the flame is completely anchored in the burner is slightly sensitive to the operating conditions but generally lies in the range $\beta_{\text{lim}} \in [0.65, 0.7]$. For all cases, the maximum of the OH* emissions, which defines the flame position, remains downstream of the burner outlet.

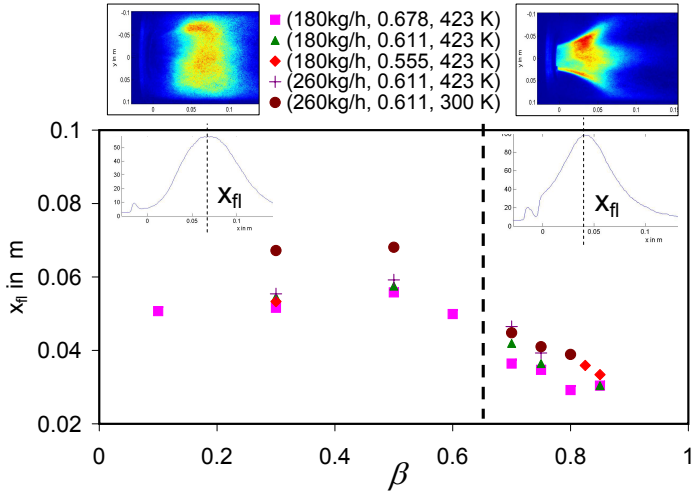

Figure 6.3: Flame position as a function of the fuel distribution parameter β ($\alpha = 0$), for different operating conditions ($\dot{m}_{\text{air}}$, ϕ, T_{air}). The axial flame location x_{fl} is defined as the position where the radially integrated OH* signal is maximal.

The experimental mixing quality function $s_{\text{x=5mm}}$ of Eq. 6.2 is used to determine the mixing quality at the burner outlet for the operating point A. With the NO_x emissions of the different fuel injections plotted against $s_{\text{x=5mm}}$ (Fig. 6.4), two distinct trends are observed. When β is increased from 0.1 to 0.6, the emissions decrease slightly. If, however, β is increased further, the emissions increase very fast. Considered separately, the two

regimes correlate well with the NO_x emissions but offer a poor correlation when they are used together, as a single degree of unmixedness corresponds to two levels of NO_x emissions, which is not possible for one operating point. One reason for this is that $s_{x=5mm}$ greatly underpredicts the real flame unmixedness when the latter in anchored in the burner and overpredicts the unmixedness when the flame stabilizes outside. As the unmixedness at the flame location is required to predict the NO_x emissions, a correction of the unmixedness parameter is needed. This correction may be obtained from the knowledge of the flame position and the decay D_s of the unmixedness over the mixing length.

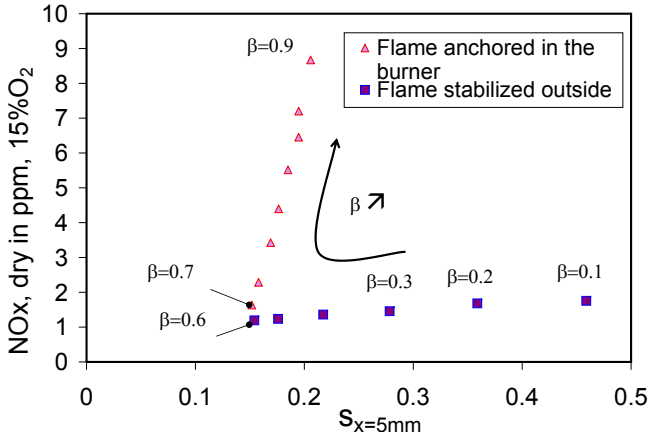

Figure 6.4: NO_x emissions as a function of the unmixedness parameter $s_{x=5mm}$ (no flame position correction), operating point A

For this, the mixing quality is measured in cold flow for four different fuel distributions at five axial locations downstream of the burner. As shown in Fig. 4.16, the regions of positive axial velocities only were taken into account for the data processing. As the recirculation of hot gases is expected to increase the homogenization before the fuel/air mixture reaches the flame front, it is assumed here that the recirculation of dye in the measurement plane has a similar effect on the degree of mixing. Indeed, it leads to a significant decrease in the instantaneous concentration gradients in the cold-flow measurements and thereby to an increase in the recorded

mixing quality. The evolution of the unmixedness parameter $s(x)$ presented in Fig. 6.5 follows an exponential function which can be expressed as

$$s(x) = s_{\mathrm{x=5mm}} \exp\left(D_{\mathrm{s}}\left(x - 0.005\right)\right), \tag{6.3}$$

where a mean decay rate D_{s} =-37 m^{-1} gives a good fit for all four of the measured curves. The region with positive axial velocity, approximated by a disk demarcating the external and internal recirculation zones, was considered for the analysis of the mixing images. These results confirm experimentally the theoretical model proposed by Syed et al. [SRM07], in which the decay of the variance of the concentration (σ^2) in the burner is also modeled by an exponential function (Eq. 2.55).

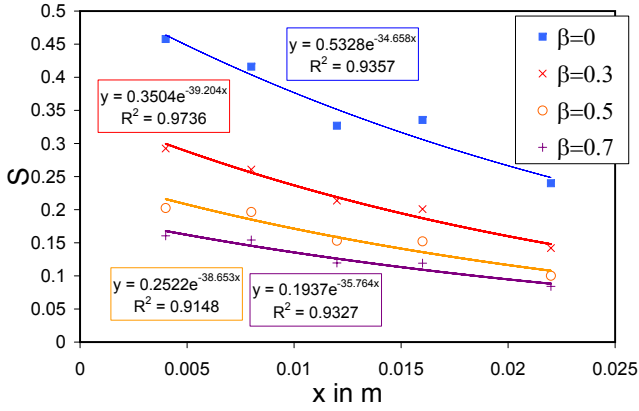

Figure 6.5: Decay of the unmixedness parameter $s = \sigma_{\mathrm{t}}\left(C^*\right)/C^*_{\infty}$ with axial location x at the burner outlet for 4 fuel injection configurations

Using Eq. 6.3, the unmixedness parameter $s_{\mathrm{fl}} = s(x_{\mathrm{fl}})$ can be estimated at the flame location x_{fl}. When the NO_x emissions are plotted against $s(x_{\mathrm{fl}})$, as shown in Fig. 6.6, a better correlation (green and $\diamond$) is achieved than without the flame position correction (violet and $\triangle$). However, the two distinct branches (in blue and ■, red and $\triangle$) are still present. This indicates that the corrected values still underpredict the unmixedness when the flame is anchored in the burner. The flow field changes induced by the

flame are too large to be corrected simply by the flame position. Therefore, the simple mixing model based on mixing decay and flame position can only be considered valid for a flame which is not anchored inside the burner, i.e., $\beta < \beta_{\text{lim}} = 0.7$ for all the operating conditions tested.

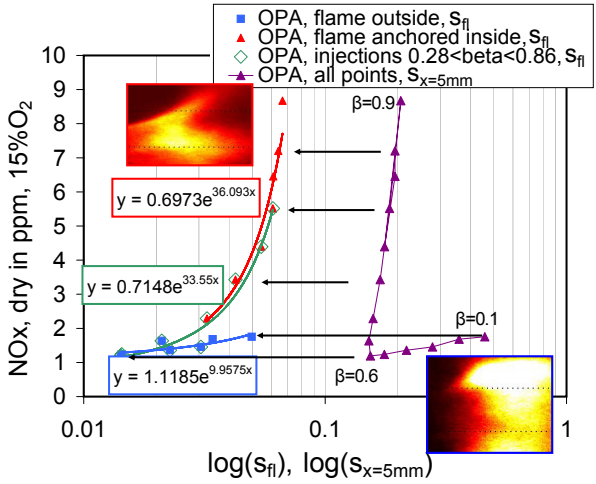

Figure 6.6: NO_x emissions as a function of the unmixedness $s(x_{fl})$ estimated at the flame position for the operating point A

6.1.3 Flame / flow field interaction increasing the mixing quality

The behavior of the flame when β is slightly less than β_{lim} is even more critical for the modeling. The POD technique applied on the single OH* snapshots [LLB+10] reveals that when the equivalence ratio ϕ is high enough, a suppression of the helical structure pattern in the OH* pictures is captured while the flame changes its position only slightly. This interaction is illustrated in Fig. 6.7, which shows the first POD mode of the OH* chemiluminescence images below images of the average OH* for fuel distributions of $\beta = 0.4$ and $\beta = 0.55$ recorded at two slightly different equivalence ratios ($\phi_1 = 0.611$, $\phi_2 = 0.649$). While no change occurs for the lowest β

value, the POD image of the injection with $\beta = 0.55$ shows a large change in the mode shape when the equivalence ratio is increased from ϕ_1 to ϕ_2. The typical antisymmetric structure disappears from the POD mode, in particular immediately next to the burner outlet, indicating either that the helical motion is strongly damped or that the flame stabilizes in a region which is not influenced by the helical motion.

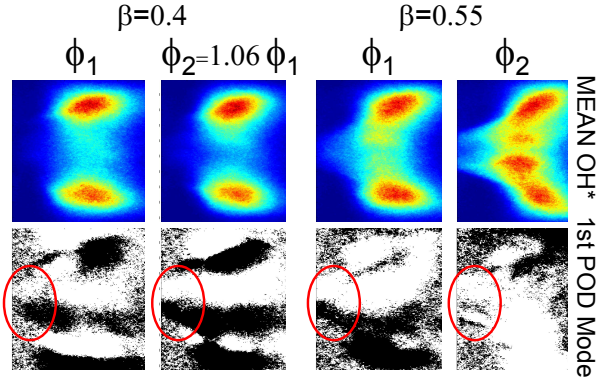

Figure 6.7: Mean OH* chemiluminescence images and corresponding first POD mode for two fuel distributions, $\beta = 0.4$ and $\beta = 0.55$, recorded at two equivalence ratios $\phi_1 = 0.611$ and $\phi_2 = 0.649$.

The PIV measurements of Fig. 5.7 and their resulting POD analysis shown in Fig. 5.11(d) can be used to determine which of these is the case. For injection distribution (α, β)=$(0, 0.75)$, i.e., when the flame is anchored inside the burner, the typical POD modes of the helical structure disappear immediately next to the burner outlet, but some much smaller structures appear downstream in the shear layer. This suggests that the helical structure, which is present when the flame stabilizes outside the burner, almost disappears when the flame is anchored in the burner. This is certainly what happens for injection with $\beta = 0.55$ as the flame moves slightly upstream while ϕ increases, as shown in Fig. 6.7.

This behavior seems to have a positive impact on the NO_x emissions, as shown in Fig. 6.8, where a reduction of these emissions is achieved with $\beta = 0.55$ for a range of equivalence ratios between 0.63 and 0.72. Below

$\phi = 0.63$, both emissions are very similar, with slightly better results for injection with $\beta = 0.55$, which is to be expected as it also produces the best mixing quality, or lowest $s_{x=5mm}$ value, in cold flow (see Fig. 6.4). However, the increase in NO_x with the equivalence ratios higher than $\phi = 0.63$ is less pronounced for injection with $\beta = 0.55$ leading to emission values which can be 3 ppm lower than with $\beta = 0.4$. This decrease in NO_x seems to correlate strongly with the change in the flame shape and the resulting suppression of the helical mode when the flame starts to stabilize inside the burner. The consequence for the model extracted from cold flow measurements is a slight overprediction of the unmixedness when the flame damps the helical structure.

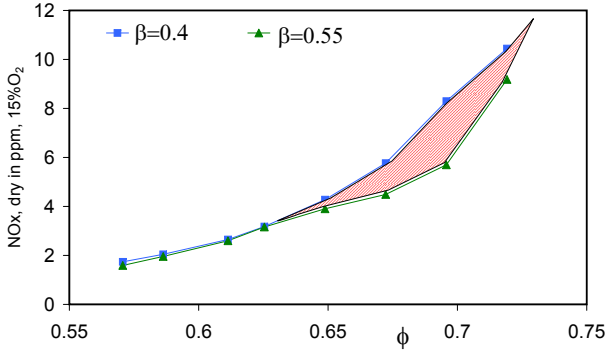

Figure 6.8: NO_x emissions recorded for the two injection configurations of Fig. 6.7. The difference between the two curves is shaded in red.

6.1.4 Empirical correlation

To verify that the newly defined mixing parameter is also suitable for predicting the NO_x emissions at different operating conditions, an empirical correlation is used with either $s_{x=5mm}$ or s_{fl}. The expression for the fitting function was inspired by the expressions of Lefebvre and Alkabie shown in Eq. 2.98 and Eq. 2.99. It takes into account the preheating temperature T_{pre}, equivalence ratio ϕ, the degree of unmixedness s and the residence time in the combustor (a function of the relative pressure loss over the

burner $\Delta p/p$, calculated here *without flame*):

$$NO_x = A \exp\left(BT_{\text{pre}}\right) \left(\frac{\Delta p}{p}\right)^C \exp\left(D\phi\left(1-s\right)+Es\right) . \qquad (6.4)$$

Here s is defined from the concentration $C*$ or fuel mole fraction Y_f while in [Alk00] it is defined in terms of the equivalence ratio ϕ. Contrary to Alkabie who considers the unmixedness s as a floating parameter, its present value is calculated from the experimental mixing model. When the different operating conditions lie within $0.28 < \beta < 0.86$, (the same range as in green and $\diamond$ in Fig. 6.6), a good quality fit ($R^2 = 0.94$) is obtained (Fig. 6.9). A total of 67 points taken for 18 distinct operating conditions are used to perform the fit. The constants A, B, C, D, E take the values $(0.72, -2.3 \times 10^{-3}, 0.88, 10.41, 40.88)$ respectively. The values of D=10.42 and E=40.86 are close to the values reported by Alkabie (9.735, 30). The experimental fit with s_{fl} is much better than the one with $s_{\text{x=5mm}}$, shown in Fig. 6.9 as empty $\diamond$ ($R^2 = 0.33$). Therefore, the correction proposed from Eq. 6.2, Eq. 6.3, and Eq. 6.4 is justified a priori.

However, if the points measured are divided as a function of the flame stabilization location (Fig. 6.10), the two distinct trends shown in Fig. 6.6 are still present. The global fit of Fig. 6.9 makes no distinction between the flame regimes but, taken alone, they present better fitting results with slightly different parameters: $R^2 = 0.977$ and (A, B, C, D, E) = $(0.084, 7.7 \times 10^{-5}, 0.60, 10.66, 20.28)$ for the flame anchored downstream (left in Fig. 6.10) and $R^2 = 0.952$ and $(0.74, -1.8 \times 10^{-3}, 0.87, 10.34, 37.9)$ for the flame anchored in the burner (right in Fig. 6.10). This can be attributed to the two different flame regimes present.

In general, the coefficients (A, B, C, D, E) confirm that an increase in ϕ (coefficient $D(1-s) > 0$) as well as an increase in s (coefficient $(E - D\phi) > 0$) increases the NO_x emissions. A positive pressure loss dependency ($C > 0$) is also observed, i.e., the NO_x emissions increase with a decrease in the mean residence time. This seems a priori contradictory (NO_x generally increases with increasing residence time) but can be explained by the weak thermal NO_x component (which depends on the residence time) at atmospheric conditions and the increase in the recorded temperature downstream of the flame when the power output or air mass

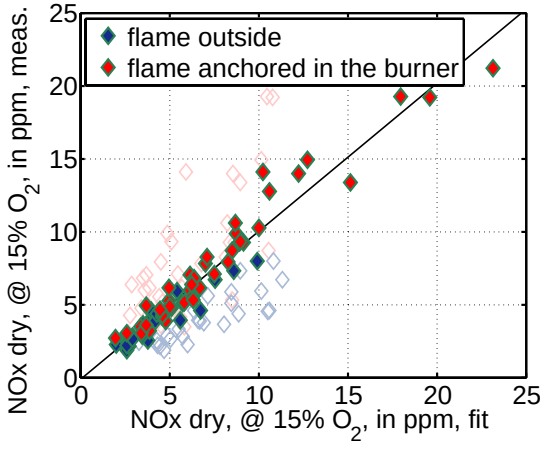

Figure 6.9: Quality of experimental fitting of Eq. 6.4 using the corrected unmixedness parameter $s_{\mathrm{x,fl}}$ ($R^2 = 0.94$). Blue $\diamond$, $0.28 < \beta < 0.7$; red $\diamond$, $0.7 \leq \beta < 0.86$ (flame anchored in the burner); empty $\diamond$: fit performed with $s_{\mathrm{x=5mm}}$.

flow are increased. This increase in temperature, due to less relative heat loss through the walls [Ale09], is responsible for increasing the production of prompt NO_x and, hence, for the positive exponent for pressure loss.

The negative dependency on the preheating temperature (constant B) for the flame anchored in the burner does not seem to be what one would expect a priori, as in combustors it is generally observed that an increase in temperature at constant air mass flow and equivalence ratio leads to an increase in NO_x emissions. However, if the pressure loss term is reformulated in terms of temperature and air mass flow, it turns out that $\Delta P/P \propto \dot{m}_{\mathrm{air}}\sqrt{T_{\mathrm{pre}}}$. The resulting term, $\exp(BT_{\mathrm{pre}})\left(\sqrt{T_{\mathrm{pre}}}\right)^C$, which is then the only term depending on the temperature, is lower for $T_{\mathrm{pre}} = 303\,\mathrm{K}$ than for $T_{\mathrm{pre}} = 423\,\mathrm{K}$ so that the NO_x emissions increase by increasing the preheating temperature, as expected. As only these two preheating temperatures are used, the term $\exp(BT_{\mathrm{pre}})\left(\sqrt{T_{\mathrm{pre}}}\right)^C$ decreases slightly for $T_{\mathrm{pre}} > 390\,\mathrm{K}$. This decrease would not be present if more preheating temperatures were used for the fit.

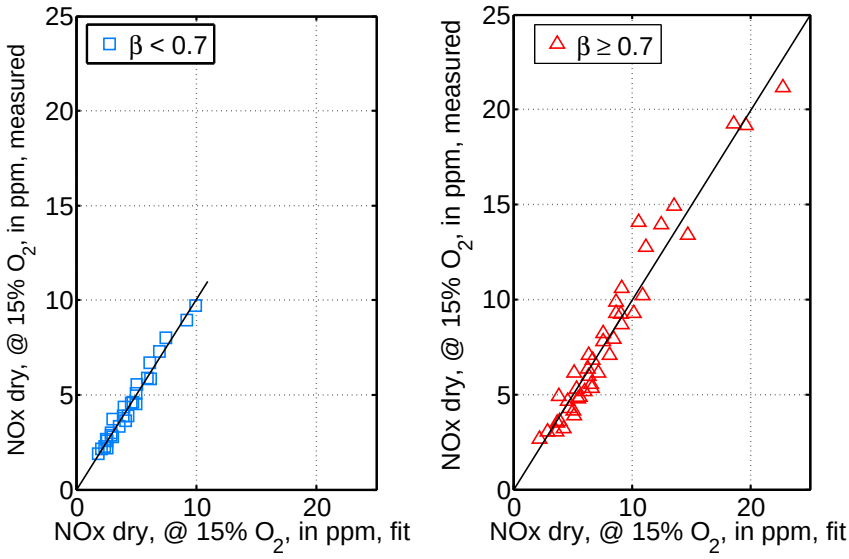

Figure 6.10: Quality of experimental fit of Eq. 6.4 using $\beta < 0.7$ (flame anchored outside the burner) or $\beta \geq 0.7$ (flame anchored inside the burner, right). Mixing quality parameter s_{fl}.

The flame position is, thus, a key parameter to improve the quality of the experimental correlation. It is not, however, sufficient to draw a direct quantitative link between the unmixedness and the PDF of the mixture at the flame. The aforementioned results suggest that, if a quantitative link may be drawn, it will only be possible with an accurate cold-flow mixing model, i.e. for injection configurations $\beta < 0.7$. This is verified in the next section.

6.2 A quantitative link between the PDF of the mixture and NO_x emissions

A good experimental correlation is a good start, but it is even more interesting to know whether the unmixedness parameter s_{fl} is a quantitative measure of the PDF of the mixture at the flame location. This is the goal of the present part.

6.2.1 PDF of the mixture

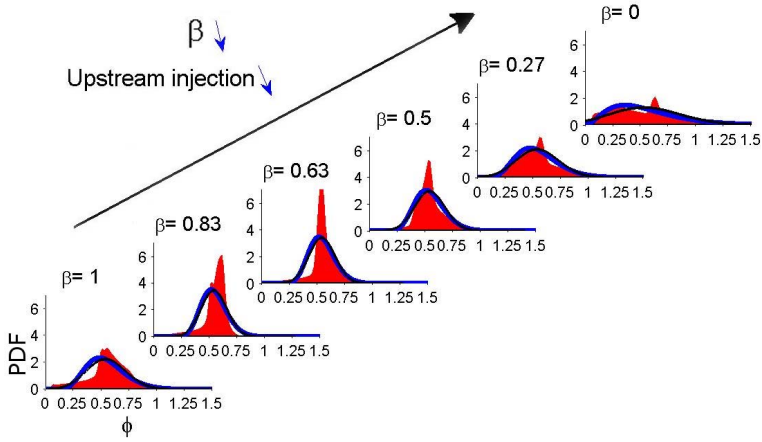

Figure 6.11: Experimental PDF of the equivalence ratio ϕ for one operating point at the position $x = 5\,\text{mm}$ for different β injections. Solid blue: beta function fit. Black: Gaussian fit. OPA, $\alpha = 0$.

The HS-LIF measurements allow the PDF of the dye concentration, $f(C^*)$, to be obtained. The later is converted into a PDF for the fuel mole fraction, $f(Y_f)$. A beta-function (or beta-PDF) is then used to approximate $f(Y_f)$. The beta-function is well suited to describe mixing processes of binary mixtures and is easily defined with two statistical moments corresponding to the mean and variance of the mixture [WMD06]. The resulting beta-PDF is then converted into a PDF of the equivalence ratio ϕ, $f(\phi)$ (note that the resulting PDF is no longer a beta-PDF), shown in Fig. 6.11. This model is a reasonably good approximation of the real PDF over the whole range of β, though the best match with the experimental curves is obtained for $\beta \leq 0.63$.

The beta distribution function is, thus, well suited to describe the decay of the PDF of the mixture, at least for fuel injections $\beta < 0.7$. With the help of a chemical reactor network model, quantitative evaluation is now undertaken.

6.2.2 NOx prediction from reactor network model and empirical PDF of the mixture

A low-order network model is used to predict the NO_x emissions from the measured unmixedness distributions. The simulations are based on a simple reactor network, consisting of a perfectly stirred reactor to model the actual flame followed by a plug-flow reactor to model the post-flame zone. The simulations are conducted with `Cantera` [Goo03] in combination with the `GRI-Mech 3.0` reaction mechanism [SGF+99]. Since a plug-flow reactor is not available in `Cantera`, it is modeled by a series of 20 perfectly stirred reactors (Fig. 6.12). The volume of the perfectly stirred reactor is derived from the PIV measurements as $2 \times 10^{-3}\,\mathrm{m}^3$, while the volume of the post-flame zone is determined from the experimental set-up, $V_{\mathrm{PFZ}} = 2 \times 10^{-3}\,\mathrm{m}^3$.

Heat transfer is calculated as the temperature difference between the gas and the environment multiplied by a heat transfer coefficient. The value of this coefficient is selected for the reactor network to match experimental data at the operating conditions $\dot{m}_{\mathrm{air}} = 220\,\mathrm{kg/h}$, $T_{\mathrm{pre}} = 423\,\mathrm{K}$, and for the fuel distribution $\beta = 0.55$; radiation is not included in the model. The same parameters are used for all simulations. The predicted NO_x emissions from the reactor network for four operating conditions are presented in Fig. 6.13. In particular, they capture the increase in NO_x emissions with increasing total power output (or air mass flow at constant ϕ), as recorded in the experiment.

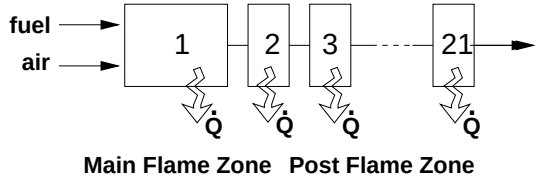

Figure 6.12: Reactor network used to simulate the NO_x emissions of the combustion chamber

The mixture variance recorded in the water test rig then makes it possible to calculate the PDF of the equivalence ratio, $f(\phi)$, which is used to weight

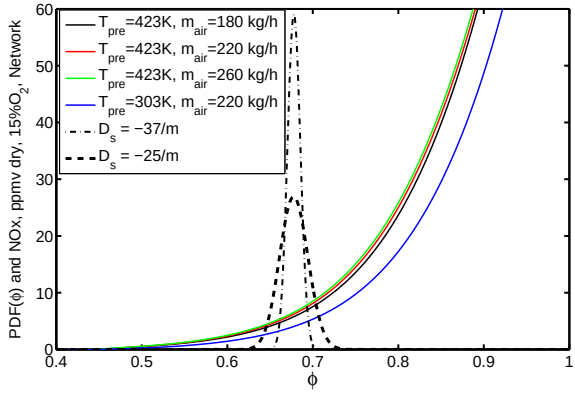

Figure 6.13: NO_x emissions calculated for 4 operating conditions and illustration of the mixture PDF for the lowest unmixedness at the flame s_{fl} of all the points tested and obtained with the decay rate $D_s = -37\,/\mathrm{m}$ (measured in cold flow, $s_{fl} = 0.0104$, dash-dot) or the decay rate $D_s = -25\,/\mathrm{m}$ (adjusted with respect to NO_x emissions, $s_{fl} = 0.0229$, dashes)

the predicted NO_x emissions according to the following expression

$$NO_x = \frac{\int NO_x(\phi) f(\phi)\, d\phi}{\int f(\phi)\, d\phi}\,. \tag{6.5}$$

A set of 18 operating conditions - 3 air mass flows (180, 220, and 260 kg/h), 2 preheat temperatures (303 and 423 K), and 3 equivalence ratios (0.555, 0.610, 0.678)- with various fuel-injection configurations β, resulting in 90 measurement points, are used to calculate emissions which are shown in Fig. 6.14 and Fig. 6.15. In Fig. 6.14 it is clear that the unmixedness recorded at the burner outlet does not quantitatively predict the NO_x emissions, which are overpredicted for a flame stabilized downstream and underpredicted for a flame anchored in the burner.

Much better agreement can be seen in Fig. 6.15 where the cases with $\beta < 0.7$ only are taken into account. Two unmixedness decay rates D_s are tested to calculate the value of the unmixedness parameter at the flame s_{fl}: D_s=-37 /m, the original value from the concentration measurements (left

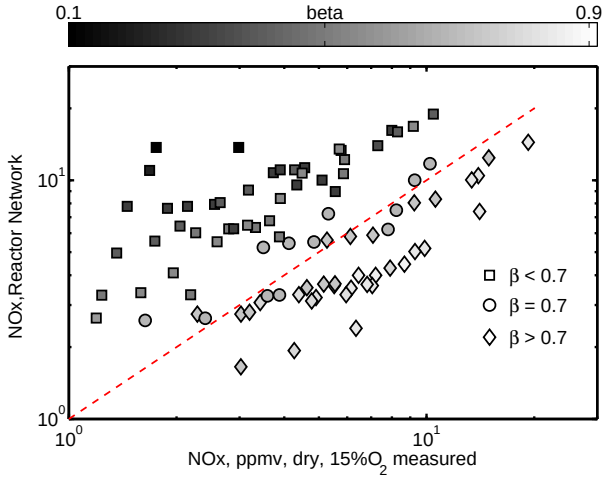

Figure 6.14: Comparison of the measured NO_x emissions with the simulated and PDF-weighted NO_x emissions (log scale). The gray scale corresponds to the value of the parameter β. $s_{x=5mm}$ is used to calculate the PDF of the mixture.

graph), and D_s=-25 /m, the decay rate which maximizes the coefficient of regression R^2. Both fits are of good quality. The decay rate D_s=-25 /m, which gives slightly better results than the decay rate D_s=-37 /m, suggests that the absolute experimental value of the scalar decay rate in reacting conditions is overpredicted by the cold mixing tests. The value D_s=-25 /m leads then to a wider mixture PDF at the flame, as illustrated in Fig. 6.13.

Several different factors may explain this overprediction. Firstly, the higher degree of turbulence of the water test rig or the fact that the recirculation of dye in the measurement plane may induce a stronger scalar homogenization in water. Secondly, and certainly more importantly, the model presented here assumes that the maximum in chemiluminescence correlates well with the flame position, the location at which all the fuel is assumed to burn. In reality, the combustion takes place across the whole flame, hence with a fuel/air distribution at the flame is more complex than the one assumed here, and the OH* chemiluminescence image remains inaccurate even to predict just the position of the maximum of heat release [LS09].

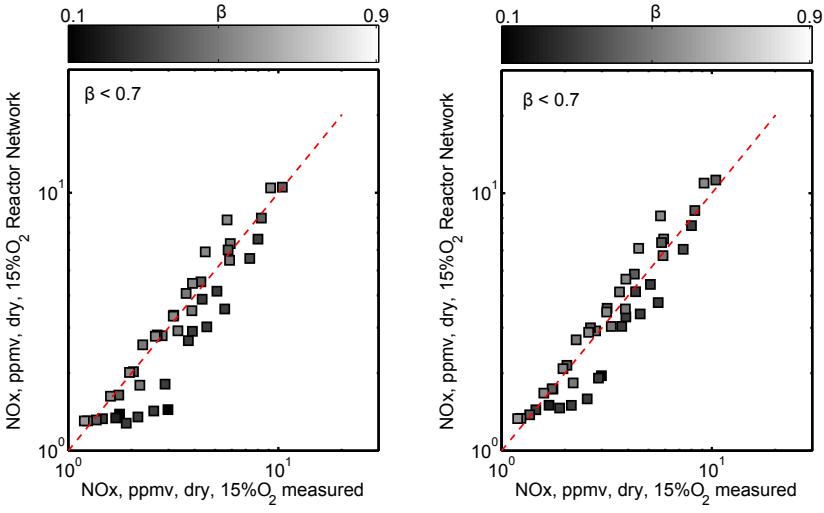

Figure 6.15: Comparison of the measured NO_x emissions with the simulated and PDF weighted NO_x emissions (log scale). The gray scale corresponds to the value of the parameter β. Left, s_{fl} calculated with scalar decay rate of the unmixedness D_s=-37 /m. Right, with D_s=-25 /m.

Nevertheless, considering the simple assumptions used here concerning the mixing process and on the network model, the results are reasonably satisfactory and allow a quantitative link to be established between the concentration measured at one axial location in cold-flows and the resulting NO_x emissions recorded in the combustor.

6.3 Evolution of the flame position and shape as a function of operating conditions

From the analysis of the reacting and chemical time scales, it appears that the Damköhler number is a function of the total air mass flow $\dot{m}_{air}$, the density upstream of the reactants ρ_u and the flame temperature, characterized by ϕ [SRM07]. In turn, the flame position is a function of the

Damköhler number and can be expressed as

$$x_{fl}(\dot{m}_{air}, \phi, \rho_u, \beta) = A'_0 \dot{m}_{air}^{A_m} \phi^{A_\phi} \rho_u^{A'_T} \tag{6.6}$$

or equivalently for an atmospheric combustor using $\rho_u \propto 1/T_{pre}$

$$x_{fl}(\dot{m}_{air}, \phi, T_{pre}, \beta) = A_0 \dot{m}_{air}^{A_m} \phi^{A_\phi} T_{pre}^{A_T} \,. \tag{6.7}$$

As shown in the previous sections, the stabilization location of the flame may be split into three regions when the fuel distribution β is varied. One region of these is where the flame stabilizes mostly outside the burner ($\beta < 0.49$), and another where the flame anchoring point is located inside the burner ($\beta \geq 0.7$). Between these regions, a third zone exists where the flame presents a much greater axial variation when the fuel distribution or other operating parameters are varied. Equation 6.7 can be rewritten as

$$x_{fl}(\dot{m}_{air}, \phi, T_{pre}, \beta) = A_0(\beta_{ri}) \dot{m}_{air}^{A_m(\beta_{ri})} \phi^{A_\phi(\beta_{ri})} T_{pre}^{A_T(\beta_{ri})} \beta^{A_\beta(\beta_{ri})} \,, \tag{6.8}$$

where β_{ri} is one of the three regions which describes the flame stabilization location. The fuel distribution β was also introduced explicitly in Eq. 6.8 so that 4 parameters describe the flame position and 5 unknowns must be calculated for each fuel injection region.

The fitted parameters calculated from 101 flame positions are summarized in Tab. 6.2 and the fitted data shown in Fig. 6.16. For comparison, values of the equivalence ratio exponents in the model proposed by Syed [SRM07] are also listed in this table. The experiments were conducted in a long combustor equipped with a 60 mm orifice. If no orifice is used, the flame stabilizes further downstream and a slight variation can be observed in the flame position in the downstream direction.

For a flame stabilizing mostly downstream ($\beta < 0.49$), the equivalence ratio exponent (A_ϕ) of the Syed model matches the experimental values of the present work fairly well: $A_{\phi,\text{Syed}} = -0.5$ versus $A_{\phi,\text{fit}} = -0.48$. A good agreement is also obtained for a flame which starts to be anchored inside the burner with $A_{\phi,\text{fit}} = -0.6$. On the other hand, though the sign of the exponents of the air flow (A_m) and of the preheat temperature (A_T) also

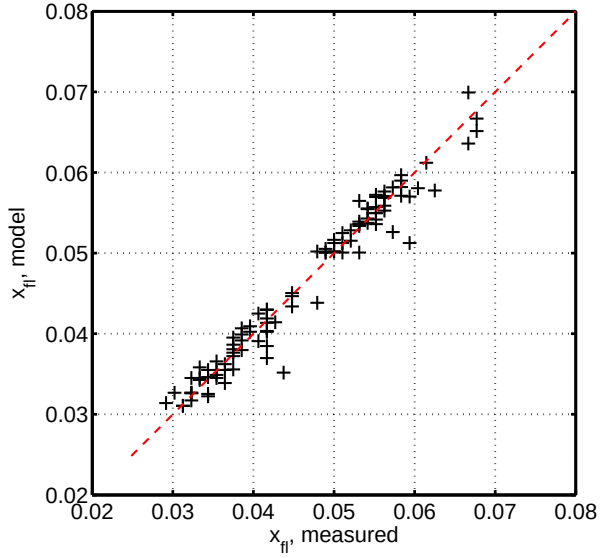

Figure 6.16: Comparison of the fitted flame position x_{fl} (Eq. 6.8) with the experimentally measured one.

agree, their absolute values are more than two to ten times lower in the present work than in the Syed model.

β-range	A_0	A_m	A_ϕ	A_T	A_β
$\beta \in [0, 0.49[$	0.5035	0.1493	-0.4842	-0.3307	0.0213
$\beta \in [0.49, 0.7[$	1.0922	0.0515	-0.6009	-0.5527	-0.3591
$\beta \in [0.7, 0.9]$	0.1883	0.434	-0.1077	-0.1126	-0.8422
Syed[SRM07]	-	3/2	-0.5	-3/2	-

Table 6.2: Parameters describing the flame stabilization location x_{fl} (Eq. 6.8) as a function of the fuel distribution β. Typical values based on the theoretical assumptions of Syed [SRM07] are reported for comparison. A total of 101 operating points is used. $L_{cc} = 1.5\,\text{m}$ with 60 mm outlet.

Two other parameters, namely the flame spatial variance and the maximum in the radially integrated OH* emissions, were fitted accordingly to Eq. 6.8

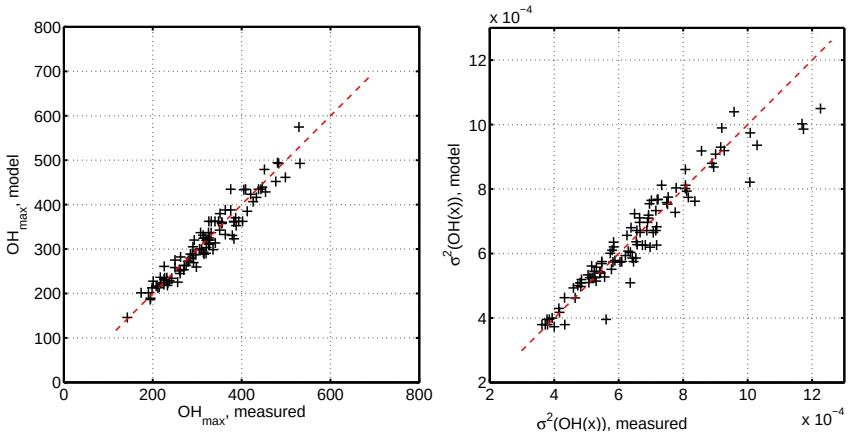

Figure 6.17: Comparison of the fitted maximal values of radially integrated OH* intensities with experimentally measured ones (left). Same comparison for the variances of the flame width (right). Fit function of the form of Eq. 6.8.

and very good fits were also achieved, as shown in Fig. 6.17. The resulting parameters of the fit are listed in Tab. 6.3 and Tab. 6.4.

β-range	A_0	A_m	A_ϕ	A_T	A_β
$\beta \in [0, 0.49[$	157.54	1.217	4.529	0.998	-0.166
$\beta \in [0.49, 0.7[$	75.31	1.202	3.863	1.039	-0.382
$\beta \in [0.7, 0.9]$	198.76	1.059	2.826	0.847	1.127

Table 6.3: Parameters describing the value of the maximum in radially integrated OH* emission profiles recorded by the camera ($I_{OH,BP}$)

β-range	A_0	A_m	A_ϕ	A_T	A_β
$\beta \in [0, 0.49[$	0.02569	0.2623	-2.106	-0.6877	0.038
$\beta \in [0.49, 0.7[$	1.204	-0.008	-0.311	-1.224	0.669
$\beta \in [0.7, 0.9]$	0.114	0.277	-0.124	-0.771	-1.085

Table 6.4: Parameters describing the value of the spatial variance of the radially integrated OH* emission profiles recorded by the camera ($I_{OH,BP}$)

The aforementioned fits can be used to predict the flame position. By using additionally the model of the mixing quality, the unmixedness at the flame can then be calculated and the experimental correlation of Eq. 6.4 can be used to finally predict the NO_x emissions. These emissions are compared to the recorded NO_x emissions in Fig. 6.18, illustrating that good agreement is obtained between the model and the measured NO_x emissions.

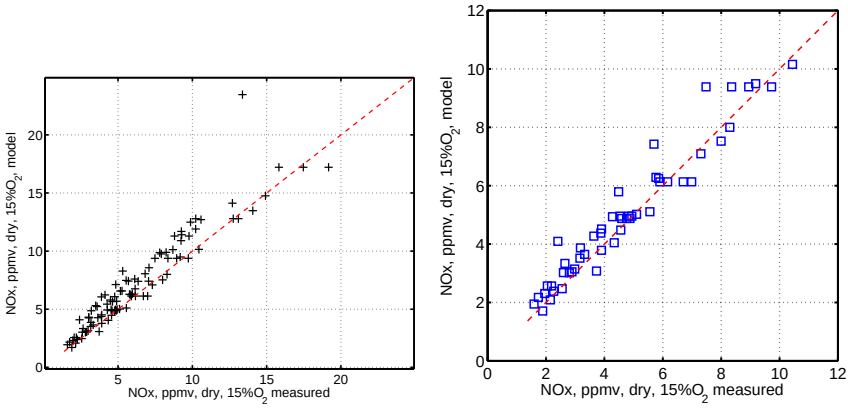

Figure 6.18: Left: Comparison of the NO_x emissions predicted by the combination of mixing quality model (Eq. 6.2), flame position model (Eq. 6.8) and NO_x emission model (Eq. 6.4) with measured NO_x emissions. Right: selection of points with the flame not completely anchored inside the burner ($\beta < 0.7$).

Furthermore, the estimation of the mixing quality at the flame location (Eq. 6.2, Eq. 6.3) combined with the model of the flame position allows the best fuel distribution for the different operating conditions to be determined. Not surprisingly, this injection is always close to the balanced distribution $\beta = 0.5$, where the cold flow mixture quality is perhaps not the most homogeneous (the best mixing is achieved for $\beta \approx 0.65$), but the flame is stabilized the furthest downstream, thus giving more time to reduce inhomogeneities in the fuel/air mixture. The fact that the minimization of the NO_x emissions occurs for some operating conditions at values close to $\beta = 0.6$ can be attributed to the suppression of the helical structure, which is not captured in the water test rig.

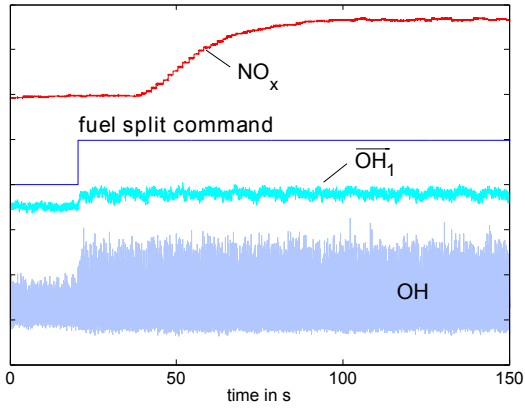

Figure 6.19: Responses of the NO_x from gas analyzer signal, instantaneous OH* signal through the band-pass filter and OH* signal averaged over one second, $\overline{OH}_1$, to a step change in the distribution of burner fuel at constant operating conditions.

6.4 PDF of the mixture, NO_x emissions and chemiluminescence

To control the emissions of the combustor, an accurate and relatively fast sensor is required. Conventional NO_x sensors have a response time which is too long (dead time of 60 to 90 s) to be used for fast control. Chemiluminescence, on the other hand, responds very fast to changes in the combustion zone, as shown in Fig. 6.19. In particular, the response of OH signals (detected through the band-pass filter) to a step change in the fuel distribution is much faster than that of the NO_x gas analyzer probe. Furthermore, Fig. 6.20 shows that the band-pass filtered chemiluminescence signals $I_{CH,BP}$ and $I_{OH,BP}$ recorded with two photomultipliers correlate very well with the NO_x emissions. These signals may be used without calibration in an extremum-seeking scheme which should minimize the emissions, as minimizing the chemiluminescence correlates with a reduction in NO_x emissions. However, the absolute intensity of the signal varies with the operating point. It may be then more appropriate to use a monitoring scheme which is less dependent on the operating conditions.

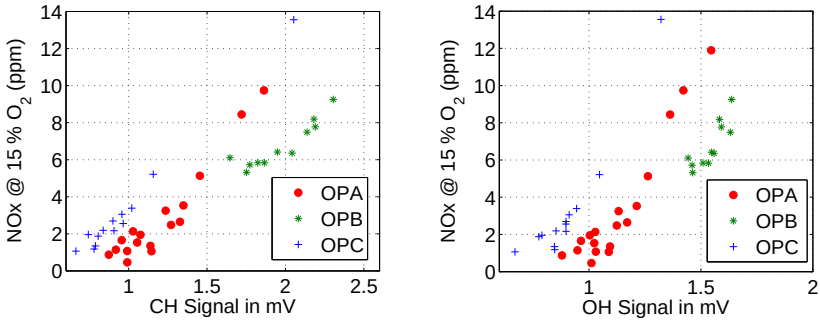

Figure 6.20: Band-pass chemiluminescence signals $I_{CH,BP}$ (left) and $I_{OH,BP}$ (right) recorded by the photomultipliers for the operating conditions OPA, OPB (180 kg/h, 0.678, 423 K), OPC (180 kg/h, 0.560, 423 K).

This improvement is achieved by combining the chemiluminescence signals recorded by the spectrometer. As has been shown by various authors ([SM00, HMLC01, MKO+03, GMPS09]), the chemiluminescence signals of CH* and OH* can be combined to measure the global or local fuel/air ratio. Typically, the ratio of the chemiluminescence intensities $I_{CH,BP}/I_{OH,BP}$ is used to monitor the average equivalence ratio $\overline{\phi}$ in different combustor types and for different pressures. The correlation takes the form

$$\frac{I_{CH,BP}}{I_{OH,BP}} = K\overline{\phi}^{B} \text{ for } \overline{\phi} < 1.2\,, \tag{6.9}$$

with K and B as constants ($B > 1$). The main advantage of this expression is that it is independent of the air mass flow. The latter correlation is optimum when the broadband $CO_2{}^*$ emission is subtracted from the total emission measured around the wavelength of 308 nm as

$$I_{CH} = I_{CH,BP} - I_{CO2} \tag{6.10}$$

where I_{CH} is the corrected signal intensity, the correction being easily calculated by integrating the intensities recorded by the spectrometer around the wavelength of interest, and the intensity I_{CO2} is calculated from the interpolation of the broadband $CO_2{}^*$ emission.

The relationship of Eq. 6.9 was used to control the fuel equivalence ratio in a premixed combustor [DLC02], with a fixed injection pattern. As the present configuration allows the mixing quality to be set through changes in the fuel distribution, it is interesting to verify if Eq. 6.9 is also valid for different mixing qualities, or if it can be modified to be somehow generalized.

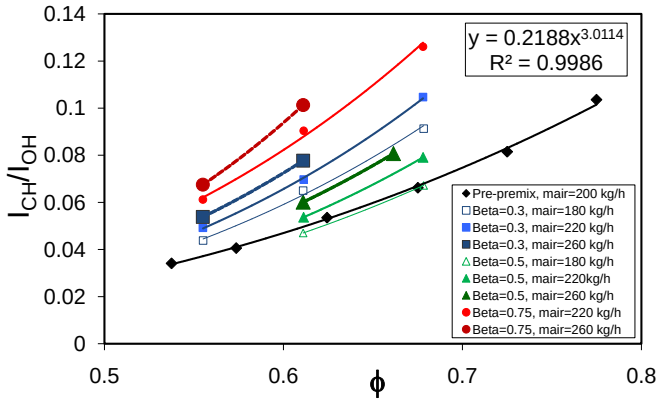

Figure 6.21: Variation of the ratio $\frac{I_{CH}}{I_{OH}}$ over the equivalence ratio ϕ for different fuel splits β and different air mass flows (T_{pre}=423 K). The perfectly premixed case (pre-premix) corresponds to the black line and $\diamond$.

Figure 6.21 presents the ratio $\frac{I_{CH}}{I_{OH}}$ as a function of the equivalence ratio ϕ for different total air mass flows $\dot{m}_{air}$ and fuel distributions β. The emissions of a perfectly premixed case (pre-premix) is also reported. Two conclusions can be drawn from this graph. The first one is that for a perfectly premixed case and at a set equivalence ratio, the ratio $\frac{I_{CH}}{I_{OH}}$ is minimized. The second one is that the fuel distribution, or the unmixedness, has a strong influence on the ratio $\frac{I_{CH}}{I_{OH}}$. Hence, when the fuel distribution is varied over a wide range, the global ratio $\frac{I_{CH}}{I_{OH}}$ cannot be considered as a measure of the equivalence ratio only. A first improvement would be to define the ratio $\frac{I_{CH}}{I_{OH}}$ as a function of the mixture probability density function

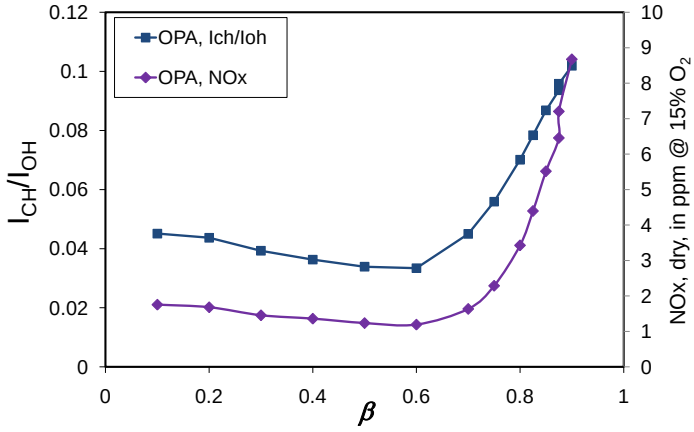

Figure 6.22: Variation of the ratio $\frac{I_{CH}}{I_{OH}}$ and of the resulting NO_x emissions over the fuel distribution β for operating point A

$f(\phi)$ as

$$\frac{I_{CH}}{I_{OH}} = K \int_{\phi} \phi^B f(\phi)\, d\phi \text{ for } \overline{\phi} < 1.2\,, \tag{6.11}$$

with K and B being determined from the pre-premix combustion case. A priori, as shown in Fig. 6.22 for the operating point A, this relationship seems to be justified as the minimal value for the ratio $\frac{I_{CH}}{I_{OH}}$ is obtained for the fuel distribution which ensures also the lowest NO_x emissions, indicating the best mixing quality ($\beta = 0.6$). Furthermore, the ratio increases with a decrease of the mixing quality, as would Eq. 6.11 do if a gaussian- or beta-distribution of the fuel concentration is assumed. However, Eq. 6.11 does not hold anymore if the air mass flow is varied, as in this case the empirical flame position model of the previous section and the results of Fig. 6.21 lead to opposite conclusions. On one hand, if the air mass flow is increased from 180 kg/h (subscript 180) up to 220 kg/h (subscript 220), the flame position model of Eq. 6.8 predicts for the whole *beta* range that

$$x_{fl,180} < x_{fl,220}\,, \tag{6.12}$$

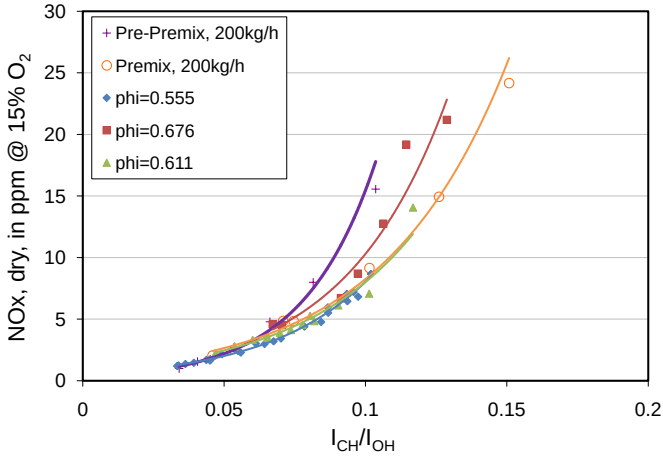

Figure 6.23: NO_x emissions as a function of the ratio $\frac{I_{CH}}{I_{OH}}$ for different equivalence ratios at the preheat temperature $T_{pre} = 423\,\mathrm{K}$. Variation of fuel distribution and air massflow for constant equivalence ratio plots. Variation of equivalence ratio only for premix and pre-premix plots.

as $A_m > 0$. As a result of the decreasing unmixedness with axial distance, the unmixedness parameters verify

$$s_{fl,180} > s_{fl,220}\,. \tag{6.13}$$

On the other hand, the recordings of Fig. 6.21 show that

$$\left(\frac{I_{CH}}{I_{OH}}\right)_{180} < \left(\frac{I_{CH}}{I_{OH}}\right)_{220}, \tag{6.14}$$

for all the equivalence ratio tested. The latter relationship is the opposite of what Eq. 6.11 would give with Eq. 6.13 and the assumption of a gaussian- or beta-distribution of the fuel concentration. Thus, the presented data does not allow to draw a direct link between the ratio $\frac{I_{CH}}{I_{OH}}$ and the mixing quality of the fuel reaching the flame. However, it seems to be a reliable sensor to reduce the NO_x emissions for different operating conditions, as illustrated in Fig. 6.23. A reduction of the ratio correlates very well with

a reduction of the NO_x emissions. Furthermore, the pre-premix operating condition depicts a minimum in both NO_x emissions and ratio $\frac{I_{CH}}{I_{OH}}$.

6.5 Summary

This section has shown that a more accurate estimation of the unmixedness s_{fl} at the flame location can be obtained using the cold flow field information on the mixing quality as well as the information on the flame position. The resulting NO_x emissions can then be estimated more accurately over a wide range of operating conditions, if a model of the mixing quality and of its spatial evolution are available. A model describing the flame position as a function of the operating parameters may also replace visualization of the flame when there is not full optical access to the combustion chamber.

In case of partially premixed flames, the ratio $\frac{I_{CH}}{I_{OH}}$ is not only a measure of the mean equivalence ratio. In fact, it also depends on the degree of mixing of the fuel distribution. For the different operating points investigated, a minimization of this ratio correlates with the minimization of the NO_x emissions of the combustor. Therefore, this parameter based on the signals from chemiluminescence sensors would be also well suited for feedback control to minimize NO_x emissions.

Chapter 7

Flame transfer function

7.1 Cold flow convective mixing model of the burner

One of the aims of the present investigations is to measure the convective time delays in burners with complex geometries and more generally evaluate the mixing transfer function of the fuel injection. Even though the flow field inside the burner can be partly analytically modeled (Flohr et al. [FSP02]), discrepancies between measured and modeled flow fields remain non-negligible, especially if the shape and orientation of the fuel injectors is changed. Since the staged fuel injection may change the inflow velocity profile for extreme distributions of the fuel, as a consequence of the high tangential momentum generated (up to 20% of the tangential momentum of the main flow), an analytical flow field model could not be derived from first principles. Thus, the mixing transfer function (MTF) has to be experimentally measured.

7.1.1 Methods

The measurement of convective time delays as well as mixing diffusion coefficient have been the subject of numerous studies over the last 50 years. The choice of the method used to record the time delays is critical and for this reason a brief overview of the possible methods is given here. All the methods were tested in the water test rig and the final comparison is presented in Tab. 7.1.

Many studies have focused on mixing in round pipes ([STS68], [Dan53]), or mixing vessels ([FPG01]). The response of the pipe outlet to a concentration pulse (Dirac response) or to a step change in concentration (Heaviside response) at the inlet is generally used for such configurations, because simple analytical solutions are available. Control theory states that the use of the Dirac function has many advantages for the identification of linear time invariant systems, as the output of the system is directly the transfer function of the system. The practical realization of such a step is more complicated, as an actuator which generates a infinitely high pulse within an infinitely small time is effectively impossible to construct. Practical applications will generally generate a Gaussian pulse. The width of the chosen pulse must be small enough compared to the characteristic time of the system, in order that the frequencies of interest will be contained in the input signal.

An alternative approach is to record the response of the system to a step, as used recently by Lans et al. [vdLGDJL97]. Such a step contains much more energy than the Dirac function. The drawback of recording a step is that the FFT cannot be applied to this signal. However, the differentiation of the step input function as well as the outlet response gives, directly, the response of the system to the Dirac function. Its Fourier transform is then the transfer function of the system.

To cancel the effect of noise, such measurements are performed many times. This is straightforward in the case of acoustic transfer functions which offer great flexibility regarding the signal shape generated and the measurement time available with a relatively small volume of data. Some difficulties arise, however, if the measurement time available is limited or the volume of data is relatively high, which is the case for HS-LIF or for unsteady CFD. To deal with such data in time-resolved CFD simulations, Polifke [PPPD01] generated a noisy excitation signal at the inlet of the domain and calculated then the correlation matrix between the inlet and outlet. The transfer function of the system (or unit impulse response) can be obtained from the finite impulse response (FIR) of the system which satisfies

$$\Gamma_{ij} h_i = c_i \,, \tag{7.1}$$

where Γ_{ij} is the auto-correlation matrix of the excitation signal, c_i the cross-correlation vector of the input and output signals and h_i the impulse response from which the transfer function is the z-transform $H(z)$. The equation above is also called the *Wiener-Hopf* equation. More details on the overall procedure are given by Polifke [PPPD01].

This method is well suited for numerical simulations where the signals (in particular the inlet signal) can be taken at any position in the domain. Although good results were obtained in a generic T-mixer configuration in the water test rig, this is more complex to achieve on the swirl-inducing burner with a distributed fuel injection line. In particular, it requires a second calibrated HS-LIF system to record the fuel flow modulations at the fuel injection location.

The concentration measurements in the water test rig offer an other possible forcing signal: instead of a step in the fuel mass flow, a step in the dye concentration can be used as input signal. Such a step could be generated upstream of the location of the fuel injection in the burner and ensure a complete passive step generation. However, its application is limited to simple injection patterns which show minimal convective delays between the single injection holes. This is not the case of the swirl-inducing burner injection lines, in particular when using a staged fuel injection, but appeared to give very good results in the generic T-mixer configuration or in an premixed swirl-inducing burner without fuel staging [GTLP11].

The last method which was tested to record the convective time delays is harmonic forcing of the main flow, with single-frequency forcing or sweep signals. Both measurements are achievable in the test rig with appropriate adjustments to the forcing valve, but have the drawback of requiring long measurement times as well as having a low SNR, due to the high degree of premixing of the burner.

Given the previous considerations, a step response of the fuel mass flow was chosen for the current configuration. This response allows both the dynamic response and the mixing quality of the burner to be characterized with a relatively small number of trials. With regards to the swirl-inducing burner setup, it also achieves a high signal-to-noise ratio and an almost immediate response at the fuel injection location.

Method	Advantages	Drawbacks
Dirac fuel mass flow	-Direct measure of MTF	-Generation of short pulses
Step fuel mass flow	-High SNR -Mixing quality recorded simultaneously	-MTF after differentiation -High SNR ratio needed -High amplitude mass flow
Step or Dirac of dye concentration	-Main flow not -High SNR disturbed	-Delay for propagation of pulse in linear injector array -Further delays if fuel staging used
Random fuel injection forcing	-Better correlation matrix	-Recording of input signal
Single-frequency forcing	-Accuracy	-Amount of data -Measurement time
Sweep signal main flow	-Steady fuel mass flow	-Harmonic signal needed -Recording of input signal -Low SNR

Table 7.1: Comparison of different methods available to record the mixing transfer function in a water test rig. SNR: Signal-to-Noise Ratio.

The principle of this measurement technique is illustrated in Fig. 7.1. Typically, a step change in the total volume flow of the fuel injection ports is applied with a magnetic step valve (ASCO posiflow). The step response of the concentration is recorded at the outlet of the burner with the HS-LIF system and the image signals are converted into concentrations following Eq. 3.10. The spatially averaged concentration, $\langle C* \rangle (t)$ recorded at the laser measurement plane is then used for the analysis. Details of the measurement and post-processing are presented in the following.

7.1.2 Measurement of time delays with fuel splitting

Figure 7.2 shows the position of the measurement plane located downstream of the burner at $xL = 5\,\text{mm}$ as well as the two recirculation zones

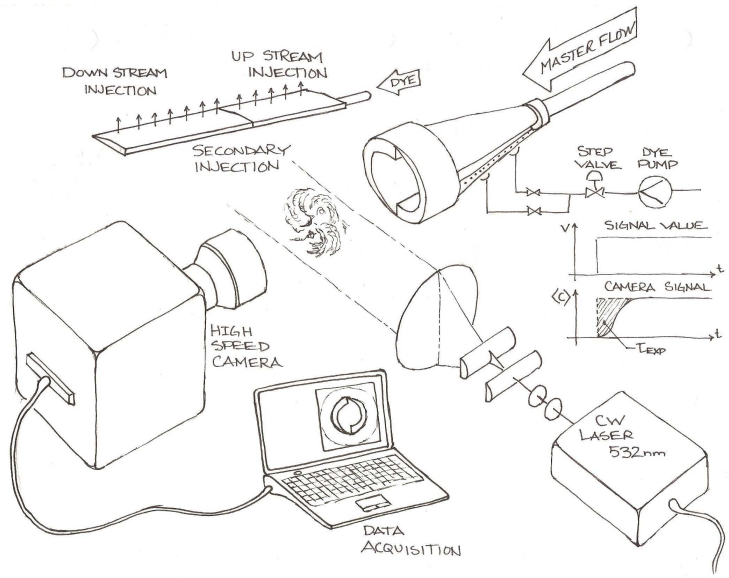

Figure 7.1: Convective time delay measurement setups for the swirl-inducing burner

at the outlet of the burner. Two phenomena have an impact on the post-processing of the step response: firstly, the helical structure shown in the previous section creates periodic fluctuations in the spatially-averaged concentration as the laser measurement plane. Secondly, the recirculation zones have an impact on the mixing response recorded at the burner outlet which is not present when reacting flows are considered.

To ensure a good model identification, the ratio of step amplitude to the relative concentration oscillation amplitude ($\approx 10\%$) has to be sufficiently high. For this reason, an almost full step ($\approx 90\%$ of end concentration) was selected to record the mixing transfer function, as shown in Fig. 7.3. This strong step may be seen as a drawback of the method, in particular if the mixing pattern is strongly dependent on the momentum ratio of the jet or if local vortices are induced by the unsteady jet. However, lower step amplitudes did not ensure a sufficiently high signal-to-noise ratio and good parameter identification and, accordingly, were not investigated further.

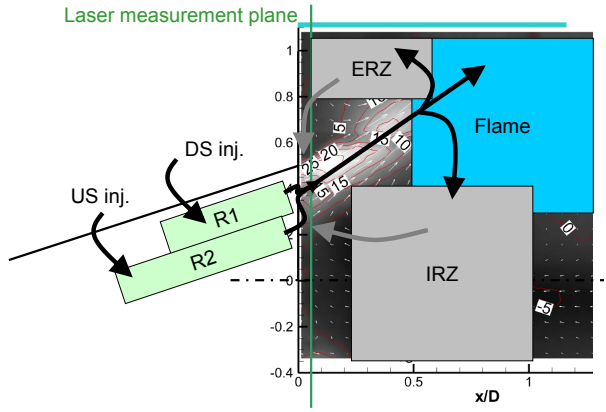

Figure 7.2: Identification of relevant zones influencing the mixing recorded at the burner outlet

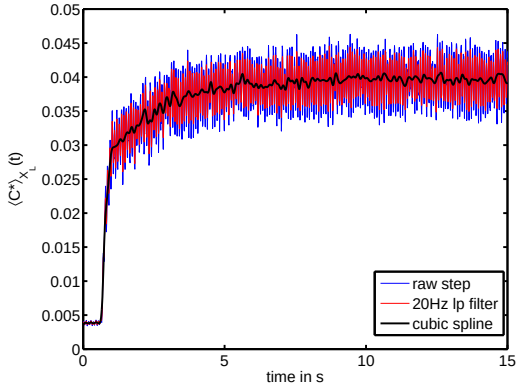

Figure 7.3: Comparison of the raw step response, the low pass filtered response, and the spline interpolated resulting signal of $\langle C^* \rangle_{xL}(t)$ recorded at the outlet for the injection $(\alpha, \beta) = (0, 1)$.

If one step response only is recorded, the phase of the helical structure relative to the fuel step will affect the phase (or mean convective time delay) of the outlet response. To obtain a mean mixing transfer function and (at least) partly remove the influence of the helical structure, three step responses are recorded. Each raw step response is then filtered with a

zero phase low pass filter followed by a spline interpolation (Fig. 7.3). Since the model identification uses values scaled between 0 and 1 (see below), the step responses are then normalized as

$$\langle C^* \rangle^*(t) = \frac{\langle C^* \rangle(t) - (C^*_\infty)_{low}}{(C^*_\infty)_{high} - (C^*_\infty)_{low}}\,, \tag{7.2}$$

with $(\cdot)_{low}$ and $(\cdot)_{high}$ being the steady states before and after the step response. The normalized concentration satisfies $\langle C^* \rangle^*(t) \in [0 - \epsilon_1, 1 + \epsilon_2]$, with $\epsilon_i << 1$ after proper filtering.

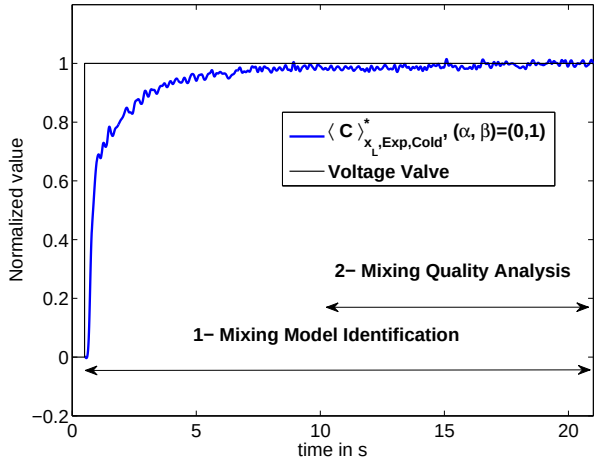

Figure 7.4: Post-processed and averaged step response of the spatially-averaged concentration recorded at the burner outlet as well as valve command signal

The three responses are then averaged resulting in a single step response shown in Fig. 7.4. This filtered and averaged step response still shows an averaged convective time delay[1], which is approximately 6 times higher than the ideal plug flow time delay of the burner $\tau_{ref} = L/U_0 = V_{tot}/Q_{tot}$. It was identified that this effect was a consequence of the response of the

[1] this time delay is calculated in non-recirculating flows with $\tau = \int_0^\infty (1 - \langle C^* \rangle(t))\, dt$[Dan52]

recirculation zones and of the non-ideal step response of the fuel injection. As the recirculation zone effect is inherent to the system, it was investigated first. The response of the fuel injection is presented in more detail in Sec.7.1.5.2 below.

7.1.3 Mixing model with recirculation zone

A simple test with two outlet chamber diameters, of 145 and 200 mm (Fig. 7.5), confirms the influence of the recirculation zone geometry on the recorded response: the modification changes the volume of the combustion chamber and hence the recirculation zone volume, with negligible changes in the flow field inside the burner down to the measurement plane. The low-pass filtered and average responses recorded by the camera are presented in Fig. 7.6. While the start of the curve is similar for both cases, the 145 mm combustion chamber reaches the steady value earlier than the 200 mm combustion chamber. This is a consequence of the smaller volume of the external recirculation zone of the 145 mm chamber.

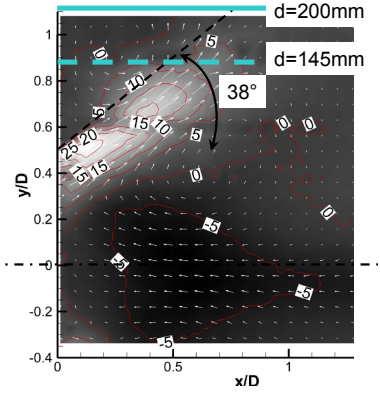

Figure 7.5: Geometry of the two configurations used for the validation of the model

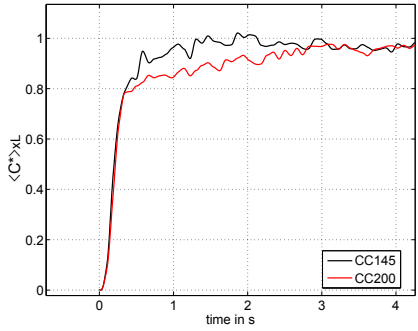

Figure 7.6: Average step responses of the two combustion chambers, with diameters of 145 mm (CC145) and 200 mm (CC200).

The mixing response of the recirculation zones explains why trying to record the mixing transfer function directly will not yield the correct results as the response of the recirculation zone recorded here is not present in reacting conditions. To extract the pure convective time delays without the influence of the recirculation zone, as well as understand the impact of a recirculating flow on the recorded transfer function, a model is needed. This model should also capture the fuel split used to control the mixing profile. These requirements lead to the model being based on connecting three reactors as illustrated in Fig. 7.7.

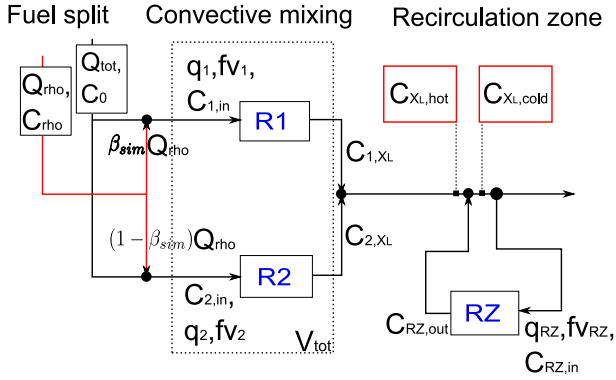

Figure 7.7: Mixing model of the burner for identification of the experimental mixing transfer function

Such a model is similar to the one presented by Ferro et al. [FPG01], who modeled the residence time distribution of vessels presenting two main peaks with two parallel reactors. The only difference is that a reactor modeling the recirculation zone is used here while Ferro et al. added a reactor simulating the dead volume of the system. Each reactor response is modeled by the 1D convection-diffusion described by Eq. 2.57. The reactors $R1$ and $R2$ describe the convective mixing inside the burner, while the reactor RZ describes the impact of the two recirculation zones, IRZ and ERZ.

Some of the parameters of the model are physically set (such as the dye volume flow Q_{rho} and its concentration C_{rho}, as well as the total water volume flow Q_{tot}, which does not contain any dye) or approximated from the

geometry (like the total volume V_{tot}). The other parameters are unknowns which have to be identified from the experimental curves.

These unknown parameters are: Pe_1, Pe_2, Pe_{RZ}, the turbulent Péclet numbers of the three reactors, $fv_1 = \frac{V_1}{V_1+V_2} = \frac{V_1}{V_{act}}$ and $fv_2 = \frac{V_2}{V_{act}}$ the volume fractions of the reactors 1 and 2. V_{act} is the active volume of the burner which satisfies $V_{act} \leq V_{tot}$. The dead volume, which does not participate in the mixing then satisfies $V_{dead} = V_{tot} - V_{act}$. To reduce the number of unknowns, it was assumed that $V_{act} = V_{tot}$ and hence $fv_1 + fv_2 = 1$. q_1 and q_2 are the volume flow fractions which satisfy $q_1 = \frac{Q_1}{Q_1+Q_2} = \frac{Q_1}{Q_{tot}}$ and $q_2 = 1 - q_1$. The recirculation zone reactor also introduces two unknowns, the recirculation zone volume fraction defined as $fv_{RZ} = \frac{V_{RZ}}{V_{tot}}$ and the recirculation zone volume flow fraction $q_{RZ} = \frac{Q_{RZ}}{Q_{tot}}$. With these definitions, it is possible that $fv_{RZ} > 1$ or $q_{RZ} > 1$. One supplementary parameter, β_{sim} is used to simulate the real fuel distribution. In the end, 8 unknown parameters (β_{mod}, Pe_1, Pe_2, Pe_{RZ}, fv_1, q_1, fv_{RZ}, q_{RZ}) must be identified from the step response.

With the previous definitions, the bulk residence time τ_i of each reactor satisfies

$$\tau_i^* = \frac{\tau_i}{\tau_{ref}} = \frac{fv_i}{q_i}\,, \tag{7.3}$$

with $\tau_{ref} = V_{tot}/Q_{tot}$. The unknown parameters can be reformulated as (β_{mod}, Pe_1, Pe_2, Pe_{RZ}, τ_1, τ_2, τ_{RZ}, τ_{ref}). As the volume flows Q_1 and Q_2 of the reactors $R1$ and $R2$ are slightly influenced by the the fuel distribution, their values may vary slightly over the distributions tested.

The response of interest for modeling the reacting flow is $C_{xL,hot}$, with no influence of the recirculation zone, while the response measured in cold flow is $C_{xL,cold}$. How the expression of $C_{xL,hot}$ can be obtained as a function of $C_{xL,cold}$ is described below.

A mole flow rate balance at the outlet of the reactors $R1$ and $R2$ gives the expression of $C_{xL,hot}$ as

$$q_1 \cdot C_{1,xL} + q_2 \cdot C_{2,xL} = C_{xL,hot}\,. \tag{7.4}$$

If the inlet concentration fluctuations are generated by fuel inlet concentration fluctuations only (the case of the present cold flow measurements), then $q_1' = q_2' = 0$. Linearizing Eq. 7.4, taking its Fourier transform and using the mixing transfer function of single reactor $MTF_i = \hat{C}_{i,xL}/\hat{C}_{i,in}$ leads to the expression

$$\overline{q_1}\hat{C}_{1,in}MTF_1 + \overline{q_2}\hat{C}_{2,in}MTF_2 = \hat{C}_{xL,hot}\,. \tag{7.5}$$

The inlet concentration of reactor $R1$ satisfies

$$C_{1,in} = \frac{C_{rho}Q_{rho}\beta}{Q_1\left(1+\beta Q_{rho}/Q_1\right)} \tag{7.6}$$

If $C_{rho}' = \beta' = Q_1' = 0$ and if the higher order terms are neglected, one obtains for the Fourier transformation of the inlet concentration fluctuations

$$\hat{C}_{1,in} = \hat{Q}_{rho}\frac{\overline{C_{1,in}}}{\overline{Q_{rho}}}\,. \tag{7.7}$$

Similar expressions are obtained for $\hat{C}_{2,in}$ if β is replaced by $(1-\beta)$. Replacing Eq. 7.6 in Eq. 7.7 and inserting the resulting expression in Eq. 7.5 (and similarly for $\hat{C}_{2,in}$) leads to the expression

$$C_{rho}\hat{Q}_{rho}\left[\frac{\beta MTF_1}{1+\beta Q_{rho}/Q_1} + \frac{(1-\beta)\,MTF_2}{1+(1-\beta)\,Q_{rho}/Q_2}\right] = \hat{C}_{xL,hot}\,(Q_1+Q_2)\,. \tag{7.8}$$

When fulfilling the jet-to-cross flow momentum similitude, the ratio Q_{rho}/Q_{tot} typically satisfies $Q_{rho}/Q_{tot} \approx 0.05$. As in the present configuration $Q_1 \approx 0.5Q_{tot}$ and $\beta \leq 1$, then $\beta Q_{rho}/Q_1 < 0.1$ and it, as well as $(1-\beta)Q_{rho}/Q_1$, can be neglected in Eq. 7.8, which simplifies further to

$$MTF_{hot} = \frac{\hat{C}_{xL,hot}\,(Q_1+Q_2)}{C_{rho}\hat{Q}_{rho}} = \beta MTF_1 + (1-\beta)\,MTF_2\,, \tag{7.9}$$

where MTF_{hot} is the transfer function of the dye molar flux in "reacting conditions" (i.e., without recirculation zones).

Further, using a second molar balance for the recirculation zone, which also neglects volume flow fluctuations, one obtains

$$\hat{C}_{xL,tot}Q_{tot} + \hat{C}_{xL,RZ,out}Q_{RZ} = \hat{C}_{xL,cold}\left(Q_{hot} + Q_{RZ}\right) . \tag{7.10}$$

After multiplying by the factor $1/\left(C_{rho}\hat{Q}_{rho}\right)$, and defining the recorded mixing transfer function $MTF_{xL,cold,rec}$ as

$$MTF_{xL,cold,rec} = \hat{C}_{xL,cold}/\left(C_{rho}\hat{Q}_{rho}\right) , \tag{7.11}$$

the final expression of the cold mixing transfer function reads

$$MTF_{xL,cold,rec}Q_{tot} = \frac{MTF_{hot}}{1 + q_{RZ}\left(1 - MTF_{RZ}\right)} , \tag{7.12}$$

with MTF_{hot} taken from Eq. 7.9. As shown in Sec. 3.3.3.2, the measurement technique does not record the *scalar flux* through the measurement plane but only the concentration. Only a combined 3D velocity / concentration measurement technique, much more complicated to handle than the HS-LIF system alone, can give access to this value. For this reason, it was assumed that the velocities at the burner outlet could only take the value of the mean bulk velocity and the passive scalar molar flux is proportional to the mean concentrations recorded at the outlet[2]. The normalized cold transfer function $MTF^{*}_{xL,cold,rec}$ then satisfies

$$MTF^{*}_{xL,cold,rec} = MTF_{xL,cold}Q_{tot} , \tag{7.13}$$

and the final expression recorded $MTF^{*}_{xL,cold,rec}$ reads:

$$MTF^{*}_{xL,cold,rec} = \frac{MTF_{hot}}{1 + q_{RZ}\left(1 - MTF_{RZ}\right)} . \tag{7.14}$$

For reasons of brevity, the expression $MTF^{*}_{xL,cold,rec}$ is referred to as $MTF_{xL,cold}$ in the coming sections. The normalized concentration response

[2]If the scalar flux can be measured, then the sum of the local molar flux over the flow cross-section of area $\mathcal{A}$ should be taken into account in Eq. 7.4 or Eq. 7.12 as $\int_{\mathcal{A}} \hat{C}_{xL,cold,rec}(\boldsymbol{x})u(\boldsymbol{x})\,dA$ to obtain a more exact scalar flux transfer function.

$\hat{C}^*_{xL,cold}$ reads also

$$\hat{C^*}_{xL,cold} = MTF_{xL,cold}\hat{C^*}_{in}\,, \tag{7.15}$$

A fit of the recorded cold mixing transfer function with the theoretical model is performed to identify the parameters of the mixing model. With the gained parameters, the mixing transfer function in reacting conditions MTF_{hot} is obtained with help of Eq. 7.9.

7.1.4 Variation of the parameters of the mixing model

7.1.4.1 Cold response

Figure 7.8 illustrates the impact of different parameter combinations $[Pe_{RZ}, q_{RZ}, fv_{RZ}]$ on the cold response $MTF_{xL,cold}$. The frequency is normalized by the reference residence time of the burner τ_{ref}, giving the axial Strouhal number $St = f\tau_{ref}$. This axial Strouhal number, which varies slightly from the standard definition $St = \frac{fD}{u_0}$, is employed in the next section to normalize the time.

The recirculation zone parameters obviously have an impact on the amplitude of the transfer function. However, a small impact on the transfer function phase is also visible, especially in the low-frequency domain. The amplitude recorded for $St > 0.3$ is dependent on the relative volume flow q_{RZ}, high values leading to low amplitude responses (green curve compared to the blue, red and gray ones), while the low-frequency response is mainly dependent on fv_{RZ} and Pe_{RZ}, high values leading to a stronger damping close to $St = 0$ (red) than cases with a lower relative volume (blue). Regarding the impact on the phase, a strong relative volume fv_{RZ} increases the relative deviation from $arg(MTF_{hot})$. The cut-off frequency from which the impact of the RZ on the phase disappears decreases with decreasing ratio $q_{RZ}/fv_{RZ} = \tau_{RZ}$. Hence, the response recorded at the outlet of the burner may be strongly affected by the recirculation zone parameters and justifies the use of the model to extract the *hot* mixing transfer function.

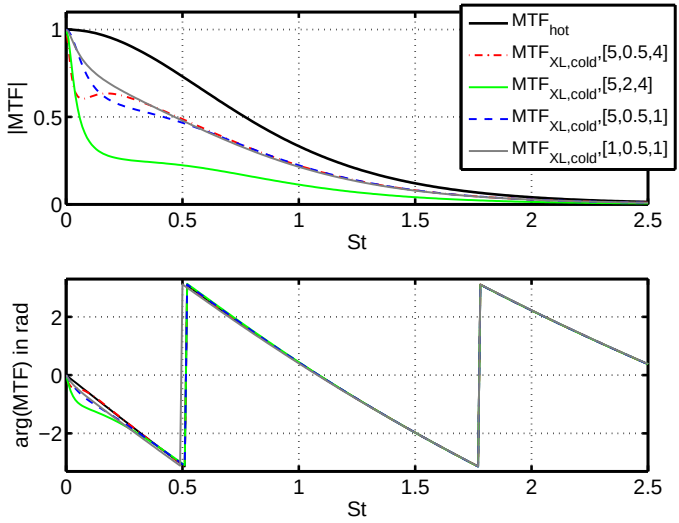

Figure 7.8: Comparison of the impact of the recirculation zone on the transfer function $MTF_{xL,cold}$ for different combinations $[Pe_{RZ}, q_{RZ}, fv_{RZ}]$. Other parameters set: Pe_1=Pe_2=30, q_1=fv_1=β=0.5.

7.1.4.2 Mixing transfer function without recirculation zones

The variation of the reactor parameters $[Pe_1, Pe_2, q_1, fv_1]$ can generally be assessed in the design phase of the burner. As numerous combinations are possible, we focus on two questions: first, if an equivalence ratio is set for each reactor, how does MTF_{hot} evolve if the air distribution (or power output in combustion) is varied between the reactors? Second, if an air distribution is set, how does MTF_{hot} evolve if the fuel distribution is varied?

Part of the response to the first question may be obtained from Fig. 7.9. The response of two identical reactors with a 50-50 air distribution, i.e. $q_1 = q_2 = 0.5$, (solid black line) is compared to a 66-34 air distribution (dashed line) and to a 75-25 air distribution. Assuming a constant geometry (reactor length) and flow properties (diffusion and Schmidt number), the Péclet numbers are adjusted with the mean flow velocity of each reactor.

A constant and identical equivalence ratio through both reactors is ensured if $\beta = q_1$. The amplitude of the MTF_{hot} can be only marginally varied over the frequency range. An amplitude reduction in the low-frequency range is compensated by an amplitude increase in the high-frequency range. However, going from the 50-50 to the 75-25 air distribution reduces the total phase and this property may be used to stabilize an unstable combustor.

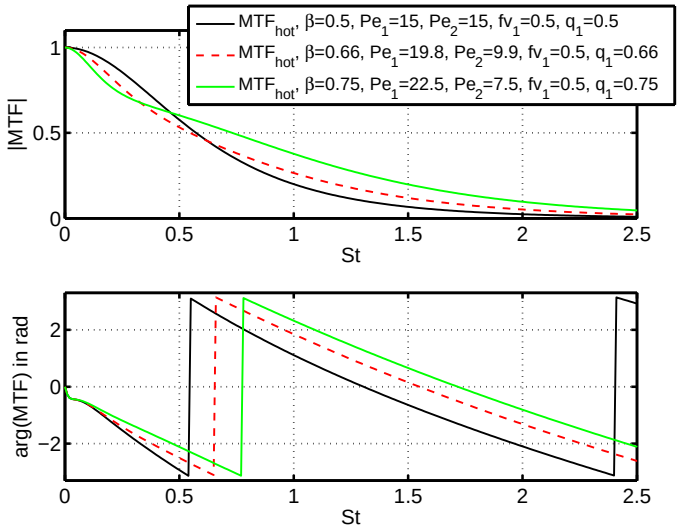

Figure 7.9: Impact of the air flow distribution on the hot mixing transfer functions MTF_{hot} for a constant and equal equivalence ratio (or mean concentration) through each reactor

Regarding the second question, Fig. 7.10 also provides at least a partial answer. To generate these curves, only the fuel distribution β is varied while a 50-50 air distribution is assumed. The 4 other parameters relevant for the reacting mixing transfer function correspond approximately to the typical values of the burner with (Pe_1, Pe_2, fv_1, q_1)=(30, 15, 0.66, 0.5). These parameters mean also that the normalized bulk residence time of $R1$ and $R2$ are equal to $\tau_1^* = 1.32$ and $\tau_2^* = 0.68$ respectively. The amplitude of the response is slightly influenced by the fuel split while the phase varies by more than 50% in the low-frequency range. The amplitude of the phase variation may thus be sufficient to avoid an unstable behavior of the

combustor. This justifies the control method used in the present study. However, if the fuel is varied over such a wide range, care should be taken that the mixing quality at the burner outlet is suffiently good to avoid rich mixture zones.

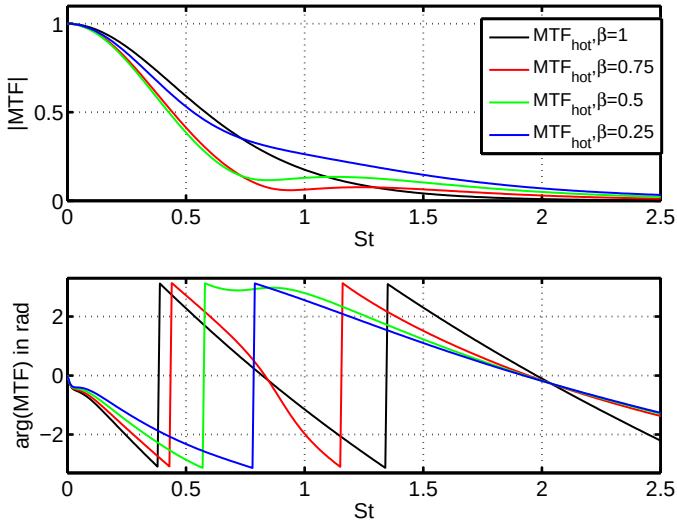

Figure 7.10: Impact of the fuel distribution β on the hot mixing transfer functions MTF_{hot} calculated for the reactor parameters (Pe_1, Pe_2, fv_1, q_1)=(30, 15, 0.66, 0.5)

7.1.5 Model parameters and system identification

7.1.5.1 Parameter identification from geometry and velocity measurements

Recirculation zone The volume of the ERZ and IRZ can be estimated from the angles of the conical jet where the second radial derivative of the axial velocity is equal to zero. One obtains the volumes $V_{ERZ} \approx 1.12 \times 10^{-3}$ m^3 and $V_{IRZ} \approx 0.16 \times 10^{-3}$ m^3. The volume of the flame is estimated to be $V_{fl} \approx 1.71 \times 10^{-3}$ m^3, while the volume of the reactor RZ is estimated to be at least equal to the recirculation zone volume and at most equal to the total volume $V_{ERZ} + V_{IRZ} + V_{fl}$ downstream of the

burner. This leads to the relationship (using the reference volume in the burner $V_{ref} = 3.48 \times 10^{-4}$ m^3)

$$fv_{RZ} = \frac{V_{RZ}}{V_{ref}} \in [3,\, 10]\ . \tag{7.16}$$

The volume flow of the recirculation zone Q_{RZ} is also estimated from (isothermal) PIV measurements from the radial and circumferential integration of the axial velocities. The recirculation volume flow $Q_{RZ}(x)$ satisfies

$$Q_{RZ}(x) = Q^{+}(x) - Q_{tot}\,, \tag{7.17}$$

with Q^{+} being the positive axial volume flow and Q_{tot} the total volume flow passing through the burner. The evolution of Q^{+} in the two main axial planes of the flow ((xy) and (xz)-planes) is depicted in Fig. 7.11. It shows that the positive volume flow increases immediately at the burner outlet, due to the entrained mass flow, reaches a maximum shortly before $x \approx D/2 = 41$ mm and then falls to values close to the total volume flow. The strong non-rotational symmetry of the flow field is the main reason for the offset between the positive volume flows calculated in the (xy) and (xz) planes. By taking the average of the two curves, one can then write

$$q_{RZ} = \frac{Q^{+}}{Q_{tot}} - 1 \in [0.2,\, 1]\ ,\ \text{ for } x \in [5,\, 40]\,. \tag{7.18}$$

The maximal recirculating volume flow Q_{RZ} can be then as high as the main volume flow Q_{tot} at the location $x \approx D/2$.

Air flow split The volume flow passing through each reactor $R1$ and $R2$ is experimentally difficult to measure because of the limited access and the complex flow field at the inlet slots. Thus, the estimation is performed from CFD simulations [SOK^{+}10] by integrating the velocity perpendicular to the slot within the slot. As there is no physical split between the reactors, their boundary was set at the junction of the two fuel injection chambers. The relation

$$q_1 \approx q_2 \approx 0.5 \tag{7.19}$$

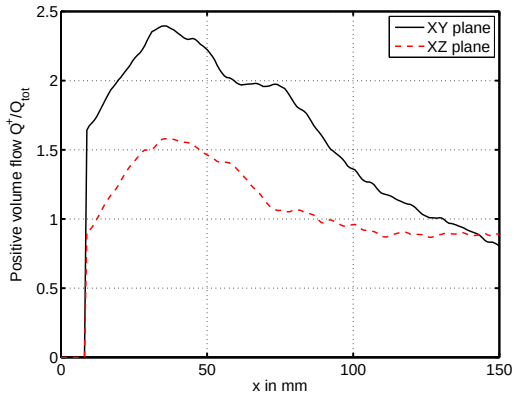

Figure 7.11: Positive volume flow Q^+, normalized by Q_{tot}, and calculated at the burner outlet from PIV measurements in two axial planes (xy) and (xz)

is obtained and is used further to reduce the number of unknowns in the model fitting to 7 parameters.

7.1.5.2 Response of the fuel injection

The 8 parameters previously mentioned (and reduced to 7 using Eq. 7.19) must be identified from the experimental step responses recorded for the different injection configurations. As the FFT of a step function leads to numerical difficulties [Kar02], the pulse response of Eq. 7.15 is calculated first. In addition, the derivative of the experimental step response is calculated and used for parameter identification. That way, the numerical problems are overcome.

A typical step function recorded at one injection hole is depicted in Fig. 7.12 and some images of the step are shown in Fig. 7.13 The initial analysis of the curve shows that the response is very similar to that of a step function. Different injection configurations were tested and the delay between the signal and the concentration response was found to be around around 28 ms, the rising time of the step being approximately 50 ms. This means that a delay of approximately 78 ms is present between the pulse signal and the full volume flow of the injection. With respect to a reference residence

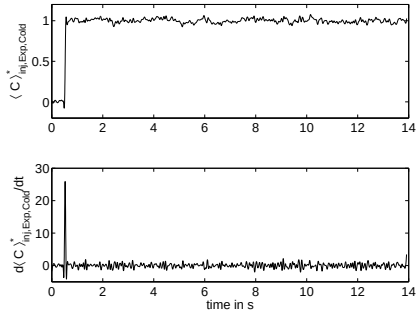

Figure 7.12: Filtered response of the dye injection to a step in the valve command for the injection configuration $(\alpha, \beta) = (0, 0.3)$

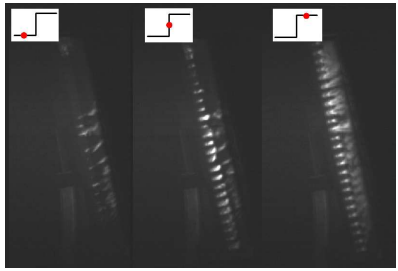

Figure 7.13: Instantaneous images of the fuel injection during volume flow steps of the dye line

time of 0.146 ms, the error is not negligible, but a positive finding is that it is identical for all the configuration tested. Furthermore, because of the length of the injection tube, it was also necessary to test whether the dye reached the injection holes at the same time at each injection location. The images in Fig. 7.13 show the evolution of the injection before, during, and after the step for an injection configuration $(\alpha, \beta) = (0, 0.3)$. The dye flows from the bottom to the top and a small time delay between the bottom and upper holes is present but is always less than 20 ms and was thus considered negligible.

As the step response of the fuel injection is not a perfect Heaviside function, it is approximated with an analytical function close to the Heaviside function which reads

$$\tilde{H}(t) = \frac{1}{1 + \exp\left(-2k\left(t - t_0\right)\right)}\,. \tag{7.20}$$

Its time derivative is then employed for the identification process. The parameter k is used to adjust the slope of the step and t_0 to translate the step so that $0 < H(0) << 1$. The cold experimental RTD were found to be the closest to the RTD calculated from the CFD simulations of Schrödinger

et al. [SOK+10] with $k = 37$ and $t_0 = -3$. The derivative of the inlet concentration step based on $\tilde{H}(t)$ is shown in Fig. 7.14.

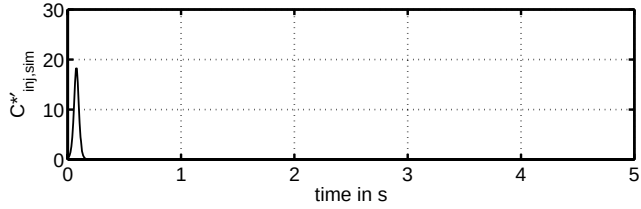

Figure 7.14: Derivative of the inlet concentration step based on $\tilde{H}(t)$ with $k = 37$ and $t_0 = -3$

7.1.5.3 Fitting procedure

Figure 7.15 summarizes the post-processing steps from the recording of the step response to the parameter identification of the model. The main idea of the processing is first to obtain a good approximation of the FFT of the experimental and model data and, second, to obtain a good and robust estimation of the parameters of the modeled transfer function $MTF_{xL,cold}$. The later model is then used to calculate the mixing transfer function in reacting conditions MTF_{hot}.

First, for each point investigated, 3 experimental step responses are recorded at a frame rate of 125 Hz. This increases the measurement accuracy and reduces the dependency of the step on the initial position of the helical structure. Each step response is low-pass filtered at 20 Hz and a spline interpolation is applied to reduce the oscillations induced by the helical structure, which are not taken into account in the model. The three step responses are averaged together, producing an average step response which is normalized between 0 and 1. The result is called $C^*_{xL,cold}$, latter denoted simply $C_{xL,cold}$. The derivative of the response is calculated giving $C'_{xL,cold}$, as well as the FFT response of the derivative $\hat{C}'_{xL,cold}$.

The response $\hat{C}'_{xL,cold,mod}$ of the model with transfer function $MTF_{xL,cold}$ is calculated from the modeled pulse response of the fuel injection response

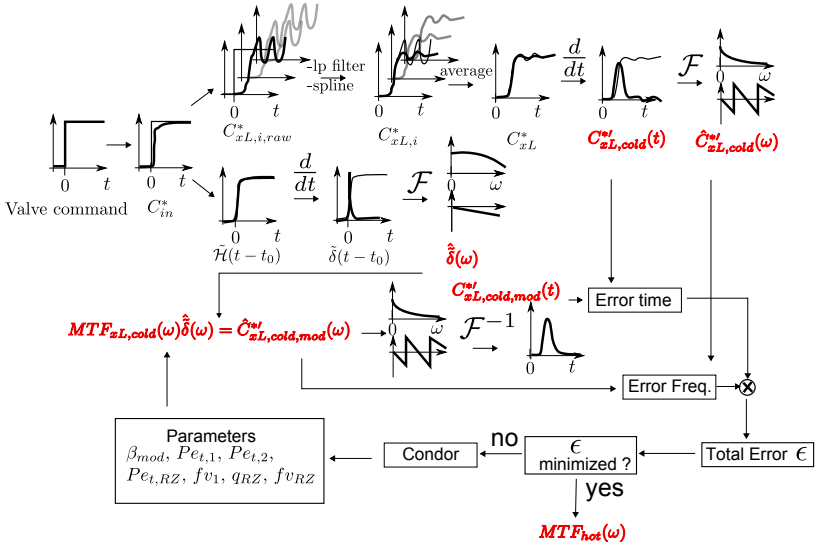

Figure 7.15: Post processing of the high-speed step response to identify the parameters of the transfer function $MTF_{xL,cold}$

$\hat{\tilde{\delta}}_f$ as

$$\hat{C}'_{xL,cold,mod} = MTF_{xL,cold}\hat{\tilde{\delta}}_f \,. \tag{7.21}$$

The inverse FFT is also calculated to give the response to the experimental pulse, $\tilde{C}'_{xL,cold}$. The modeled and temporal pulse responses describe the temporal error of the system and the corresponding modeled and experimental FFT responses describe the error in the frequency domain. Both errors are multiplied together to calculate the total error of the fit which is then minimized by the optimizer CONDOR [BB05][3], running under MATLAB, by adjusting the parameters (β, Pe_1, Pe_2, Pe_{RZ}, fv_1, q_{RZ}, fv_{RZ}) of the transfer function $MTF_{xL,cold}$.

The time and frequency errors are calculated with a weighted form of the least mean square optimization. Using a cut-off time and a cut-off frequency, it is possible to take only the high-frequency and low-frequency part of the pulse response, respectively. The time response should be well

[3]CONDOR is a constrained, nonlinear algorithm which has the advantage of reducing the number of function evaluations compared to standard optimization algorithms.

approximated immediately after the pulse and the weight of the measured points in the error should decrease with increasing time. The same approach holds in the frequency domain where the low frequencies exhibit little noise. Values above a certain limit were not taken into account for the fit, and typical cut-off values were $(\tau/\tau_{ref})_{lim}$= 13 and St_{lim}=0.3. The resulting fit had the strength of being fairly insensitive to the initial conditions and the cut-off values used.

7.1.5.4 Model parameters identification

A typical transfer function of the step derivative $\hat{C}'_{xL,cold}$ with its identified function $\hat{C}'_{xL,cold,mod}$is presented in Fig. 7.16 and the corresponding step and pulse responses are shown in Fig. 7.17. Both figures confirm that the quality of the fit in both time and frequency domains is very good. Also shown in Fig. 7.17 are the responses of the model without recirculation zones, $C_{xL,hot,mod}$ and $C'_{xL,hot,mod}$ (in blue).

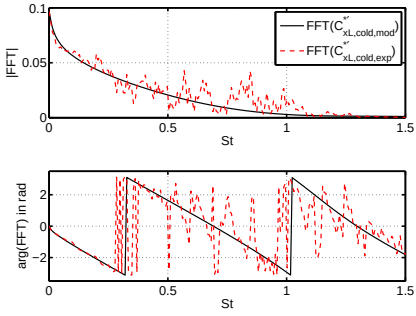

Figure 7.16: Experimental ($\hat{C}'_{xL,cold}$, dashed red) and modeled ($\hat{C}'_{xL,cold,mod}$, solid black) transfer functions of the derivative of the concentration response. Injection configuration $(\alpha, \beta) = (0, 0.7)$.

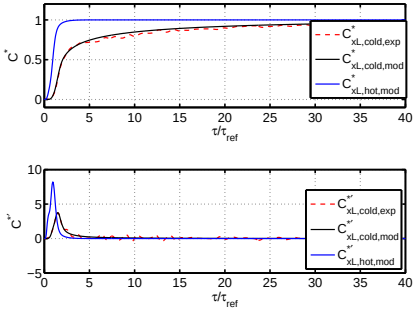

Figure 7.17: Temporal step response (top) and its time derivative (bottom) with the identified model curves

The resulting transfer functions constituting $MTF_{xL,cold}$ are presented in Fig. 7.18. The injection configuration is (α, β)=(0, 0.7) and the fitting parameters are (β, Pe_1, Pe_2, Pe_{RZ}, fv_1, q_{RZ}, fv_{RZ})=(0.47, 40, 4.7, 0.24, 0.51, 1.2, 5.76). The curves show that two reactors with two distinct time delays build the response $MTF_{xL,hot}$. Reactor $R1$ is characterized by a higher Péclet number and a smaller mean bulk residence time, fv_1/q_1, than those of reactor $R2$. The combination of the two reactors, which gives the transfer function $MTF_{xL,cold}$, is closer to the response of reactor $R2$ regarding the amplitude and closer to that of reactor $R1$ in terms of the phase. Some cancelation effects also lead to the total amplitude response being smaller at high St numbers than the amplitude of the two reactors taken together, which shows the positive effect of combining different reactors with different characteristic reference times and Péclet numbers.

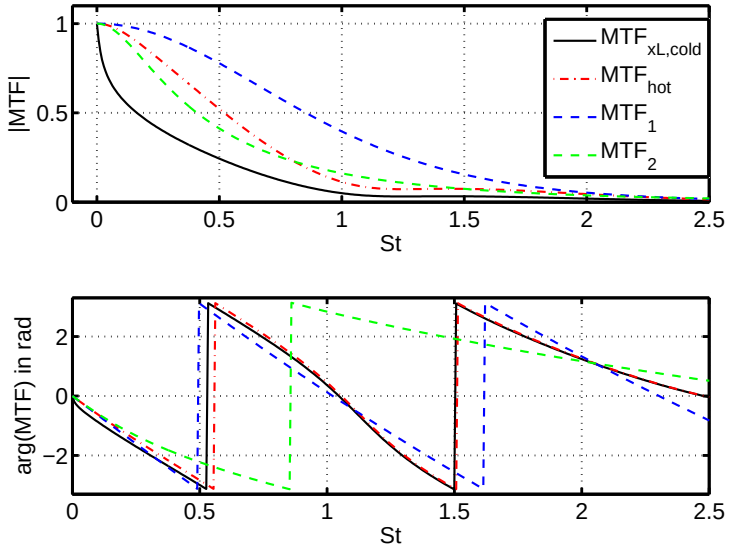

Figure 7.18: Typical transfer functions $MTF_{xL,cold}$, $MTF_{xL,hot}$, MTF_1, MTF_2, obtained for the identified transfer function shown in Fig. 7.17

The whole measurement and analysis procedure is then applied for one combination main/fuel volume flow (8.55 m^3/h for the main and 300 l/h for

the fuel) on 9 injection configurations which are distributed as follow: ($\alpha = 0, \beta = [0, 0.2, 0.35, 0.5, 0.7, 1]$), ($\alpha = 0.5, \beta = [0.5, 0.75]$), ($\alpha, \beta$)=$(1, -)$. To ensure reproducibility and reliability in the fitting method, the identification of each parameter is performed with the same initial values. No adjustments are made to optimize one configuration independently from the others. The (α, β)-maps for the 7 parameters identified are generated from linear interpolation of the measured points and are shown in Fig. 7.19.

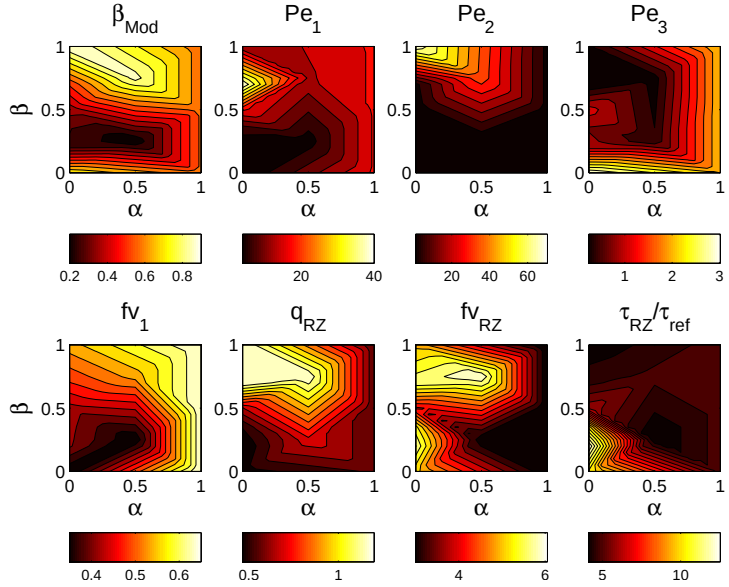

Figure 7.19: Identified parameters of the mixing model for different (α, β) injection configurations

First, the change in fuel distribution is well captured by the parameter β_{Mod} with values ranging from 0.2 to 0.9. The highest values are obtained for the upstream-dominated injection and the lowest for downstream-dominated injection. As the values of β_{Mod} do not take the whole range (0-1), the reactors $R1$ and $R2$ are not completely decoupled as assumed in the model. The turbulent Péclet number of reactor $R1$, Pe_1, ranges from 4 to 40 and Pe_2 from 3 up to 70. The Péclet number of the recirculation zone

is, as expected, quite low ($Pe_{RZ} \in [0.2, 3]$), indicating a low convection velocity and/or a high turbulent diffusion. The normalized residence time of reactor $R1$, which is equal to $fv_1/q_1 = fv_1/0.5$ remains centered around 1, decreasing when $\alpha \to 0$ and $\beta \to 0$, increasing when $\alpha \to 1$.

The normalized volume flow $q_{RZ} = Q_{RZ}/Q_{tot}$ indicates that the recirculating volume flow is approximately 0.6 times the reference volume flow when the standard or upstream injections are used. This value increases up to very high value of $q_{RZ} = 1.2$ when only upstream injection is used. However, at the same time, the relative volume of the recirculation zone, fv_{RZ} also increases strongly and the normalized recirculation time τ_{RZ}/τ_{ref} remains almost unchanged when compared to the standard injection. A faster homogenization of the recirculation flow with the fresh incoming flow is thus obtained with upstream-dominated injection, while downstream injection results in an increase in the recirculation time by a factor 2. This increase is from a geometrical point of view possible, as the characteristic times of the IRZ and ERZ, which are not split in the mixing model, satisfy $\tau_{ERZ}/\tau_{IRZ} \approx 1.75$ [4]. As reactors $R1$ and $R2$ mainly feed the IRZ and the ERZ respectively, homogenization is faster with injection mostly through reactor $R1$.

This modeling and fitting approach helps us to understand the mixing mechanisms inside and outside the staged burner, information which cannot be obtained with a standard velocity measurement technique. The unsteady HS-LIF measurement technique allows an experimental cold mixing model to be obtained and its parameters to be identified. The parameters presented in Fig. 7.19 can then be used to estimate the mixing transfer function of the different fuel injections.

7.1.6 Hot mixing transfer function

The mixing transfer functions without the impact of the recirculation zone, $MTF_{xL,hot}$, can then be calculated. They are presented in Fig. 7.20 and Fig. 7.21 for the upstream-dominated injections and downstream-dominated

[4] The volume ratio of the ERZ to the IRZ in cold flow satisfies $V_{ERZ}/V_{IRZ} \approx 7$ and the integral mass flow ratio of the ERZ to the IRZ just downstream of the laser location, $Q^-_{ERZ}/Q^-_{IRZ} \approx 4$.

injections respectively. The standard injection configuration is displayed on both graphs for comparison. Regarding the low combustion instability

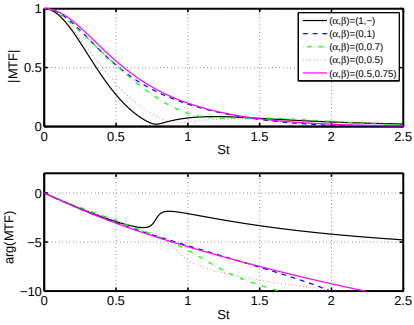

Figure 7.20: Amplitude and phase of $MTF_{xL,hot}$ for the upstream-dominated injections

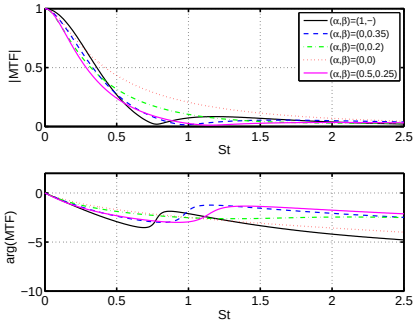

Figure 7.21: Amplitude and phase of $MTF_{xL,hot}$ for the downstream-dominated injections

frequencies obtained in the combustor ($f \leq 150\,\text{Hz}$), as well as the maximum bulk residence time achieved in the present setup ($\tau_{ref,CC}$ =4.79 ms), the range of Strouhal numbers which should be considered is $St \in [0,\ 0.75]$. A single time delay τ can be then estimated from the slope of the phase until $St \approx 0.7$. The resulting map of the normalized time delays τ/τ_{ref} as a function of the fuel distribution is depicted in Fig. 7.22. It shows that changing the injection from an upstream-dominated one to a downstream-dominated one reduces the convective time delay by approximately 50%. The injection (α, β)=(0,0.5) and the standard injection (α, β)=(1,-), which have very similar mixing properties, both result in a convective time delay approximately equal to $\tau/\tau_{ref} \approx 0.85$. The main tendencies of the mixing inside the burner can thus be considered as well captured.

7.1.7 Variation of the combustion chamber geometry

Finally, the ability of the model to capture the changes in the geometry of the combustor is investigated. The modeled responses of step responses of the standard injection with the combustion chamber diameters d=145 mm and 200 mm (see Fig. 7.6) are depicted in Fig. 7.23. The resulting model parameters are listed in Tab. 7.2.

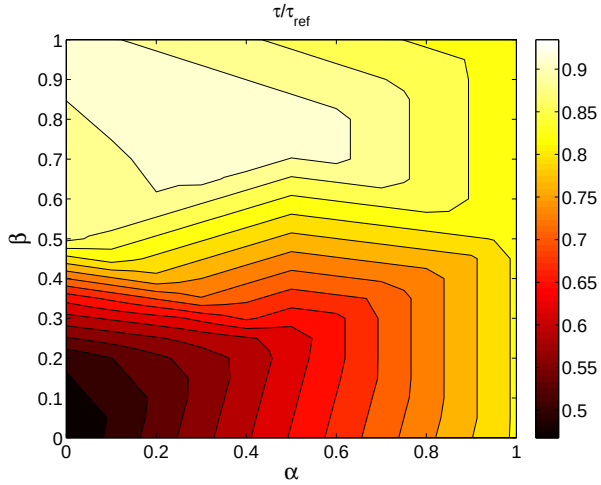

Figure 7.22: Normalized average convective time delay from $MTF_{xL,hot}$of Fig. 7.21 and Fig. 7.20 assuming a single time delay until $St \approx 0.7$, $\tau_{ref,WL}$ =146.7 ms

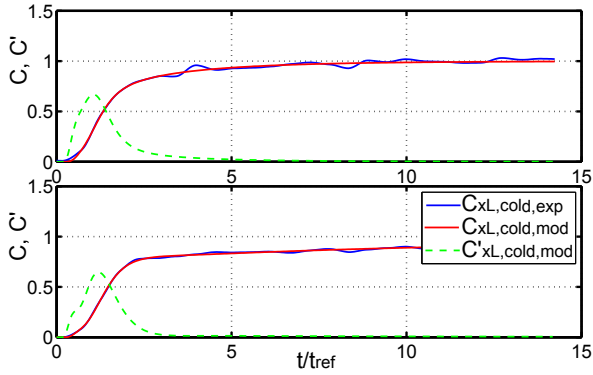

Figure 7.23: Experimental and identified responses of the mixing models for the combustion chamber sizes 145 mm (top) and 200 mm (bottom)

Some of the identified parameters as Pe_1, Pe_2, and Pe_{RZ} are very similar between the two configurations. However, higher discrepancies apear

d	β_{Mod}	Pe_1	Pe_2	Pe_{RZ}	q_1	fv_1	q_{RZ}	fv_{RZ}
145 mm	0.43	23	7.7	1.5	0.18	0.23	0.42	0.77
200 mm	0.82	16	9.8	1.6	0.47	0.66	0.24	3.2

Table 7.2: Parameters obtained from the fit of the step responses of the two combustion chamber diameters d=145 and 200 mm.

for the parameters β_{Mod}, q_1, and fv_1 which may be due to the unperfect fitting immediately at the start of the step response of the 145 mm combustions chamber. However, the two last parameters, q_{RZ} and fv_{RZ}, which describe the long tail of the curves, are less subject to fitting errors. They show that the bulk residence time of the recirculation zones, τ_{RZ}, is then approximately 7.3 times lower with the small combustion chamber than with the large one.

If a comparison is made from a geometrical point of view, neglecting the volume of the IRZ, which represents only around 10% to 20% of the total volume of the recirculation zones, the ratio of the recirculation zone volumes is around $V_{RZ,200}/V_{RZ,145} \approx 2.2$ and the reactor length ratio approximately satisfies $L_{RZ,200}/L_{RZ,145} = r_L \in [2, 3.5]$ (a ratio smaller than the ratio of the perimeter of the transversal sections of the recirculation zones). As the Péclet numbers identified are very similar, and assuming that the turbulent diffusion properties are independent of the recirculation zone length, it follows that $\tau_{RZ,200}/\tau_{RZ,150} = r_L^2 \in [4, 12.25]$. The characteristic time ratio of 7.3 previously identified falls within that range and confirms that the model is able to capture the mixing response of the system burner-combustion chamber.

7.2 Flame transfer function estimation

Now that a mixing transfer function has been recorded in the water test rig, the question arises as to how to draw the link with the flame response in the combustor. Figure 7.24 is a schematic presentation of the different time delays involved from the fuel injection down to the flame as well as the OH* distribution recorded by the flame. While the transfer function of the convective time delays down to the laser measurement plane located at

$x = xL$ has been measured, an estimation of the delay from the cold measurement plane down to the flame is now needed to obtain an estimation of the flame transfer function in the combustor.

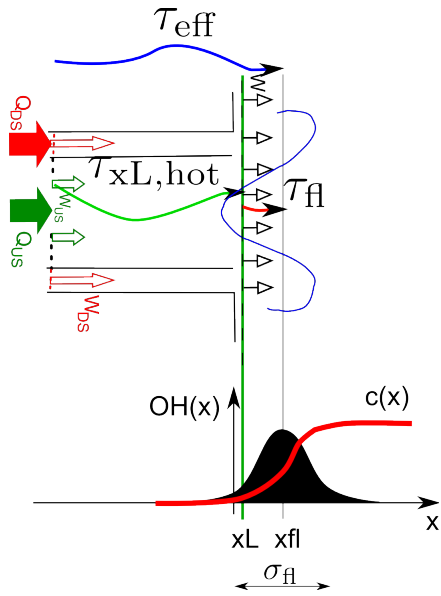

Figure 7.24: Schematic diagram of the time delays involved in the model as well as OH*(x) distribution and estimated reaction progress variable c

The following questions should be answered prior to any modeling attempt:

1. Where does the flame stabilize in the combustor?
2. What is the impact of the flame on the velocity field upstream of the reaction zone?
3. Are chemiluminescence images reliable to predict the location of heat release?
4. How can the time delay distribution (the RTD), measured at the burner outlet, be linked to a spatial heat release distribution?

While the two first questions can be answered through measurements of the velocity field and of the OH* chemiluminescence, the two last questions require more careful analysis.

7.2.1 Impact of the fuel injection on flame position and shape for OPA

A general description of the influence of the fuel injection on the flame shape has been shown in Sec. 6.3 for different operating conditions. Here a more detailled description of the flame position an shape for the operating point A is presented. For different fuel injections the radially integrated OH* band-pass emissions $I_{OH,BP}$ is illustrated in Fig. 7.25. The experimental curves are fitted with an exponential function of the form

$$I_{OH,BP} = A \exp(Bx^2 + Cx + d) \tag{7.22}$$

which is a very good approximation to the curves and is plotted below the experimental curves. The profiles show that when the flame stabilizes outside the burner (all curves except the three closest to the burner exit), the axial spreading of the OH* emissions is small. By contrast, the variation in amplitude is much higher.

The flame position x_{fl}, the corresponding maximal OH* intensity $I_{OH^*,BP,max}$, and the flame width, defined by the distance between the axial quartiles of 5% and 95% of the fitted $I_{OH^*,BP}$ distribution, are presented in Fig. 7.26. The images show that the flame stabilizes more downstream when the fuel is equally split between the upstream and downstream mixing paths ($\beta = 0.5$). This is a consequence of the almost perfect fuel/air premixing which requires lower axial velocities to ensure a stable flame. The flame moves slightly upstream when β decreases (downstream injection), while an increase in β from $\beta = 0.5$ to $\beta = 1$ leads to a stronger upstream shift of the flame position (-25 mm). The position of the flame also correlates well with the maximum of OH* intensity, increasing values being observed when the flame moves upstream, confirming that the chemiluminescence is also related to the mixing quality of the fuel with air. The standard fuel injection gives the highest flame width and the flame gets more compact when $\beta \to 0$.

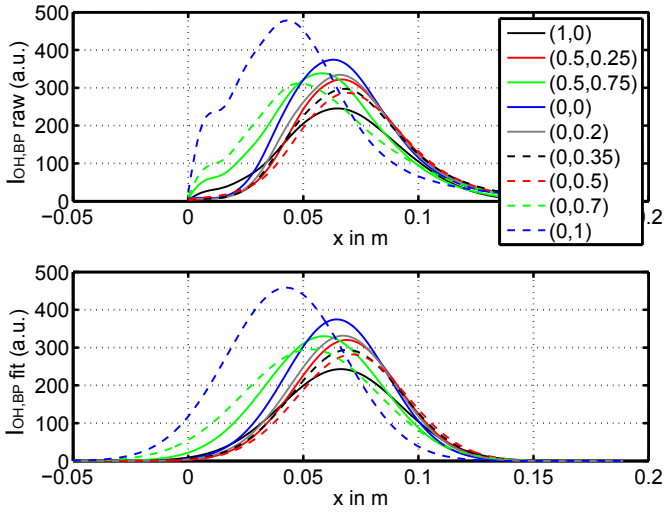

Figure 7.25: Axial distribution of radially integrated $I_{OH,BP}$ for different fuel distributions for the operating point OPA. top: raw $I_{OH,BP}$ signal. bottom: fit of $I_{OH,BP}$ with Eq. 7.22

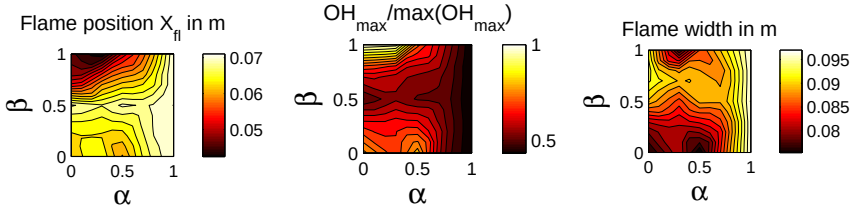

Figure 7.26: Impact of the fuel distribution (α, β) on the flame position at the burner outlet. OPA, stable and short combustor.

7.2.2 Impact of the fuel injection on the velocity field

The impact of the flame on the velocity field measured with PIV has already been presented in Sec. 5. For modeling the heat release response, we are interested in the expression of the velocity at which the reactants are transported toward the flame. To this end, the mean positive axial velocity

$\langle\overline{u^+}\rangle_{A^+}(x)$ was calculated from the PIV recordings as

$$\langle\overline{u^+}\rangle_{A^+}(x) = \frac{\overline{Q^+}(x)}{\overline{A^+}(x)} \tag{7.23}$$

with $\overline{Q^+}(x)$ being the total radially integrated axial volume flow and $\overline{A^+}(x)$ being the area occupied by the positive velocities and delimited by the isoline (in an axial plane) $\overline{u}(\boldsymbol{x})$=0. The profiles $\langle\overline{u^+}\rangle_{A^+}(x)$ taken for a cold case and 4 fuel distributions are shown in Fig. 7.27. The axial decay of the mean velocity is moderate and approximately equal to -0.18 m/s/mm for a flame stabilized downstream of the burner (compared to a decay in cold flow slightly slower than -0.23 m/s/mm). The mean positive convective velocity, $\langle\overline{u^+}\rangle_{A^+}(x)$ is thus slightly higher in reacting cases than in cold flow but is weakly influenced by the flame position, in particular when the flame is anchored outside the burner.

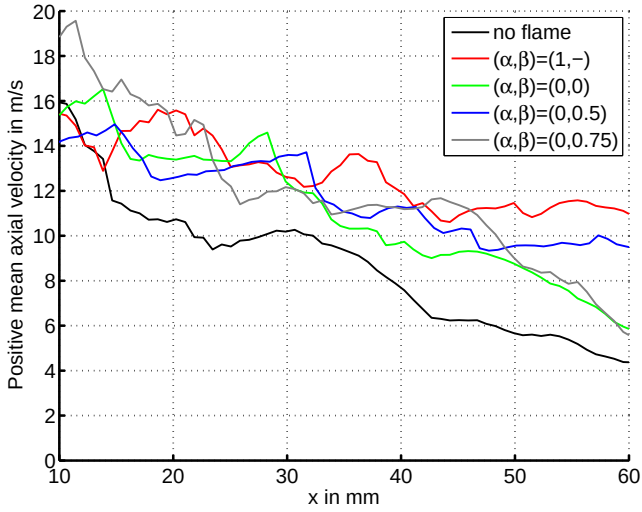

Figure 7.27: Average positive axial velocity $\langle\overline{u^+}\rangle_{A^+}(x)$ for different reacting fuel injections. OPA, stable and short combustor, (xy) plane.

The resulting modeled shape of the positive velocity is shown in Fig. 7.28 and is assumed to be independent of the fuel injection configuration as

the differences in the profiles of the average positive axial velocity shown in Fig. 7.27 remain small. The mean positive outlet velocity of 17 m/s is slightly higher than the mean bulk velocity ($\langle\overline{u^+}\rangle_{A^+}(x)/u_0 = 1.21$) as a consequence of the presence inside the burner of the recirculation zone. The lowest axial velocity is also calculated from the area of positive velocity which, from the PIV measurements, satisfies

$$\overline{A^+}(x) \approx \overline{A^+}_{max} \approx 0.9 A_{cc}\,, \tag{7.24}$$

with A_{cc} being the total cross-section area of the combustion chamber. The velocity is then calculated from the mean bulk velocity of the products $u_{0,prod}$ in the combustion chamber as

$$\langle\overline{u^+}\rangle_{min} = \frac{A_{cc}}{\overline{A^+}_{max}} u_{0,prod}. \tag{7.25}$$

The temperature of the product is difficult to measure close to the flame. Instead, the temperature recorded 660 mm downstream of the burner was used to calculate $u_{0,prod}$. For the operating point OPA, the temperature is equal to $T \approx 1150\,\mathrm{K}$. Then $u_{0,prod} \approx 6.4\,\mathrm{m/s}$ and $\langle\overline{u^+}\rangle_{min} \approx 7\,\mathrm{m/s}$. These boundaries result in the axial velocity profile shown in Fig. 7.28.

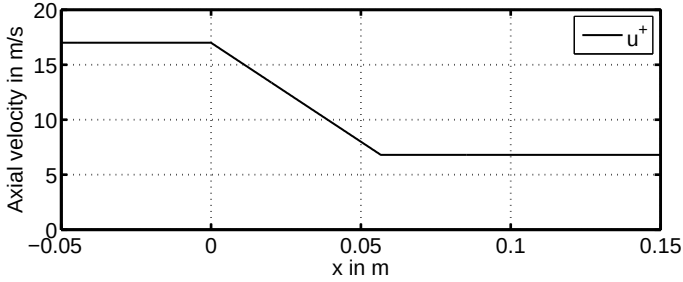

Figure 7.28: Axial velocity profile of $\langle\overline{u^+}\rangle_{A^+}(x)$ in the burner and combustion chamber from PIV measurements

The model of the axial velocity is known to be valid here for one operating point, as no further PIV measurements were performed at other operating conditions. Furthermore, the influence of the non-symmetrical injection of fuel on the flow field and on the flame would require PIV measurements

performed in different axial planes. Given the difficulty and the time required to acquire a high number of valid snapshots, such measurements were not performed in the combustor but would be expected to give important information on the flame/flow field interaction if a more exhaustive characterization were required.

7.2.3 A statistical link between the Lagrangian cold RTD and the heat release location

From the notation of Fig. 7.24, the expression of the Lagrangian effective total time delay for one particle p of fuel from the injection down to the flame reads

$$\tau_{eff}(p) = \tau_{xL,hot}(p) + \tau_{fl}(p)\,. \tag{7.26}$$

Taking N particles representative of the location and momentum of fuel injections, the PDFs of the time delay considered, $f_{\tau_{eff}}$, $f_{\tau_{xL,hot}}$, and $f_{\tau_{fl}}$ are obtained. The unknown PDF is $f_{\tau_{fl}}$; $f_{\tau_{xL,hot}}$ can be measured in cold flow, and $f_{\tau_{eff}}$ can be considered to be the response of the flame to fuel concentration fluctuations, which can be measured from the chemiluminescence response (see below). If one assumes that the variables $\tau_{xL,hot}$ and τ_{fl} are *statistically independent* (which is not exactly true as mixtures with an equivalence ratio close to 1 will tend to burn more quickly than lean ones), then the corresponding probability density functions $f_{\tau_{xL,hot}}$ and $f_{\tau_{fl}}$ satisfy

$$f_{\tau_{eff}} = f_{\tau_{xL,hot}} * f_{\tau_{fl}} \tag{7.27}$$

where the symbol $*$ represents the convolution operation. Using the multiplicative property of the convolution in the frequency domain (Fourier transformation) and the definitions $\mathcal{F}(f_{\tau_{eff}}) = FTF_{Y_f}$, $\mathcal{F}(f_{\tau_{xL,hot}}) = MTF_{hot}$, and $\mathcal{F}(f_{\tau_{fl}}) = F_{fl}$, one obtains the transfer function of the mixture fluctuations at the flame location

$$FTF_{Y_f} = MTF_{hot}F_{fl}\,. \tag{7.28}$$

The function F_{fl} will act as a low-pass filter and further increase the total time delay and the temporal spreading of the function MTF_{hot}. FTF_{Y_f} is

the transfer function of the fuel mole fraction fluctuations at the flame as

$$FTF_{Y_f} = \frac{\hat{Y}'_{f,fl}}{\hat{Y}'_{f,inj}} \,. \tag{7.29}$$

This definition does not take the other source of heat release fluctuations which is linked with the flame surface fluctuations, as this information is lacking from cold flow measurements.

An expression for F_{fl}, or equivalently $f_{\tau_{fl}}(t)$, now needs to be obtained. This can be done indirectly though an estimation of the axial heat release probability density function $f_{HR}(x)$ and the change of variable $x \mapsto t$. If the axial velocity field in and at the burner outlet is split into the three regions shown in Fig. 7.28 as

$$u = \begin{cases} u_0^+ & \text{if } x < 0 \\ ax + u_0^+ & \text{if } x \in [0, x_{lim}] \\ u_{lim}^+ & \text{if } x > x_{lim} \end{cases} \tag{7.30}$$

then the time delay t can be expressed as a function of the axial distance x as

$$t = \begin{cases} \frac{x}{u_0^+} & \text{if } x < 0 \\ \frac{1}{a}\left[\ln\left(ax + u_0^+\right) - \ln\left(u_0^+\right)\right] & \text{if } x \in [0, x_{lim}] \\ \frac{x - x_{lim}}{u_{lim}^+} + \frac{1}{a}\left[\ln\left(u_{lim}^+\right) - \ln\left(u_0^+\right)\right] & \text{if } x > x_{lim} \end{cases} \tag{7.31}$$

The resulting function $t = g(x)$ is thus strictly monotonic (the time delay always increases with the distance) and is continuous within each interval (three distinct intervals). A univariate change of variable technique [GLD97] can be used to convert the spatial PDF $f_{HR}(x)$ to the temporal PDF $f_{\tau_{fl}}(t)$ as

$$f_{\tau_{fl}}(t) = \sum_i f_{HR}\left(g_i^{-1}(t)\right) \left| \frac{dg_i^{-1}}{dy} \right| . \tag{7.32}$$

For strictly increasing functions, and regarding discretized problems, it is often easier to handle the cumulative distribution function $F_{\tau_{fl}}(t) =$

$\int_{-\infty}^{t} f_{\tau_{fl}}(\theta)\, d\theta$ which in this case reads

$$F_{\tau_{fl}}(t) = F_{HR}(g^{-1}(t))\,. \tag{7.33}$$

The PDF $f_{HR}(x)$ should come from measurement of the heat release; in our case (though this only provides an approximation), it is derived from the OH* chemiluminescence data. The resulting PDF of the fuel concentration fluctuations $f_{\tau_{eff}}$ is then obtained from Eq. 7.27 or after Fourier transformation from Eq. 7.28.

Finally, if a real transfer function is to be approximated, other mechanisms like the changes in the flame surface due to turbulent fluctuations would have to be taken into account. Otherwise, considering the response of the flame for completely premixed mixtures (i.e., with no fuel/air fluctuations) would produce a flame transfer function equal to zero, (or for the flame transfer matrix $T_{22} = 1$), which is not the case as shown by Schuermans et al. [SBFP04] and Borghesi et al. [BBS09]. However, these other mechanisms cannot be captured by the present model as it focuses on the fuel fluctuations.

7.2.4 Heat release location and band-pass filtered OH* chemiluminescence

The previous sections have presented the impact of the flame on the flow field, and the impact of fuel injection on the OH* chemiluminescence. However, the parameter of interest is not the axial chemiluminescence profile of the flame but rather the heat release rate profile, which remains complex to capture experimentally. Though measurements of total chemiluminescence may capture the overall heat release rate, the spatial distribution seems to require much more effort, as shown in a work of Lauer [LS08] on an axisymmetric flame from which Fig. 7.29 is reproduced. His results show that the use of whether OH* or CH* signal leads to some errors in the localization of the heat release location. Assuming that these results can be generalized to other swirling flames and operating points, they indicate that the peak of the heat release rate is located more upstream than that of the chemiluminescence profiles. The effective flame position $x_{fl,eff}$ is then less far along the combustor than the one measured with these filters, leading

to a shorter convective time delay $\tau_{fl,eff} = x_{fl,eff}/u_0 < x_{fl,OH}/u_0$, typically used to generate stability maps [LTJZ01] or scaling of flame transfer functions [LB04]. However, as shown by the PIV measurements, the mean bulk velocity u_0 is a decreasing function of the axial position at the burner outlet as $\langle\overline{u^+}\rangle_{A^+}(x)$, and the effective time delay should be expressed as

$$\tau_{fl,eff} = \int_0^{x_{fl,eff}} \frac{dx}{\langle\overline{u^+}\rangle_{A^+}(x)} \,. \tag{7.34}$$

It may then occur that the convective time delay generally assumed, $\frac{x_{fl}}{u_0}$, is equal to the effectively measured one as

$$\frac{x_{fl}}{u_0} \approx \int_0^{x_{fl,eff}} \frac{dx}{\langle\overline{u^+}\rangle_{A^+}(x)} \,. \tag{7.35}$$

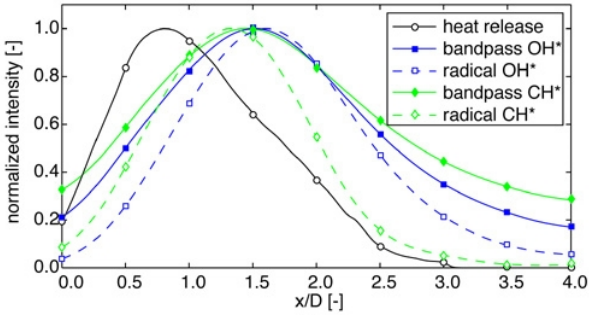

Figure 7.29: Comparison of measured heat release and OH* as well as CH* integral emissions of a premixed swirling flame [LS08]

Furthermore, the flame profiles of Fig. 7.25 combined with the corresponding mixing quality indicate that the signal $I_{OH,BP}$ increases with increasing unmixedness. Figure 7.30 shows that $I_{OH,BP}$, recorded by the camera, also increases with increasing equivalence ratio and that the emissions are minimum for the pre-premix injection. Thus, an increase in the unmixedness leads also to an increase in the chemiluminescence signal recorded by the camera, similar to the photomultiplier data.

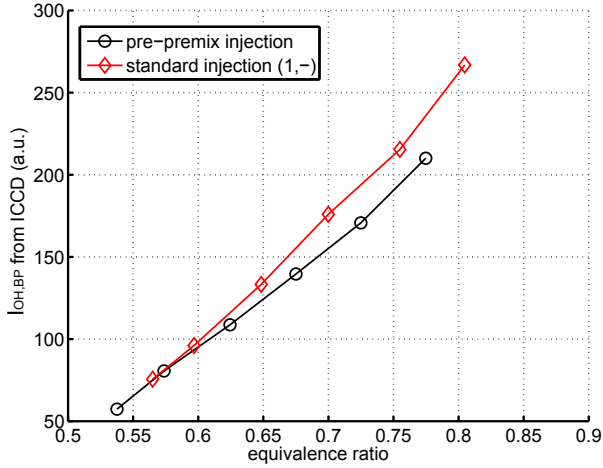

Figure 7.30: Band-pass filtered OH* emissions $I_{OH,BP}$ as a function of equivalence ratio ϕ for the premix and pre-premix injection configurations.

The results described above thus lead to the following assertions regarding the behavior of chemiluminescence of the flame:

- An increase in the equivalence ratio ϕ leads to an increase in the emissions recorded at the OH* wavelength;
- A decrease in the premixing quality leads to an increase in band-pass filtered OH* emissions;
- The minimum in the band-pass filtered OH* signal is reached for perfectly premixed fuel/air mixtures at set operating conditions;
- Locally rich fuel pockets are able to stabilize more upstream (where high flow velocities are present) than their lean counterpart;
- The band-pass filtered OH* signal is not a measure of the heat release as any variations in the mixture quality change the chemiluminescence intensity;

- OH* is a long living species and may be present in high quantities downstream of the main reaction zone (Thermal OH, Griebel et al. [GSJ07]).

However, even though it is not possible to directly measure the real heat release profile, it is reasonable to assume that it is related to the OH* chemiluminescence emission $I_{OH,BP}$ recorded by the camera. The recorded profile $I_{OH,BP}(x)$ can then be used to approximate the combustion progress variable c. In the present configuration, the progress variable identifies the degree of advancement of the combustion along the flow axis, with 0 characterizing the reactant side and 1 the product side. The first test with $c_0(x)$ defined as

$$c_0 = \begin{cases} \frac{I_{OH,BP}(x)}{I_{OH,BP,max}} & \text{if } x < x_{fl} \\ 1 & \text{if } x \geq x_{fl} \end{cases} \tag{7.36}$$

without any scaling, leads to a poor agreement between the time delay recorded directly with the flame transfer function and the time delays calculated from the product of the mixing transfer function and flame response. To improve the results, a scaling parameter was introduced. The first assumption made was that the maximum slope of the progress variable increases with an increasing OH* for a defined operating point (i.e., when the fuel distribution is varied). A reference position x_{ref} obtained from the OH* profile is used as an invariant point of the profile. This reference may be the starting point of the OH* profile or the location x_{fl} for example. The correction reads then

$$\begin{cases} (x_2 - x_{ref}) = a\,(x_1 - x_{ref}) \\ c\,(x_2) = c_0\,(x_1) \end{cases} \tag{7.37}$$

with the scaling factor a being equal to

$$a = \frac{A}{I_{OH,BP,max}}\,, \tag{7.38}$$

where $I_{OH,BP,max}$ is the maximum OH* chemiluminescence signal recorded by the ICCD camera for the operating point considered and A a constant

that depends on the operating point. The advantage of this scaling definition is that only one variable, the parameter A has to be be fitted to reacting measurements of the time delays. Different shapes of the progress variable c with different scaling rules were tested and are presented in Fig. 7.31. The best results were obtained with the first case, when the reference point for the scaling is the first 1% quartile of the fitted $I_{OH,BP}(x)$ curve. The third case also produced good results. As an example, the

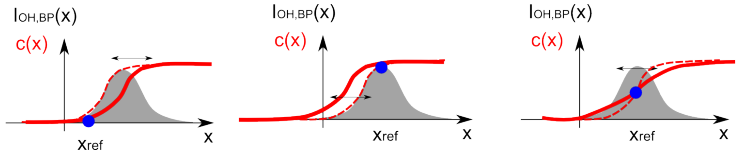

Figure 7.31: Shape assumed for the progress variable c in relation to the OH* chemiluminescence images

calculated PDF of the flame time delays, $f_{\tau_{fl}}$ is presented in Fig. 7.32 for the injection (0, 0.7). An estimation of the flame transfer function is thus obtained.

7.2.5 Model for the optically-measured flame transfer function

In recent work, Schuermans [SBFP04, SGM08] uses the property of the global chemiluminescence signal (whether CH* or OH*) of Eq. 3.5 to derive an expression of the heat rate release fluctuations $\dot{Q}'$. The total heat release rate $\dot{Q}$ is defined as

$$\dot{Q} = \rho_a S_t Z_f h_f A_t \,, \tag{7.39}$$

where ρ_a is the density of oxidizer upstream of the flame, S_t the turbulent flame speed, Z_f the fuel mass fraction, h_f the reaction enthalpy of the fuel and A_t the turbulent flame surface area. Using the property for lean mixtures

$$\phi \propto Z_f \,, \tag{7.40}$$

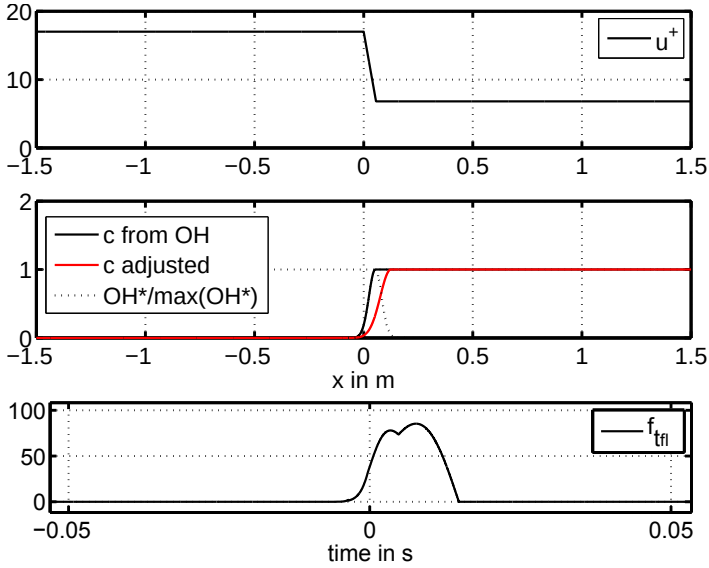

Figure 7.32: Top: mean combustor velocity as a function of axial position, middle: normalized OH* profile, original and fitted progress variable as a function of axial position; bottom: probability distribution of the time delays τ_{fl}

then, considering that $\dot{m}_{air} = S_t A_t \rho$ and $\dot{Q} = \dot{m}_{air} Z_f h_f$, then Eq. 3.5 can be re-written in terms of the heat release rate as

$$I_i \propto \dot{Q} Z_f^{\gamma_i - 1} \,. \tag{7.41}$$

Assuming small perturbations for Eq. 7.41, one obtains the relation

$$\frac{I_i'}{I_i} = \frac{Q'}{\overline{Q}} + (\gamma_i - 1)\,\frac{Z_f'}{\overline{Z_f}} \,. \tag{7.42}$$

Linearizing the heat release rate expression of Eq. 7.39, the heat release rate fluctuations become

$$\frac{\dot{Q}'}{\overline{\dot{Q}}} = \frac{S_t'}{\overline{S_t}} + \frac{A_t'}{\overline{A_t}} + \frac{Z_f'}{\overline{Z_f}} + \frac{\rho_a'}{\overline{\rho_a}} + \frac{h_f'}{\overline{h_f}} \,. \tag{7.43}$$

The two last terms can be neglected, as can the flame surface oscillations A'_t. The latter is not true at a scale of the order of the flame thickness, but as S_t and A_t are somewhat arbitrarily linked together by the condition $S_t A_t \rho = \dot{m}_{air}$, for the modeling task it is justified to assume that the air flow modulations only induce turbulent flame speed fluctuations. Equation 7.43 leads then to the final expression of Eq. 7.42, where the oscillating terms are taken at the flame location

$$\frac{I'_i}{\overline{I_i}} = \left(\frac{S'_t}{\overline{S_t}}\right)_{fl} + \gamma_i \left(\frac{Z'_f}{\overline{Z_f}}\right)_{fl} . \tag{7.44}$$

The first term can be well approximated by the convection of turbulent velocity fluctuations from the acoustic reference plane with a time delay and a temporal spreading [SBFP04]. In the frequency domain, the final expression reads

$$\left(\frac{\hat{S}'_t}{\overline{S_t}}\right)_{fl} = \left(\frac{\hat{u}'}{\overline{u}}\right)_{ref} e^{-i\omega\tau_t} e^{\frac{1}{2}\omega^2\sigma_t^2} . \tag{7.45}$$

The turbulent flame speed fluctuations are then directly proportional to the mean velocity fluctuations taken at a defined reference plane (which is not necessarily the laser measurement plane).

The model proposed in Eq. 7.29 describes only the transfer function of the fuel mole fraction fluctuations from the fuel injection location down to the flame and can be rewritten as

$$\left(\frac{\hat{Y}'_f}{\overline{Y_f}}\right)_{fl} = \left(\frac{\hat{Y}'_f}{\overline{Y_f}}\right)_{inj} FTF_{Y_f} . \tag{7.46}$$

It can be shown that the mole fraction fluctuations are identical to the mass-fraction fluctuations so that Eq. 7.46 becomes

$$\left(\frac{\hat{Z}'_f}{\overline{Z_f}}\right)_{fl} = \left(\frac{\hat{Z}'_f}{\overline{Z_f}}\right)_{inj} FTF_{Y_f} . \tag{7.47}$$

In a next step, this term should be linked to the velocity fluctuations at the reference plane, $\left(\frac{\hat{u}'}{\overline{u}}\right)_{ref}$. The result will depend on the fuel injection considered and more precisely on its impedance $\mathcal{Z}_{inj}$, the impact of which can on the stability of a combustor be quite substantial as shown by Richards [RSR03, RR08]. The linearized definition of the fuel/air fluctuations at the fuel injection location reads

$$\left(\frac{Z'_f}{\overline{Z_f}}\right)_{inj} = \left(\frac{u'_f}{\overline{u_f}}\right)_{inj} - \left(\frac{u'}{\overline{u}}\right)_{inj} . \tag{7.48}$$

If the fuel flow is choked, i.e., $Z_{inj} \to \infty$ and the fuel mass flow through the injectors is constant, then the fuel mass fraction fluctuations at the fuel injectors solely depend on the air flow fluctuations at the injection location as

$$\left(\frac{Z'_f}{\overline{Z_f}}\right)_{inj} = -\left(\frac{u'}{\overline{u}}\right)_{inj} . \tag{7.49}$$

However, as shown in Annex A, with the standard fuel injection the flow is unchoked. The fuel flow becomes choked when only half of the injection holes are used, i.e., when β=0 or β=1. Given the geometry of the injection slots and the complex flow field around them, it is almost impossible to determine the impedance of the fuel injection experimentally. Further, it may become very complex to model this when a shift of the fuel distribution is applied. The influence of the fuel fluctuations was thus neglected, assuming that the fuel injection impedance was sufficiently high. Furthermore, compared to the convective time delay, the acoustic time delay between the reference plane and the injection plane is negligible and Eq. 7.49 can be transformed to

$$\left(\frac{Z'_f}{\overline{Z_f}}\right)_{inj} = -\left(\frac{u'}{\overline{u}}\right)_{ref} . \tag{7.50}$$

In the frequency domain, Eq. 7.44 finally reads

$$\frac{\hat{I}'_i}{\overline{I}_i} = \left(\frac{\hat{u}'}{\overline{u}}\right)_{ref} \left[e^{-i\omega\tau_t} e^{\frac{1}{2}\omega^2\sigma_t^2} - \gamma_i FTF_{Y_f}\right] . \tag{7.51}$$

Measurements performed on the same burner without secondary injection

indicate that typical values for γ are $\gamma_{CH,BP} \approx 4$ for the CH* signal and $\gamma_{OH,BP} \approx 2.7$ for the OH* signal [GGS+10]. Like the present measurements, neither of these values are background corrected. Due to the high coefficient γ the signal recorded by the chemiluminescence will be dominated by the fuel/air ratio fluctuations, and this will be even more true if CH* is used to record the transfer function. Therefore, Eq. 7.44 can be simplified as

$$\frac{\hat{I}'_{CH,BP}}{\overline{I}_{CH,BP}} \approx -\left(\frac{\hat{u}'}{\overline{u}}\right)_{ref} \gamma_{CH,BP} FTF_{Y_f}\,, \tag{7.52}$$

and can be considered as a measure of the response of the flame to fuel/air fluctuations. In terms of the experimentally recorded flame transfer function, Eq. 7.52 can be rewritten as

$$FTF_{Y_f,meas} \approx MTF_{hot} F_{fl}\,, \tag{7.53}$$

with

$$FTF_{Y_f,meas} = \frac{-1}{\gamma_{CH,BP}} \frac{\hat{I}'_{CH,BP}/\overline{I}_{CH,BP}}{(\hat{u}'/\overline{u})_{ref}}\,. \tag{7.54}$$

The flame transfer functions $FTF_{Y_f,meas}$ of 6 chosen injection configurations presented in Fig. 7.33 are compared with the total transfer functions obtained from cold flow and flame visualization, which are depicted in Fig. 7.34.

Except for the injection (α, β)=(0,1) which shows a high gain over a wide frequency range, all the measured FTFs are similar in amplitude. The normalized amplitude becomes smaller than 0.5 for Strouhal numbers higher than $St > 0.5$. The phase decreases almost linearly for all the configurations. The slope of the phase is a measure of the convective time delay of the fuel/air injection. In particular, the phase of injection (α, β)=$(0, 0.5)$ remains close to the baseline case $(1, 0)$ up to a frequency of $St = 0.6$, confirming that both injection configurations, which are almost identical, have similar convective time delays. The injection (α, β)=$(0, 0.5)$ also has the advantage of having a lower gain in the low-frequency range. The other injection configurations present similar phase slopes and hence convective time delays, indicating that except for injection configurations close to

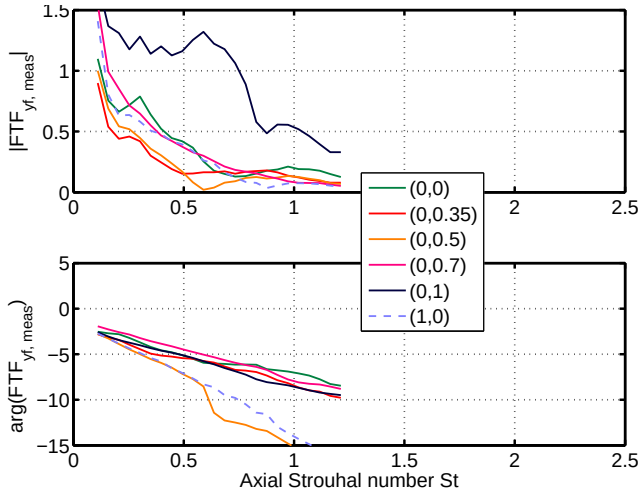

Figure 7.33: Flame transfer function $FTF_{Y_f,meas}$ (Eq. 3.17) recorded in the combustor for different fuel injection configurations (α, β). Operating point A.

$(0, 0.5)$, the impact of controlling the time delays by fuel shifting is limited due to changes in flame stabilization location.

The total time delays derived from the slope of the FTF phase for the range $St \in [0, 0.7]$ were then extracted and used to calibrate the cold flow + flame model ($FTF_{Y_f} = MTF_{hot}F_{fl}$) presented earlier. In particular, the parameter A (Eq. 7.38) was adjusted and Fig. 7.34 depicts the resulting flame transfer function. The amplitude of the response evolves in a similar way to the response recorded in reacting conditions, with local minima obtained around $St \approx 0.75$. The phase slopes present a more continuous variation between the two extremal phases slopes of the fuel distributions (α, β)=$(0, 1)$ and (α, β)=$(1, -)$ when compared to the phases obtained from the direct FTF measurements. A comparison of these slopes, which correspond to the mean convective time delays, is shown in Fig. 7.35.

The direct measured time delay $\tau^*_{eff,FTF}$ and the cold + flame shape time delays $\tau^*_{eff,MTF.F}$ are compared with the time delay τ^*_{eff} calculated from Eq. 7.26 with $\tau_{fl} = x_{fl}/u_0$. The 9 injection configurations which were investigated in cold flow are reported here. Both cold-flow-based time delay

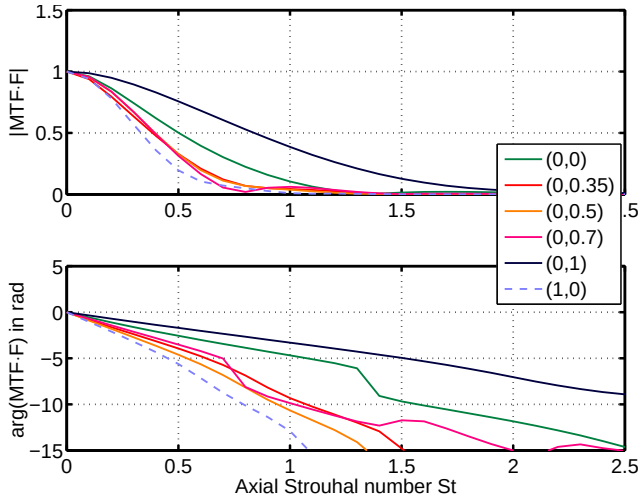

Figure 7.34: Total transfer function $FTF_{Y_f} = MTF_{hot}F_{fl}$

calculation methods qualitatively generate the main tendencies observed in the direct measurements $\tau^*_{eff,FTF}$. In particular, the evolution of the time delay τ^*_{eff} reproduces the evolution of $\tau^*_{eff,FTF}$ very well. However, the difference between the shortest and the longest time delays does not exceed 0.5 while the directly measured time delays present a difference of 1. This amplitude of variation is better captured with the new proposed method and resulting $\tau^*_{eff,MTF_{hot}F_{fl}}$. However, the main disadvantage is that some strong outliers appear for injections $(\alpha, \beta) = (0.5, 0.75)$ and (0,1) .

7.3 Summary

In this section, a method has been presented which can be used to experimentally record and model the mixing transfer function in burner with short bulk residence times. The important characteristic of the model is that it captures the effect of the recirculation zone on the mixing response at the burner outlet. The result allows the residence time distribution of fuel in the burner to be estimated experimentally prior to any combustion tests.

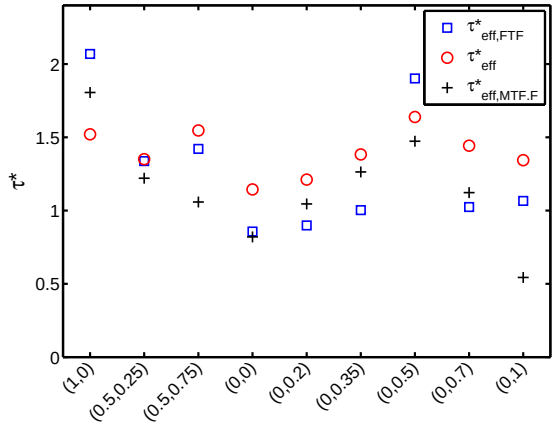

Figure 7.35: Comparison of the convective time delays calculated from the FTF ($\tau^*_{eff,FTF}$), from the standard definition of the time delay (τ^*_{eff}) and from the product $MTF \cdot F$ ($\tau^*_{eff,MTF_{hot}F_{fl}}$)

Links have been made between the directly-measured flame transfer function and the cold-mixing transfer function with help of a model of the velocity decay downstream of the burner and of the flame shape information. The velocity model is valid for the operating point considered, as the focus of the measurements was to assess the impact of changes in the fuel distribution on the flow field. Extrapolation to other operating conditions should not be made without further measurements of the velocity field as the flame may strongly change the mean flow. In particular, an increase in the equivalence ratio may increase the velocity further downstream as shown by Alemela [Ale09]. Furthermore, due to the non-axisymmetric flow and mixing configuration, which becomes even more true for a non-equal fuel distribution, measurements in other planes are required to achieve a more accurate mean velocity model.

The methodology presented is only able to capture the response of the system to fuel/air fluctuations. The interaction of the non-stationary velocity field with the flame is not taken into account (i.e., the term $e^{-i\omega\tau_t}e^{-0.5\omega^2\sigma_t^2}$ of the flame transfer function model). This mechanism is, however, present in all burner configurations and must be considered if the fuel/air fluctuations are not the source of the recorded thermoacoustic instabilities.

Further, the method that has been presented cannot match the quality of direct measurements of the flame transfer function and such data continues to be required to perform a precise stability analysis of a combustion system. However, the knowledge obtained from non-reacting measurements is increased as the variations of the convective time delays can be captured. The residence time distribution obtained can be used to validate numerical simulations, which are commonly compared to velocity or concentration profiles but seldom to residence time distributions or mixing transfer functions.

Chapter 8

Control of combustion instabilities and NO_x emissions

One of the goals of the thesis is to use the cold flow model of the mixing quality and stability to control the pressure pulsations and NO_x emissions of the combustor. However, the modeling task is slightly more complex than when direct measurements on the final test rig are performed. There is some error or uncertainty due to the use of slightly different test rigs and media. However, the main trends are qualitatively well captured by the models. The model obtained from cold flow measurement is valuable but the modeling uncertainties have to be taken into account.

As the fuel distribution must ensure low NO_x emissions and low-pressure pulsations, a gradient-based controller is appropriate to optimize the fuel split in real-time. Extremum-seeking control (ESC) based on slight variation of the fuel distribution is thus well suited to minimizing the NO_x and pressure pulsations. The principle and the results obtained for the control of NO_x emissions with the fuel distribution β are presented in Sec. 8.1.

To take the cold flow model into account, this extremum-seeking control scheme was extended with the knowledge gained from the cold flow model. The principle and the results obtained with this controller are described in Sec. 8.2.

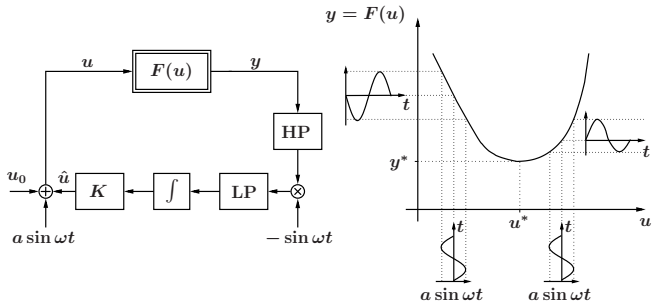

Figure 8.1: Block diagram of a SISO extremum-seeking feedback scheme for minimization of the output y (from Moeck et al. [MBP+07])

8.1 Control of emissions and pulsations with standard ESC

8.1.1 Extremum-seeking control, the principle

In order to find the optimal values for α and β an extremum-seeking control algorithm is used. Extremum-seeking control (ESC) is an adaptive, closed-loop control scheme for finding an extremum in an unknown field of parameters. A major advantage of ESC is that no plant model is required for controller synthesis. Furthermore, the algorithm guarantees closed-loop stability, if designed properly (see Krstić and Wang [KW00] and Ariyur and Krstić [AK03] for details). The method has been used in recent years in various applications (such as maximizing the pressure rise in an axial flow compressor [WK00] and controlling the separation of the flap of a high-lift airfoil [BKPN06]). The basic principles of ESC are briefly explained here, based on the example of searching for the minimum of a single-input/single-output (SISO) system (see Fig. 8.1). The plant is considered to be a block with a static nonlinear input-output-map $y = F(u)$. The idea is to perform gradient-based online optimization in order to find the control input u^* that achieves the minimal steady-state

system output y^*. The steady-state input-output-map $F(u)$ and in particular its extremum $y^* = \min(y) = F(u^*)$ are unknown and/or changing in time due to variations in the operating conditions.

A small amplitude sine signal $a \sin \omega t$ is superimposed on the initial control input u_0. With the prerequisite that the period of the harmonic perturbation is larger than the largest plant time constant, an approximately sinusoidal output y will be obtained, initially oscillating around $y_0 = F(u_0)$. To achieve gradient-based optimization, the output signal is passed through a high-pass filter (HP), which removes the mean value but not the sinusoidal perturbation. Information about the slope of F is obtained by multiplying this zero-mean signal by a negative sine of the same perturbation frequency ω. The product of the filtered output and the sine signal has a non-zero mean component unless the minimum is attained. If the plant is initially to the right of the minimum, the input and output perturbations are in phase, and hence the product will be negative. Conversely, an anti-phase relation, giving a positive product, will be an indication of the plant being located to the left of the minimum. The subsequent low-pass filter (LP) smooths the signal, which is then integrated and multiplied by K yielding an additional term $\hat{u}$. As long as the output of the LP is positive, i.e., the system is one the left of the minimum, the value of $\hat{u}$ is positive, thus moving $u = \hat{u} + u_0 + a \sin \omega t$ closer to the optimal value u^*. For a negative output of the LP, the opposite is true [BKPN06].

The choice of certain design parameters is dependent on the dynamics of the plant. The overall feedback system has a fast, a medium and a slow timescale corresponding to the plant dynamics, the periodic perturbation and the filters in the extremum-seeking scheme, respectively. If the plant behavior varies due to uncertainties, the timescale of the perturbation signal must be larger than the slowest possible plant dynamics. Cut-off frequencies of the HP and the LP need to be lower than the frequency ω of the perturbation signal. For these reasons, the speed of the algorithm is limited. The permanent harmonic input and output perturbations are another disadvantage.

8.1.2 Improvements to the ESC

The ESC algorithm was implemented in a Simulink model running under MATLAB and the model is then compiled to run on a dSPACE board, which controls then the fuel distribution. In order to achieve reliable and faster control over the (α, β) injection field, the following modifications were made to the algorithm:

- To achieve a faster control of the mass flows through the valves, a combination of a PI controller with a feed-forward compensator and an input compensator (to compensate for the nonlinear static map of the valve at low and high mass flows) was used.
- As α and β are bounded between 0 and 1, the controller has to be able to run even if the limits of the domain are reached. For this reason, the integrators of the α and β ESC modules are limited when extreme values are reached, so that the α or β cannot move out of the domain $0 \leq \alpha \leq 1, 0 \leq \beta \leq 1$.
- The amplitude of oscillations of the controller output can be scaled with the amplitude of the controller input. This implementation leads, for example, to higher oscillations of α when the combustion is unstable and smaller oscillations when the system is stable. High oscillation amplitudes are needed in the event of unstable combustion to drive significant changes in pressure amplitudes, in order that the controller can move faster toward the stable point.
- A further improvement of the control scheme concerns the estimation of the local gradient within the algorithm. As suggested in [HBF$^+$08] an extended Kalman filter is used for the estimation instead of the classical high and low-pass combination. That way a faster and better estimation of the gradient is achieved.

8.1.3 Control of NO_x emissions with an ESC controller (SISO control)

The implementation of the ESC algorithm in the combustor is first demonstrated for a SISO configuration, the NO_x emissions being controlled solely

by the fuel distribution β ($\alpha = 0$). The steady-state chemiluminescence measurements (OH* and CH*) showed a very good correlation with the NO_x emissions. Furthermore, as the response of chemiluminescence to changes in the fuel/air profile is very fast (see Fig. 6.19), the test should prove whether CH* is suitable as a fast surrogate for the NO_x emissions in closed-loop control situations. The function F which must be minimized by the ESC is thus only the CH* emission processed with a moving average filter with a 1-second window.

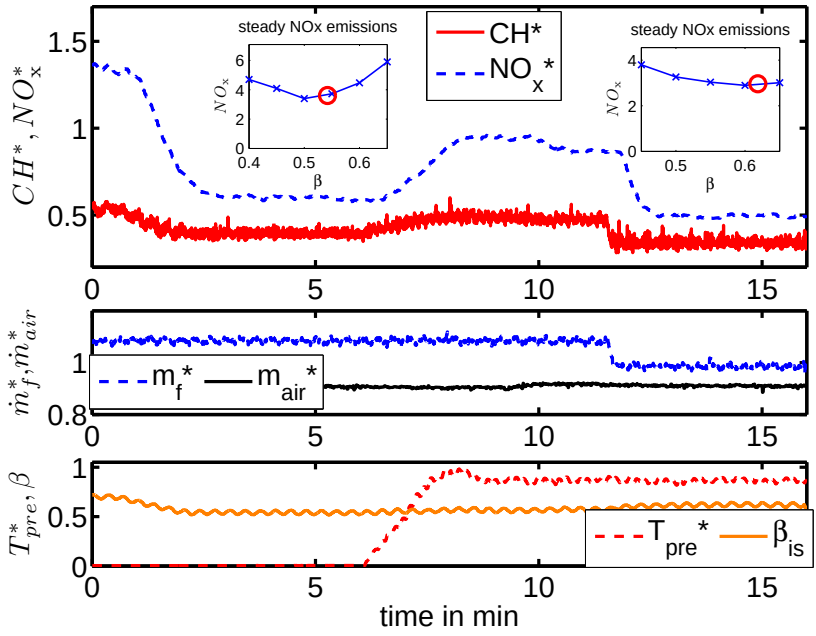

Figure 8.2: Evolution of the normalized NO_x and CH* emissions in the combustor when the ESC is applied with CH* as input and β as output. A transient in preheating conditions starts after 6 minutes, and a transient in the fuel mass flow after 11.5 minutes. The fuel injections (red circles) obtained during the control for the operating conditions before the temperature transient and after fuel mass flow transient are compared to steady emissions recorded before and after the test. Combustor length 1.5 m, 60 mm orifice (stable conditions).

The combustion chamber end ($L_{cc} = 1.5\,\mathrm{m}$) was equipped with a 60 mm-orifice with low reflectance to ensure stable combustion. Figure 8.2 shows how the fuel distribution evolves when the ESC is switched on and when variations in the operating conditions are set. It is found that the combination of ESC and CH* chemiluminescence is able to adjust the fuel injection when there are transients in the operating conditions, and the average fuel distribution around which the controller stabilizes the system (red circle in the top of Fig. 8.2) is very close to the fuel distribution which minimize the NO_x emissions. For ease of representation and as it is the relative variations that are of interest, the values of the NO_x emission, air and gas mass flows, and preheat temperature were normalized between 0 and 1.5.

At the start of the recording, the oscillation amplitude of β is set to 0.025 and this appears sufficient to bring the fuel distribution from the starting point β=0.7 with high NO_x down to $\beta \approx$0.55 very close of the optimal fuel injection recorded at these operating conditions. The controller takes approximately two minutes to drive the system toward the best injection. The transient in temperature starting after 6 minutes leads to an increase in the NO_x and CH* emissions. A slight increase in the value of β can be observed. After 11.5 minutes, the fuel mass flow is decreased. The controller increases the value of β only slightly but rapidly to $\beta \approx 0.61$ so that the NO_x emissions are again very close to their minimum. Hence the ability of the CH* sensor and of the controller to achieve low NO_x emissions during transient operations is demonstrated.

The information from the CH* and pressure sensors can also be linearly combined together to build the function which must be minimized. Depending on the goal of the controller (low NO_x priority or low pulsation priority), weighting parameters can be introduced to put more weight on one or the other sensor.

The disadvantage of such an ESC is that it is not able to move out of a local minimum of the function. Therefore, an extension of the ESC was developed to take into account the information concerning the model presented in the previous sections.

8.2 Control of emissions and pulsations with extended ESC (SIDO control)

Using different test rigs as well as a simple time lag model, which captures one aspect of the mixing dynamics, uncertainties of the model are identified. A robust controller is needed to deal with these model uncertainties. For this reason, the cold flow model is implemented in the feedback loop of a gradient-based extremum-seeking controller as shown in Fig. 8.3. The information from the model allows the speed of the controller to be increased and to avoid local minima if better fuel injection configurations are predicted by the model.

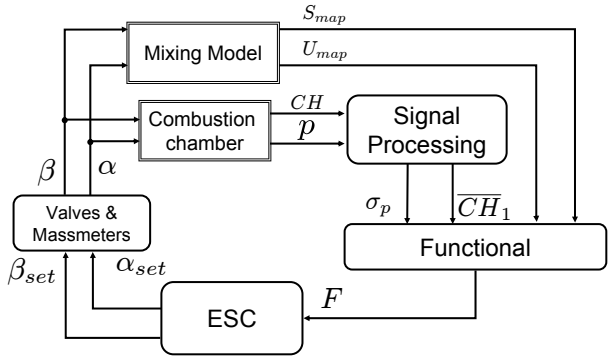

Figure 8.3: Modified ESC controller using the mixing model to optimize the fuel distribution in a SIDO case

The goal of the controller is to find the optimal fuel distribution minimizing a function F by varying the fuel distribution parameters α and β. A single-input/dual-output (SIDO) controller is thus required. The function that is to be minimized contains the measured pressure pulsations, characterized by their standard deviation σ_p, as well as the average over 1 s of the CH* signal ($\overline{CH}_1$), which is in this configuration, like OH*, a surrogate measurement of NO_x emissions. Depending on the actual values of α and β in the combustor, the model adds values of the unmixedness and stability maps (U_map and S_map) to the function in regions that should be avoided. That way, the ESC performs its gradient-based optimization over a map

defined by the model, and the weight of the map decreases as the controller narrows the optimal region. Specifically, the function F reads:

$$F(\alpha,\beta) = a\sigma_p + b\overline{CH}_1 + cU_{\text{map}}(\alpha,\beta) + dS_{\text{map}}(\alpha,\beta)\ . \qquad (8.1)$$

The three parameters σ_p, $\overline{CH}_1$, and U_{map}, are normalized to values between 0 and 1, and the positive weighting coefficients satisfy the criteria $a+b+c+d=1$. The values of c and d depend on the level of confidence in the model. If the confidence in the model is high, then c and d take high values and the controller moves α and β toward the minimum of the sum of U_{map} and S_{map}. On the contrary, low values c and d mean that the fuel distribution is altered mainly as a function of measurements from the pressure and CH* sensors.

The emission map U_{map} is, for the presented test, the normalized standard deviation of the temporal fluctuations of the spatially-averaged concentration recorded at the burner outlet. This value, which also correlates with the NO_x emissions [LMP+09], could be replaced by s_{fl}. The stability map S_{map} is defined as the square distance of the injection (α,β) to the point which is expected to be the most stable (i.e., with the lowest mean time delay), in this case $(\alpha,\beta)\approx(0,0)$, for the operating point A (220 kg/h, 0.555, 423 K) (see also Fig. 7.22). The maps corresponding to the weighting parameters (a,b,c,d)=$(0.2,0.2,0.2,0.4)$ are shown in Fig. 8.4. The substantial drop in the value recorded around (α,β)=(0,0) is due to the strong lifting of the flame which could not be fully captured by the photomultiplier, leading to a decrease in the recorded intensity.

An example of instability control with the transients for moving from operating point OPA to a second operating point is presented in Fig. 8.5. The parameters of the combustor $(\dot{m}_{\text{f}}^*, \dot{m}_{\text{air}}^*, \alpha, \beta)$, the output of the controller $(\alpha_{\text{set}}, \beta_{\text{set}})$, the measured signals (CH^*, σ_p, NO_X) and the value of the function F are shown. All the parameters are normalized between 0 and 1.

At the beginning of the experiment, F is defined by the weighting parameters (a,b,c,d)= $(0.5,0.5,0,0)$, which means that only the sensor values are used for the optimization. The system starts at the injection configuration

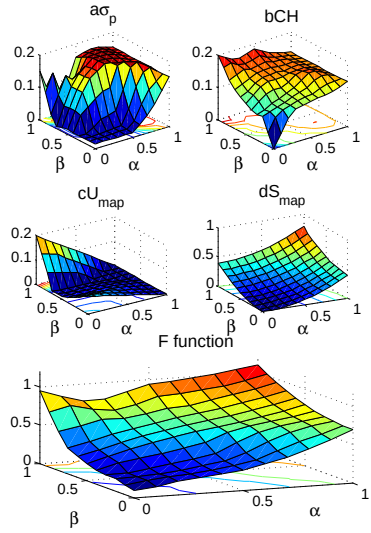

Figure 8.4: Weighted maps building the function F used by the ESC controller

(α, β)=(0.8,0.8). The amplitude of the perturbation is 0.05 for both parameters α and β. After a minute (vertical line 1), the controller is started and the system moves toward a local minimum of the pressure oscillations at $(\alpha, \beta) = (1, -)$, which still exhibits strong pressure oscillations.

After 4 minutes (vertical line 2), the weighting parameters are set to (a, b, c, d)=$(0.2, 0.2, 0.2, 0.4)$ and the function F takes the shape of Fig. 8.4. The system then moves in the direction of the injection $(\alpha, \beta) = (0, 0)$ to stabilize finally close to the global minimum around (0.1, 0.25), where the combustor is stable and NO_x emissions are very low. For clarity, the paths of fuel injection are plotted on the pressure, NO_x and function F maps in Fig. 8.6.

After 19 minutes, a move to a second operating point with lower equivalence ratio is started, and the controller remains at the optimal point.

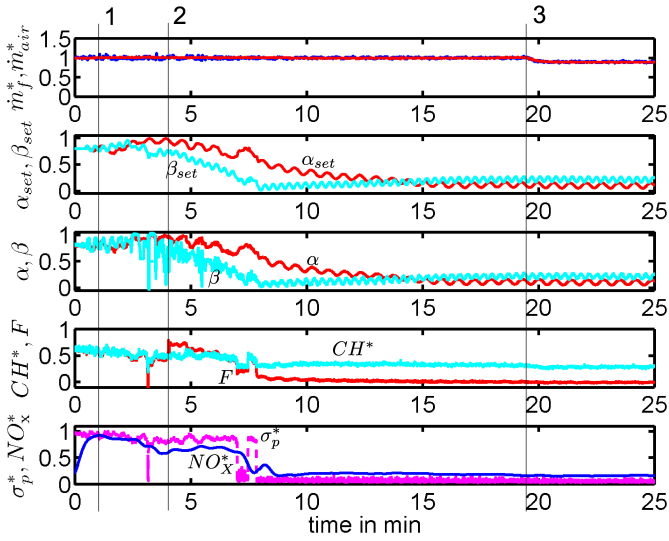

Figure 8.5: Time signals of the SIDO control system showing the evolution of the system parameters with the control map F

8.3 Summary

This chapter has demonstrated the feasibility of using an extremum-seeking controller to control the fuel distribution of the combustion chamber. The chemiluminescence can be used as a fast NO_x sensor, which is very effective during transient operations which require fast adjustment of the fuel distribution to minimize the emissions. An improvement of the ESC has been achieved by using the information coming from the cold flow measurements (i.e., the time delay) to control the thermoacoustic instabilities of the operating point A. That way, local minima, in which the combustor was still unstable, can be avoided.

The model used in the ESC can also be progressively extended with the data obtained on site. An adjustment of the coefficients of the function may then further increase the speed of the controller to move faster toward a stable point with low NO_x emissions.

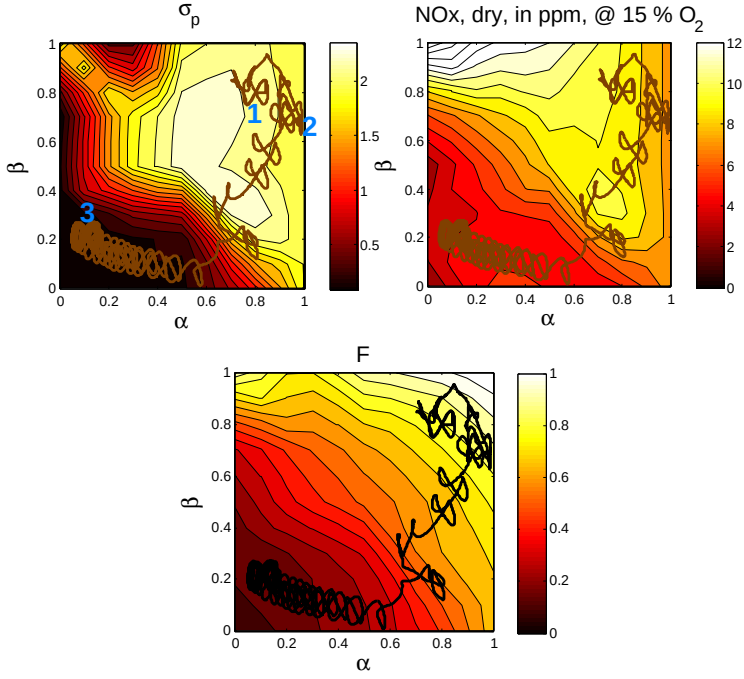

Figure 8.6: Fuel distribution evolution of Fig. 8.5 plotted on maps of the standard deviation of the pressure (top left), NO_x emissions (top right), and function F (bottom).

Chapter 9

Scalar mixing quality enhancement

9.1 Motivation

Even if modern premixed combustors have an optimized mixing quality, there remains potential to reduce the NO_x emissions through further improving the mixing quality, as the fuel which reaches the flame is almost but not completely perfectly mixed. To investigate the potential for further reducing NO_x, the emissions of the standard premix injection of the berner were compared with those of a so-called pre-premixed system, where the fuel and air are premixed well upstream of the burner (similar injection to the one used to obtain homogeneous images in the LIF experiments). The resulting NO_x emissions as well as their ratio are presented in Fig. 9.1. A fall in emissions is visible over the whole ϕ-range tested, and the gain in NO_x reduction is more pronounced moving to leaner mixtures (up to a 30% reduction at the air mass flow and preheating temperature considered here).

Even though some degree of unmixedness is recommended to stabilize the flame [BG07], a reduction in the NO_x emissions is indeed possible if the mixing quality of the burner is further improved, as this is the only parameter changed for the tests shown in Fig. 9.1.

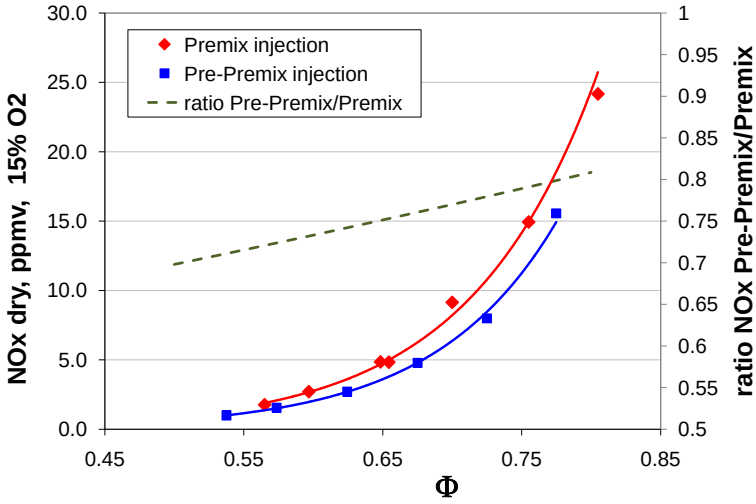

Figure 9.1: NO_x emissions of the standard premix injection (red and ♦) compared to those of the pre-premix case (blue and ■). The pre-premix injection is performed by mixing fuel and air 600 mm upstream of the burner. Operating conditions: m_{air}=200 kg/h, T_{pre} = 423 K.

9.2 Passive control

The mixing quality of the injectors I01, I02, and I03 shown in Fig. 3.5 is measured at the burner outlet (xL = 5 mm). The measurements are performed for 3 fuel distributions β = 0.3, β = 0.5 and β = 0.7, and for different equivalent jet-to-crossflow momentum ratios J_{eq} (momentum obtained with an injection $\beta = 0.5$ with the same dye mass flow).

The evolution of the temporal unmixedness is presented in Fig. 9.2 (the spatial unmixedness presented the same trends and is not shown here). The injector I03, which was designed to reduce the convective time delays, exhibits the worst mixing quality for all the configurations tested. It is, thus, not suitable to ensure low NO_x emissions. Furthermore, injecting the fuel further upstream ($\beta \to 0.7$) increases the mixing quality recorded at the burner outlet (change of more than one order of magnitude for all injections). For a given fuel distribution, injector I02 gives the best mixing quality for β = 0.3 and β = 0.5, but performs slightly less than injector

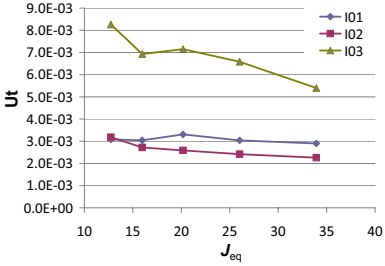

(a) $\beta = 0.3$

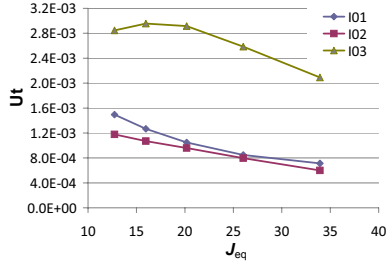

(b) $\beta = 0.5$

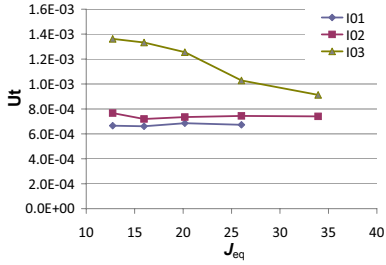

(c) $\beta = 0.7$

Figure 9.2: Temporal unmixedness for the fuel distributions $\beta = 0.3$, 0.5, and 0.7, as a function of the equivalent jet-to-crossflow momentum ratio J_{eq}

I01 for $\beta = 0.7$. The maximum decrease in temporal unmixedness with I02 compared to I01 is 21% for fuel distributions of 0.3 and 0.5. Therefore, a slight improvement in the mixing quality is possible when using injection at alternating angles (I02). However, no injection is optimum for all the fuel distribution and methods are thus investigated to further improve the mixing.

9.3 Active flow control

The question which then arises is, considering a passive fuel injection configuration, what other approaches can be used to increase the mixing quality at the burner outlet? Two possibilities are investigated here: forcing of the main air flow and forcing of the fuel injection. The results obtained with forcing of the main air flow are obtained without the 200 mm outlet cylinder, while the setup for the forced fuel injection reproduces the geometry of the atmospheric combustor downstream of the burner dump plane.

9.3.1 Influence of forcing on the velocity field

As shown previously, the MTF of the burner (Eq. 2.61) characterizes the response of the burner to concentration fluctuations at the inlet, whether they are induced by fluctuations of the main air flow or fluctuations of the fuel flow. Figure 2.9 showed that for a typical Péclet numbers of a standard premix burner ($Pe \in [15, 50]$), the response of the mixer to perturbation frequencies higher than $St > 1$ is strongly damped. Regarding the mixing quality, this means that low-frequency temporal fluctuations will increase the unmixedness, while higher forcing frequencies will produce slight temporal fluctuations in the mean concentration. They can thus be used to further increase the mixing quality, as reduction in the coherent concentration fluctuations is also a condition to reduce the unmixedness. Other nonlinear phenomena like flow resonant frequencies may occur, but are not explicitly described by the MTF.

LDA measurements made inside the inlet slots of the burner (see setup in Fig. 3.7) show that the oscillation amplitude inside the slot increases linearly with the forcing amplitude. The fluctuation amplitude also increases with the axial distance (Fig 9.3). The effect of forcing on the mean velocity field is marginal as long as very high amplitudes leading to back flow are not set (Fig 9.4).

In contrast, the flow field at the burner outlet reveals more changes in the mean field and in the coherent structures. The mean vorticity distribution is strongly altered with the forcing frequency as shown in the first row of

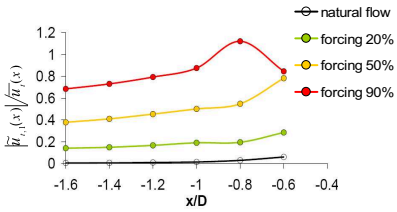

Figure 9.3: Relative oscillation amplitude of $\tilde{u}_t$ as a function of the axial position x/D for three forcing amplitudes at the natural helical Strouhal number $St \approx 1$

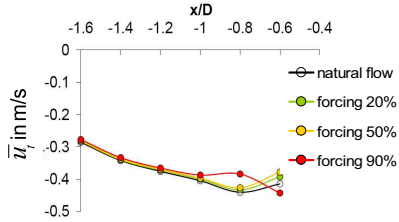

Figure 9.4: Impact of the forcing on the mean flow velocity $\overline{u}_t$ in slot 1 at helical Strouhal number $St \approx 1$.

Fig. 9.5. Increasing the forcing frequency reduces also the opening angle of the conical jet.

Phase-locked PIV performed for a forcing frequency equal to the helical structure frequency provided evidence that the helical flow structure is then replaced by an axisymmetric structure [LFG+09]. POD analysis of the velocity field (central column in Fig. 9.5) shows that the dominant modes are indeed axisymmetric (modes 1 to 3), while they are antisymmetric for the unforced case (left column in Fig. 9.5). However, antisymmetric modes, like mode 4, are still present in the flow. Surprisingly, at a forcing frequency of $St_f \approx 1.55$ (right column in Fig. 9.5), the axisymmetric modes no longer dominate the coherent flow field, as the first two modes and certainly also the third mode are antisymmetric. The axisymmetric forcing is then only visible in the fourth mode.

Reacting flow measurements performed with high forcing amplitudes produced by a loudspeaker also provided evidence that forcing at the helical structure frequency shifts the frequency of this structure to lower and higher frequencies while also damping its amplitude [LLB+10]. The previous work showed also that the helical structure is unaffected by forcing frequencies higher or lower than its characteristic frequency. These measurements therefore confirm the findings obtained with the velocity recordings. The effect of axisymmetric forcing on the passive scalar mixing

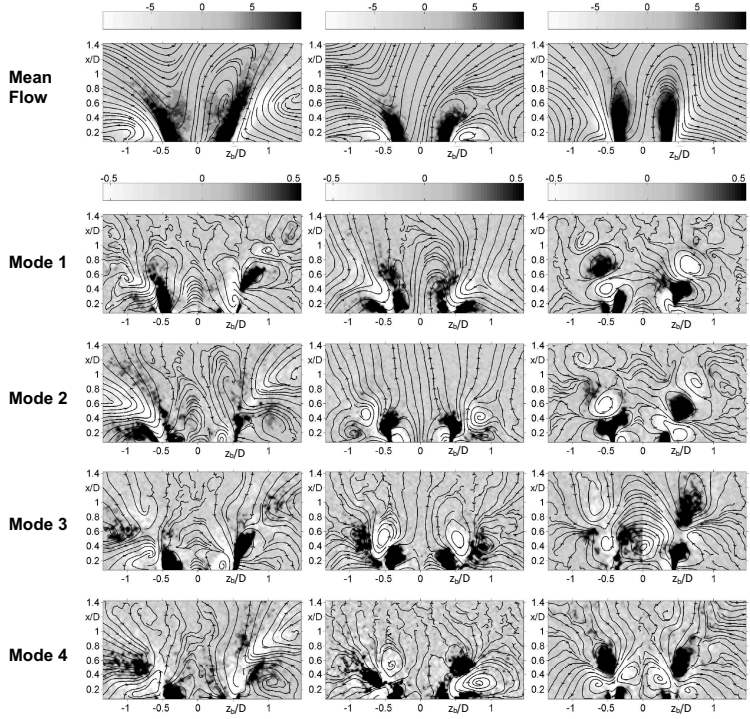

Figure 9.5: Contour plot of the azimuthal vorticity Ω of the mean flow and four first POD modes from PIV measurements in the (x_b, z_b)-plane for the unforced flow (left), forcing at the natural flow frequency $St_f \approx 1$ (center), and forcing at $St \approx 1.5$ (right)

quality recorded at the burner outlet is further investigated in the coming section.

9.3.2 Impact of axisymmetric forcing on the passive scalar field

The impact of the axisymmetric forcing on the scalar mixing is illustrated in Fig. 9.6 and Fig. 9.7 where the RMS value of the concentration fluctuations in the axial plane (xy) is depicted. For these tests, no staged injection is used and the fuel is injected through the standard injector. The upstream

and downstream injection configurations are obtained by obstructing in the injection slots the 30 injection holes located downstream or upstream respectively.

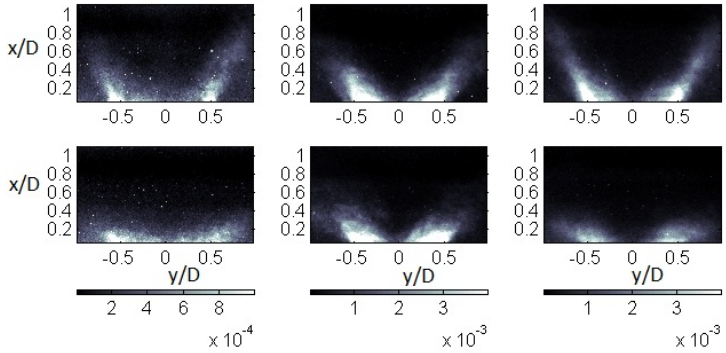

Figure 9.6: Impact of forcing on the RMS value of the local concentration fluctuations $C^{*\prime}$. Top: unforced case. Bottom: $St \approx 1$. Left: standard injection. Middle: downstream injection. Right: upstream injection.

When forcing is applied at the frequency of the helical structure, the zone of maximal fluctuations in concentration flattens radially (bottom row in Fig. 9.6). On the contrary, when forcing is applied at a lower ($St \approx 0.55$ and Fig. 9.7) or higher ($St \approx 1.2$, not shown here) frequency, the amplitude of the concentration fluctuations increases, though the main mixing profile remains very similar to the unforced case.

These observations can be quantified when the unmixedness is calculated over the streamwise position, assuming that the system is rotationally symmetric [LMK+07]. The results presented in Fig. 9.8 show that the forcing at the natural helical frequency reduces the spatial unmixedness U_x (left plot) mainly for the baseline and upstream injection. These changes are less pronounced when downstream injection is considered. The temporal unmixedness U_t (right plot) is marginally affected by forcing directly at the burner outlet, but the effect is more pronounced further downstream. When lower or higher forcing frequencies are considered (left and right plot

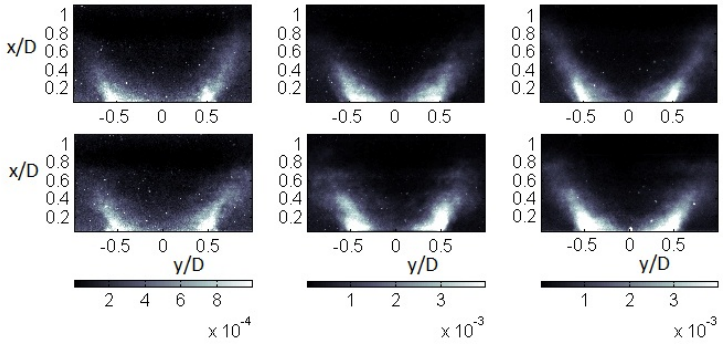

Figure 9.7: Impact of forcing on the RMS value of the local concentration fluctuations $C^{*\prime}$. Top: unforced case. Bottom: $St \approx 0.55$. Left: standard injection. Middle: downstream injection. Right: upstream injection.

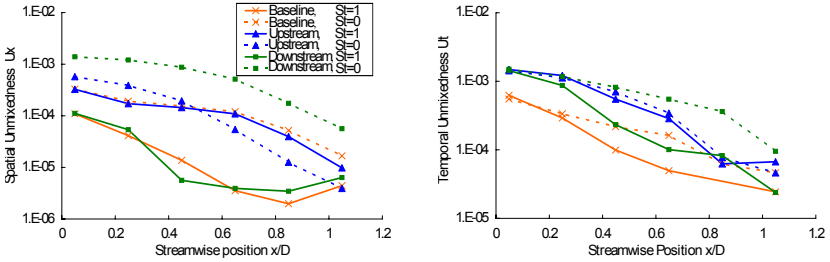

Figure 9.8: Axial evolution of the spatial (left) and temporal (right) unmixedness parameter. The parameter is calculated for baseline, upstream, and downstream injection for the forcing frequencies $St \approx 1$ and $St = 0$ (cases of Fig. 9.6) with a main flow Reynolds number $Re = 3.3 \times 10^4$. It is calculated after applying radial weighting, assuming a rotationally symmetric concentration profile.

in Fig. 9.9 respectively), the mixing quality tends to worsen for the different injection configurations at almost all axial locations.

Overall, these results show that nonlinear effects may influence the mixing quality and lead to an increase in the mixing quality recorded at the burner outlet when the forcing frequency is properly set. Here, such positive mechanisms occur when forcing is applied at the natural frequency of

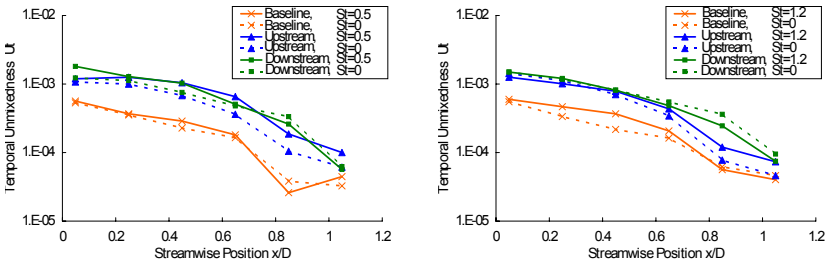

Figure 9.9: Axial evolution of the temporal unmixedness parameter U_t for the normalized forcing frequencies $St \approx 0.5$ (left, with $Re = 5 \times 10^4$) and $St \approx 1.2$ (right, with $Re = 3.3 \times 10^4$) showing the slight worsening of the mixing quality with such forcing frequencies.

the helical structure.

9.3.3 Impact of fuel flow pulsation on the mixing quality

The impact of square pulsations on the mixing quality of the jet-in-crossflow configuration was investigated. One advantage of this approach is the lower energy input required to modulate the fuel injection compared to modulation of the total air flowing through the burner.

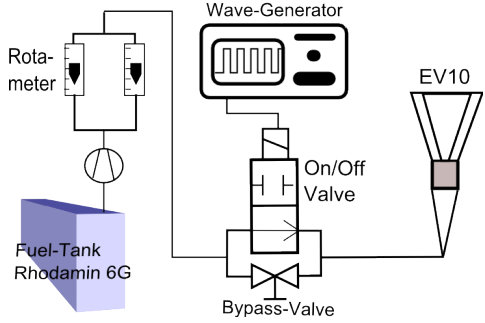

Figure 9.10: Setup for the pulsating fuel injection

A pulsed control signal is therefore imposed on the standard 90° crossflow fuel injection of the burner ($(\alpha, \beta) = (1, -)$) as illustrated in Fig. 9.10. The tests are conducted for different forcing frequencies and duty-cycles for a fully modulated fuel mass flow. The maximum axial Strouhal numbers set are St=2.49, 1.91, 1.47, 0.73, for duty-cycles of 20%, 35%, 50%, and 70% respectively. The concentration is once again measured with HS-LIF 5 mm downstream of the burner outlet. The temporal unmixedness parameter U_t is presented in Fig. 9.11 and shows that a decrease in the unmixedness is possible when using high forcing frequencies (St = 2.49, 1.91, 1.47). A maximum decrease of approximately 31.5% is obtained for a duty-cycle of dc=35% and a forcing frequency of St=1.91, while all the duty-cycles working with high-frequency actuation are able to reduce the unmixedness parameter U_t.

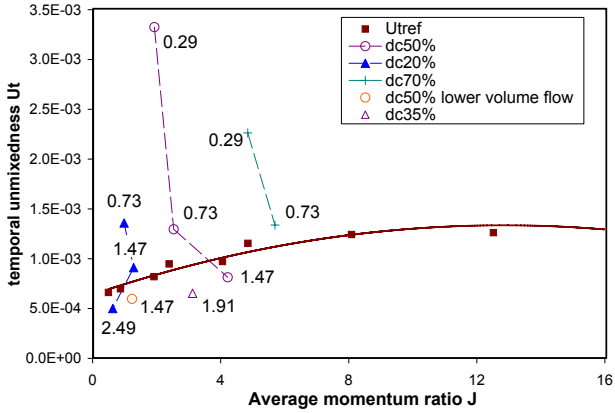

Figure 9.11: Temporal unmixedness U_t recorded 5 mm downstream of the burner outlet for the fully modulated fuel distribution $(\alpha, \beta) = (1, -)$ as a function of the average jet-to-crossflow momentum ratio J and the forcing frequency. The frequency is normalized with the mean residence time in the burner $St = f\tau_{ref}$ and displayed in italics.

For the highest forcing frequencies (Fig. 9.11), which deliver the best results, the temporal and spatial unmixedness parameters are compared in Fig. 9.12. Though the gains in temporal unmixedness U_t are still clearly visible, the spatial unmixedness U_x of the pulsated fuel does not vary very much from the reference spatial unmixedness. This is an expected result,

as axial fuel forcing, even if it increases the penetration of the fuel jet, does not completely change the mixing path, which is mostly determined by the main flow field. Hence, zones with lean or rich mixtures are expected to remain at the same location at the burner outlet. As the temporal unmixedness is reduced, one can conclude that the pulsation of fuel has more influence on the micromixing than the macromixing. Indeed, as reported by Johari et al. [Joh06], the generation of small puffs increases the contact area between between the dye issuing from the jet and the surrounding water crossflow and leads to a faster homogenization of the mixture than a steady jet would do.

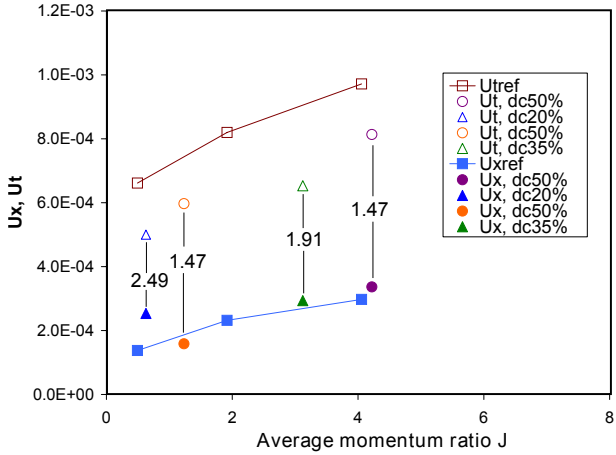

Figure 9.12: Comparison of temporal and spatial unmixednesses U_t and U_x 5 mm downstream of the burner outlet as a function of the average jet-to-crossflow momentum ratio J for the fuel distribution $(\alpha, \beta) = (1, -)$

These considerations are illustrated in Fig. 9.13(a) where the images of the time-averaged concentrations $\overline{C^*(\boldsymbol{x})}$ for forced and unforced cases are compared. A better homogenization is obtained with the pulsated fuel flow while the locations of the lean zones (in blue and in the top and bottom of the image) and of the rich ones (on the left and right) remain almost unchanged. The images of the time-averaged concentration fluctuations $\sqrt{\overline{C^{*\prime 2}(\boldsymbol{x})}}$ (on the right side in Fig. 9.13(a)) show that the locations of the

maximum fluctuations do not vary much, but that the amplitude of the fluctuation decreases when forcing is applied.

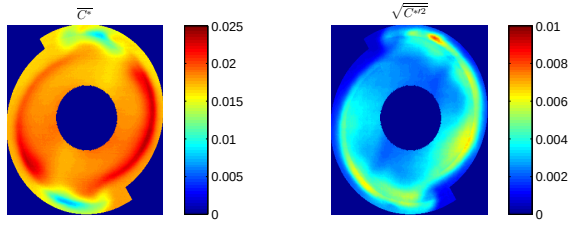

(a) Reference case (no forcing), J_{ref}=4.06

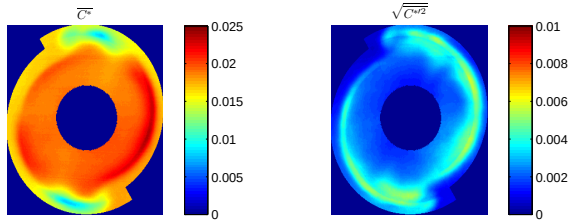

(b) Forcing, dc=50%, St = 1.47, maximal volume flow, J=4.22

Figure 9.13: Local time-averaged concentration $\overline{C^*(\boldsymbol{x})}$ (left) and corresponding local fluctuation $\sqrt{\overline{C^{*\prime 2}(\boldsymbol{x})}}$ (right) for the reference (top) and forced cases (bottom, dc=50%, 10Hz, 100 % fuel modulation, maximum volume flow)

This is confirmed when the probability density functions of both the time-averaged concentration and the concentration fluctuations for the two cases are compared in Fig. 9.14. The PDF of the time-averaged concentration shows the slightly improved mixing for the forced case, as the dominant central peak becomes higher. The slight shift of the main peak toward higher concentrations when forcing takes place is mainly due to the slightly higher mean concentration recorded at the outlet ($\langle\overline{C^*}\rangle_{ref} = 0.01768$ against $\langle\overline{C^*}\rangle = 0.01796$). The PDF of the concentration fluctuations indicates

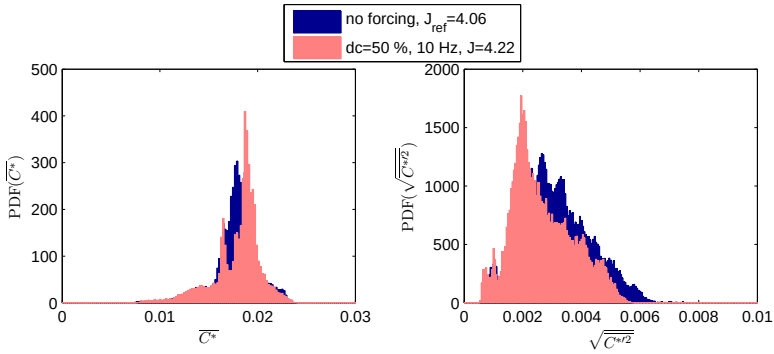

Figure 9.14: Comparison of the probability density functions of the time-averaged concentration $\overline{C^*(\boldsymbol{x})}$ (left) and the time-averaged concentration fluctuations $\sqrt{\overline{C^{*\prime 2}(\boldsymbol{x})}}$ (right) for the reference (dark blue) and actuated (red) cases of Fig. 9.13.

how the concentration oscillations decrease in amplitude when the forcing is applied, explaining the reduction of the temporal unmixedness previously observed. This confirms that the forcing enhances the micromixing inside the burner more than the macromixing. The latter is mostly influenced by the burner flow field, the fuel distribution and the geometry of the fuel injection lines.

The results described above are valid for relatively small jet-to-crossflow momentum ratios. To investigate the impact of higher jet momentum, the main volume flow was decreased from 8.55 m^3/h to 2.85 m^3/h, i.e., the Reynolds number was decreased from 3.5×10^4 to 1.2×10^4. The results presented in Fig. 9.15 show that the pulsed injection then has a negative impact on the unmixedness when J is increased above $J \geq$30. The positive effect of pulsation of the fuel injection is thus restricted, for this injection configuration, to lower jet-to-crossflow momentum ratios.

Adjusted to air flow conditions, the frequencies of interest should be higher than 200 Hz, which is a constraint if the pulsation needs to operate continuously. The manufacturing of devices capable of reaching such frequencies will be key to further improving the mixing quality of premixed burners.

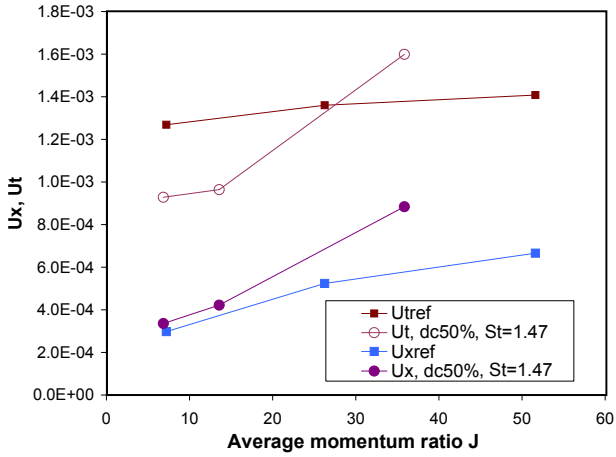

Figure 9.15: Spatial and temporal unmixednesses of the pulsed injection case (dc=50%, $St = 1.47$) compared with the non-pulsed cases

The implementation of such actuators is expected to reduce the unmixedness and, as a consequence, the NO_x emissions. For this reason, a new injection concept was tested on the burner: the fluidic injector.

9.4 Pulsations without moving parts: Fluidic injectors

To circumvent the need to implement an external pulsating device, self-oscillating fuel injectors are manufactured in a linear array on staged fuel injection lines. A sketch of the type of fluidic setup investigated is provided in Fig. 9.16. It is similar to the one used by Guyot et al. [GPR09] which was successfully used to control the thermoacoustic instabilities of a combustion chamber. The main difference is that the present design has only one outlet port instead of two. Furthermore, the actuator was scaled down by a factor of nearly 10 to fit within the geometrical constraints of the system tested. Design and manufacturing were performed by Advanced Fluidics Corporation.

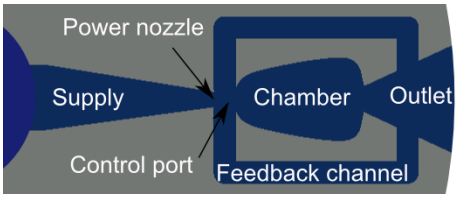

Figure 9.16: Simplified sketch of the fluidic injector

The steady flow enters the fluidic device through the power nozzle and is converted into a planar oscillating flow through the combination of flow attachment in the chamber and alternating feedback of the two feedback channels (for a more extensive description consult [GPR09]). The flapping motion of the exit jet produced is expected to generate locally discontinuous puffs of concentration, which should have a positive effect on the micromixing. Given fluidic geometrical constraints, the spacing of the injectors had to be greater than the spacing of the standard injection configuration (6.4 mm versus 4 mm). Hence, to compare the mixing efficiency, similar square injectors were manufactured with an outlet area equal to the power nozzle area (0.7 x 0.6 mm^2). Photographs of the fluidic device and of the reference injector are presented in Fig. 9.17.

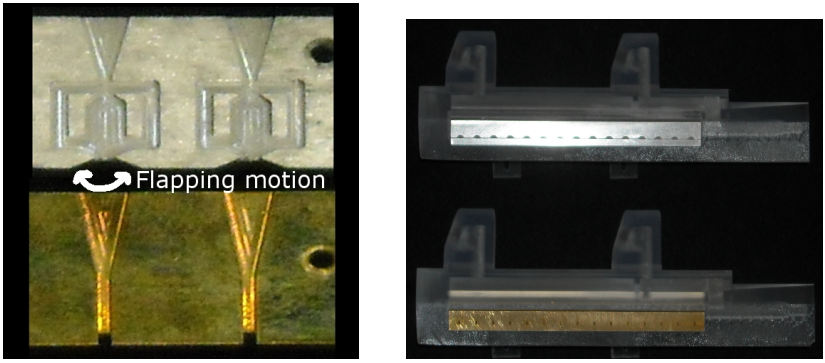

Figure 9.17: Photographs of the fluidic and reference injectors.

Figure 9.18 depicts the oscillation of the jet over one period at the outlet

of the fluidic device and provides evidence of the radial spreading of the jet. The mixing quality tests were performed for one main mass flow and different fuel injection mass flows. No variation of the fuel distribution was tested. The concentration measurement procedure was similar to the procedure described in the previous sections.

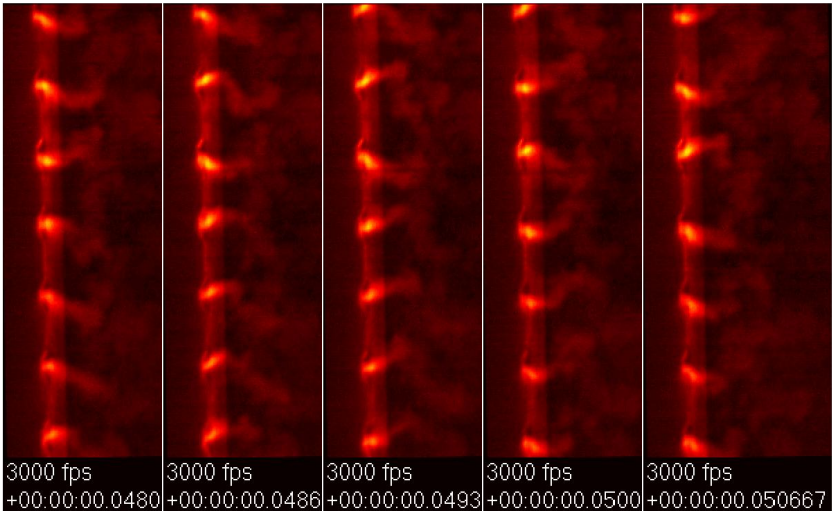

Figure 9.18: One period of oscillation of the fluidic matrix in a fluid at rest. Recording with a high-speed camera at 3000 fps.

The mixing quality of the two injector arrays is depicted in Fig. 9.19 as a function of the jet-to-crossflow momentum based on the outlet area of one jet. The graph shows that the fluidic injectors do not lead to an improvement of the temporal mixing quality over the whole range of momentum ratio investigated. A slight improvement of the spatial mixing quality can only be achieved for high values of J. Furthermore, as shown in Fig. 9.20, the power required by the fluidic injector is much higher than the one required by the standard injector.

Thus, this experiment shows that the fluidic injection design tested does not perform better than a standard fuel injection system. However, no design rule is yet available for optimizing the design of crossflow fluidic injectors in terms of the resulting scalar mixing quality. In particular,

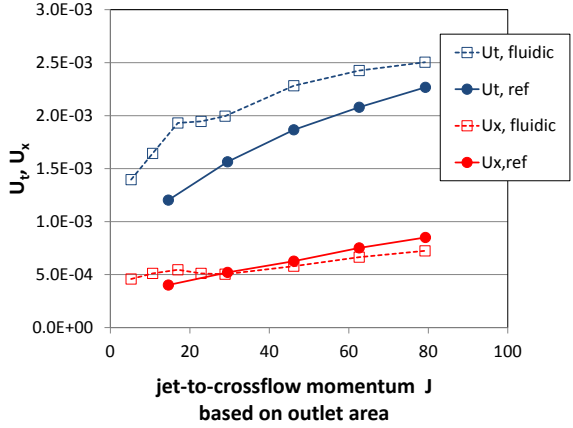

Figure 9.19: Comparison of temporal and spatial unmixedness, U_t and U_x, for the fluidic and reference injections as a function of the jet-to-crossflow momentum J based on the outlet area of one jet

the critical spacing ratio of the fluidic injection holes will depend both on the momentum and on the flapping angle of the injectors. As reported by Nathan et al. [NMA+06], for a different self-oscillating configuration, the mixing efficiency of such fluidic injectors is the highest close to the injection location, the far-field behavior being less influenced by the initial oscillation conditions. Therefore, an optimal design has to take the mixing length into account. If the flame is located close to the injector, then such fluidic actuation can be expected to considerably improve the mixing quality.

For the present configuration and considering a flame stabilized outside the burner, better results are expected if the jet oscillation plane were to be rotated by 90°around the jet main axis. The flapping motion would then no longer cause interaction between neighboring injection holes but rather would act similarly to the pulsed fuel injection tested in the previous section. Here the design plans of the scientist had to be scaled back due to manufacturing constraints for such an array; the originally conceived design would have been much more complex to manufacture and mount on the burner (due to geometrical constraints). Accordingly, in future work,

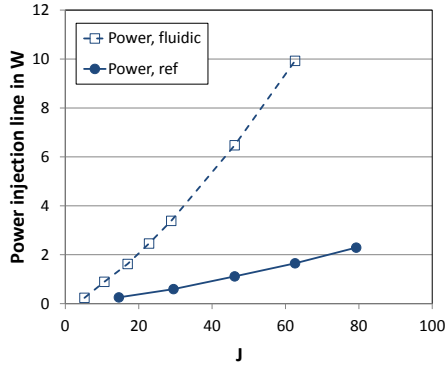

Figure 9.20: Power ($Q_{fuel}\Delta p$, in Watt) of the injectors as a function of the jet-to-crossflow momentum J. Pressure recorded approximately 1 m upstream of the fuel injection location.

it would be very interesting to go on to test the impact of other angles on the mixing quality in a generic crossflow configuration.

However, the efficiency of the fluidic injector could be demonstrated on another fuel injection configuration which is presented below.

9.4.1 Mixing improvement with fluidic implemented in a generic configuration

The investigated setup is a generic jet-in-crossflow configuration; a lance is mounted centered in a square channel of side length L. The ratio of the lance diameter to the channel side length is equal to 0.296. Through four rectangular holes a mixture of fluorescent dye and water is injected with an angle of 90° relative to the main water flow. The main direction of the dye injection is colinear to the diagonal of the cross-section of the square channel as illustrated in Fig. 9.21.

Similar to the fluidic implementation on the swirl-inducing burner, two types of injectors are considered: a standard jet and a fluidic jet. Both jets have the same rectangular outlet corresponding to a hydraulic diameter d_h. The ratio of the rectangle sides is equal to 2.35 with the longest side parallel to the main flow direction. The fluidic injectors induce a jet oscillation in

a plane perpendicular to the direction of the main flow. This oscillation is expected to increase the dilution of the jet with the surrounding fluid by increasing first the macro-mixing (i.e. the spatial distribution of the fuel) close to the injection and then the micromixing, as the surface of contact between the dye and the main flow is expected to augment when compared to a standard jet injection. The tests are performed in the water test rig and

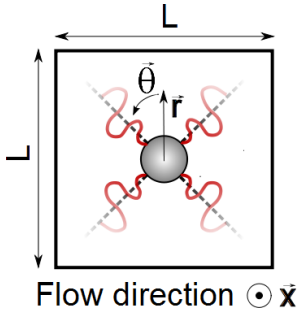

Figure 9.21: Jet-in-crossflow configuration and illustration of the fluidics oscillation plane

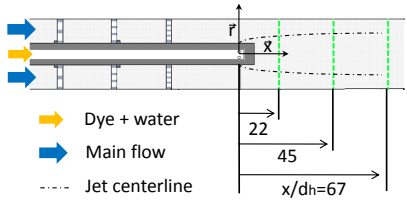

Figure 9.22: Slice of the test channel and localization of the axial measurement planes downstream of the injection location

the test section is illustrated in Fig. 9.22. Three screens placed upstream of the injection location ensure a symmetrical velocity profile of the main flow. The Reynolds number in the square test section is calculated as

$$Re = \frac{u_0 D_h}{\nu}\,, \tag{9.1}$$

where D_h is the hydraulic diameter of the cross-section area of size $L \times L$, u_0 the mean bulk velocity of the test section and ν the water viscosity. In the present work, the Reynold number was hold constant at Re=72300, which is high enough to ensure a relative independency of the mixing process and resulting quality with a variation of the mean bulk velocity. The jet-to-crossflow momentum ratio is equal to 2.3, 6.4, 17.7, or 55.

The concentrations are recorded with the HS-LIF system at a frequency of 125 Hz or 250 Hz in the axial planes shown in Fig. 9.22. The ratio of the average particle displacement in the flow direction due to the camera shutter

time δ_s to the jet hydraulic diameter d_h is equal to δ_s/d_h =0.11. Furthermore, the average axial displacement in the measurement plane is two times smaller than the laser sheet thickness. As the radial and azimuthal velocity components are much smaller than the axial one, the recorded pictures can be considered as a frozen pattern of the mixing process.

A comparison of instantaneous concentrations recorded in the plane located at $x/d_h = 67$ for a momentum ratio $J = 17.7$ is first presented in Fig. 9.23. The structure of the concentration distribution greatly changes between the fluidic and the reference injectors; the fluidic injectors present a more homogenized pattern than the reference injection. The maximal concentrations encountered are also lower in the fluidic case, indicating a better dilution of the fuel with the surroundings. These snapshots are thus qualitatively indicating that the mixing quality increases when the fluidic injectors are used. Similar conclusions could be drawn for instantaneous snapshots recorded in the two other measurement planes.

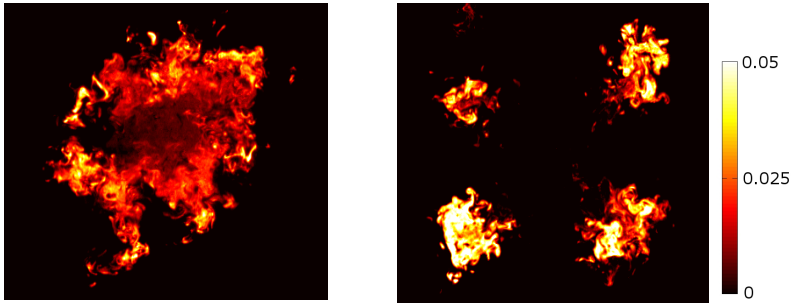

Figure 9.23: Instantaneous concentrations C^* recorded at the measurement plane $x/d_h = 67$. Top: fluidics injection, bottom: standard injection. $Re = 72300$, $J = 17.7$.

The total unmixedness U_t is then recorded for different jet-to-crossflow momentums J at the measurement planes shown in Fig. 9.22. The ratio of the total unmixedness of the fluidics injectors to the total unmixedness of the reference standard jet is calculated and presented in Fig. 9.24. All the investigated cases present a great improvement of the mixing quality over the whole mixing path. The best mixing quality improvements are achieved for the jet to crossflow momentum $J = 17.7$, with a decrease in

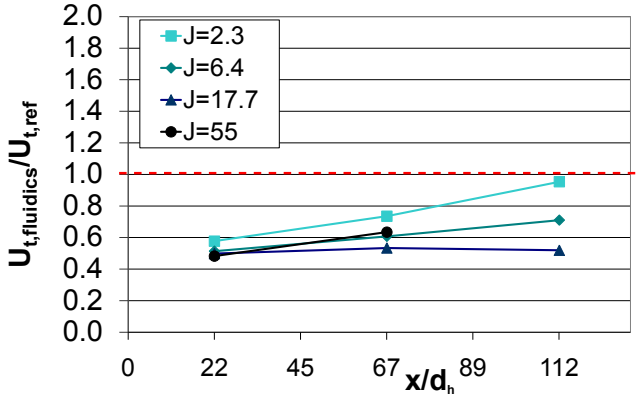

Figure 9.24: Relative gain in temporal unmixedness $U_t/U_{t,ref}$ depending on the axial position normalized by the hydraulic jet diameter, x/d_h, and for different jet-to-crossflow momentums J

the relative temporal unmixedness by approximately 50%, and this over the whole mixing path! These results confirm thus the potential of fluidic actuators to improve the mixing quality of jet-in-crossflow mixers. Further results concerning this configuration are presented in Annex C.

9.5 Summary

In this last chapter, the effect of passive and active control methods on the passive scalar mixing quality at the outlet of two configurations was reported. Passive modifications of the fuel injection arrangement can improve the mixing quality but offer a poor flexibility. Active forcing of the main flow or of the fuel flow injection can also lead to improvements if the frequency of actuation is properly adjusted. When considering a fuel injection modulation, the mean jet-to-crossflow momentum must also be maintained low to influence positively the mixing quality. Finally the use of fluidics actuators shows great potential to improve the mixing quality of the last configuration investigated. Unlike for standard jets, which were relatively well investigated over more than 30 years, further investigations

are required to characterize the influence of geometrical and dynamical parameters on the mixing quality when self-oscillating devices are used.

Conclusions

By adjusting the fuel injection profile, (open-loop) control of the pressure pulsations and NO_x emissions has been achieved in a lean premixed combustor using fuel staging. To implement a closed-loop controller, a model of the mixing inside the burner is required. Adjusting the fuel injection leads to strong changes in the flame shape and stabilization location which have to be taken into account for the modeling task. As most burner design tests start with non-reacting experiments, this thesis shows how cold flow measurements can be combined with flame visualization to model the spatio-temporal response of fuel/air mixing in a lean premixed combustor using fuel staging.

As water flow tests allow better quality data to be obtained than experiments in air, the similitude between water, air and reacting flow measurements is investigated. A good agreement was obtained between the velocity and turbulent fields in the two media. The slight discrepancies observed, in particular regarding the degree of turbulence, are mainly due to the different inflow conditions of the two types of test rigs. The passive scalar mixing quality, which is a normalized expression of the variance of the concentration fluctuations, exhibits a weak Reynolds number dependency, suggesting that the mixing quality in water and in air remain very similar. Therefore, it is concluded that the use of water experiments to model the mixing is valid.

The velocity and concentration measurements performed at the burner outlet as well as in the burner slot reveal strong coherent fluctuations. Phase-locked particle image velocimetry, laser Doppler anemometry and hydrophone measurements confirmed that a helical structure rotating with the swirl but winding in the opposite sense (mode = +1) is present inside and outside the burner. The Strouhal number is close to unity ($St \approx 1$). Periodic oscillations are measured upstream of the inlet slots and induce fuel/air concentration fluctuations which can be detected at the slot as

well as outside the burner using high-speed laser-induced fluorescence (HS-LIF). The simultaneous measurement of concentration and velocity with PIV/LIF confirms the strong coupling mechanism between the velocity and concentration fluctuations.

The reacting flow also bears a strong similitude with the non-reacting flow. However, the degree of similarity was strongly dependent on the flame stabilization location. Proper orthogonal decomposition (POD) applied to the velocity field demonstrated that if the flame remains stabilized downstream of the burner, the helical structure is almost unaffected by the flame. As the coherent oscillations are associated with concentration fluctuations, they also induce local heat release fluctuations which can be seen in phase-averaged OH* chemiluminescence images and when POD is applied to the chemiluminescence signals. On the contrary, when the flame anchors inside the burner, the helical structure is almost completely damped.

For a flame stabilized outside the burner, the turbulent velocity length scales also have a strong similitude and can be used to estimate the combustion regime within the Borghi diagram. Hence, depending on the stabilization location, the cold flow measurements can capture the mixing properties upstream of the flame very well and this property is used to derive the temporal mixing model.

Using the water test rig, the mixing quality of the different fuel injection configurations is recorded in different axial planes at the burner outlet. An experimental model of the scalar variance is derived for different fuel distributions and operating conditions. The measured probability density function (PDF) of the mixture is reasonably well approximated by a beta function distribution, which can be then calculated from the variance and mean concentration of the experimental PDF. The latter values build the unmixedness parameter of the mixture. The flame position as well as an exponential decay of the fuel/air unmixedness measured in cold flow are then used to estimate the mixing quality at the flame location. An empirical correlation predicting the NO_x emissions for various operating parameters, such as air and gas mass flows and preheating temperature, is thus greatly enhanced. A simple chemical network model, developed in CANTERA, is used to cross-check this estimated PDF of the mixture. It reveals that a good quantitative agreement is obtained for a flame stabilized

outside the burner but with a shorter decay coefficient of the unmixedness than the one measured experimentally. Due to the strong changes in the flow field, the real PDF of the mixture for a flame anchored in the burner is not accessible without further modeling effort. However, the modeled unmixedness can be used for both flame types with a controller minimizing the NO_x emissions.

Control of NO_x emissions requires a fast sensor. Chemiluminescence-based sensors are shown to be appropriate, as they are very fast compared to conventional gas analyzers and a minimization of their value correlates with a decrease in the unmixedness and, hence, in the NO_x emissions. Measurements performed with a spectrometer indicate that a reduction of the ratio CH*/OH* correlates even better with a reduction of NO_x emissions. However, it does not allow for quantitatively capturing the mixing quality of the fuel/air mixture.

To control the stability of a lean premixed combustor, the response of the fuel/air mixture to velocity perturbations has to be modeled, both time delays and temporal spreading playing a key role in the stability of the combustion process. Accordingly, the residence time distribution (RTD) or mixing transfer function (MTF) needs to be recorded. For this, a measurement technique based on a step response measured using high-speed laser-induced fluorescence (HS-LIF) is developed, making it possible to record the short convective time delay (or high-frequency response) of such burners. A mixing model-based on the interconnection of three reactors solving the one-dimensional convection-diffusion equation is built. The necessary parameters are identified from the step response recorded using HS-LIF and the model then allows the MTF for different fuel injection distributions to be predicted. The link of the cold mixing transfer function with the flame transfer function recorded in the combustor is made by estimation of the one-dimensional axial heat release distribution obtained from the OH* chemiluminescence images, assuming statistical independence between the MTF and the heat release distribution. The evolution of the main convective time delay as a function of the fuel injection distribution is reasonably well captured by this method. The discrepancies observed

can be attributed, firstly, to the differences between OH* chemiluminescence and heat release distributions and, secondly, to the statistical independence assumption. Both assumptions weaken as the fuel/air mixture inhomogeneity increases.

Active control of the fuel split is achieved with help of an extremum-seeking control (ESC) scheme to adjust the pressure pulsations and NO_x emissions of the combustor. The standard ESC is able to stabilize and reduce the emissions. However, it does not use the knowledge of the mixing model and may stabilize in local minima. Therefore, the temporal and mixing quality models are combined with the ESC approach to develop an extended extremum-seeking controller. Specifically, the stability and mixing quality maps are added to the sensor signal and generate a new model-based function, which must be minimized by the controller. Local minima can then be removed from the map if there is strong confidence in the models. The system is able to stabilize at the optimal injection and to remain stable when transients in the operating conditions occur.

Finally, the effect of different passive (modification of the injection hole arrangement) and active control strategies on the mixing quality is investigated, as a decrease in the NO_x emissions is recorded when a perfectly premixed mixture is burnt in the combustor. It is shown that passive fuel arrangements involving different fuel injection angles can slightly increase the mixing quality of the staged fuel injection over a range of different jet-to-cross-flow momentum ratios. This improvement is not, however, true for all the fuel distributions and restricts thus the effectivity of passive fuel injection modifications. Therefore, the effect on the mixing quality of actively pulsating the fuel injection is investigated. It is shown that high-frequency pulsations increase the mixing quality at the burner outlet by decreasing the amplitude of local temporal fluctuations in concentration. On the basis of these results, a self-oscillating injector based on fluidic concepts is developed and implemented for the first time in a premixed burner. A reference injector with a similar geometry allows for a comparison of the mixing qualities. An increase in the mixing quality for a given mass flow is achievable. However, the ratio of unmixedness to the power used by the actuator clearly favors the standard fuel injection. Further optimization of the design is expected to enable the mixing properties of fluidic injectors

to be fully exploited to reduce the mixing length of premixed combustors. Indeed, the concept of fluidic injection is validated in another cross-flow injection configuration, which showed an increase in the mixing quality of up to 50% compared to a standard fuel cross-flow injection.

Outlook

Mixing transfer function measurement technique As stated in the thesis, an improvement of the measurement technique would allow a more accurate mixing transfer function to be identified. This improvement requires the simultaneous use of high speed LIF and PIV measurement techniques in order to record precisely the passive scalar flux. Without the velocity information, the inhomogeneity in the velocity profile may induce some errors in the mixing transfer function. The drawback of such a technique is the amount of data that would be produced by such a complex measurement as well as the time needed to set up and calibrate the system. Therefore, a first step could be to quantify the error when the local velocity information is not taken into account.

Another improvement of the measurement technique would be to use a second calibrated HS-LIF system immediately downstream of the fuel injection location in order to increase the precision of the inlet transfer function. If simple fuel injection is used, with no staging but which offers optical access, a step of the concentration in the fuel line recorded by a photomultiplier would allow the inlet step to be recorded more accurately. Furthermore, a step in the concentration does not affect the flow field, a fact which is neglected when a step of the fuel mass flow is used.

Mixing model In the present work, it appears that a statistical analysis of the mixture quality has been sufficient to obtain information which can be used in a relatively low frequency fuel adjustment scheme to minimize the NO_x emissions. However, for a model to capture the mixing quality at higher frequencies, two approaches might be considered. A mixing network model, similar to the one used for the convective time delays, could be built to capture the spatial and temporal variations in the scalar variance. For this, the approaches of Fox [Fox03] or Osenbroch [Ose04] could be used to derive the network model. The advantage of this approach would be to describe with one model the time delay as well as the mixing quality

information. An alternative approach would be to use POD analysis to extract the dominant passive scalar modes of the flow and obtain a low order model of the main coherent fluctuations. The latter can be used to evaluate the instantaneous mixture quality. The disadvantage of the POD approach is that the time delay information would not be contained in the model obtained.

Scalar mixing optimization It has been shown that fluidic actuators may bring a large increase in mixing quality, in particular in generic jet-in-crossflow configurations. Unlike simple jets which have been extensively investigated for more than 20 years, the mixing characteristics of fluidic injectors are just starting to be explored. The present results demonstrate the great potential of such actuators and should open the door to further research projects in that field. In particular, reductions in costs, as well as in the pressure loss of the actuators, should be considered at the same time as gains in mixing quality.

Appendix A

Compressible jet mass flow

The gas injection through a series of small holes is similar to the discharge of a pressurized tank in the state p_0, ρ_0, T_0, and the initial velocity u_0 through a small orifice of area A_e. The gas at the outlet is in the state p_e, ρ_e, T_e and has the velocity u_e. Assuming an isentropic process, the theoretical outlet velocity can be calculated after a simple enthalpy balance as

$$u_e^{'} = \sqrt{2\frac{\gamma}{\gamma-1}\frac{p_0}{\rho_0}\left[1-\left(\frac{p_e}{p_0}\right)^{\frac{\gamma-1}{\gamma}}\right]}\,. \tag{A.1}$$

The resulting equation is also called the Saint-Venant and Wantzel equation. Because of energy losses caused by the contraction (separation, vortices), the expansion cannot be considered as purely isotrop. Thus, the effective velocity at the jet outlet is smaller and the effective temperature higher. Both values are depending on the geometry of the orifice and the expression of the effective velocity u_e at the nozzle outlet is then

$$u_e = \phi u_e^{'}\,. \tag{A.2}$$

This velocity occurs at the location of the smallest cross-section equal to αA_e where α is the jet contraction. For the calculation, ϕ was equal to 0.82 and α was equal to 1 [Boh98]. The product $\phi\alpha$ is also known as the orifice flow coefficient. The velocity being the searched parameter, and no information being known on the pressure p_0 just upstream of the injection in the actual combustor setup, an iterative procedure is used to calculate total gas mass flow $\dot{m}_{th}$ by adjusting the upstream pressure p_0

until the theoretical mass flow $\dot{m}_{th} = \rho_e u_e A_e$ matches the set mass flow. The theoretical expression of the gas mass flow $\dot{m}_{th}$ is:

$$\dot{m}_{th} = A_e \sqrt{2\rho_0 p_0} \sqrt{\frac{\gamma}{\gamma - 1} \left[\left(\frac{p_e}{p_0} \right)^{\frac{2}{\gamma}} - \left(\frac{p_e}{p_0} \right)^{\frac{\gamma+1}{\gamma}} \right]} = A_e \sqrt{2\rho_0 p_0} \psi \,, \quad \text{(A.3)}$$

where ψ is the outflow function. The resulting real total gas massflow $\dot{m}_f$ is

$$\dot{m}_f = \phi \alpha \dot{m}_{th} \,. \quad \text{(A.4)}$$

The outflow function shows a maximum of 0.473 at a critical pressure ratio $(p_e/p_0)_{crit}$ of 0.546 for $\gamma = 1.3$ as it is the case for methane. This condition is necessary to obtain a chocked fuel injection. Regarding the atmospheric combustion chamber used, and neglecting first the pressure loss inside the burner, the pressure at the outlet of the jet is $p_{slot} = 1.013 \cdot 10^5 \,\text{Pa}$. A critical pressure ratio of 0.546 means that the pressure in the injection line should be at least equal to $p_0 = 2.026 \cdot 10^5$ Pa.

In modern premixed combustors, chocked fuel inlet conditions are often achieved and assumed for modeling of the thermo-acoustics [LTJZ01]. This condition is achieved when the Mach number of the fuel at the outlet of the injection holes is equal to unity, which means also that the function ψ reaches a maximum. Looking at the geometry of the combustor and using Eq. A.1, this means that a minimal fuel mass flow of 17.5 kg/h is needed to obtain chocked conditions. As the actual operating conditions of the burner remain generally well below 10 kg/h, an unchocked injection of gas at the burner inlet is obtained.

Appendix B

Forcing mechanism of the water test rig

B.1 Forcing mounted in the bypass of the pump

One of the particularity of the test rig is its forcing mechanism, placed upstream of the test section. It was previously developed by Wang [Wan00], who used the shape of a standard valve (a big hole through a sphere) to force the flow of a shear layer. This mechanism was mounted first in the bypass of the pump, as shown in Fig 3.6. The forcing amplitude was first adjusted with the valve of the bypass. Very high forcing amplitudes could be achieved, but a proper sinus wave was difficult to obtain, and was limited to high forcing frequencies. The amplitude of the response was also strongly depending on the frequency set, as shown in Fig. B.1.

To circumvent this problem, a simulation in Simulink based on the unsteady Bernoulli equation, and quasi-steady response of the pump was performed. The simulation showed that the test rig would be more receptive if the forcing mechanism was mounted in the main piping (see also Fig 3.6). Furthermore, the shape of the valve was modified to improve the signal quality and control the amplitude of the forcing. If the pressure drop over the forcing valve is considered as constant over one forcing period, the volume flow through the valve depends solely on the blockage ratio and its corresponding pressure loss coefficient. If the temporal shape of the volume flow oscillation is set (a sinusoid), then the blockage ratio of the valve can

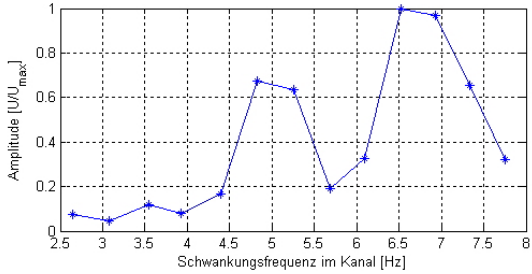

Figure B.1: Response of the forcing amplitude in the test section for different rotation frequencies of the forcing mechanism. Standard valve, mounted in the bypass.

be calculated over one period. This results in a valve which has an ellipsoidal shape. Figure B.2 illustrates the two geometries used to generate small and large sinusoidal volume flow oscillations. Rapid prototyping was used to manufacture the vales.

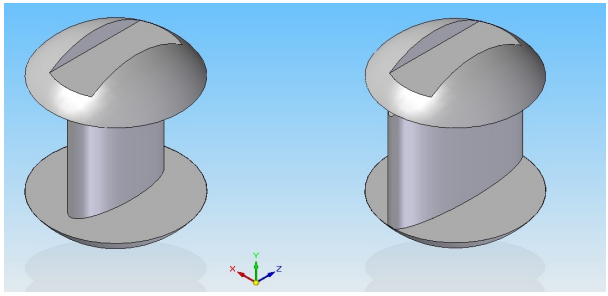

Figure B.2: Geometry of valves used for forcing in the main piping. Low forcing amplitude (left, ball D), strong forcing amplitude (right, ball B).

B.2 Forcing mounted upstream of the test rig

The impact of the different valves on the velocity oscillations recorded at the burner outlet was recorded with LDA for different forcing frequencies. The axial velocity is recorded close to the hydrophone mounted as in Fig. 3.7. As the measurements are performed at the burner outlet, the characteristic peak of the helical structure is visible in all the recorded spectra (peak close to 5 Hz). Still, the velocity spectra presented in Fig. B.3 show that the forcing can be considered as purely harmonic and that a decrease of the forcing amplitude occurs when the forcing frequency is increased. The spectra of the hydrophone are close to the LDA spectra even if they present harmonics which are not shown by the velocity spectra.

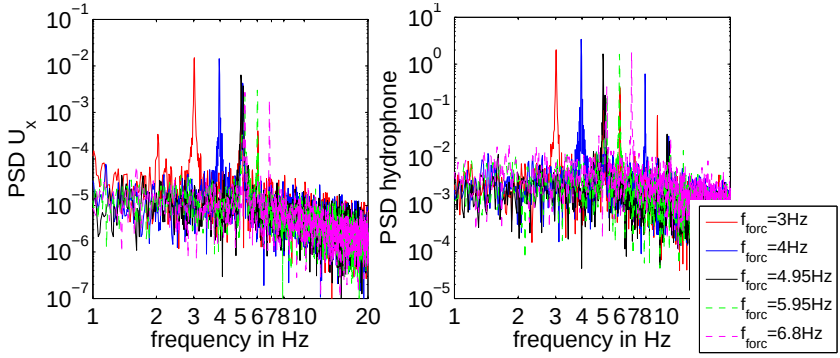

Figure B.3: Power spectra of the responses of the axial velocity u_x (left) and hydrophone (right) for the ball B, at different forcing frequencies. Forcing mechanism equipped with ball B and located upstream of the test section. Hydrophone located at the burner exit as in Fig. 3.7 and LDA measurement volume located close to the hydrophone.

LDA measurement were further conducted in the inlet slot for the two different valve sizes and at the same frequencies as in Fig. B.3. Table B.1 summarizes the measured relative amplitude a of the axial velocity oscillations defined as $u_x(t) = \overline{u_x}\,(1 + a \cdot sin(\omega t))$ measured at the position (x, y, z)=(-61 mm, -9.5 mm, -29 mm). Forcing amplitudes of up to 90% are

possible with ball B; this amplitude being aproximately 3 times the one achieved with ball D.

Frequency (Hz)	3	4	4.95	5.95	6.8
a, ball B	0.90	0.88	0.59	0.40	0.32
a, ball D	0.16	0.32	0.25	0.09	x

Table B.1: Amplitude of axial velocity oscillation a recorded with LDA in the burner inlet slot at the position (x, y, z)=(-61 mm, -9.5 mm, -29 mm) and for a volume flow of 8.55 m^3/h, forcing mechanism located upstream of the test section

Further measurements performed at the outlet of a simple bluff-body showed that the coherence between hydrophone signal and forcing valve sweep signal as well as the forcing bandwidth increase with increasing volume flow. However, as the response of the valve is still depending on the pressure loss in the whole test rig, tests of the response of the forcing at the frequency of interest should be performed prior to any measurement.

Appendix C

Fluidic oscillator in a generic cross-flow configuration

This section describes more in details the mixing mechanisms which take place in the generic jet-in-crossflow configuration shown in Sec. 9.4.1.

C.1 Oscillation frequency recorded at the fluidic outlet

The oscillation frequency of the fluidic was calculated from the FFT analysis of local concentration fluctuations recorded at a distance $x/d_h = 2.2$ downstream of the fuel injection location.The flapping motion of the fluidic at this location is illustrated in Fig. C.1 and confirms the wide azimuthal spreading of the jet. The measurements were performed for different dye mass flows and hence different jet Reynolds numbers. The main volume flow was set at a very low value simply to avoid the accumulation of dye in the measurement plane. Figure C.2 depicts the evolution of the normalized frequency (the Strouhal number based on the hydraulic diameter of the rectangular injector) of the fluidic with the jet Reynolds number.

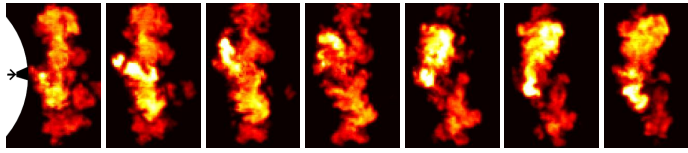

Figure C.1: One period of oscillation of the fluidic injector recorded at x/d_h=2.2

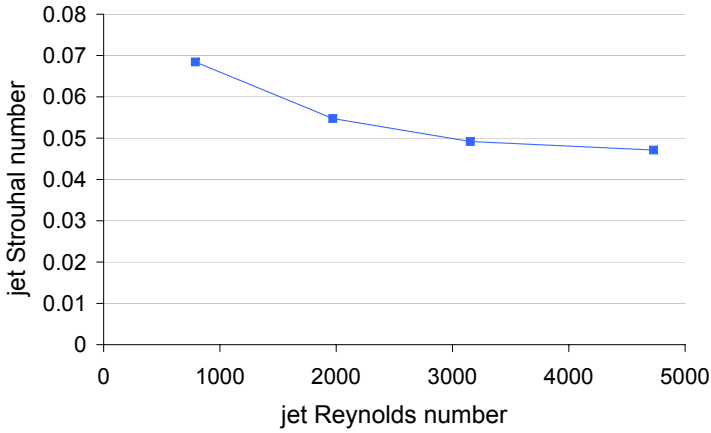

Figure C.2: Strouhal number of the oscillation frequency depending on the jet Reynolds number of the fuel injection

A small decrease in the Strouhal number (from 0.07 down to 0.05) is visible with an increasing jet Reynolds number. This means that the frequency of the jet oscillation is not a linear function of the velocity. Regarding the present work and a constant main flow Reynolds number, this means also that an increase in the jet-to-crossflow momentum will induce an increase in the oscillation frequency. This frequency change may certainly also affect the mixing process. However, the variation of one parameter at once (frequency or jet momentum) would have required hardware modifications to adjust the oscillation frequency. This was not performed in the present work, as it is not relevant for practical applications where one fluidic geometry should work well for different operating conditions. Hence the reader should bear in mind when looking at the following charts that an increase of the jet momentum is linked with an increase of the fluidic oscillation frequency. The frequencies involved in the air with the present fluidic would be typically of the order of 1000 Hz (not measured here). In water, they were of the order of 20 Hz and higher.

C.2 Mixing comparison at one axial location

C.2.1 Time-averaged concentration

The comparison of the time-averaged concentrations confirms the first impressions gained from the instantaneous pictures: the dye distribution of the fluidic injectors is more concentrated in the center of the square channel while 4 distinct islands are visible for the standard injectors. Even if the injector geometry ensures an equal mean bulk velocity at the outlet of the injectors (and hence an identical absolute jet to crossflow momentum), it is clear that the oscillating motion leads to a much lower penetration of the fluidic injector. This low jet penetration is responsible for the centered pattern obtained with the fluidic injectors.

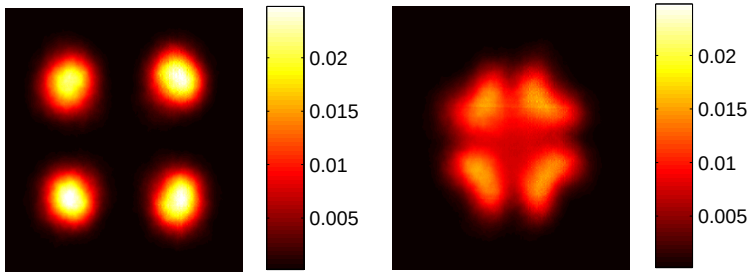

Figure C.3: Time-averaged concentration pictures $\overline{C^*}(\boldsymbol{x})$ for the standard (top) and fluidics (bottom) injections, recorded at $x/d_h = 67$, $J = 17.7$.

Furthermore, the maximal time-averaged concentrations are slightly lower for the fluidic injection than for the reference jet-in-crossflow. This result is well illustrated by the probability density functions of the time-averaged concentration shown in Fig. C.4: the maximal value of the reference case is close to $\overline{C^*}$ =0.025 while the fluidic case presents a much lower maximal time-averaged concentration of $\overline{C^*}$ =0.015. This confirms that the dilution of the fluidic jet with the surrounding flow is much higher than the one of the standard crossflow jet.

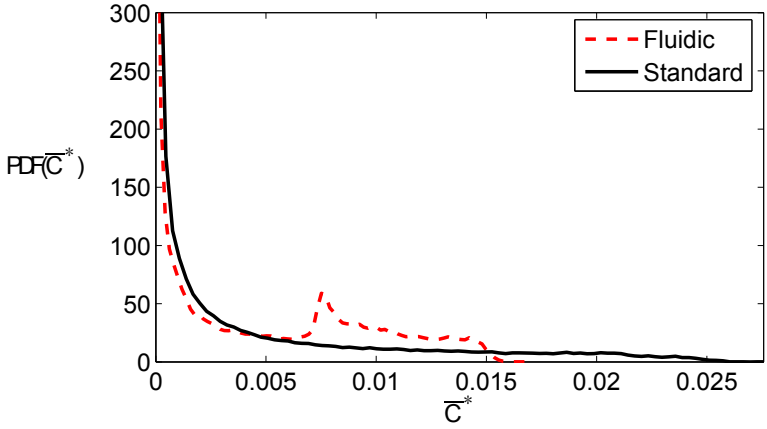

Figure C.4: Comparison of the probability density functions of the local time-averaged concentrations $\overline{C^*}(\boldsymbol{x})$ for the standard and the fluidic injections, recorded at $x/d_h = 67$, $J = 17.7$

C.2.2 Concentration fluctuations

The improvement in the mixing quality is also visible in the pictures of the RMS values of the local concentration fluctuations. The images shown in Fig. C.5 present first a pattern similar to the time-averaged concentration pictures shown in the previous section. This is particularly true for the standard jet injection. For the fluidic injection, the position of the maxima in concentration fluctuations are slightly shifted toward the corners of the channel when compared to the maxima of the time-averaged concentration pictures (Fig. C.3).

The amplitude of the local concentration fluctuations is also much lower with the fluidic injection than with the standard jet injection, as confirmed by the PDF of the two injection types shown in Fig. C.6. This decrease in the local concentration fluctuations is an indication of an increase in the micro-mixing quality.

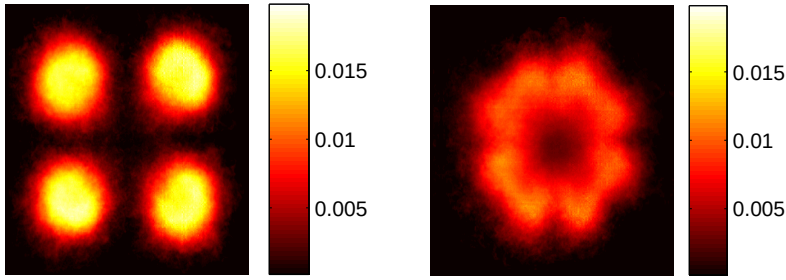

Figure C.5: Pictures of the RMS value of the local concentration fluctuations $C'^{*}_{RMS}(\boldsymbol{x})$ for the standard (top) and fluidic (bottom) injections, recorded at $x/d_h = 67$, $J = 17.7$.

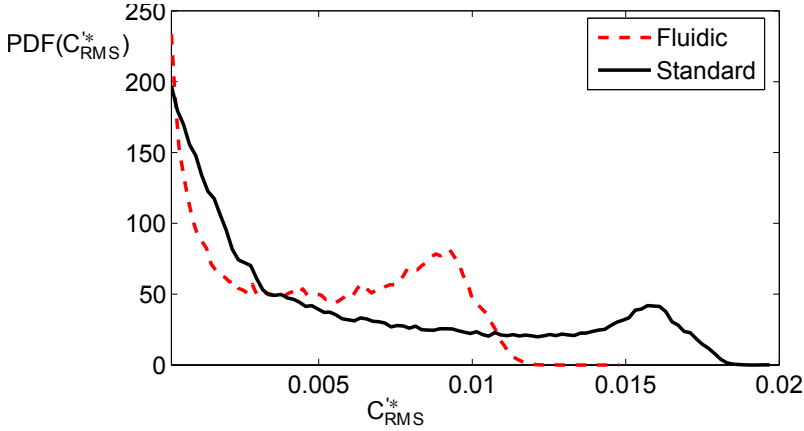

Figure C.6: Comparison of the probability density functions of the local RMS value of the concentration fluctuations $C'^{*}_{RMS}(\boldsymbol{x})$ for the standard and the fluidic injections, recorded at $x/d_h = 67$, $J = 17.7$

C.3 Mixing quality improvement

C.3.1 Evolution of the unmixedness parameters at x/d_h=22 and x/d_h=112

The spatial and temporal unmixedness parameters allow the mixing quality to be quantified. Looking at the results recorded at x/d_h=22 downstream

of the injection location (Fig. C.7), the fluidic injectors present a dramatic enhancement of the mixing quality when compared to the standard injection: a decrease by 50% in the spatial unmixedness U_x and by 40% in the temporal unmixedness U_t are recorded. Even if less pronounced, the gain in mixing quality at $x/d_h = 112$ can still reach 50% if the momentum ratio is properly adjusted (J=17.7 in Fig. C.8).

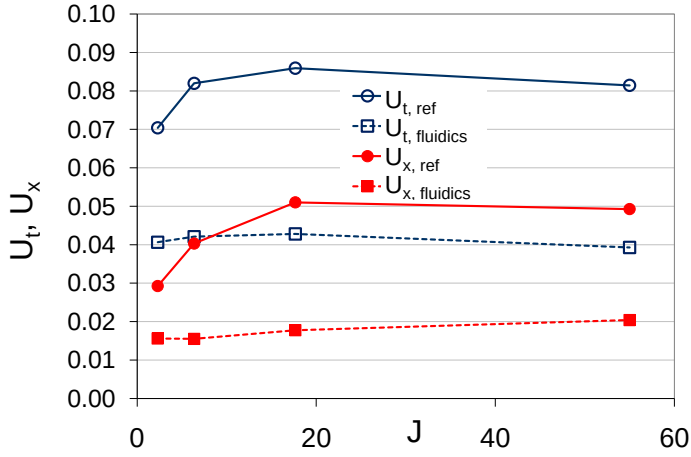

Figure C.7: Spatial and temporal unmixedness criteria depending on the jet-to-crossflow momentum recorded at $x/d_h = 22$

Furthermore, for the fluidic injector and the two illustrated measurement planes, the mixing quality is mostly independent of the injection momentum J, while the standard injection presents stronger variations. These results may be of strong importance if different operating points involving different momentum ratios are used in practical application. The fluidic injectors would ensure a constant mixing quality over the different operating conditions.

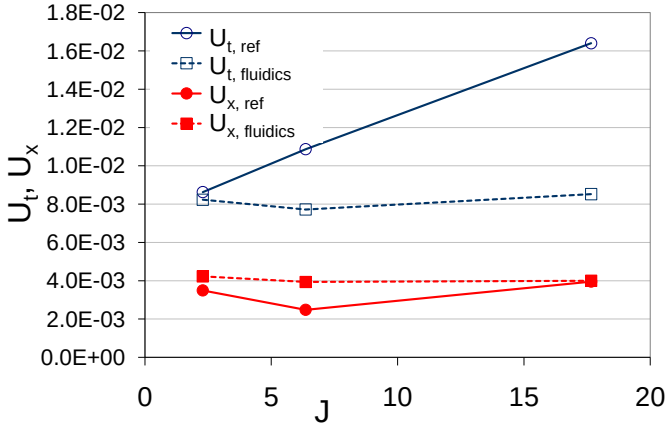

Figure C.8: Spatial and temporal unmixedness criteria depending on the jet to crossflow momentum recorded at $x/d_h = 112$

C.3.2 Evolution of U_x and U_t for J=17.7

The same data are plotted over the mixing length x/d_h and are shown in Fig. C.9. It confirms that the fluidic injector presents a better macromixing (lower U_x) close to the injection location, consequence of the oscillating motion. This improvement decreases while moving further downstream until x/d_h=112 is reached and where both injectors present the similar spatial unmixedness. However regarding, for example, NO_x emissions in gas turbine combustors, the total mixing quality is relevant and therefore the important parameter is the total unmixedness U_t. In this respect, the fluidic technology leads to the best results, at least over the range of parameters investigated. For the momentum ratio J= 17.7, the fluidic injectors reduce the temporal unmixedness by approximately 50%. Indeed, it would potentially be possible to reduce the combustor length by 50% and still achieve the same mixing quality.

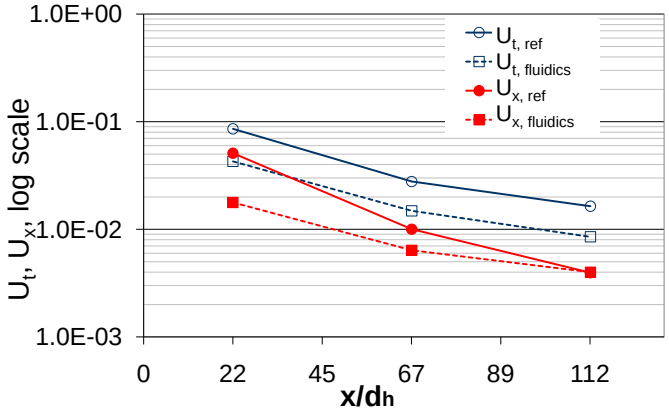

Figure C.9: Spatial and temporal unmixedness criteria, U_x and U_t, depending on the streamwise location for J=17.7

Bibliography

[ABB+06] P. Albrecht, F. Bauermeister, M. Bothien, A. Lacarelle, J. P. Moeck, C. O. Paschereit, and E. Gutmark. Characterization and control of lean blowout using periodically generated flame balls. *ASME Paper 2006-GT-90340*, 2006.

[AK03] K. B. Ariyur and M. Krstić. *Real-Time Optimization by Extremum-Seeking Control*. John Wiley & Sons, Hoboken, 2003.

[Ale09] P. R. Alemela. *Measurement and Scaling of Acoustic Transfer Measurement and Scaling of Acoustic Transfer*. PhD thesis, Technische Universität München, 2009.

[Alk00] H. Alkabie. Design methods of ABB Power GT DLE combustion system. *Proceedings of the Institution of Mechanical Engineers, Part A: Journal of Power and Energy*, 214(4):293–315, 2000.

[AOC96] G. M. Abu-Orf and R. S. Cant. Reaction rate modelling for premixed turbulent methane-air flames. *Joint Meeting of the Portuguese, British, Spanish and Swedish Sections of the Combustion Institute, 1-4 April 1996, Madeira, Portugal.*, 1996.

[Bal89] J. Baldyga. Turbulent mixer model with application to homogeneous, instantaneous chemical reactions. *Chemical Engineering Science*, 44(5):1175–1182, 1989.

[Bar74] M. Barrère. Modèles de combustion. *Revue Générale de Thermique*, 148:295–308, 1974.

[BB82] J. E. Broadwell and R. E. Breidenthal. A simple model of mixing and chemical reaction in a turbulent shear layer. *Journal of Fluid Mechanics*, 125:397–410, 1982.

[BB99] J. Baldyga and J. R. Bourne. *Turbulent mixing and chemical Reactions*. John Wiley & Sons, 1999.

[BB05] F. Vanden Berghen and H. Bersini. CONDOR, a new parallel, constrained extension of powell's UOBYQA algorithm: Experimental results and comparison with the DFO algorithm. *Journal of Computational and Applied Mathematics*, 181:157–175, 2005.

[BBS09] G. Borghesi, F. Biagioli, and B. Schuermans. Dynamic response of turbulent swirling flames to acoustic perturbations. *Combustion Theory and Modelling*, 13:487–512, 2009.

[BCB03] C. Bailly and G. Comte-Bellot. *Turbulence*. Sciences et techniques de l'ingénieur, 2003.

[BG07] F. Biagioli and F. Güthe. Effect of pressure and fuel-air unmixedness on NOx emissions from industrial gas turbine burners. *Combustion and Flame*, 151:274–288, 2007.

[Bia06] F. Biagioli. Stabilization mechanism of turbulent premixed flames in strongly swirled flows. *Combustion Theory and Modelling*, 10(3):389–412, June 2006.

[BKPN06] R. Becker, R. King, R. Petz, and W. Nitsche. Adaptive closed-loop separation control on a high-lift configuration using extremum seeking. *AIAA Paper 2006-3493*, 2006.

[BM91] J. E. Broadwell and M. G. Mungal. Large-scale structures and molecular mixing. *Physics of Fluids*, 3(5):1193–1206, 1991.

[BMLP07] M. R. Bothien, J. P. Moeck, A. Lacarelle, and C. O. Paschereit. Time domain modelling and stability analysis of complex thermoacoustic systems. *Proceedings of the Institution of Mechanical Engineers, Part A: Journal of Power and Energy*, 221(5):657–668, 2007.

[BMP09] M. R. Bothien, J. P. Moeck, and C. O. Paschereit. Assessment of different actuator concepts for acoustic boundary

control of a premixed combustor. *Journal of Engineering for Gas Turbines and Power*, 131(2):021502, 2009.

[Boh98] W. Bohl. *Technische Strömungslehre*. Vogel, 1998.

[Bot08] M. R. Bothien. *Impedance Tuning: A Method for Active Control of the Acoustic Boundary Conditions of Combustion Test Rigs*. PhD thesis, TU-Berlin, 2008.

[BP08] F. Bonzani and C. Piana. From test rig to field operation: a lesson learned. *ASME Paper GT2008-50833*, 2008.

[Bro11] J. G. Brown. New records of soundwaves from a vibrating flame. *Physical Review (Series I)*, 33(5):442–446, 1911.

[BS09] F. Bauermeister and C. Schrödinger. Dokumentation der abgasanalyseanlage. Technical report, Institut für Strömungsmechanik und Technische Akustik, Fachgebiet Experimentelle Strömungsmechanik, Technische Universität Berlin, 2009.

[BSMS07] G. Bulat, D. Skipper, R. McMillan, and K. Syed. Active control of fuel splits in gas turbine DLE combustion systems. *ASME Paper GT2007-27266*, 2007.

[Can02] S. Candel. Combustion dynamics and control: progress and challenges. *Proceedings of the Combustion Institute*, 29:1–28, 2002.

[CBFY07] W. A. Chishty, G. Bourque, M. Furi, and I. Yimer. Experimental characterization of the damping of fuel-air ratio fluctuations using transfer function analysis. *ASME Paper GT2007-27937*, 2007.

[CC56] L. Crocco and S. I. Cheng. *Theory of combustion instability in liquid propellant rocket motors*. AGARD Monograph No 8, Butterworths Scientific Pub., Ltd. London, 1956.

[CGH63] A. E. Clarke, A. J. Gerrard, and L. A. Holliday. Some experiences in gas turbine combustion chamber practice using

water flow visualization techniques. In *Symposium (International) on Combustion*, volume 9, pages 878–891. Elsevier, 1963.

[CGSD10] A. Coussement, O. Gicquel, T. Schuller, and G. Degrez. Large eddy simulation of pulsed jet in crossflow. *AIAA Paper 2010-561*, 2010.

[Chu65] B. T. Chu. On the energy transfer to small disturbances in fluid flow (Part I). *Acta Mechanica*, 1(3):215–234, 1965.

[Cla58] T. Clark. Studies of OH, CO, CH and C2 radiation from laminar and turbulent propane-air and ethylene-air flames. *NACA Technical Note 4266*, 1958.

[Coa96] C. M. Coats. Coherent structures in combustion. *Progress in Energy and Combustion Science*, 22(5):427–509, 1996.

[Cri97] J. P. Crimaldi. The effect of photobleaching and velocity fluctuations on single-point LIF measurements. *Experiments in Fluids*, 23:325–330, 1997.

[CSP01] J. M. Cohen, J. H. Stufflebeam, and W. Proscia. The effect of fuel/air mixing on actuation authority in an active combustion instability control system. *Journal of Engineering for Gas Turbines and Power*, 123:537–542, 2001.

[CY08] W. A. Chishty and I. Yimer. Optimization mixing for maximum damping of fuel-air ratio oscillations in gas turbine premixers. *ASME Paper GT2008-50454*, 2008.

[Dan52] P. V. Danckwerts. The definition and measurement of some characteristics of mixtures. *Applied Science Research*, A3:279–296, 1952.

[Dan53] P. V. Danckwerts. Continuous flow systems, distribution of residence times. *Chemical Engineering Science*, 2:1–13, 1953.

[DB76] P. E. Dimotakis and G. L. Brown. The mixing layer at high Reynolds number: Large-structure dynamics and entrainment. *Journal of Fluid Mechanics*, 78:535–560, 1976.

[DFL+98] H. Du, R. A. Fuh, J. Li, A. Corkan, and J. S. Lindsey. PhotochemCAD: A computer-aided design and research tool in photochemistry. *Photochemistry and Photobiology*, 68:141–142, 1998.

[DFL+07] C. Duwig, L. Fuchs, A. Lacarelle, M. Beutke, and C. O. Paschereit. Study of the vortex breakdown in a conical swirler using LDV, LES and POD. *ASME Paper GT2007-27006*, 2007.

[DH04] D. Dussault and P. Hoess. Noise performance comparison of ICCD with CCD and EMCCD cameras. *Proceedings of SPIE*, 5563:195, 2004.

[Dim00] P. E. Dimotakis. The mixing transition in turbulent flows. *Journal of Fluid Mechanics*, 409:69–98, 2000.

[DKP+94] K. Doebbeling, H. P. Knoepfel, W. Polifke, D. Winkler, C. Steinbach, and T. Sattelmayer. Low NOx combustion of MBTU fuels using the ABB double cone burner (EV burner). *ASME Paper No.94-GT-394*, 1994.

[DLC02] N. Docquier, F. Lacas, and S. Candel. Closed-loop equivalence ratio control of premixed comustors using spectrally resolved chemiluminescence measurements. *Proceedings of the Combustion Institute*, 29:139–145, 2002.

[EB01] A. Eroglu and R. E. Breidenthal. Structure, penetration, and mixing of pulsed jets in crossflow. *AIAA Journal*, 39(3):417–423, 2001.

[EPA08] Latest findings on national air quality. Technical report, United States Environmental Protection Agency, 2008. Contract No. EP-D-05-004 Work Assignment No. 3-4.

[FHS06] E. C. Fernandes, M. V. Heitor, and S. I. Shtork. An analysis of unsteady highly turbulent swirling flow in a model vortex combustor. *Experiments in Fluids*, 40:177–187, 2006.

[Fie03] E. Fielder. *Turbulente Strömungen*. Technische Universität Berlin, Technische Universität Braunschweig, 2003.

[FKS00] J. Fritz, M. Kröner, and T. Sattelmayer. Simultaner Einsatz optischer Messmethoden zur Untersuchung der Flammenausbreitung in verdrallten Rohrströmungen. *Tagungsbericht GALA*, 2000.

[Fox03] R. O. Fox. *Computational models for turbulent reacting flows.* Cambridge University Press, 2003.

[FPB03] P. Flohr, C.O. Paschereit, and V. Bellucci. Steady CFD analysis for gas turbine burner transfer function. *AIAA Paper 2003-1346*, 2003.

[FPG01] S. P. Ferro, R. J. Principe, and M. B. Goldschmidt. A new approach to the analysis of vessel residence time distribution curves. *Metallurgical and Materials Transactions*, 32B:1185–1193, 2001.

[Fri93] T. F. Fric. Effects of fuel-air unpremixedness on NOx emissions. *Journal of Propulsion and Power*, 9:708, 1993.

[Fri03] J. Fritz. *Flammenrückschlag durch verbrennungsinduziertes Wirbelaufplatzen.* PhD thesis, Technische Universität München, 2003.

[FSP02] P. Flohr, P. Schmitt, and C. O. Paschereit. Mixing field analysis of a gas turbine burner. *ASME Paper 2002-39317*, 2002.

[GG99] E. J. Gutmark and F. F. Grinsten. Flow control with non circular jets 1. *Annual Review of Fluid Mechanics*, 31(1):239–272, 1999.

[GGS+10] D. Guyot, F. Guethe, B. Schuermans, A. Lacarelle, and C. O. Paschereit. CH*/OH* chemiluminescence response of an atmospheric premixed flame under varying operating conditions. *ASME Paper GT2010-23135*, 2010.

[GIM08] E. J. Gutmark, I. M. Ibrahim, and S. Murugappan. Circular and noncircular subsonic jets in cross flow. *Physics of Fluids*, 20:075110, 2008.

[GL85] A. K. Gupta and D. G. Lilley. Flowfield modelling and diagnostics. *Abacus, Kent, UK*, 1985.

[GLD97] A. G. Glen, L. M. Leemis, and J. H. Drew. A generalized univariate change-of-variable transformation technique. *INFORMS Journal on Computing*, 9:288–295, 1997.

[GMPS09] D. Guyot, J. P. Moeck, C. O. Paschereit, and B. Schuermans. Optical transfer function measurement for a premixed swirl-stabilized flame at atmospheric conditions. *AIAA Paper 2009-1236*, 2009.

[Goo03] D. G. Goodwin. An open source, extensible software suite for CVD process simulation, 2003. California Institute of Technology, Division of Engineering and Applied Science.

[GPR09] D. Guyot, C.O. Paschereit, and S. Raghu. Active combustion control using a fluidic oscillator for asymmetric fuel flow modulation. *International Journal of Flow Control*, 1(2):155–166, 2009.

[GS07] F. Guethe and B. Schuermans. Phase-locking in post-processing for pulsating flames. *Measurement Science and Technology*, 18(9):3036–3042, 2007.

[GSJ07] P. Griebel, P. Siewert, and P. Jansohn. Flame characteristics of turbulent lean premixed methane/air flames at high pressure: Turbulent flame speed and flame brush thickness. *Proceedings of the Combustion Institute*, 31(2):3083–3090, 2007.

[GTLP11] K. Göckeler, S. Terhaar, A. Lacarelle, and C. O. Paschereit. Residence time distribution in a swirl.stabilized combustor at cold conditions. *AIAA Paper 2011-3585*, 2011.

[Gui73] G. G. Guilbault. *Practical Fluorescence; Theory, Methods and Techniques*. Dekker, New York, 1973.

[Hab00] L. C. Haber. An investigation into the origin, measurement and application of chemiluminescent light emissions from

premixed flames. Master's thesis, Virginia Polytechnic Institute and State University, 2000.

[HAG00] J. P. Hathout, A. M. Annaswamy, and A. F. Ghoniem. Modeling and control of combustion instability using fuel injection. In *AVT Nato Symposium*, Braunschweig, Germany, May 8-11 2000.

[HBF+08] L. Henning, R. Becker, G. Feuerbach, R. Muminovic, R. King, A. Brunn, and W. Nitsche. Extensions of adaptive slope-seeking for active flow control. *Proceedings of the Institution of Mechanical Engineers, Part I: Journal of Systems and Control Engineering*, 222:309–322, 2008.

[HLB98] P. Holmes, J. L. Lumley, and G. Berkooz. *Turbulence, Coherent Structures, Dynamical Systems and Symmetry*. Cambridge University Press, Cambridge, 1998.

[HMLC01] B. Higgins, M. Q. McQuay, F. Lacas, and S. Candel. An experimental study on the effect of pressure and strain rate on CH chemiluminescence of premixed fuel-lean methane/air flames. *Fuel*, 80(11):1583–1591, 2001.

[Hol83] J. D. Holdeman. Perspectives on the mixing of a row of jets with a confined crossflow. *AIAA Paper 1983-1200*, 1983.

[HR70] A. K. M. F. Hussain and W. C. Reynolds. The mechanics of an organized wave in turbulent shear flow. *Journal of Fluid Mechanics*, 41:241–258, 1970.

[HW77] J. D. Holdeman and R. E. Walker. Mixing in a row of jets with a confined crossflow. *AIAA Journal*, 15:243–249, 1977.

[HWJ98] J. C. Hermanson, A. Wahba, and H. Johari. Duty-cycle effects on penetration of fully modulated, turbulent jets in crossflow. *AIAA Journal*, 36(10):1935–1937, 1998.

[HWJ+99] S. Hoffmann, G. Weber, H. Judith, J. Hermann, and A. Orthmann. Application of active combustion control to

Siemens heavy duty gas turbines. In *Applied vehicle technology panel symposium, Lisbon, Portugal (12/10/1998)*, volume 14, pages 12–16, 1999.

[ITT08] ITTC. Uncertainty analysis particle image velocimetry. *Recommended Procedures and Guidelines*, 2008.

[Joh06] H. Johari. Scaling of fully pulsed jets in crossflow. *AIAA Journal*, 44(11):2719–2725, 2006.

[Joo06] F. Joos. *Technische Verbrennung*. Springer, 2006.

[JPTH99] H. Johari, M. Pacheco-Tougas, and JC Hermanson. Penetration and mixing of fully modulated turbulent jets in crossflow. *AIAA Journal*, 37(7):842–850, 1999.

[Kar02] U. Karrenberg. *Signale-Prozesse-Systeme*. Springer, 2002.

[KB61] S. Krishnamahari and H. Broida. Effect of molecular oxygen on the emission spectra of atomic oxygen-acetylene flame. *Journal of Chemical Physics*, 193:417–443, 1961.

[KFDK05] S. Kato, T. Fujimori, A.P. Dowling, and H. Kobayashi. Effect of heat release distribution on combustion oscillation. *Proceedings of the Combustion Institute*, 30(2):1799–1806, 2005.

[KGTS06] S. Kokanovic, G. Guidati, S. Torchalla, and B. Schuermans. Active combustion control system for reduction of NOx and pulsation levels in gas turbines. *ASME Paper 2006-GT-90895*, 2006.

[Kie05] F. Kiesewetter. *Modellierung des verbrennungsinduzierten Wirbelaufplatzen in Vormischbrennern*. PhD thesis, Technische Universität München, 2005.

[Kol41] A. N. Kolmogorov. Dissipation of energy in a locally isotropic turbulence. *Doklady Akad. Nauk SSSR, 32, 141, (English translation in: American Mathematical Society Translations 1958, Series 2, Vol 8, p. 87, Providence R.I)*, 1941.

[Kon76] J. H. Konrad. *An experimental investigation of mixing in two-dimensional turbulent shear flows with applications to diffusion-limited chemical reactions*. PhD thesis, California Institute of Technology, 1976.

[KST91] J. J. Keller, T. Sattelmayer, and F. Thüringer. Double cone burner for gas turbine type 9 retrofit application. In International Council on Combustion Engines (CIMAC), editor, *19th International Congress on Combustion Engines*, 1991.

[KSTA98] H. Kawanabe, M. Shioji, T. Tsunooka, and Y. Ali. CFD simulation for predicting combustion and pollutant formation in a homogeneous-charge spark-ignition engine. *International Symposium COMODIA 98, Tokyo*, pages 233–238, 1998.

[KW00] M. Krstić and H.-H. Wang. Stability of extremum seeking feedback for general nonlinear dynamic systems. *Automatica*, 36:595–601, 2000.

[LB04] M. Lohrmann and H. Büchner. Scaling of stability limits in lean-premixed gas turbine combustors. *ASME Paper GT2004-53710*, 2004.

[LC02] A. N. Lipatnikov and J. Chomiak. Turbulent flame speed and thickness: Phenomenology, evaluation, and application in multi-dimensional simulations. *Progress in Energy and Combustion Science*, 28:1–74, 2002.

[LC03] J. H. W. Lee and V. H. Chu. *Turbulent jets and plumes - a lagrangian approach*. Kluwer Academic Publishers, 2003.

[Lef83] A. H. Lefebvre. *Gas turbine combustion*. Taylor & Francis, 1983.

[LFG+09] A. Lacarelle, T. Faustmann, D. Greenblatt, C. O. Paschereit, O. Lehmann, D. M. Luchtenburg, and B. R. Noack. Spatiotemporal characterization of a conical swirler flow field under strong forcing. *Journal of Engineering for Gas Turbines and Power*, 131:031504, 2009.

[LLB+10] A. Lacarelle, D. M. Luchtenburg, M. R. Bothien, B. R. Noack, and C. O. Paschereit. A combination of image post-processing tools to identify coherent structures of premixed flames. *AIAA Journal*, 48(8):1708–1720, 2010.

[LMK+07] A. Lacarelle, J. P. Moeck, H. J. Konle, S. Vey, C. N. Nayeri, and C. O. Paschereit. Effect of fuel/air mixing on NOx emissions and stability in a gas premixed combustion system. *AIAA Paper 2007-1417*, 2007.

[LMP+09] A. Lacarelle, J. P. Moeck, C. O. Paschereit, G. Gelbert, and R. King. Model based control of emissions and pulsations in a premixed combustor using fuel staging. *ASME Paper GT2009-59300*, 2009.

[LS08] M. Lauer and T. Sattelmayer. Heat release calculation in a turbulent swirl flame from laser and chemiluminescence measurements. *Proceedings of 14th International Symposium on Applications of Laser Techniques to Fluid Mechanics*, 2008.

[LS09] M. Lauer and T. Sattelmayer. On the adequacy of chemiluminescence as a measure of heat release in turbulent flames with mixture gradients. *ASME Paper GT2009-59631*, 2009.

[LTH93] D. S. Liscinsky, B. True, and J. D. Holdeman. Experimental investigation of crossflow jet mixing in a rectangular duct. *AIAA Paper 93-2037*, 1993.

[LTH95a] D. S. Liscinsky, B. True, and J. D. Holdeman. Crossflow mixing of noncircular jets. *AIAA Paper 95-0732*, 1995.

[LTH95b] D. S. Liscinsky, B. True, and J. D. Holdeman. Effects of initial conditions on a single jet in crossflow. *AIAA Paper 95-2998*, 1995.

[LTJZ01] T. Lieuwen, H. Torres, C. Johnson, and B. T. Zinn. A mechanism of combustion instability in lean premixed gas turbine combustors. *Journal of Engineering for Gas Turbines and Power*, 123:182–189, 2001.

[LTVH92] D. S. Liscinsky, B. True, A. Vranos, and J. D. Holdeman. Experimental study of cross-stream mixing in a rectangular duct. *AIAA Paper 92-3090*, 1992.

[LZ98] T. Lieuwen and B. T. Zinn. The role of equivalence ratio oscillations in driving combustion instabilities in low NOx gas turbines. *27th Symposium (International) on Combustion/The Combustion Institute*, pages 1809–1816, 1998.

[MBP+07] J. P. Moeck, M. R. Bothien, C. O. Paschereit, G. Gelbert, and R. King. Two-parameter extremum seeking for control of thermoacoustic instabilities and characterization of linear growth. *AIAA Paper 2007-1416*, 2007.

[MD91] P. L. Miller and P. E. Dimotakis. Reynolds number dependence of scalar fluctuations in a high Schmidt number turbulent jet. *Physics of Fluids*, 3(5):1156–1163, 1991.

[MHD+04] K. McManus, F. Han, W. Dunstan, C. Barbu, and M. Shah. Modeling and control of combustion dynamics in industrial gas turbines. *ASME Paper GT2004-53872*, 2004.

[Mil91] P. L. Miller. *Mixing in High Schmidt Number Turbulent Jets*. PhD thesis, California Institute of Technology, 1991.

[MKO+03] T. M. Muruganandam, B. Kim, R. Olsen, M. Patel, B. Romig, and J. M. Seitzman. Chemiluminescence based sensors for turbine engines. *AIAA Paper 2003-4490*, 2003.

[MM05] S. Muppidi and K. Mahesh. Study of trajectories of jets in crossflow using direct numerical simulations. *Journal of Fluid Mechanics*, 530:81–100, 2005.

[MNL00] J. Mi, G. J. Nathan, and R. E. Luxton. Centerline mixing characteristics of jets from nine differently shaped nozzles. *Experiments in Fluids*, 28:93–94, 2000.

[Moo97] M. J. Moore. NOx emission control in gas turbines for combined cycle gas turbine plant. *Proceedings of the Institution of Mechanical Engineers, Part A: Journal of Power and Energy*, 211:43–52, 1997.

[MTH+96] R. K. Mongia, E. Tomita, F. K. Hsu, L. Talbot, and R. W. Dibble. Use of an optical probe for time-resolved in situ measurement of local air-to-fuel ratio and extent of fuel mixing with application to low NOx emissions in premixed gas turbines. *26th Symposium (International) on Combustion/The Combustion Institute*, pages 2749–2755, 1996.

[Mun87] M. L. Munjal. *Acoustics of dutcs and mufflers with application to exhaust and ventilation system design.* John Wiley & Sons, 1987.

[NCJ97] C. E. Niederhaus, F. H. Champagne, and J. W. Jacobs. Scalar transport in a swirling transverse jet. *AIAA Journal*, 35:1697–1704, 1997.

[NDSC08] N. Noiray, D. Durox, T. Schuller, and S. Candel. A unified framework for nonlinear combustion instability analysis based on the flame describing function. *Journal of Fluid Mechanics*, 615:139–167, 2008.

[NMA+06] G. J. Nathan, J. Mi, Z. T. Alwahabi, G. J. R. Newbold, and D. S. Nobes. Impacts of a jet's exit flow pattern on mixing and combustion performance. *Progress in Energy and Combustion Science*, 32(5-6):496–538, 2006.

[Nor64] E. R. Norster. Jet penetration and mixing studies. unpublished work at College of Aeronautics, Cranfield, England, 1964, Presented in Lefebvre "Gas Turbine Combustion", 1964.

[NP05] F. Nicoud and T. Poinsot. Thermoacoustic instabilities: Should the Rayleigh criterion be extended to include entropy changes? *Combustion and Flame*, 142(1-2):153–159, 2005.

[OHY09] J. Oh, P. Heo, and Y. Yoon. Acoustic excitation effect on NOx reduction and flame stability in a lifted non-premixed turbulent hydrogen jet with coaxial air. *International Journal of Hydrogen Energy*, 34(18):7851–7861, 2009.

[Ose04] L. K. H. Osenbroch. *Experimental and Computational Study of Mixing and Fast Chemical Reactions in Turbulent Liquid Flows*. PhD thesis, The Faculty of Engineering and Science, Aalborg University, 2004.

[PAOK04] E. L. Paul, V. A. Atiemo-Obeng, and S. M. Kresta. *Handbook of industrial mixing: science and practice*. Wiley-IEEE, 2004.

[PB67] B. D. Pratte and W. D. Baines. Profiles of round turbulent jet in cross flow. *Journal of the Hydraulics Division*, 92(53):53–64, 1967.

[Pet86] N. Peters. Laminar flamelet concepts in turbulent combustion. *21st Symposium (International) on Combustion/The Combustion Institute*, pages 1231–1250, 1986.

[Pet99] N. Peters. The turbulent burning velocity for large-scale and small-scale turbulence. *Journal of Fluid Mechanics*, 384:107–132, 1999.

[PFS01] C. O. Paschereit, P. Flohr, and B. Schuermans. Prediction of combustion oscillations in gas turbine combustors. *AIAA Paper 2001-0484*, 2001.

[PGS00] C. O. Paschereit, E. Gutmark, and B. Schuermans. Performance enhancement of gas-turbine combustor by active control of fuel injection and mixing process - theory and practice. In *Applied vehicle technology panel symposium on active control technology for enhanced performance operation capabilities of military aircraft, land vehicles and sea vehicles, North Atlantic Treaty Organization*, Braunschweig, Germany, May 8-11 2000.

[PGW99] C. O. Paschereit, E. J. Gutmark, and W. Weisenstein. Control of thermoacoustic instabilities in a premixed combustor by fuel modulation. *AIAA Paper 99-0711*, 1999.

[PLV01] N. Peters and P. Luc Vervisch. *Turbulent combustion*, volume 125. Elsevier, 2001.

[PM01] G. Pan and H. Meng. Experimental study of turbulent mixing in a tee mixer using PIV and PLIF. *AIChE Journal*, 47(12):2653–2665, 2001.

[Pop00] S. B. Pope. *Turbulent Flows*. Cambridge University Press, Cambridge, UK, 2000.

[PP98] C. O. Paschereit and W. Polifke. Investigation of the thermoacoustic characteristics of a lean premixed gas turbine burner. In *The 1998 International Gas Turbine & Aeroengine Congress & Exhibition*, 1998.

[PPPD01] W. Polifke, A. Poncet, C. O. Paschereit, and K. Doebbeling. Reconstruction of acoustic transfer matrices by instationary computational fluid dynamics. *Journal of Sound and Vibration*, 245(3):483–510, 2001.

[Pra75] D. T. Pratt. Theories of mixing in continuous combustion. *15th Symposium (International) on Combustion/The Combustion Institute*, pages 1339–1351, 1975.

[PSB03] C. O. Paschereit, B. Schuermans, and D. Büchey. Combustion process optimization using evolutionary algorithm. *ASME Paper 2003-GT-38393*, 2003.

[PSPM02] C. O. Paschereit, B. Schuermans, W. Polifke, and O. Mattson. Measurement of transfer matrices and source terms of premixed flames. *Journal of Engineering for Gas Turbines and Power*, 124(2):239–247, 2002.

[Put71] A. A. Putnam. *Combustion Driven Oscillations in Industry*. American Elsevier, New York, 1971.

[PV05] T. Poinsot and D. Veynante. *Theoretical and numerical combustion*. RT Edwards, Inc., 2005.

[PVC91] T. Poinsot, D. Veynante, and S. Candel. Quenching processes and premixed turbulent combustion diagrams. *Journal of Fluid Mechanics*, 228:561–605, 1991.

[Ray78] J. W. S. Rayleigh. The explanation of certain acoustical phenomena. *Nature*, 18(455):319–321, 1878.

[RM00] A. Ramond and P. Millan. Measurements and treatment of LDA signals, comparison with hot-wire signals. *Experiments in Fluids*, 28:58–63, 2000.

[RR08] G. A. Richards and E. H. Robey. Effect of fuel system impedance mismatch on combustion dynamics. *Journal of Engineering for Gas Turbines and Power*, 130(1):011510, 2008.

[RSR03] G. A. Richards, D. L. Straub, and E. H. Robey. Passive control of combustion dynamics in stationary gas turbines. *Journal of Propulsion and Power*, 19(5):795–810, 2003.

[Sat03] T. Sattelmayer. Influence of the combustor aerodynamics on combustion instabilities from equivalence ratio fluctuations. *Journal of Engineering for Gas Turbines and Power*, 125:11–19, 2003.

[SBFP04] B. Schuermans, V. Bellucci, P. Flohr, and C. O. Paschereit. Thermoacoustic flame transfer function af a gas turbine burner in premix and pre-premix combustion. *AIAA Paper 2004-0456*, 2004.

[Sch03] B. Schuermans. *Modeling and Control of Thermoacoustic Instabilities*. PhD thesis, Ecole Polytechnique Federale de Lausanne, 2003.

[SF00] T. Scarinci and C. Freeman. The propagation of a fuel air ratio disturbance in a simple premixer and its influence on pressure wave amplification. *ASME Paper 2000-GT-106*, 2000.

[SFD04] T. Scarinci, C. Freeman, and I. Day. Passive control of combustion instability in a low emissions aeroderivative gas turbine. *ASME Paper GT2004-53767*, 2004.

[SFH+92] T. Sattelmayer, M. P. Felchlin, J. Haumann, J. Hellat, and D. Styner. Second generation low-emissions ABB combustors for gas turbines: Burner development and tests at atmospheric pressure. In *Transactions of the American Society of Mechanical Engineers*, volume 114, pages 118–24, 1992.

[SGE00] R. Sonnenberger, K. Graichen, and P. Erk. Fourier averaging: a phase-averaging method for periodic flow. *Experiments in Fluids*, 28:217–224, 2000.

[SGF+99] G. P. Smith, D. M. Golden, M. Frenklach, N. W. Moriarty, B. Eiteneer, M. Goldenberg, C. T. Bowman, R. K. Hanson, S. Song, W. C. Gardiner, and V. V Lissianski. GRI-Mech 3.0. `http://www.me.berkeley.edu/gri_mech/`, 1999.

[SGM08] B. Schuermans, F. Guethe, and W. Mohr. Optical transfer function measurements for technically premixed flames. *ASME Paper GT2008-51500*, 2008.

[SGP+09] B. Schuermans, F. Guethe, D. Pennell, D. Guyot, and C. O. Paschereit. Thermoacoustic modeling of a gas turbine using transfer functions measured at full engine pressure. *ASME Paper, GT2009-59605*, 2009.

[SJMS01] S. Shahidinejad, I. Jerphanion, F. Magaud, and M. Souhar. Effects of pulsation on grid-generated turbulence. *Journal of Fluids Engineering*, 123:951–953, 2001.

[SKS99] J. H. Stufflebeam, D. W. Kendrick, and W. A. Sowa. Quantifying fuel/air unmixedness in premixing nozzles using an acetone fluorescence technique. *ASME Paper 99-GT-399*, 1999.

[SM98] S. H. Smith and M. G. Mungal. Mixing, structure and scaling of the jet in crossflow. *Journal of Fluid Mechanics*, 357:83–122, 1998.

[SM00] J. Samuelson and M. Miyasoto. Active control for reducing the formation of nitrogen oxides in industrial gas burners and stationary gas turbines. Technical report, California Energy Commission, 2000.

[SOK+10] C. Schrödinger, M. Oevermann, O. Krüger, A. Lacarelle, and C. O. Paschereit. CFD modeling of the influence of fuel staging on the mixing quality and flame characteristics in lean premixed combustion. *ASME Paper GT2010-22910*, 2010.

[Squ50] H. B. Squire. Jet flow and its effects on aircraft. *Aircraft Engineering : Journal of Aeronautical Engineering*, 22:62–67, 1950.

[SRM07] K. J. Syed, K. Roden, and P. Martin. A novel approach to predicting NOx emissions from dry low emissions gas turbines. *Journal of Engineering for Gas Turbines and Power*, 129:672–679, 2007.

[STS68] C. N. Sittel, W. D. Threadgill, and K. B. Schnelle. Longitudinal dispersion for turbulent flow in pipes. *Industrial and Engineering Chemistry Fundamentals*, 7:39–43, 1968.

[Syr06] N. Syred. A review of oscillation mechanisms and the role of the precessing vortex core (PVC) in swirl combustion systems. *Progress in Energy and Combustion Science*, 32:93–161, 2006.

[TLW08] K. M. Tacina, C. M. Lee, and C. Wey. NASA Glenn high pressure low NOx emissions research. *NASA/TM-2008-214974*, 2008.

[TNI+08] S. Tanimura, M. Nose, K. Ishizaka, S. Takiguchi, and J. Rodriguez. Advanced dry low NOx combustor for Mitsubishi G class gas turbine. *ASME Paper GT 2008-50819*, 2008.

[UC97] M. Ulitsky and L. R. Collins. Relative importance of coherent structures vs background turbulence in the propagation of a premixed flame. *Combustion and Flame*, 111(4):257–275, 1997.

[Van04] K. Vanoverberghe. *Flow, Turbulence and Combustion of Premixed Swirling Jet Flames*. PhD thesis, Katholieke Universiteit Leuven, 2004.

[vdLGDJL97] R. P. van der Lans, P. Glarborg, K. Dam-Johansen, and P. S. Larsen. Residence time distributions in a cold, confined swirl flow. Implications for chemical engineering combustion modelling. *Chemical Engineering Science*, 52(16):2743–2756, 1997.

[VPDM96] D. Veynante, J. Piana, J. M. Duclos, and C. Martel. Experimental analysis of flame surface density models for premixed turbulent combustion. In *Symposium International on Combustion*, volume 1, pages 413–420. Combustion Institute, 1996.

[Wal87] D. A. Walker. A fluorescence technique for measurement of concentration in mixing liquids. *Journal of Physics E: Scientific Instruments*, 20, 1987.

[Wan00] G. Wang. *Turbulent mixing, stability and secondary flow in a confined configuration.* PhD thesis, Technische Universität, Berlin, 2000.

[Wäs08] J. G. Wäsle. *Vorhersage der Lärmemission turbulenter Vormischflammen.* PhD thesis, Technischen Universität München, 2008.

[WK00] H. H. Wang and M. Krstić. Extremum seeking for limit cycle minimization. *IEEE Transaction On Automatic Control,*, 45(12):2432–2437, 2000.

[WMD06] J. Warnatz, U. Maas, and R. W. Dibble. *Combustion: Physical and Chemical Fundamentals, Modeling and Simulation, Experiments, Pollutant Formation.* Springer, 4th edition, 2006.

[WWRS06] J. Wäsle, A. Winkler, E. Rößle, and T. Sattelmayer. Development of an annular porous burner for the investigation of adiabatic unconfined flames. *13th Int. Symp. on Applications of Laser Techniques to Fluid Mechanics*, 2006.

Author's Publications

Patent

[1] A. Lacarelle and C. O. Paschereit. Verfahren und Mischvorrichtung zum Mischen von zwei Fluiden sowie deren Verwendung. German patent application number 102010017523.4-23, 2010.

Journals with Peer Review

[1] A. Lacarelle and C. O. Paschereit. Increasing the passive scalar mixing quality of jets in crossflow with fluidics actuators. *Journal of Engineering for Gas Turbines and Power*, 2011. in press.

[2] A. Lacarelle, D. M. Luchtenburg, M. R. Bothien, B. R. Noack, and C. O. Paschereit. A combination of image post-processing tools to identify coherent structures of premixed flames. *AIAA Journal*, 48(8):1708–1720, 2010.

[3] P. Albrecht, S. Bade, A. Lacarelle, C. O. Paschereit, and E. J. Gutmark. Instability control by premixed pilot flames. *Journal of Engineering for Gas Turbines and Power*, 132(4):041501, 2010.

[4] A. Lacarelle, T. Faustmann, D. Greenblatt, C. O. Paschereit, O. Lehmann, D. M. Luchtenburg, and B. R. Noack. Spatiotemporal characterization of a conical swirler flow field under strong forcing. *Journal of Engineering for Gas Turbines and Power*, 131:031504, 2009.

[5] M. R. Bothien, J. P. Moeck, A. Lacarelle, and C. O. Paschereit. Time domain modelling and stability analysis of complex thermoacoustic systems. *Proceedings of the Institution of Mechanical Engineers, Part A: Journal of Power and Energy*, 221(5):657–668, 2007.

Conferences

[1] A. Lacarelle and C. O. Paschereit. Increasing the passive scalar mixing quality of jets in crossflow with fluidics actuators. *ASME Paper GT2011-45583*, 2011.

[2] A. Lacarelle, S. Göke, and C. O. Paschereit. Prediction of NOx emissions of premixed burners with cold flow measurements and reactor network model. *ASME Paper GT2010-23132*, 2010.

[3] C. Schrödinger, M. Oevermann, O. Krüger, A. Lacarelle, and C. O. Paschereit. CFD modeling of the influence of fuel staging on the mixing quality and flame characteristics in lean premixed combustion. *ASME Paper GT2010-22910*, 2010.

[4] A. Lacarelle, L. Matho, and C. O. Paschereit. Sacalar mixing enhancement in a swirl stabilized combustor through passive and active injection control. *AIAA Paper 2010-1332*, 2010.

[5] D. Guyot, F. Guethe, B. Schuermans, A. Lacarelle, and C. O. Paschereit. CH*/OH* chemiluminescence response of an atmospheric premixed flame under varying operating conditions. *ASME Paper GT2010-23135*, 2010.

[6] A. Lacarelle, J. P. Moeck, C. O. Paschereit, G. Gelbert, and R. King. Model based control of emissions and pulsations in a premixed combustor using fuel staging. *ASME Paper GT2009-59300*, 2009.

[7] A. Emara, A. Lacarelle, and C. O. Paschereit. Pilot flame impact on flow fields and combustion performances in a swirl inducing burner. *AIAA Paper 2009-0729*, 2009.

[8] A. Lacarelle, J. P. Moeck, A. Tenham, and C. O. Paschereit. Dynamic mixing model of a premixed combustor and validation with flame response measurements. *AIAA Paper 2009-0986*, 2009.

[9] J. P. Moeck, M. R. Bothien, S. Schimek, A. Lacarelle, and C. O. Paschereit. Subcritical thermoacoustic instabilites in a premixed combustor. *AIAA Paper 2008-2946*, 2008.

[10] C. Duwig, L. Fuchs, A. Lacarelle, M. Beutke, and C. O. Paschereit. Study of the vortex breakdown in a conical swirler using LDV, LES and POD. *ASME Paper GT2007-27006*, 2007.

[11] A. Lacarelle, J. P. Moeck, H. J. Konle, S. Vey, C. N. Nayeri, and C. O. Paschereit. Effect of fuel/air mixing on NOx emissions and stability in a gas premixed combustion system. *AIAA Paper 2007-1417*, 2007.